Effects of Mechanical Interventions on Human Locomotion

by

Jongwoo Lee

Submitted to the Department of Mechanical Engineering
in partial fulfillment of the requirements for the degree of

Doctor of Philosophy in Mechanical Engineering

at the

MASSACHUSETTS INSTITUTE OF TECHNOLOGY

September 2021

Author .....
Department of Mechanical Engineering
Aug 13, 2021

Certified by .....
Neville Hogan
Professor of the Department of Mechanical Engineering and the
Department of Brain and Cognitive Sciences
Thesis Supervisor

Accepted by .....
Nicolas Hadjiconstantinou
Chairman, Department Committee on Graduate Theses

Effects of Mechanical Interventions on Human Locomotion

by

Jongwoo Lee

Submitted to the Department of Mechanical Engineering
on Aug 13, 2021, in partial fulfillment of the
requirements for the degree of
Doctor of Philosophy in Mechanical Engineering

Abstract

Due to population ageing and increasing incidence of neurological disorders, the demand for robotic technologies for assisting, augmenting, and restoring human locomotion is rapidly increasing. Recent approaches aim to make the devices adaptive to improve performance and to deal with individual differences. When developing adaptive devices, however, it should be remarked that humans are also adaptive, and physical interaction with mechanical interventions may substantially change their behavior. To advance technologies for human locomotion, therefore, not only it is important to understand fundamentals of human locomotion itself, but also it is required to understand how human locomotion is altered by the mechanical interventions.

In this thesis, I aimed to understand and establish fundamentals of the effects of mechanical interventions on human locomotion. In the first part of the thesis, I characterized how human walking was changed with a powered hip exoskeleton robot and investigated its underlying principles. In the second part of the thesis, I quantified how human balance on a narrow beam was substantially and immediately changed by altering mechanical interface or using mechanical support (i.e., canes). Behavioral indicators of changes in central neural processes were investigated, which is critical to determine the potential of an intervention for rehabilitation or compensation. In the last part of the thesis, I developed methods to quantify human balance mechanisms during normal standing without applying perturbations which may evoke perturbation-dependent changes to the identified human behavior. Throughout this work, simple models were extensively used to design and interpret human experiments as well as to quantify human behaviors with a handful of parameters.

Thesis Supervisor: Neville Hogan
Title: Professor of the Department of Mechanical Engineering and the Department of Brain and Cognitive Sciences

Acknowledgments

First and foremost, I would like to thank my advisor, Prof. Neville Hogan. The very first class that I took at MIT was his "Advanced System Dynamics and Control" and that entirely changed my life. All of my accomplishments and academic and personal growth in the last four years wouldn't have been possible without his insights, patience, intuition, and encouragement. I sincerely respect him as a professor, scholar, educator, mentor, and as a human.

I sincerely thank my committee members, Prof. Dagmar Sternad, Prof. Jean-Jacques Slotine, and Prof. Harry Asada, who were willing to provide their perspectives and share their expertise as I struggled.

Special thanks to my inter-disciplinary collaborators. Meghan Huber, Marta Russo, Kaymie Shiozawa, Rika Sugimoto-Dimitrova, Kuangen Zhang, and UROPs. I really enjoyed intellectual discussions we had and the moments we talked about possible future research ideas.

I appreciate Samsung scholarship for supporting my entire graduate school life, and offering many opportunities to network with great people.

Thank you the members of the Newman Lab. I miss a lot the days and all-nighters we had on the mezzanine before pandemic. I wish everything goes well with you all. Let's keep in touch.

Thank you to the wonderful staff of the MIT mechanical engineering department.

Thank you to the MIT KGSA, MIT KGSAME, and Boston Korean community.

Thank you to all of my friends here in the US, and there in Korea, who always supported me and inspired me to complete my journey.

Last but not least, my family, Mom, Dad, Jongmin, Daeun, and Alkong-Dalkong, thank you for always being there, thank you for your endless support and love. I love you.

Contents

List of Figures

List of Tables

Chapter 1

Introduction

1.1 Background

Due to population ageing and increasing incidence of neurological disorders, the demand for robotic technologies for assisting, augmenting, and restoring human locomotion is rapidly increasing. Between 2017 and 2050, the percentage of the global population over 60 is expected to nearly double from 13% to 21.5% [214]. In the U.S., more than 14% of the elderly population (about 6.8 million) required mobility assistive devices to compensate for impaired gait and/or balance [92]. Population ageing is also accompanied by an exponential increase in the incidence of neurological disorders that lead to locomotion impairment [58, 137]. For example, 65% of post-stroke survivors experience considerable gait deficits [90, 95, 227] and 795,000 people have a stroke each year [136]. As a whole, about 20.6 million individuals in the U.S. suffered from ambulatory disability in 2019 [105].

Robot-aided locomotor rehabilitation therapies have emerged as promising methods to meet this enormous demand, as robots facilitate safe and efficient delivery of repetitive, high-intensity, and task-oriented training, which are considered important for rehabilitation [36, 61, 121]. Moreover, various types of passive walk-aids [19] and active robotic devices such as exoskeleton with and without crutches [46] have been developed for assisting balance and walking for physically challenged persons.

On the other hand, research on orthotic devices and active exoskeletons to aug-

ment able-bodied human performance has rapidly expanded over the previous decades [46, 236]. This type of robotic devices is designed to add and dissipate power at one or multiple joints of the lower-extremities to increase strength, provide greater endurance, and improve other physical capabilities by able-bodied individuals. In particular, the potential of using lower-limb exoskeletons to augment human walking and running by reducing metabolic cost and muscle effort has been successfully demonstrated over the past decades [183]. Despite the differences in the intended use, developing effective devices either for augmenting, assisting, or restoring human locomotion face many of the same challenges and constraints [46].

Recent breakthroughs in wearable robotics to improve locomotor economy was achieved by making devices adaptive to automatically adjust the torque profile provided by the robots while users were walking or running [44, 60, 239]. Despite several challenges, these works found evidence of participant-specific responses to the parameters of the robot, highlighting the importance of adaptive and individualized control strategies that can offer substantial benefits over fixed control strategies.

When developing adaptive devices, however, it should be remarked that humans are notoriously adaptive as well. Physical interaction with mechanical interventions may substantially change human locomotion, and these changes would be intervention-specific. As evidenced by the previous work [239], finding a good generic assistance pattern and specifying the parameters to adapt are the prerequisites for developing successful adaptive devices. In order to find the 'good' generic pattern, characterizing how humans interact with mechanical interventions is needed.

This prompts us to step back and ask fundamental research questions. To advance technologies for human locomotion, not only it is important to understand fundamentals of how healthy humans walk and balance, but also it is critical to understand how human locomotion is altered by the various mechanical interventions. It will lead us to identifying effective interventions either for augmenting, assisting, or restoring human locomotion — and that invites active interdisciplinary research between many fields.

1.2 Challenges to Develop Effective Devices for Human Locomotion

1.2.1 Understanding Fundamentals of Human Locomotion

Despite many seminal works [75, 225] that describe normal healthy human balancing and walking, we still do not have a comprehensive and constructive understanding of how humans could manage their many-degrees-of-freedom body (about 200 bones) using highly redundant actuators (about 600 muscles) in a coordinated manner.

Characterizing common patterns across subjects is an important first step towards understanding human behavior; however, it is not sufficient. The signals we measure, e.g. joint motion, task-space motion, muscle or neural activities, are outputs of the closed-loop system constructed by human neuro-motor controller and bio-mechanical constraints imposed by human body and the environment (e.g., gravity, ground, etc.). The observed pattern may be the target control variable or an emergent consequence of regulating other variables. For example, it was found that humans exhibit a specific ground reaction force patterns during walking [66, 125], but a subsequent study suspected that the pattern might be emergent rather than controlled [138]. Therefore, when analyzing human behaviors, it is important to dissociate the contributions from control and mechanics (i.e., "bugs or features?").

Identifying functional control variable of human locomotion is important for generalization because different systems, such as humans with exoskeletons, prosthetics, canes, or other assistive/rehabilitative devices, have different biomechanical constraints. Simply mimicking and imposing 'normal' human patterns may not lead to success; for example, early-robotic gait rehabilitation technology that imposed a prescribed 'normal' kinematic trajectory has not met our expectation [51, 71].

To make progress, we may begin with reasonable assumptions on the structure of the controller when analyzing human behaviors. Due to physical limitations, humans may have simplified their control [72]. Identifying the competent structure of the simple controller and human models and evaluating whether it can account for the

experimental observations may promote insights.

1.2.2 Understanding Interaction Between Humans and Mechanical Interventions

Humans are notoriously adaptive to mechanical interventions, but predicting how humans would adapt to a novel intervention is challenging. The predictions made by state-of-the-art computational human models often mismatch the experimental observations [2, 35], even though those models could successfully reproduce many aspects of normal human walking. This is because the behavior of a system in isolation and the same system physically coupled to another may significantly differ [29, 72], and because we have limited measurements and data to build a complete human model that can precisely predict human behaviors in any novel environments.

At this stage of human motor control research [10], characterizing human responses to individual interventions would be valuable. As mentioned above, this is a required step to validate potential of an intervention and to justify further improvement. Moreover, it will add a valuable data to understand interaction between human locomotion and mechanical intervention.

Characterizing behavioral response evoked by an intervention provides useful information to determine whether the intervention holds promise for neuro-recovery [18, 80]. An intervention that does not evoke any changes in central neuro-motor control does not hold promise for long-term recovery, but may successfully assist or augment human locomotion while it is active.

1.3 Contribution

In this thesis, I designed, conducted, and/or participated in healthy human experiments to investigate how simple mechanical interventions alter human locomotion (balance and walking), quantified behavioral changes to understand their neuro / mechanical origin, developed simple models to account for experimental observations

and to gain insight, and developed methods to quantitatively assess human balance without applying perturbations.

1.3.1 Principles

To gain insight and make progress, I conducted my research based on the following principles.

- To study unimpaired population because it promises a faster route to insight than highly-variable impaired population.
- To study mechanical (kinematic and kinetic) behaviors rather than detailed neuro-muscular activities that are hard to measure without invasion and often incompatible with experiments conducted outside the lab. Dynamical systems point of view and control theories of articulated mechanical systems can enhance our understanding of human locomotion.
- To work with simple models rather than high-fidelity complex models. The purpose of modeling is to gain insight, not just to make precise predictions. Well-established simple models with known structures are useful to design experiments, interpret the results, and quantify human locomotion.

1.4 Thesis Organization

Several complementary projects were conducted, with special attention to the effects of mechanical interventions on human walking and balancing. The three projects conducted in this thesis are illustrated in Fig. 1-1.

Part I presents how healthy humans changed their walking pattern in response to different interventions applied by a hip exoskeleton robot (Fig. 1-1a).

The sense of balance is another mechanism that is important for locomotion. Part II presents how human balance on a beam was affected by the (passive) mechanical interventions such as wearing rigid soles or using canes (Fig. 1-1b).

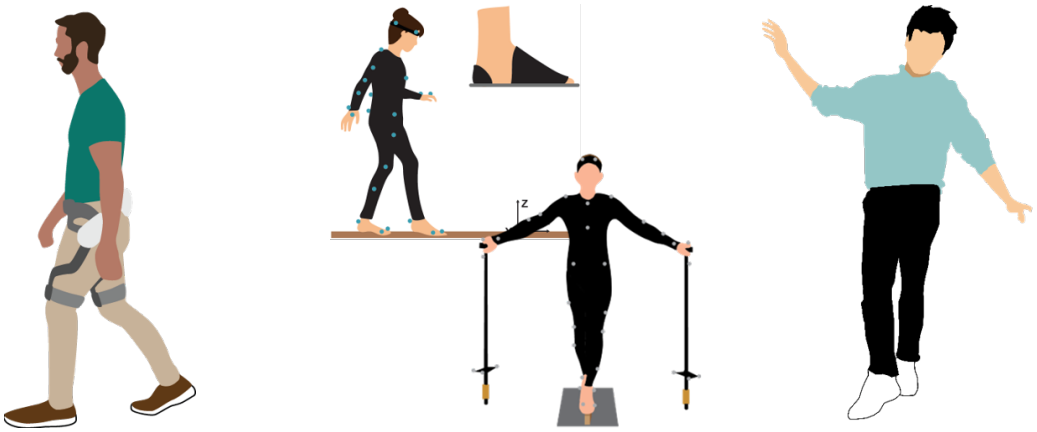

(a) Characterize human walking with mechanical interventions

(b) Characterize human balance with mechanical interventions

(c) Quantifying human balance mechanisms without applying perturbations

Figure 1-1: Several complementary projects conducted in this thesis

As presented in Part I and Part II, humans are highly adaptive to mechanical perturbations. Therefore, Part III presents two complementary methods to identify human balance mechanisms during normal standing, without applying external perturbations to avoid evoking adaptation during estimation process (Fig. 1-1c).

All of these works were conducted with close collaboration with many researchers. At the beginning of each chapter, I highlighted contributions of the collaborators and funding sources.

Part IV will conclude the thesis with some general points of discussion and open research questions that would be useful to advance the field.

Part I

Walking with a Hip Exoskeleton

Chapter 2

Overview

While rehabilitation of upper-limb motor function with human-interactive robots has met with success, robot-aided locomotor rehabilitation has been challenging. To inform more effective approaches to robotic gait therapy, it is important to understand neuro-mechanical dynamics and control of unimpaired locomotion and how it interacts with the robotic interventions.

In Chapter 3, we investigated how human gait was altered when a hip exoskeleton robot applied periodic sequences of torque pulses, especially when the period of intervention was close to but different from natural preferred stride duration. This intervention was designed to test the generality of mechanical entrainment-based rehabilitation which was first proposed in [4]. Experiments were conducted outside the lab to investigate more natural human behavior.

In Chapter 4, we investigated how human gait was altered when a hip exoskeleton robot applied torques to emulate a virtual spring in between thighs. Changes in spatio-temporal gait parameters were characterized in response to both positive and negative stiffness during walking overground and on a treadmill.

Both experimental studies were conducted using a wearable hip exoskeleton robot, the Samsung Gait Enhancing and Motivating Systems for Hip (GEMS-H), developed by Samsung Advanced Institute of Technology (SAIT). This low-mass autonomous exoskeleton device enabled human subject experiments during overground walking. All experiments were conducted with young unimpaired subjects.

With a view to applications in locomotor rehabilitation, the studies assessed whether each intervention induced changes in the gait pattern during walking, and whether any behavioral changes were indicative of changes in central neuro-motor control. Lack of such evidence would imply that the intervention is only suitable for compensation; otherwise, the intervention may hold promise for rehabilitation.

Finally, in Chapter 5, we developed a mathematical model and simulation to encapsulate the results of both experimental studies. A necessary neuro-motor control structure of human walking was discussed and then a simple human walking model was presented.

Chapter 3

Human walking with torque pulses between thighs

This work was done in collaboration with Dr. Meghan E. Huber (Newman Lab for Biomechanics and Human Rehabilitation, MIT; now Prof. Meghan E Huber at Human Robot Systems Laboratory, University of Massachusetts). We implemented controller, designed and conducted human experiments, and analyzed data together. We would like to thank Devon Goetz (MIT) and Vibha Agarwal (MIT) for their help in collecting and analyzing the data.

This work was supported by the Global Research Outreach program of Samsung Advanced Institute of Technology and a Samsung scholarship. Devon Goetz and Vibha Agarwal were also supported by the MIT Undergraduate Research Opportunity Program (UROP). Prof. Neville Hogan was also supported by the Eric P. and Evelyn E. Newman fund, NIH-R01-HD087089, NSF-NRI 1637824, and NSF-CRCNS-1724135.

This work was partially presented in [108], and submitted as in [111].

3.1 Introduction

While there is evidence to suggest that complementing conventional gait therapy with robot-aided training can be beneficial [127], but on its own, robot-aided gait

therapy does not outperform conventional physical therapy in terms of clinical measures (such as walking speed, step length, and step frequency) [71]. The recent rise of autonomously powered exoskeleton robots promises new avenues of delivering therapy in more ecological contexts, outside of a formal clinical setting [83, 121, 130]. To live up to their promise and maximize gait recovery, however, we must better understand natural human locomotion and how humans react to exoskeletal robotic interventions.

Earlier robotic gait rehabilitation approaches have been criticized as they enforced repetition of preprogrammed kinematics which may have discouraged active engagement of participants and suppressed their natural rhythmic dynamics of walking [31, 71, 145]. Our previous studies proposed a novel robotic intervention to modulate gait frequency that respects the rhythmic dynamic nature of walking: gait entrainment [5]. It was shown that applying periodic torque pulses at the ankle, using an ankle exoskeleton robot, could induce subjects to increase their cadence to synchronize with the period of the pulses, when the pulse period was close to but shorter than subjects' preferred stride duration. This experimental observation also suggests that a nonlinear neuro-mechanical limit cycle oscillator is a reasonable description of the dynamics of human walking. Moreover, subjects adapted their gait so that plantar-flexion torque pulses from the robot aligned with ankle push-off, which maximized their mechanical assistance. Subsequent studies showed that entrainment was observed more often, occurred earlier, and persisted longer during overground walking compared to treadmill walking [145]. Motivated by this success with healthy individuals, Ahn et al. studied the feasibility of this intervention to treat locomotor deficits of neurologically-impaired patients and increase their cadence and walking speed [8]. This paradigm is similar to the auditory entrainment but different in that it involves physical interaction and energy exchange.

Gait entrainment to rhythmic, auditory signals is well-known and has been studied in depth [40, 41, 115, 166], but synchronization to other forms of rhythmic stimuli is underexplored. Since the pioneering work of Ahn and Hogan that investigated gait entrainment to exoskeletal mechanical signals [5], there is a growing interest in gait entrainment to various types of stimuli, including an oscillating treadmill [141, 203],

periodic vertical force [186], and electrical muscle stimulation [144,207]. These studies share the motivation that gait entrainment holds promise for locomotor rehabilitation, as well as providing a useful experimental paradigm to better inform neuro-motor control of human walking. However, results also show that while promising, gait entrainment is not straightforward to achieve.

The goal of the present study was to test whether humans similarly entrain to periodic torque pulses applied at the hip joints while walking overground. Torque pulses were applied by an autonomous hip exoskeleton robot, the Samsung Gait Enhancing and Motivating Systems for Hip (GEMS-H). We hypothesized that subjects would entrain their gait to periodic perturbations applied to the hip joint, consistent with prior results from the ankle entrainment studies. A preliminary study showed that entrainment to hip torque pulses seemed promising [108]. In the study reported here, experiments were conducted for two consecutive days to evaluate whether the second day elicited more entrainment. We also assessed how increasing the difference between the torque pulse period and subjects' preferred stride duration affected human's responses. Finally, we investigated whether subjects aligned the torque pulses to a specific phase of the gait cycle; and whether it was related to the mechanical power or work done by the hip exoskeleton robot, similar to the behavior observed in prior entrainment studies using an ankle exoskeleton [4, 145]. Assessment of gait entrainment requires accurate and reliable phase estimation. We developed an off-line stride segmentation algorithm and applied a phase estimation algorithm developed in [220], which do not requiring external sensors such as motion capture or foot-switches.

3.2 Methods

3.2.1 Subjects

A total of fifteen healthy young adults (gender: 4 females, 11 males; mean age: 25.53 years old) participated in this study. They were divided into two groups: group-25ms ($N = 7$) and group-50ms ($N = 8$). All subjects gave informed written consent

before the experiment. The experimental protocol was reviewed and approved by the Institutional Review Board of the Massachusetts Institute of Technology (protocol #: 1809534122; approval date: 10/18/2018).

3.2.2 Equipment: Samsung GEMS-H Exoskeleton.

The Samsung Gait Enhancing and Motivating Systems for Hip (GEMS-H) developed by Samsung Advanced Institute of Technology (Suwon, South Korea) was used in this study (Figure 1a; [106, 114, 116, 189]). This low-mass (2.1 kg) robot is worn around the waist and fastened to the thighs. A pair of actuators, one at each hip joint, applies torque in the sagittal plane (hip flexion and extension). Passive hinges allow unencumbered hip ab/adduction motion in the frontal plane. The torque output of each actuator is estimated and controlled by sensing electrical current in the respective motor. Encoders embedded in the actuator modules measure hip joint angles. All electronics, actuators, and power sources are located onboard the device, allowing for untethered operation. Unlike laboratory-based tethered exoskeleton testbeds [33, 65, 160, 239], this autonomous exoskeleton allows experiments to be conducted overground, thereby enabling study of the effects of intervention in more ecological contexts.

3.2.3 Experimental Procedure

On two consecutive days, all subjects performed ten walking trials (two baseline trials followed by eight pulse trials) per day wearing the GEMS-H exoskeleton (Fig. 3-1A). Each trial consisted of 120 strides, and all trials were performed in a long corridor (approximately 250 m) with low foot traffic to simulate real-world walking conditions. Throughout the trials, subjects listened to white noise through wireless, over-the-ear headphones to mask the sound of the exoskeleton and environment. Subjects were instructed to walk at their comfortable pace, but they were neither informed that the torque pulses would be delivered periodically, nor asked to “entrain" to these perturbations. The experiment lasted approximately 45 minutes on each day.

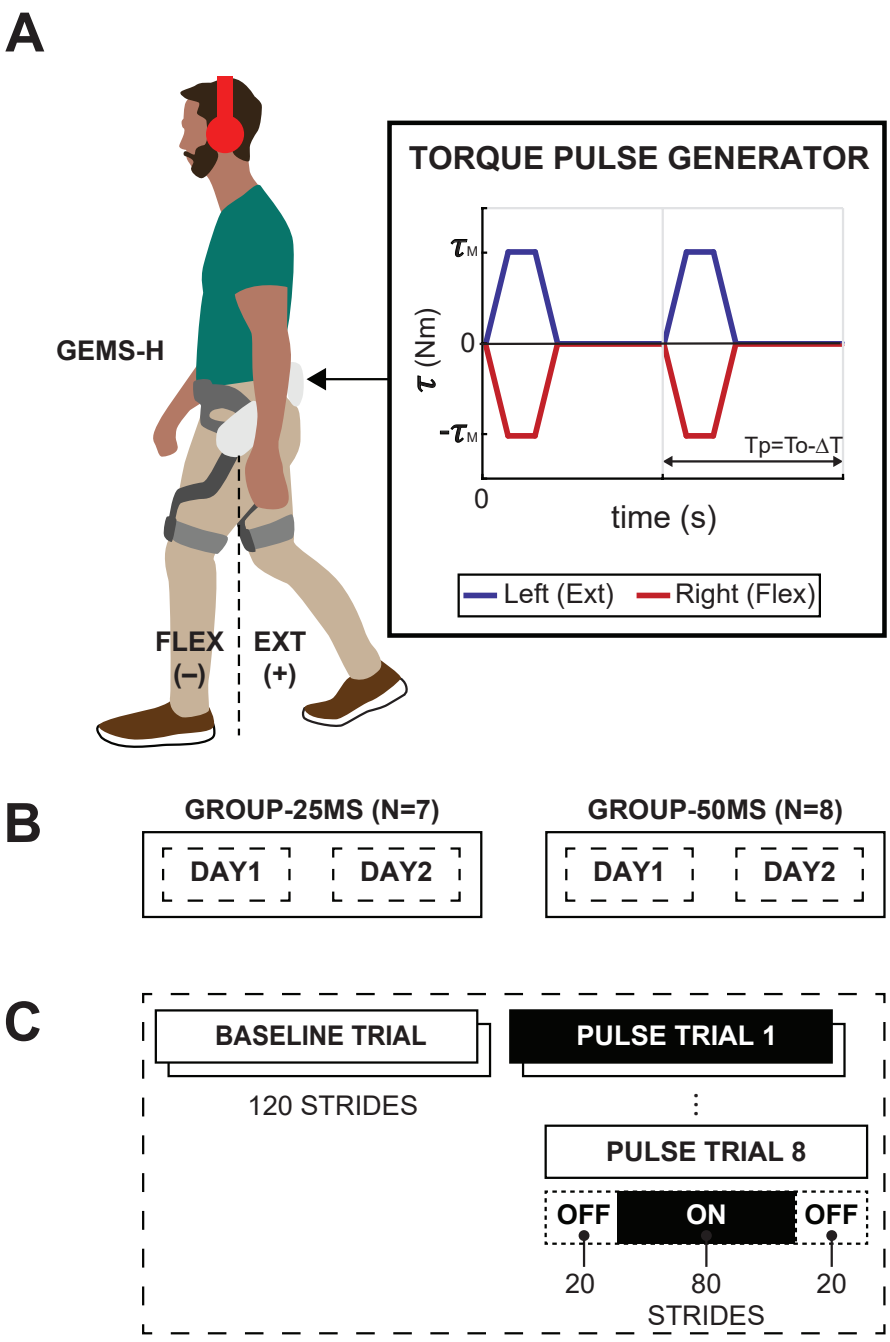

Figure 3-1: **A** The Samsung GEMS-H exoskeleton applied torque pulses between the two thighs. Subjects were instructed to walk comfortably. **B** Subjects were divided into two groups. **C** Experimental protocol for each day.

Baseline Trials

In baseline trials, the hip exoskeleton was unpowered (i.e., zero motor current), and subjects were instructed to walk at a comfortable pace. On each day, preferred stride

duration (T_o) was quantified as the average stride period from the middle 30 strides in the second baseline trial.

Pulse Trials

In the pulse trials, the hip exoskeleton was unpowered during the first 20 strides, powered during the subsequent 80 strides, and unpowered for the remaining 20 strides (Fig. 3-1B). When powered, the exoskeleton delivered periodic torque pulses to both legs simultaneously. The torque pulses were trapezoidal in shape with a duration (T_d) of 200 ms (Fig. 3-1A). The magnitude of peak torque (τ_M) was set to 0.1 times the subject body mass in kg. For safety, the torque magnitude was upper bounded by 8 Nm.

The torque pulse applied to the right hip (τ_R) was always in the flexion direction (negative) and in the extension direction (positive) for the left hip (τ_L). The torques to the left and right hips were always of the same magnitude but opposite direction, i.e., $\tau_R + \tau_L = 0$ (Fig. 3-1A). For subjects in group-25ms, the pulse period (T_p) was set to be 25 ms faster than their preferred stride duration ($\Delta T = T_o - T_p = 25$ ms); for subjects in group-50ms, the pulse period was set to be 50 ms faster than their preferred stride duration ($\Delta T = T_o - T_p = 50$ ms). Subjects were instructed to walk in whatever way they found most comfortable. They were aware that the exoskeleton would alternate between powered and unpowered states during these trials, but they were not informed how the exoskeleton was controlled.

3.2.4 Hypotheses

To understand whether a nonlinear stable limit cycle oscillator is a reasonably competent descriptive model of the neuro-mechanical system controlling human walking, we assessed how the difference between torque pulse period and subjects' preferred stride duration affected entrainment. We hypothesized that entrainment would be observed more often when the difference was smaller, i.e., more often in group-25ms than in group-50ms (**hypothesis 1**). Synchronization itself does not specify the

phase at which entrainment occurs. However, if entrainment occurs due to the dynamic structure of the human walking controller, a consistent phase when entrained was expected. Therefore, we hypothesized that the phase when entrained would be consistent across different trials and subjects, i.e., for all entrained trials the distributions of the terminal pulse phases would not be different (**hypothesis 2**).

It is important to assess neural and/or biomechanical contributions. Experiments were conducted for two consecutive days to evaluate whether the second day elicited more entrainment. If the central nervous system (CNS) learned the adapted behavior, repeated bouts should evoke more frequent entrainment. We hypothesized that entrainment would be observed more often in day 2 than in day 1 (**hypothesis 3**). Lastly, we tested whether mechanical energy/work done by the robot had any relation to entrainment, similar to the behavior observed in the prior entrainment studies using an ankle exoskeleton. We hypothesized that the locking phase would be commensurate with the phase where the torque pulse could provide maximal positive power (**hypothesis 4**).

3.2.5 Data Processing

Stride Segmentation

Each stride began with maximum extension (positive) of the left hip angle (θ_L), which approximately corresponds to left toe-off [157]. Because torque pulses applied during the pulse trials affected position measurements, simple peak detection was not reliable to separate each stride from the entire time-series data. To account for the inevitable relative motion between the exoskeleton and the wearer, we developed an off-line stride segmentation algorithm, as described in Section **3.6**.

Phase Estimation

Determining phase variables from experimental signals is not trivial, especially when the signals are non-stationary [23, 175]. Previous studies [172, 173] proposed to compute phase from kinematic observations (kinematic phase) to understand neu-

romechanical control of animal locomotion subject to mechanical perturbation. Recent work in the robotics community exploited kinematic phase variables to design biped walking controllers, and this showed more robust performance than using a time-based phase variable [224]. Inspired by these previous studies, Gregg and colleagues [161, 218–220] recently proposed reliable and robust methods to determine a phase variable for human walking, using hip angle. We adopted this method to estimate the gait phase of human subjects ϕ. The estimated phase was used to assess entrainment, and to investigate to which phase of the gait cycle the mechanical perturbations converged. We briefly present the method in Section 3.7, but readers are referred to the original work for details.

3.2.6 Dependent Measures

Pulse Phase

Pulse phase ϕ_P (%) was defined as the phase at which the onset of the torque pulse occurred within the gait cycle.

Pulse Phase Slope

Pulse phase slope (%/#) was defined as the average change of pulse phase (%) with respect to pulse number (#). Pulse phase slope was computed over the first 10 pulses (*initial pulse phase slope*) and the last 10 pulses (*terminal pulse phase slope*) of each trial by linear regression (MATLAB function `lmfit`).

Period Deviation

Period deviation ΔT (ms) was defined as the difference between each stride duration and the torque pulse period for each respective trial.

Pulse Mechanical Energy

Pulse mechanical energy E_P (J/Nm) passed from the robot to the human was estimated for each torque pulse by integrating instantaneous power over time. To

normalize the measure, the net energy was divided by peak commanded torque (τ_M) of the corresponding trial($E_p = \frac{1}{\tau_M}\int \tau_R\dot{\theta}_R + \tau_L\dot{\theta}_L dt$). The joint torques were estimated from the current sensors. The angular velocities were obtained by filtering the measured joint angular positions and compensating for group delay (MATLAB function `designfilt`).

Predicted Pulse Phase

Ignoring kinematic variation induced by the robot perturbation, one can approximate the pulse mechanical energy as a function of pulse phase. Assuming an ideal pulse was applied to the wearers with magnitude $\tau_M (= \tau_L = -\tau_R)$, and using the kinematics obtained during baseline trials, the pulse mechanical energy is calculated as

$$\hat{E}_P(\phi_P) \approx \frac{1}{\tau_M}\int \tau_M(\dot{\theta}_L - \dot{\theta}_R)dt = \Delta\theta_{REL}(\phi_P), \tag{3.1}$$

where $\theta_{REL} = \theta_L - \theta_R$, $\Delta\theta_{REL} = \theta_{REL}(t_{on}(\phi_P) + T_d) - \theta_{REL}(t_{on}(\phi_P))$, and t_{on} is the pulse onset time corresponding to ϕ_P. Based on **hypothesis 4**, we predicted the pulse phase $\hat{\phi}_P$ (%) would maximize the pulse mechanical energy, i.e. $\hat{\phi}_P = \text{argmax}_{\phi_P}\hat{E}_P(\phi_P)$.

3.2.7 Entrainment Criteria

Each trial was classified as entrained if the magnitude of the *terminal pulse phase slope* was < 0.5 (%/#), i.e., the total change of pulse phase (%) within the last 10 pulses (#) was below 5%; otherwise, it was considered not entrained.

3.2.8 Statistical Analyses

Statistical analyses were conducted using the Statistics and Machine Learning Toolbox of MATLAB R2018b (Mathworks, MA). For all statistical tests, the significance level was set to $p = 0.05$.

A 2 (group: 25ms vs. 50ms: between subjects factor) $\times$ 2 (day: 1 vs 2: within-

subjects factor) mixed model ANOVA on the number of entrained trials was performed to test whether entrainment more often occurred when difference between natural stride duration and pulse period was smaller (**hypothesis 1**) and whether the second day elicited more entrainment (**hypothesis 3**).

A 2 (group: 25ms vs. 50ms) $\times$ 2 (day: 1 vs. 2) ANOVA on the average of last 10 pulse phases of the entrained trials was performed to test whether the distribution of pulse phases depends on the experimental conditions(**hypothesis 2**).

A residual analysis was conducted to compare the agreement between the actual pulse phase and predicted pulse phase for maximizing mechanical work $\hat{\phi}_P$ (%) (**hypothesis 4**).

3.3 Results

3.3.1 Representative Trials

Fig. 3-2 presents two representative trials: entrained (group-25ms, day 1, subject 1, trial 1) and not entrained (group-50ms, day 1, subject 2, trial 1). In the entrained trial (Fig. 3-2A), the pulse phase converged at the end of the trial (M: 65.6%, SD: 0.54% in the last 10 pulse phases). The stride duration was approximately matched to the torque pulse period (period deviation close to zero). After the torque pulses ceased, stride duration slowly returned towards its pre-perturbation value (stride number 100 - 120). However, in the not-entrained trial (Fig. 3-2B), the pulse phase drifted through all phases of the gait cycle and stride duration was little affected by the intervention (non-zero period deviation).

3.3.2 Group Results

Consistent with **hypothesis 1**, gait entrainment was observed more frequently in group-25ms (day1: 71%, 40 out of 56 trials; day2: 79%, 44 out of 56 trials) than in group-50ms (day1: 39%, 25 out of 64 trials; day2: 45%, 29 out of 64 trials), and this difference was statistically significant ($F[1, 13] = 7.8, p = 0.015$). Counter to

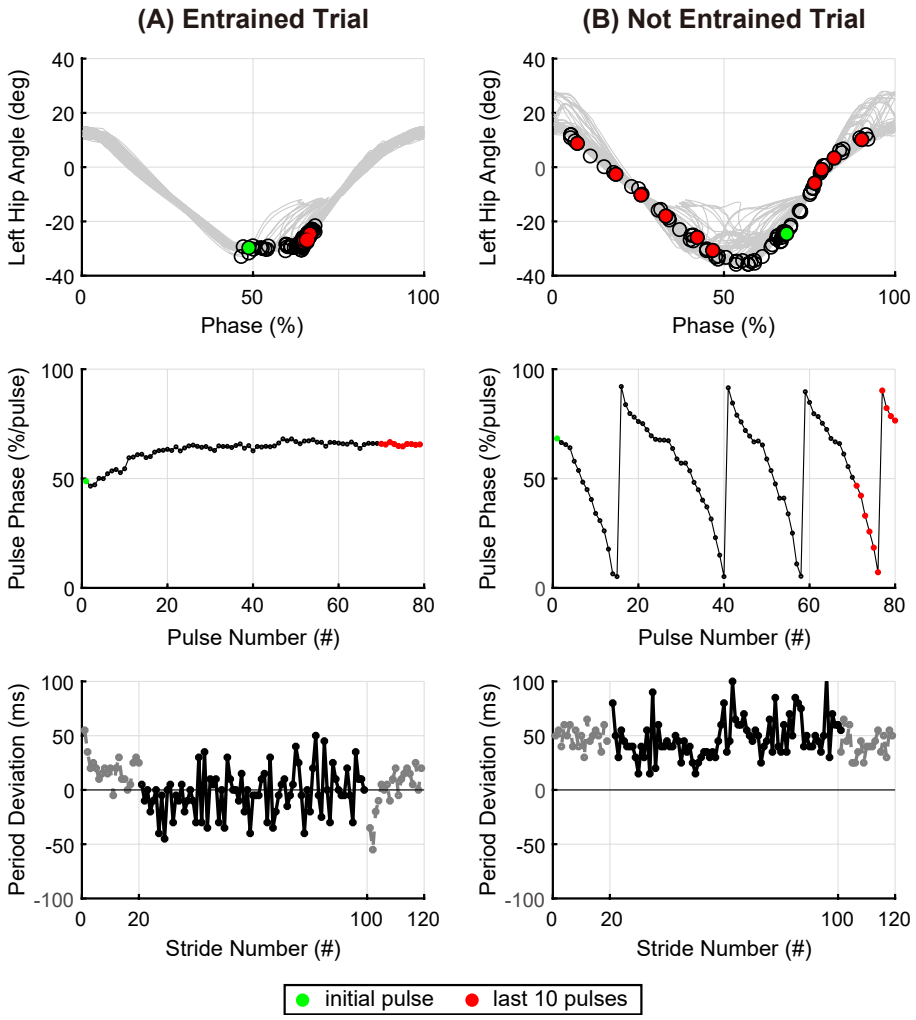

Figure 3-2: **A** Representative entrained trial. **B** Representative not-entrained trial Top: Left hip angle vs. phase, all strides. Black circles denote onsets of torque pulses. Middle: Pulse phase vs. pulse number. Bottom: Period deviation vs. stride number. Torque pulses were applied during 20-100 strides (black, solid). Pre- and post-pulses are also plotted (gray, dotted). In the top and middle rows, the initial pulse (green dot) and the last 10 pulses (red dots) are highlighted.

hypothesis 3, there was no statistical difference between consecutive days of experiments ($F[1, 13] = 0.37, p = 0.55$). There was no statistically significant interaction between groups and days ($F[1, 13] = 0.002, p = 0.97$).

Fig. 3-3 presents the progression of pulse phase vs. pulse number for all entrained trials for each condition. In entrained trials, pulse phase converged to an approximately constant value before the perturbation ceased. Within each trial, the pulse phases tended to drift in one direction (either increasing or decreasing). Fig. 3-3 (bottom) presents the distribution of the initial pulse phase slopes and the terminal pulse phase slopes of the entrained trials. After initial transients, subjects adapted their gait and reached steady-state motion within 80 strides.

3.3.3 Gait Phase Convergence

Fig. 3-4 presents initial pulse phases (the first pulse phase) and terminal pulse phases (the last ten) of the entrained trials. While the initial pulse phases were distributed widely across the entire gait cycle, the terminal pulse phases formed a unimodal distribution in each condition. Consistent with **hypothesis 3**, the terminal pulse phase was consistent across all entrained trials (M =63.8 %); neither the effect of period difference (group-25ms vs. group-50ms; $F[1, 137] = 0.001, p = 0.97$), day (day1 vs. day2: $F[1, 137] = 0.08, p = 0.78$), nor their interaction ($F[1, 137] = 2.96, p = 0.088$) were statistically significant.

3.3.4 Mechanical Energy

Fig. 3-5 compares the pulse mechanical energy E_P and the terminal pulse phase ϕ_P of the last ten pulses of (A) entrained trials and (B) not-entrained trials for all conditions. The histograms of the entrained trials show that the pulse phase and the positive work done by the robot were closely related. The unimodal distribution of the terminal pulse phases of all entrained trials ($M = 63.8\%, SD = 10.4\%$) were centered about those at which subjects could gain the most mechanical benefit from the exoskeleton robot ($M = 65.1\%, SD = 1.57\%$). On the other hand, those of the

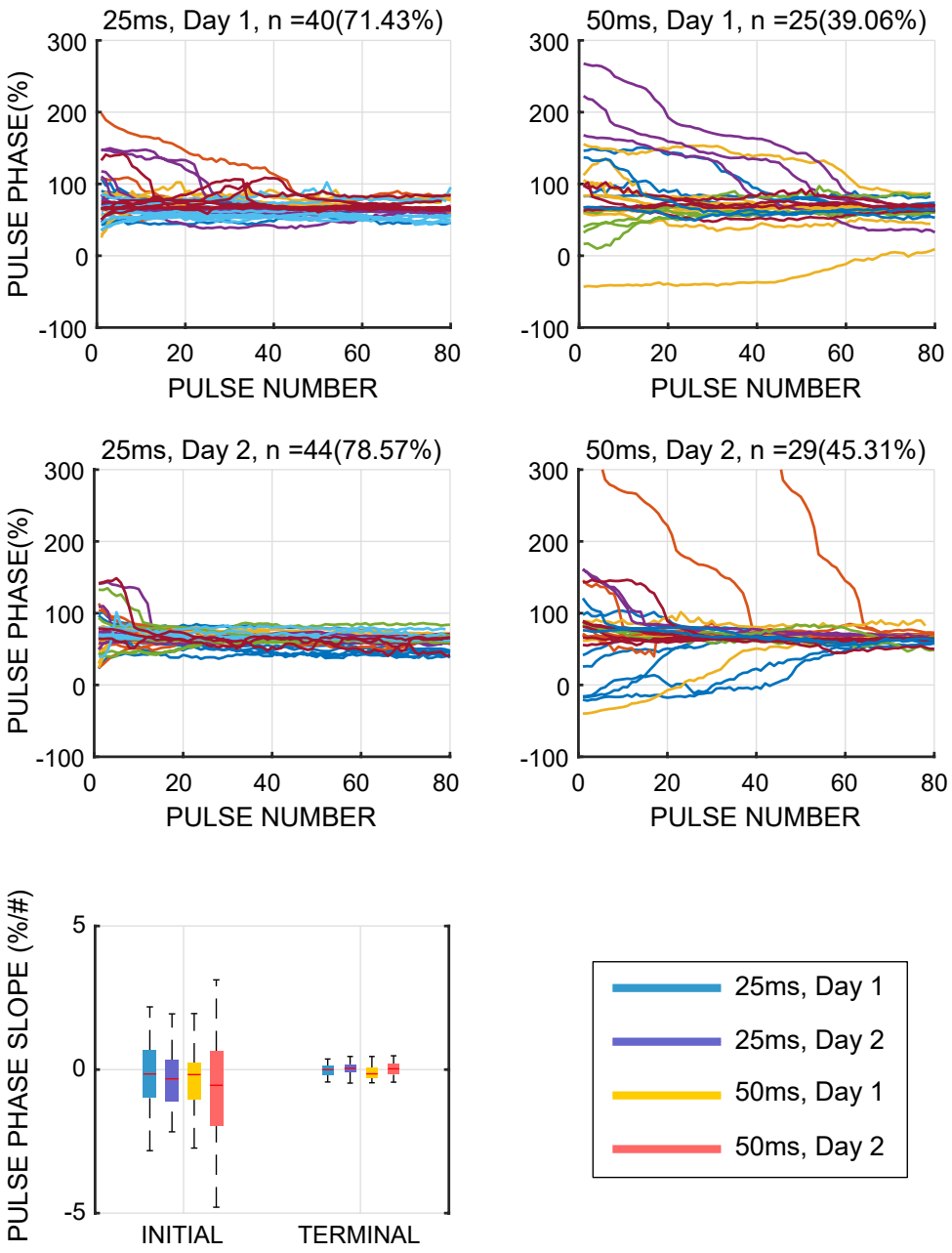

Figure 3-3: Pulse phase vs. Pulse number of all entrained trials for all conditions. The number (n) of entrained trials for each condition is also presented. Different colors represent different subjects. The pulse phases are unwrapped such that the last value of each trial is between 0 % and 100 %. Pulse phase slope of initial and terminal segments of the entrained trials are also presented.

not-entrained trials were more widely distributed in terms of both energy and pulse phase.

The representative trial exemplifies the similarity between the actual terminal

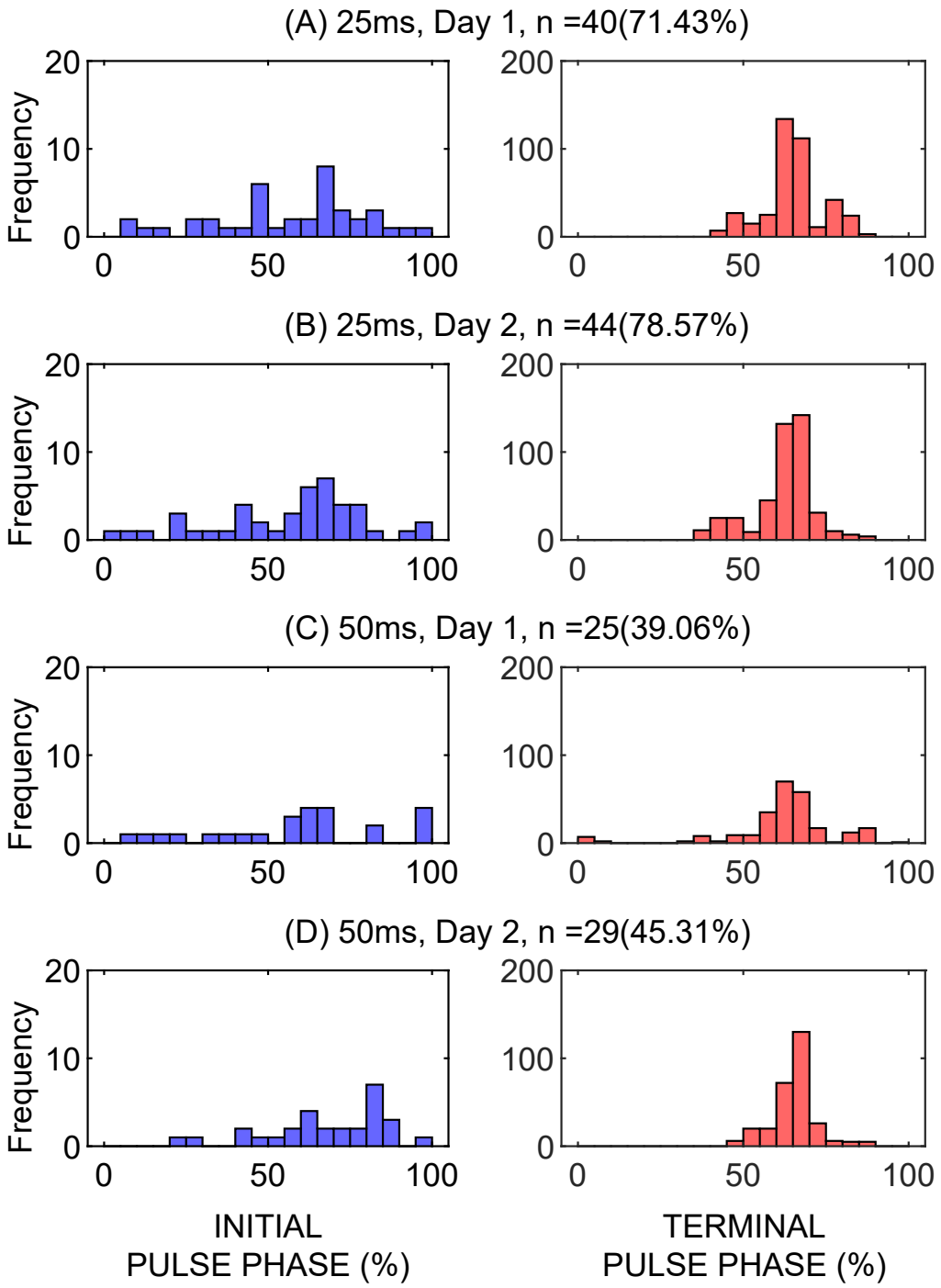

Figure 3-4: Initial pulse phases and mean of 10 terminal pulse phases of the entrained trials for all conditions.

pulse phase ϕ_P and the phase for maximal work of robot $\hat{\phi}_P$ (Fig. 3-6A). The distribution of the error between prediction and actual of all entrained trials ($\phi_{err} = \hat{\phi}_P - \phi_P$) (Fig. 3-6B) was centered around zero ($M = -1.3\%, SD = 10.2\%$). These results in-

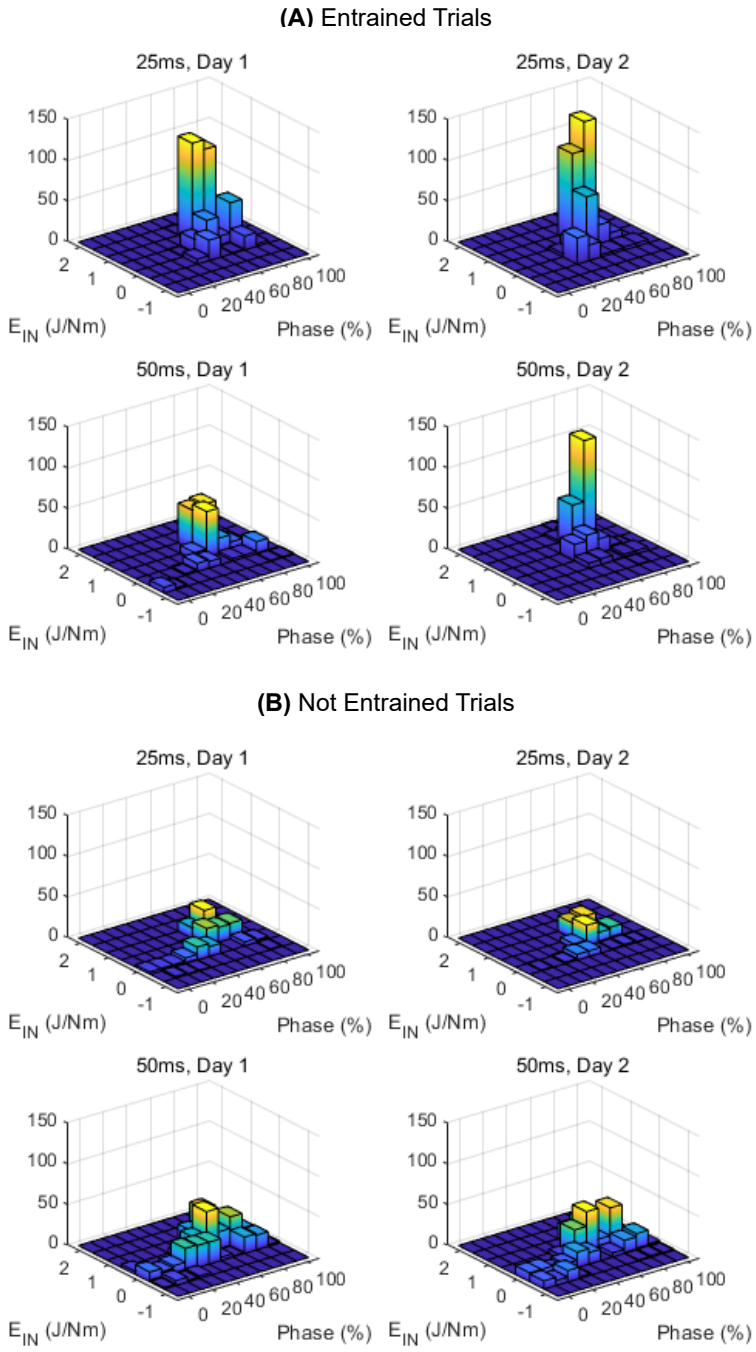

Figure 3-5: Histograms of mean terminal pulse phase and mean terminal work done by the robot for each condition of **(A)** the entrained trials and **(B)** not-entrained trials (mean of the last 10 strides).

dicate a close relationship between the converged phase and positive mechanical work done by the robot in support of **hypothesis 4**.

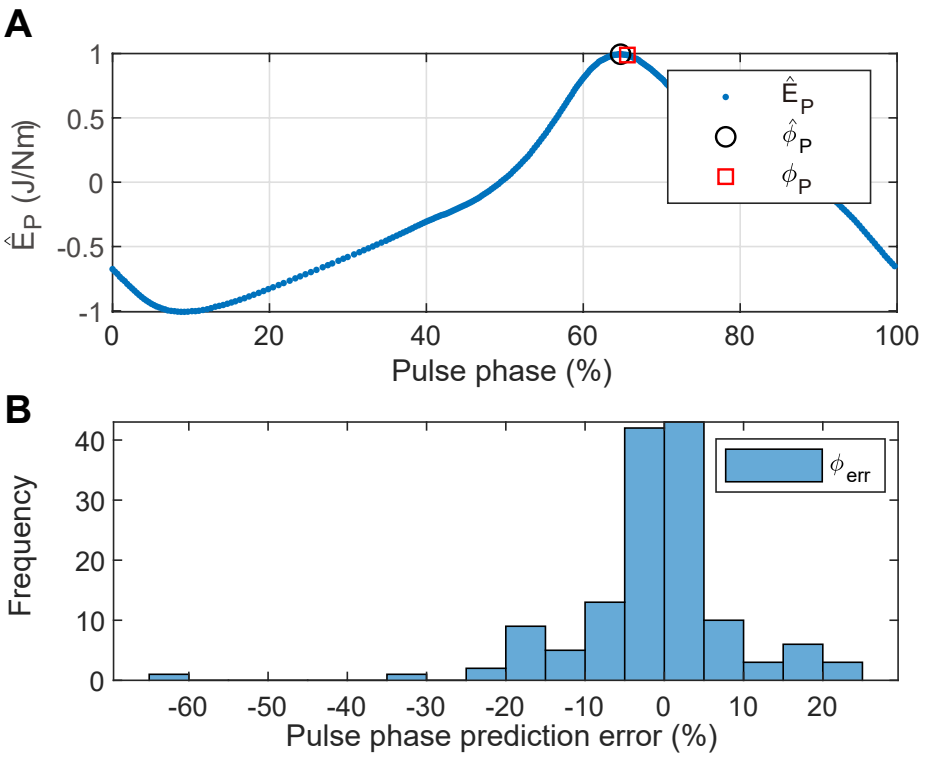

Figure 3-6: **(A)** Prediction of pulse mechanical energy as a function of pulse phase $\hat{E}_P(\phi_P)$ of the representative trial (group-25ms, day 1, subject 1, trial 1), with predicted locking phase $\hat{\phi}_P$ (black, circle) and actual locking phase ϕ_P (red, square). **(B)** Histogram of error of prediction, $\phi_{err} = \hat{\phi}_P - \phi_P$ for all 10 terminal pulse phases for all entrained trials.

3.3.5 Stride Period

Fig. 3-7 presents how the period deviation of entrained trials and not-entrained trials varied in each condition. In all entrained trials, stride duration adapted to match the torque pulse period, resulting in a mean period deviation close to zero. Upon removal of the robotic intervention, stride durations slowly returned to their pre-perturbation values. Conversely, stride duration did not converge to the torque pulse period in not-entrained trials. T-tests indicated that in each condition, the mean period deviation was not significantly different from zero during entrained trials (group-25ms x day1: $p = 0.51$, group-25ms x day 2: $p = 0.77$, group-50ms x day1: $p = 0.61$, group-50ms x day2: $p = 0.11$), but was significantly different from zero during not-entrained trials (group-25ms x day1: $p < 0.001$, group-25ms x day 2: $p < 0.001$, group-50ms x day1: $p < 0.001$, group-50ms x day2: $p < 0.001$). There was a constant offset in

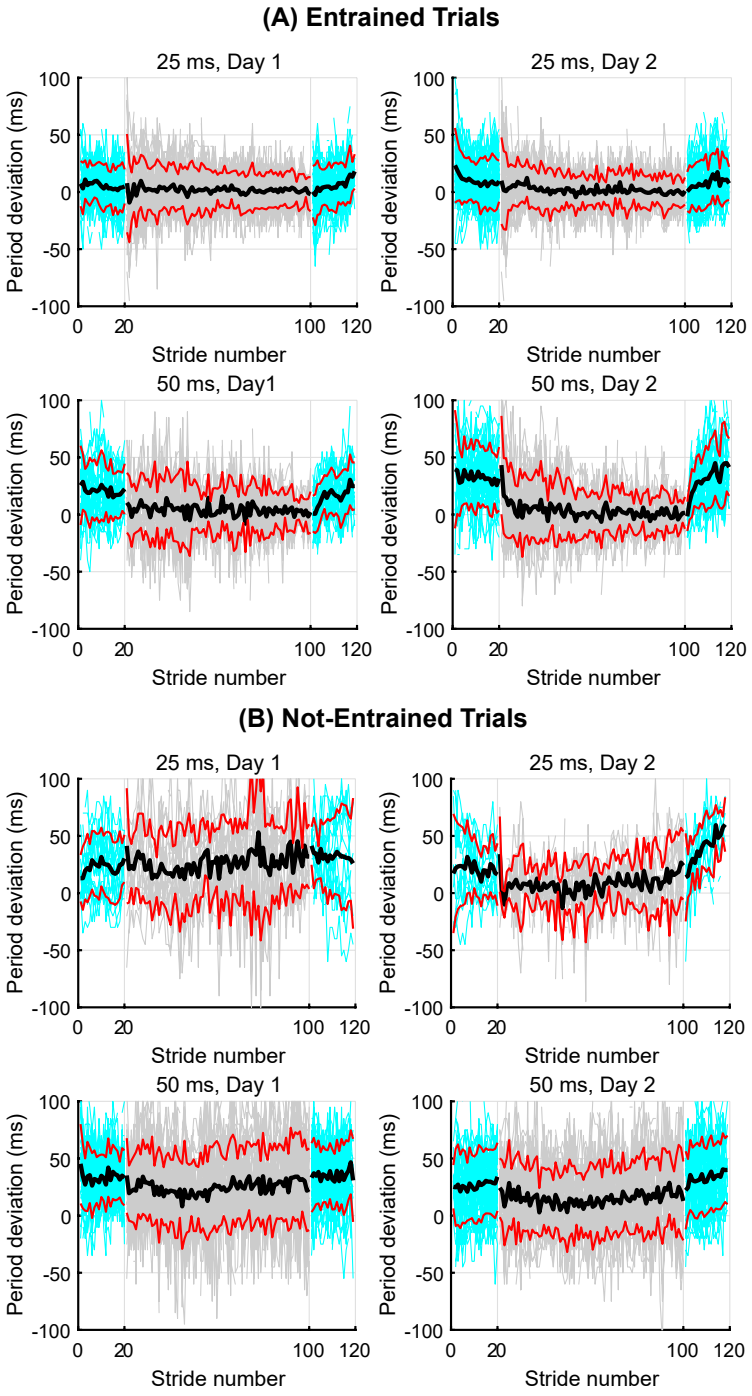

Figure 3-7: Period deviation vs. stride number of **A** entrained trials and **B** not-entrained trials. Pre-pulse strides and post-pulse strides are distinguished (cyan). The means and standard deviations of trials for each condition are presented as black, thick lines and red, thin lines, respectively. In computing means and standard deviations for each stride number, outliers were omitted using MATLAB function `rmoutliers` with its default setting.

period deviation for not-entrained trials. While this offset was smaller on day 2 of not-entrained trials, in particular of group-25ms, it was larger than that of entrained trials.

3.4 Discussion

3.4.1 Summary of Results

This study characterized unimpaired human subjects' responses to periodic torque pulses applied about the hip joints during overground walking.

We observed that human subjects entrained their gait to the periodic mechanical torque pulses applied by a hip exoskeleton robot. During this process, subjects synchronized their stride duration to match that of the external mechanical perturbation (Fig. 3-7). For all groups, by the end of entrained trials, pulse phase converged to a unimodal distribution centered around 63-65 % (Fig.3-3 and Fig. 3-4). Further analysis revealed that entrainment occurred such that the mechanical energy flow from the robot to the wearer was maximized (Fig. 3-5).

Gait entrainment was observed more often when the pulse period was closer to subjects' preferred stride duration, and this difference was statistically significant ($p = 0.015$). However, there was no statistical difference between the two days of experiments ($p = 0.55$), suggesting that longer training periods might be required to elicit further changes in neuro-motor behavior.

3.4.2 Limitation: Robot-embedded Measurements

There are trade-offs between tightly-controlled lab experiments and experiments in real-world conditions. For example, walking overground enables a study of natural human behaviors in more ecological contexts, but the ability to measure human behavior is limited. On the other hand, walking on a treadmill in a lab enables reliable collection of various data (e.g., ground reaction forces using force plates or whole-body kinematics using a motion capture system). However, walking on a treadmill is me-

chanically different from walking overground. For instance, the treadmill belt speed changes periodically depending on the gait phase, and may require motor adaptation to a dynamic environment [208]. The goal of this study was to investigate entrainment in real-world conditions, despite the associated limitations.

Entrainment was assessed based on robot-embedded joint position measurements. Because the exoskeleton robot did not perfectly conform to each individual, the hip joint angles measured by the robot-embedded encoders may have differed from the true human joint angles. The robot actuators transmitted power and/or torque through a thigh frame and belt assembly that was tightly coupled to the human subjects. However, torque transmission may have been imperfect due to a myriad of reasons (e.g., friction in the actuator, elasticity in human tissue or the thigh frame, and relative motion between the exoskeleton robot and the wearer). The difference between torque estimated from on-board sensors and external force-sensitive resistor (FSR) sensors was presented in [38]. Nonetheless, our conclusion that periodic torque pulses at the hip joints induced gait entrainment is still valid because it relies on the trend of behavior rather than exact values. Inaccurate kinematic measurement and inaccurate torque application cannot dismiss our results.

Measurements based on whole-body kinematics (e.g., stride length), or stride segmentation based on external sensors (e.g., foot-mounted sensors) would be useful to confirm and further illuminate our results. In addition, direct measurements of muscle activity (e.g., surface electromyography; sEMG) would be useful to further identify neuro-muscular mechanisms associated with gait entrainment. Measurements of metabolic cost would also add useful information to track consequential changes in locomotion economy following adaptation.

3.4.3 Gait Entrainment to Mechanical Perturbations

Periodic torque pulses applied by a hip exoskeleton evoked gait entrainment, accompanied by convergence of pulse phase to a constant value across all conditions. Entrainment occurred more often when the period of perturbation was closer to subjects' natural stride duration. The results are consistent with previous studies that

showed entrainment to mechanical perturbations [5, 141, 145, 186, 203, 206]. However, the basin of entrainment was smaller and rate of successful entrainment was lower with the hip exoskeleton than with an ankle exoskeleton [5, 145, 206].

While entrainment itself does not enforce convergence to a particular constant phase, subjects entrained their gait to maximize the work done by the hip exoskeleton robot, as illustrated in Fig. 3-5. This result is consistent with previous studies with different mechanical interventions, in which individuals adapted to leverage positive power from the devices [20], aligning the timing of robotic torques from an ankle exoskeleton with ankle propulsion [5, 65, 145]. Subjects tended to get the most mechanical assistance during the gait phase when the ankle does the most positive work [56].

3.4.4 Gait Entrainment: Neural or Mechanical?

Does gait entrainment involve any central neural process, or was it purely due to peripheral neuro-mechanics? The potential bio-mechanical benefits discussed in the previous section seem to suggest that biomechanical mechanisms at least played a significant role. In fact, a previous modeling study suggested that gait entrainment may not require any supra-spinal mechanisms [4]. However, that model could not reproduce some experimental results (e.g., entrainment to periodic perturbations slower than preferred walking period [145, 174]), suggesting that some higher-level neural contribution may be required. Indeed, it is hard to dismiss the role of supra-spinal control in gait entrainment.

The intervention in this study was designed to either drive the legs apart or pull them together, depending on the phase at which the pulse occurred. Since the torque pulse period was similar to the stride duration not the step duration, this intervention influenced inter-leg coordination, breaking symmetry, which might be detected by the CNS as an error to be corrected [169]. Mechanical perturbations affecting inter-leg coordination have been shown to evoke locomotor adaptation, e.g., split-belt treadmill walking [169] and many other studies involving unilateral perturbation [21, 59, 103, 223]. Conversely, our companion study [110] showed that an intervention that did

not affect symmetry did not evoke motor adaptation.

Moreover, the timing of locomotor patterns is thought to be mediated at the spinal level (e.g., central pattern generators) but under supraspinal control (e.g., motor cortex, via brainstem centers) and afferent sensory feedback [52, 67, 123, 129, 205]. While auditory signals cannot directly influence inter-leg coordination, substantial studies have shown that the rhythmic adaptation observed in auditory-motor synchronization involves central neural mechanisms (e.g. cortical areas, basal ganglia and the cerebellum) [40]. There is also evidence that neuro-motor adaptation to a mechanical perturbation was predominantly due to descending drive from supra-spinal levels [91]. For example, an intact cerebellum and motor cortex appear to be critical for motor adaptation [190].

In sum, it seems reasonable to suggest that both high-level (supra-spinal) control and low-level peripheral biomechanical structures contributed to the observed gait entrainment to mechanical perturbation at the hip joints.

3.4.5 Gait Entrainment: Clinical Implications

Mechanical gait entrainment may serve as a novel *permissive* locomotor rehabilitation therapy that minimally encumbers the natural dynamics of walking. Similar to the auditory gait entrainment which has shown promising therapeutic effects [41], mechanically entraining gait to increase cadence may result in increased walking speed [49, 115] or stride length [41], which might be important functional outcomes for post-stroke survivors [155, 184]. In addition, walking in recovering stroke patients (and in some healthy elders) looks a lot like a sporadic slow sequence of individual steps. Mechanical entrainment may promote more natural (rhythmic) action and hence be beneficial.

To maximize the potential therapeutic effects of mechanical gait entrainment, different torque pulse profiles (including continuous rhythmic torque patterns) and performance-based protocols for gradual improvement [8, 98, 206] should be investigated. To understand underlying neuro-mechanical mechanisms of entrainment, a modelling study would be insightful [2]. Once the most effective method has been

established, studies with patient populations should follow to evaluate whether neuromotor adaptation in healthy subjects translates to neuro-recovery in clinical settings. These matters are left for future studies.

3.4.6 A Nonlinear Limit-cycle Oscillator as a Descriptive Model of Human Walking

When exposed to external periodic forcing, a nonlinear limit cycle oscillator is entrained and synchronizes its frequency with that of the stimuli [63]. This synchronization only occurs when the frequency and strength of the stimuli are in a finite region called the basin of entrainment[1]; outside this region in parameter space, entrainment does not occur.

The experiments reported here were designed based on a working hypothesis that a nonlinear, stable limit cycle oscillator is a reasonable descriptive model of human walking. The experimental observations of this study can be summarized by two characteristics: phase-locking to a unimodal phase distribution; and a finite basin of entrainment (more entrainment in group-25ms than in group-50ms). Inevitable noise in biological systems was also observed, e.g., in stride durations or pulse phase distributions. Despite the unquestionable complexity of the human neuromotor system, there is considerable practical value to describing human walking with an exoskeleton robot by a simplified mathematical model: a nonlinear limit-cycle oscillator with periodic forcing, subject to the presence of stochasticity. Note that a linear model (e.g. a second-order mass-spring-damper system) cannot exhibit a finite basin of entrainment. Despite the evident power of linear analysis, some phenomena require nonlinearity. Stochasticity is also required, though deterministic chaos may not be necessary [6].

This simple theoretical model provides useful insights to predict and interpret complicated experimental observations. First, the finite basin of entrainment is determined by two parameters: the period of perturbation and the coupling strength.

[1]It is also said that the system exhibits the Arnold's tongue structure, due to the shape of the basin of entrainment.

From this point of view, it is natural to observe less entrainment in group-50ms than in group-25ms. When the parameters are outside the basin of entrainment, entrainment will not occur and the pulse phase will drift. However, when the parameters are close to the boundary, the pulse phase will drift slowly when it is near the converged phase (critical slowing [202]). In that case, stochasticity may 'push' the system into the basin of entrainment. We believe this is what we observed in some trials in Fig. 3-3.

Second, this simple theoretical model might potentially be useful to quantify individuals with a small number of parameters. For example, the model presented in [63] only requires three parameters: the convergence rate of the limit cycle (this may be a characteristic of individual subjects), the relative frequency between the stimulus (pulse period T_p) and the oscillator (subjects' preferred stride duration T_o), and the coupling strength (which may be related to pulse magnitude τ_m or pulse duration T_d or both). A model of this kind may serve to customize treatment protocols to individual patients.

3.5 Conclusion

This study characterized unimpaired human subjects' responses to periodic torque pulses applied by a hip exoskeleton robot during overground walking. The perturbation evoked gait entrainment, accompanied by convergence of pulse phase to a similar value across all conditions. Entrainment occurred more often when the period of perturbation was closer to subjects' natural stride duration. The ability of a hip exoskeleton robot to induce gait entrainment is promising. Exploiting the natural oscillatory dynamics of walking to induce entrainment may provide a novel, minimally-encumbering approach to locomotor rehabilitation therapy.

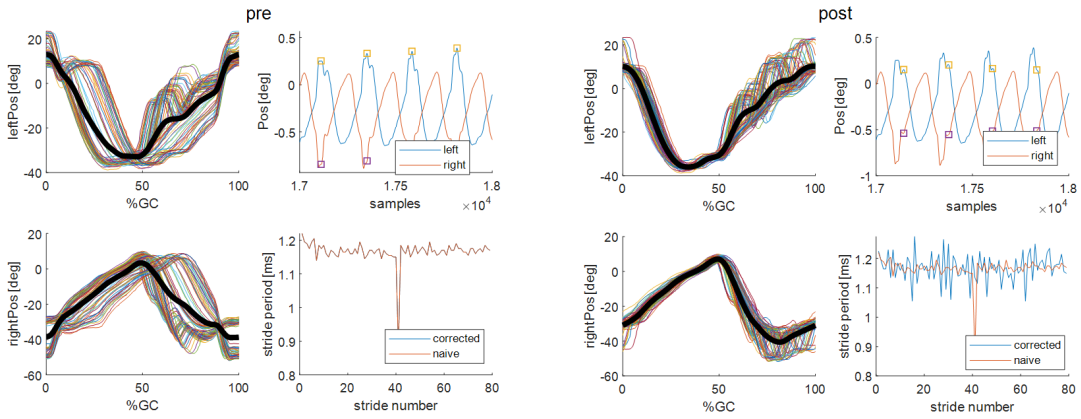

Figure 3-8: Stride segmentation using naive peak detection algorithm (**A**) and using the proposed algorithm (**B**).

3.6 Appendix: Off-line stride segmentation

For each pulse trial, first the peaks in the time-series of left hip angle θ_L are identified using a peak detection algorithm (MATLAB `findpeaks`). This set of indices of the identified peaks, $i_{pk} \in \mathcal{I}_{PK}$, serve as an initial seed for optimization. Note these indices are integers. The tuples of indices of the onset-offset pairs of torque pulses are also identified from applied torque τ_L: $(i_{on}, i_{off}) \in \mathcal{I}_{ON-OFF}$. If the torque pulses occurred near the identified peaks of the hip angle, it is likely that the corresponding peaks were affected by the pulses and need corrections. These peaks are removed from $\mathcal{I}_{PK}$ and then stored as decision variables to be updated, $\mathcal{I}_{DV}$ (See Algorithm 1).

Algorithm 1 Off-line stride segmentation initialization

1: Given left hip angle peak indices $\mathcal{I}_{PK}$, torque pulse onset-offset index tuples $\mathcal{I}_{ON-OFF}$
2: Initialize decision variable $\mathcal{I}_{DV}$
3: **for** $i_{pk} \in \mathcal{I}_{PK}$ **do**
4: **if** $\exists (i_{on}, i_{off}) \in \mathcal{I}_{ON-OFF}$ s.t. $i_{pk} \in [i_{on}, i_{off}]$ **then**
5: $i_{dv} \leftarrow i_{pk}$
6: Append $\mathcal{I}_{DV}$ with i_{dv}
7: Remove i_{pk} from $\mathcal{I}_{PK}$
8: **end if**
9: **end for**

The affected peaks are then corrected in a way to minimize inter-stride variability

V. To compute inter-stride variability V, the time-series of left hip angle θ_L and right θ_R are first segmented using $\mathcal{I}_{PK} \cup \mathcal{I}_{DV}$, each stride is time-normalized with length N using interpolation (MATLAB `interp1`), ensemble average is computed, then sum of squared error of each stride and the ensemble average is computed; see Algorithm 2. In this work, the genetic algorithm (MATLAB function `ga`) was used to find the integer-valued decision variables $\mathcal{I}_{DV}$ that globally minimize V, but other more efficient solvers may be used. To avoid over-correction, each of the corrected peak index is bounded in time by $\pm T_d$ ($= \pm$ 200 ms) from its initial value.

Algorithm 2 Inter-stride variability

procedure INTER-STRIDE VAR($\theta_L, \theta_R, \mathcal{I}_{PK}, \mathcal{I}_{DV}, N$)
  Initialize $V \leftarrow 0$
  Initialize stride segments $\mathcal{S}$
  Sort $\mathcal{I}_S = \mathcal{I}_{PK} \cup \mathcal{I}_{DV}$ in ascending order
  for s-th index $i_s \in \mathcal{I}_S$ **do**
    $\boldsymbol{\theta_L^{(s)}} \leftarrow (\theta_L[i_s], \theta_L[i_s+1], \cdots, \theta_L[i_{s+1}])$
    $\boldsymbol{\theta_R^{(s)}} \leftarrow (\theta_R[i_s], \theta_R[i_s+1], \cdots, \theta_R[i_{s+1}])$
    $\boldsymbol{\theta_L^{(s)}} \leftarrow$ `interp1`$((i_s, \cdots, i_{s+1}), \boldsymbol{\theta_L^{(s)}}, (1, \cdots, N))$
    $\boldsymbol{\theta_R^{(s)}} \leftarrow$ `interp1`$((i_s, \cdots, i_{s+1}), \boldsymbol{\theta_R^{(s)}}, (1, \cdots, N))$
    Store $\boldsymbol{\theta_L^{(s)}}, \boldsymbol{\theta_R^{(s)}}$ in $\mathcal{S}$
  end for
  Compute ensemble average: $\bar{\boldsymbol{\theta}}_{\boldsymbol{L}}$ and $\bar{\boldsymbol{\theta}}_{\boldsymbol{R}}$
  for $\boldsymbol{\theta_L^{(s)}}, \boldsymbol{\theta_R^{(s)}} \in \mathcal{S}$ **do**
    $V \leftarrow V + \|\boldsymbol{\theta_L^{(s)}} - \bar{\boldsymbol{\theta}}_{\boldsymbol{L}}\|^2 + \|\boldsymbol{\theta_R^{(s)}} - \bar{\boldsymbol{\theta}}_{\boldsymbol{R}}\|^2$
  end for
  return V
end procedure

The optimal stride segments $\mathcal{S}$ were used to calculate dependent measures for each stride. The effect of the developed algorithm is clearly shown in Fig. 3-8. When motion artifacts were significant as in this study (due to relative motion between exoskeleton robots and the wearers), this method could outperform the näive peak detection algorithm to segment strides from a long time-series data. Of course, using external sensors such as motion capture systems or force plate to detect gait events would be more convenient and accurate, but sometimes it is not compatible with the human studies outside the lab.

3.7 Appendix: Phase estimation algorithm

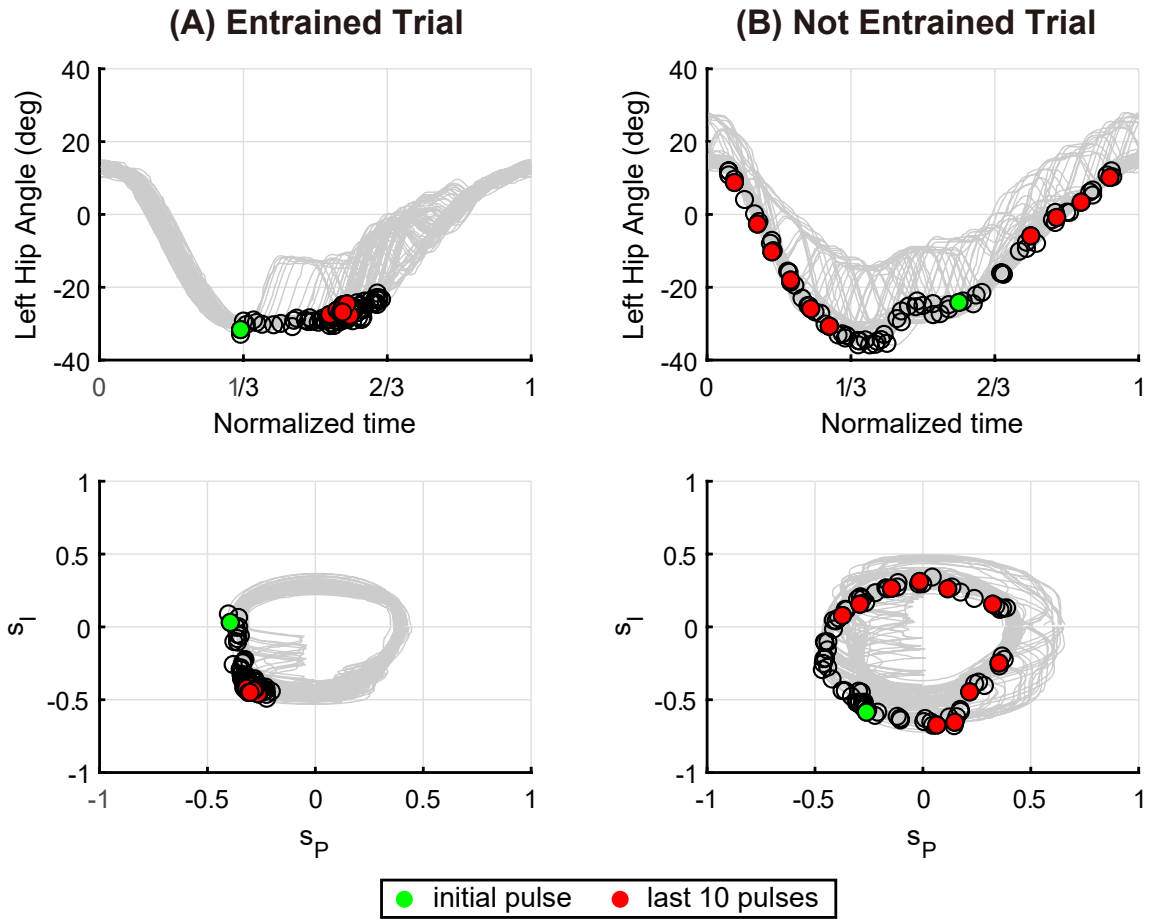

Figure 3-9: Representative entrained trial **(A)** and not entrained trial **(B)**. Top: Hip angle (positive: extension; negative: flexion) vs. normalized time. All 80 strides of the representative trial. Bottom: trajectory of $\boldsymbol{s_P}$ vs. $\boldsymbol{s_I}$ of all strides on the phase plane. Black circles indicate the onsets of torque pulses. Green dot indicates the initial pulse. Red dots indicate the onsets of ten terminal pulses.

The phase estimation algorithm is adopted from [161, 219, 220]. For s-th stride $\boldsymbol{\theta}_{\boldsymbol{L}}^{(s)} \in \mathcal{S}$ from Appendix 3.6, the angle and its integral are shifted and scaled to obtain

two signals $\boldsymbol{s_P^{(s)}}$ and $\boldsymbol{s_I^{(s)}}$.

$$\boldsymbol{s_P^{(s)}} = \theta_L^{(s)} - \frac{1}{N}\sum_{i=1}^{N}\theta_L^{(s)}[i] \tag{3.2}$$

$$\hat{s}_I^{(s)}[k] = \sum_{i=1}^{k} s_P^{(s)}[i] \tag{3.3}$$

$$g^{(s)} = \frac{\max s_P^{(s)} - \min s_P^{(s)}}{\max \hat{s}_I^{(s)} - \min \hat{s}_I^{(s)}} \tag{3.4}$$

$$\boldsymbol{s_I^{(s)}} = g\hat{s}_I^{(s)} \tag{3.5}$$

The two signals $\boldsymbol{s_P^{(s)}}$ and $\boldsymbol{s_I^{(s)}}$ construct a closed-orbit on the phase plane. The phase of each data point for each stride is computed as the angle of the data point on the phase plane as shown in Fig. 3-9.

$$\phi[i] = \frac{1}{2\pi} atan(\frac{s_I[i]}{s_P[i]}) \in [0, 1]. \tag{3.6}$$

Chapter 4

Human walking with virtual stiffness between the thighs

This work was done in collaboration with Dr. Meghan E. Huber (Newman Lab for Biomechanics and Human Rehabilitation, MIT; now Prof. Meghan E Huber at Human Robot Systems Laboratory, University of Massachusetts). We implemented controller, designed and conducted human experiments, and analyzed data together. We would like to thank Vibha Agarwal (MIT) and Haley R. Warren (University of Vermont) for their help in collecting and analyzing the data.

This work was supported by the Global Research Outreach program of Samsung Advanced Institute of Technology and a Samsung scholarship. Vibha Agarwal was also supported by the MIT Undergraduate Research Opportunity Program (UROP). Haley R. Warren was also supported by the MIT Summer Research Program (MSRP). Prof. Neville Hogan was also supported by the Eric P. and Evelyn E. Newman fund, NIH-R01-HD087089, NSF-NRI 1637824, and NSF-CRCNS-1724135.

This work was partially presented in [78, 107], and is under review in [110].

4.1 Introduction

Current portable lower-limb exoskeleton robots can successfully improve locomotion economy (i.e., reduce metabolic cost during normal walking and running) [183]. While

concurrent changes in kinematic and kinetic measures were also observed, they were not the primary objective, but investigated to understand how the improved locomotion economy was achieved [96, 132, 160, 237].

Re-establishing healthy gait patterns is further complicated by the fact that the human nervous system responds differently to different robot interventions. Some evoke changes or adaptation in neuro-motor control. These changes can be person-specific and occur over multiple timescales, lasting from minutes to years. It seems reasonable that induced changes in the nervous system are a pre-requisite for an intervention to be considered as a viable treatment option for neuro-recovery. However, it is as yet uncertain what promises persistent neuro-motor recovery, and even if so, how long the required training would be [168].

Compensation is another approach through which healthy gait patterns can be reinstated. While they may not induce long-term changes in the central nervous system, compensatory interventions may immediately augment locomotor capabilities, and that may evoke secondary benefits. Therefore, understanding a robot's influence on locomotor behavior – and the underlying neural controller – is needed to determine whether an intervention is suitable for treatment (to promote long-term recovery) or compensation (by providing assistance).

In the work reported here, we characterized how gait kinematics change with the application of virtual stiffness using a hip exoskeleton robot, to determine its potential for gait rehabilitation, either therapeutic or compensatory. We surmised that the mismatch of gait kinematics between healthy and impaired individuals may result from (or at least can be mathematically described as) an inability to properly tune joint stiffness [74]. Thus, it may be possible to restore healthy kinematics by applying a compensatory joint stiffness, positive or negative, to the affected joint(s). We also assessed whether the altered kinematics that resulted from applying hip stiffness contained behavioral signatures indicative of changes of central neuro-motor control. Modulating stiffness is an appealing approach for several reasons. First, it makes the exoskeleton act in a predictable manner. Second, it can be used for various walking conditions without requiring on-line estimation or prediction of the

gait phase, human intent, or the environment (e.g., ground slope and height). Third, stiffness can be passively implemented as a low-cost, low-mass, and low-power device, as shown in [140, 151, 193].

We used the Samsung Gait Enhancing and Motivating Systems for Hip (GEMS-H) exoskeleton [106,114,116,189] to emulate a virtual spring between the thighs of unimpaired subjects. We first evaluated whether applying stiffness induced quantifiable changes in gait kinematics (hip range of motion and stride duration) under various conditions (treadmill and overground). With a view to applications in locomotor rehabilitation, we also assessed whether the altered kinematics resulting from applying hip stiffness contained behavioral signatures indicative of changes in neuro-motor control. Preliminary reports of portions of this work were presented in [78, 107].

4.2 Methods

4.2.1 Participants

A total of 12 healthy, young adults (mean age: 25.3 years; gender: four females, eight males) took part in this study. Three independent experiments were conducted and four subjects participated each experiment. Each subject took part in only one experiment. None had previously worn a hip exoskeleton nor partaken in a similar experiment. All participants gave informed written consent before the experiment. The experimental protocol was approved by the Institutional Review Board of the MIT (protocol #: 1809534122; approval date: 10/18/2018).

4.2.2 Equipment: Samsung GEMS-H Exoskeleton

The Samsung Gait Enhancing and Motivating Systems for Hip (GEMS-H) developed by Samsung Advanced Institute of Technology (Suwon, South Korea) was used in this study (Fig. 4-1A; [106, 114, 116, 189]). Detailed description of the device can be found in Chapter 3.

4.2.3 Stiffness Controller

In all experiments, the GEMS-H was programmed to emulate a virtual torsional spring between the thighs using the following control law (Fig. 4-1A):

$$\theta_{\mathrm{REL}} = \theta_{\mathrm{L}} - \theta_{\mathrm{R}} \tag{4.1}$$

$$\theta_{\mathrm{REL,DZ}} = \begin{cases} \theta_{\mathrm{REL}}, & \text{if } |\theta_{\mathrm{REL}}| \geq \theta_{\mathrm{th}} \\ 0, & \text{otherwise} \end{cases} \tag{4.2}$$

$$\begin{bmatrix} \tau_{\mathrm{L}} \\ \tau_{\mathrm{R}} \end{bmatrix} = \begin{bmatrix} -k\theta_{\mathrm{REL,DZ}} \\ k\theta_{\mathrm{REL,DZ}} \end{bmatrix} \tag{4.3}$$

where k is the torsional stiffness, θ_{REL} is the relative angle between two legs, and $\tau_{\mathrm{L}}, \tau_{\mathrm{R}}$ are hip joint torques on the left (L) and right (R), respectively. To ensure a smooth sign change in the output torque, a deadzone (θ_{th}, approximately ± 2 deg) was applied to the relative angle ($\theta_{\mathrm{REL,DZ}}$). The commanded torque was determined by a high-level controller running at 200 Hz and implemented by a low-level current controller running at 10 kHz. Torques with the same magnitude and opposite direction were applied to left and right legs. This minimized the net moment applied to the robot base and minimized relative motion between the robot and the human subject, improving both user comfort and measurement accuracy. When the applied stiffness was positive (i.e., $k > 0$ Nm/rad), the exoskeleton pushed the thighs together to a stable equilibrium point at $\theta_{\mathrm{REL}} = 0$ rad. When it was negative (i.e., $k < 0$ Nm/rad), the robot pulled the thighs apart from an unstable equilibrium point at $\theta_{\mathrm{REL}} = 0$ rad. When the stiffness controller was off (i.e., $\tau_{\mathrm{L}} = \tau_{\mathrm{R}} = 0$ Nm), the backdrivable exoskeleton exerted minimal torque.

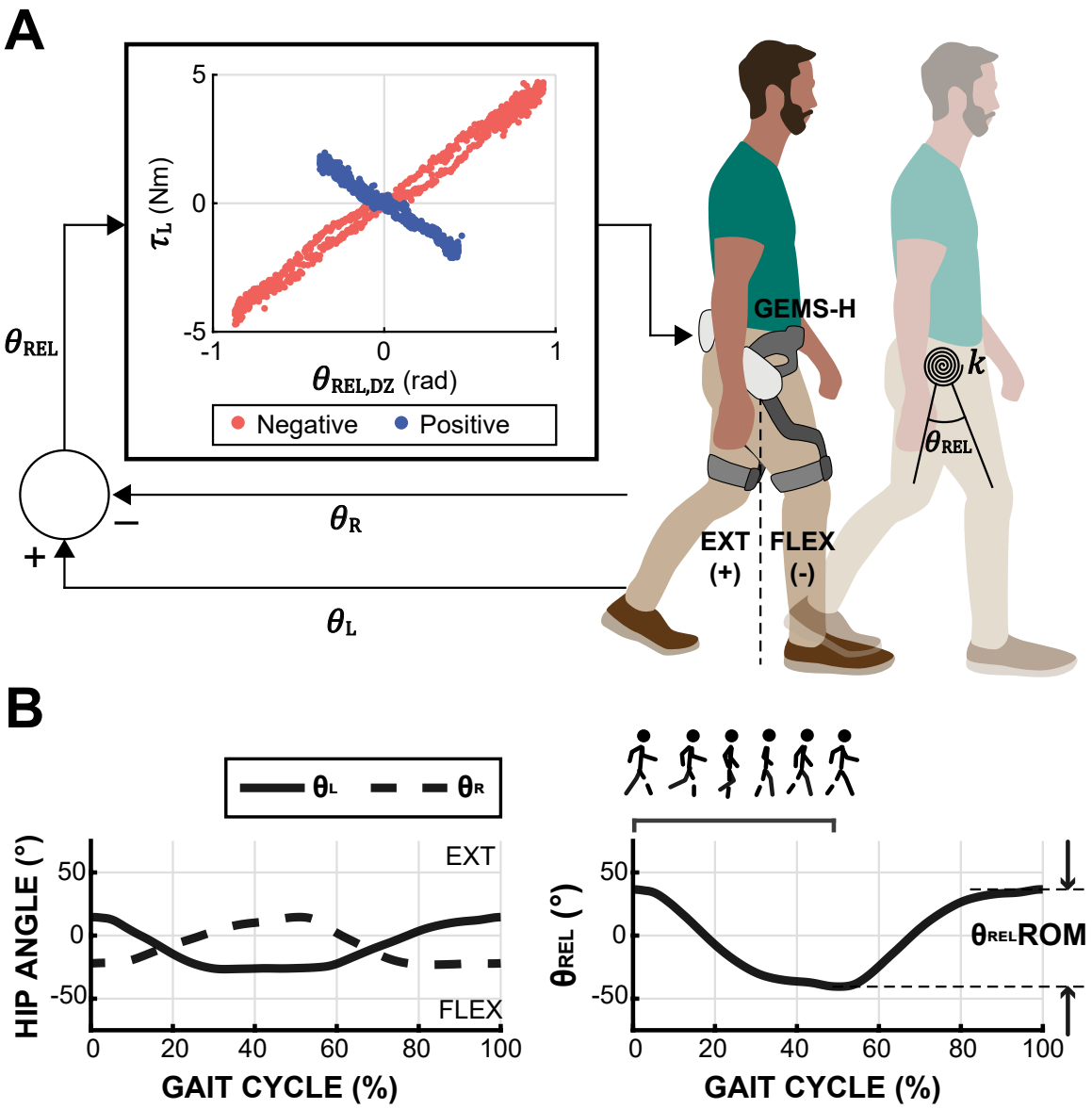

Figure 4-1: **A** The Samsung GEMS-H exoskeleton emulated positive and negative stiffness between the two thighs. Subjects were instructed to walk comfortably either on a treadmill (TM) or overground (OG). **B** Stride segmentation and θ_{REL}ROM of normal walking without torque applied.

4.2.4 Data Processing and Dependent Measures

Signal Processing

Encoders embedded in the actuator modules directly measured joint angular positions (sampling rate: 200 Hz). Using an FIR filter (order: 50, passband: 20 Hz, stopband: 30 Hz) approximating an ideal low-pass filtered differentiator, the position signals were filtered to estimate joint velocities off-line. The group delay of the filter was used to compensate for the time shift of the signals due to the filtering process. Signal processing was performed using MATLAB R2018b (Mathworks, MA; function: `designfilt`).

Stride Segmentation

To calculate dependent measures, we first segmented and time-normalized the signals for each stride. Each stride began with maximum extension of the left hip joint (0 % of the gait cycle), which approximately corresponds to left toe-off [157]. The left thigh flexed (negative velocity), approximately from 0 % to 50 % of the gait cycle and extended (positive velocity) approximately from 50 % to 100 % of the gait cycle.

Dependent Measures

The temporal aspects of gait behavior were characterized by stride duration. The spatial aspects were quantified by the range of motion (ROM) of the relative angle (θ_{REL}). Note that the ROM of hip motion is highly correlated with stride length. The ROM of the i-th stride was computed as $\theta_{\mathrm{REL}}\mathrm{ROM}\ [i] = \theta_{\mathrm{REL,max}}[i] - \theta_{\mathrm{REL,min}}[i]$ as illustrated in Fig.4-1B.

Statistical Analysis

Statistical analyses were performed using the Statistics and Machine Learning Toolbox of MATLAB R2018b (Mathworks, MA). Statistical tests are detailed under individual experiments described below. Within-subject ANOVA was conducted using MATLAB function `anovan`. For all statistical tests, the significance level was

set to $p = 0.05$. When a significant effect was found with more than two levels, planned comparisons in the form of pairwise t-tests for within-subject effects were conducted to determine which pairs of levels were significantly different from one another, using the MATLAB function `ttest` without applying any corrections. The results were double-checked with MATLAB function `fitrm, ranova, multcompare`. Mixed-effect within-subject ANOVA was conducted using an online-available function [88].

4.2.5 Experimental Protocols

Experiment 1

The first experiment evaluated how applied stiffness affected kinematics during overground walking. This included an investigation of transient and steady-state behavior to determine if adaptation or learning occurred.

Each subject performed a total of 8 trials while wearing the GEMS-H exoskeleton. In each trial, subjects walked for 120 strides at their preferred pace in a long corridor (approximately 250 m) with low foot traffic to simulate real-world walking conditions. The first two trials were considered baseline trials. During these trials, the stiffness controller was off for all 120 strides (BL). In the six experimental trials, the stiffness controller was off for the first 20 strides (PRE), turned on for the next 50 strides (ON), and then turned off for the remaining 50 strides (OFF). Half of the trials were performed with negative stiffness (k = -5 Nm/rad), and the other half were performed with positive stiffness (k = 5 Nm/rad). Trials performed in each stiffness condition were blocked and counterbalanced across subjects.

To assess the effect of applied stiffness on kinematics during overground walking, a 3 (Condition: PRE vs. ON vs. POST) x 3 (Trial: 1 vs. 2 vs. 3) within-subjects ANOVA was conducted on mean θ_{REL}ROM and mean stride duration separately for each stiffness condition.

Experiment 2

Given the prevalent use of treadmills for gait rehabilitation, the second experiment evaluated whether the effect of applied stiffness on kinematics differed during treadmill walking compared to overground walking. Because the treadmill affords longer walking trials, the response to both long and short repeated exposures was examined. Kinematic changes during overground (Experiment1) and treadmill (Experiment2) walking were then compared.

The experiment took place over two consecutive days. On each day, subjects performed three trials (BL: baseline, SE: short-exposure, and LE: long-exposure) wearing the GEMS-H exoskeleton while walking on a Sole Fitness F80 treadmill (0.84 m $\times$ 1.90 m deck; 0.045 m/s belt speed resolution). Preferred treadmill speed was established by each subject at the beginning of each experiment and then maintained for all remaining treadmill trials. Subjects were given up to 200 strides to self-adjust the speed of the treadmill to one they felt could comfortably be maintained for the duration of the experiment.

In the BL trials, subjects walked with the stiffness controller off for 1000 strides (BL). In the SE trials, subjects walked for 540 strides. The stiffness controller started in the off state for the first 60 strides (SE0-OFF) and then toggled between on and off for four blocks (SE1, SE2, SE3, SE4). Each block consisted of 60 strides with the controller on (SE1-ON, ..., SE4-ON), followed by 60 strides with the controller off (SE1-OFF, ..., SE4-OFF). Stiffness was positive (5 Nm/rad) on one day and negative (-5 Nm/rad) on the other, and this order was counterbalanced across subjects. While subjects were informed that the controller would turn on and off during the trial, they were not told how the exoskeleton was controlled. For safety purposes, subjects walked for approximately 10 strides overground with the exoskeleton powered before the start of the SE trial. In the LE trials, subjects walked for 1000 strides with the stiffness controller on (LE). The stiffness value was the same as that used in the SE trial of that day.

To assess the effect of applied stiffness on kinematics during treadmill walking, a 2

(Stiffness: positive vs. negative) x 2 (Condition: BL vs. LE) within-subjects ANOVA was conducted on mean θ_{REL}ROM and mean stride duration. A 2 (Controller state: ON vs. OFF) x 4 (Block: SE1 vs. SE2 vs. SE3 vs. SE4) within-subject ANOVA was conducted on mean θ_{REL}ROM and mean stride duration separately for each stiffness condition to determine whether the effect of applied stiffness differed across short, repeated exposures.

To test whether the effect of applied stiffness differed between overground (Experiment1) and treadmill walking (Experiment2), a 2 (Terrain: TM vs. OG) x 2 (Stiffness: positive vs. negative) mixed ANOVA was conducted on mean $\Delta\theta_{\mathrm{REL}}$ROM and mean Δstride duration. Terrain was a between-subjects factor, and stiffness was a within-subjects factor. The dependent measures were calculated for all strides across all trials when the controller was 'ON (Experiment1: ON, Experiment2: LE)' and 'OFF (Experiment1: POST, Experiment2: BL)'; ANOVA was conducted on the mean of difference of 'OFF' from 'ON'.

Experiment 3

The third experiment was designed to test whether changes in kinematics affect or transfer to subsequent tasks with different stiffness values.

Each subject performed four experimental trials. Each trial was performed either on the treadmill (TM) or overground (OG). In decreasing (DEC) trials, stiffness was applied between thighs by the exoskeleton robot and its value was incrementally decreased from positive (k = 7 Nm/rad) to negative (k = -3.5 Nm/rad) by Δk = 3.5 Nm/rad. In increasing trials (INC), the stiffness was increased from negative to positive over the same range. For each stiffness value, subjects walked 100 strides on the treadmill or 15 strides overground. Before and after each experimental trial, subjects walked at their preferred speed for 50 strides on the treadmill (or 10 strides overground) with the robot controller off. All trials were conducted in a single day. Treadmill and overground trials were grouped, and the order of each group was randomized for each subject. The order of trials (increasing or decreasing stiffness) were also randomized in each group.

To determine whether the effect of applied stiffness on kinematics depended on the order in which the different values were applied, a 2 (Order: increasing vs. decreasing) x 2 (Terrain: treadmill vs. overground) x 3 (Stiffness: -3.5 Nm/rad vs. 3.5Nm/rad vs. 7 Nm/rad) within-subjects ANOVA was conducted on mean θ_{REL}ROM.

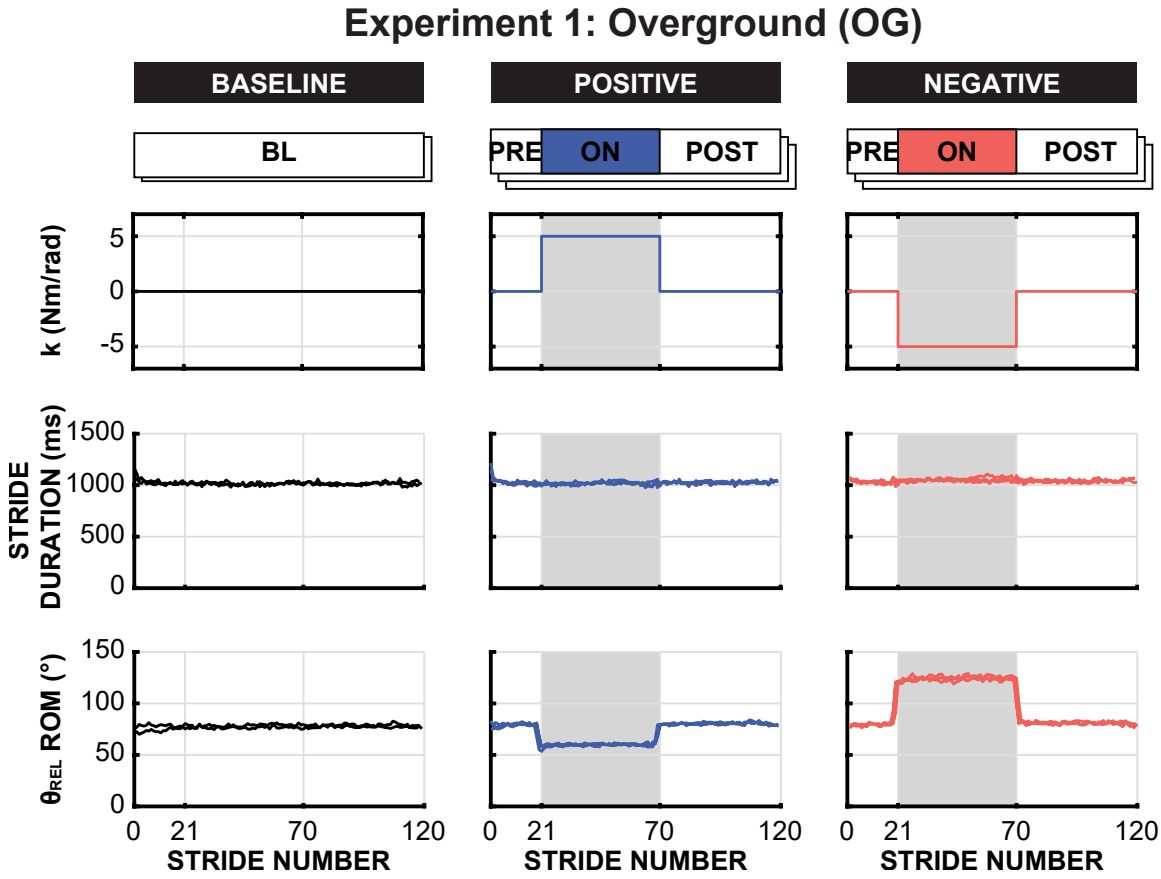

Figure 4-2: Representative subject data of experiment 1. Stride duration and θ_{REL}RoM of all trials during baseline (left), positive (middle), and negative (right) stiffness conditions are shown. Shaded regions represent when the controller was on.

4.3 Results

4.3.1 Experiment 1

Fig. 4-2 exemplifies how gait patterns changed over strides in different stiffness conditions (baseline, positive, and negative). Note that the graph shows all trials of the same representative subject in each panel; the response was consistent across

repeated exposure to the intervention. During the baseline trials, both stride duration and θ_{REL}ROM remained unchanged. When the positive (negative) stiffness was applied, θ_{REL}ROM immediately decreased (increased) and remained unchanged over 50 subsequent strides with the controller ON. When the stiffness was removed, again θ_{REL}ROM immediately recovered to the baseline level and remained unchanged thereafter. On the other hand, stride duration was essentially unaffected by the robot controller. Fig. 4-3 shows ensemble averages of the left, right, and relative hip angles during a single stride for different stiffness conditions (Baseline BL, Positive ON, Negative ON). Note that the symmetry between left and right legs, typical of unimpaired and unperturbed walking, was preserved despite the presence of applied stiffness.

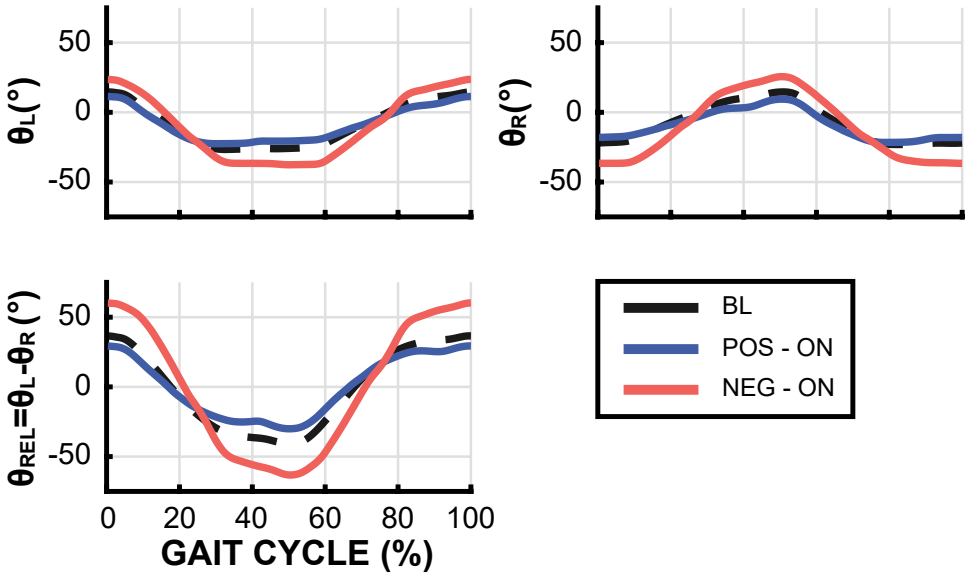

Figure 4-3: Ensemble average of all trials of the same representative subject's hip angles (left: top, right: bottom) over a gait cycle from baseline, positive stiffness on (POS-ON), and negative stiffness on (NEG-ON) of experiment 1. For each stride, the maximum left hip angle was used to determine 0 % gait cycle.

Phase plane trajectories at the controller transitions (ON-to-OFF and OFF-to-ON) from a representative subject are shown in Fig. 4-4. It also shows the strides immediately before and immediately after the controller state transition as well as the last stride in the 'new' (transitioned) state. Steady-state behavior was reached within a single stride.

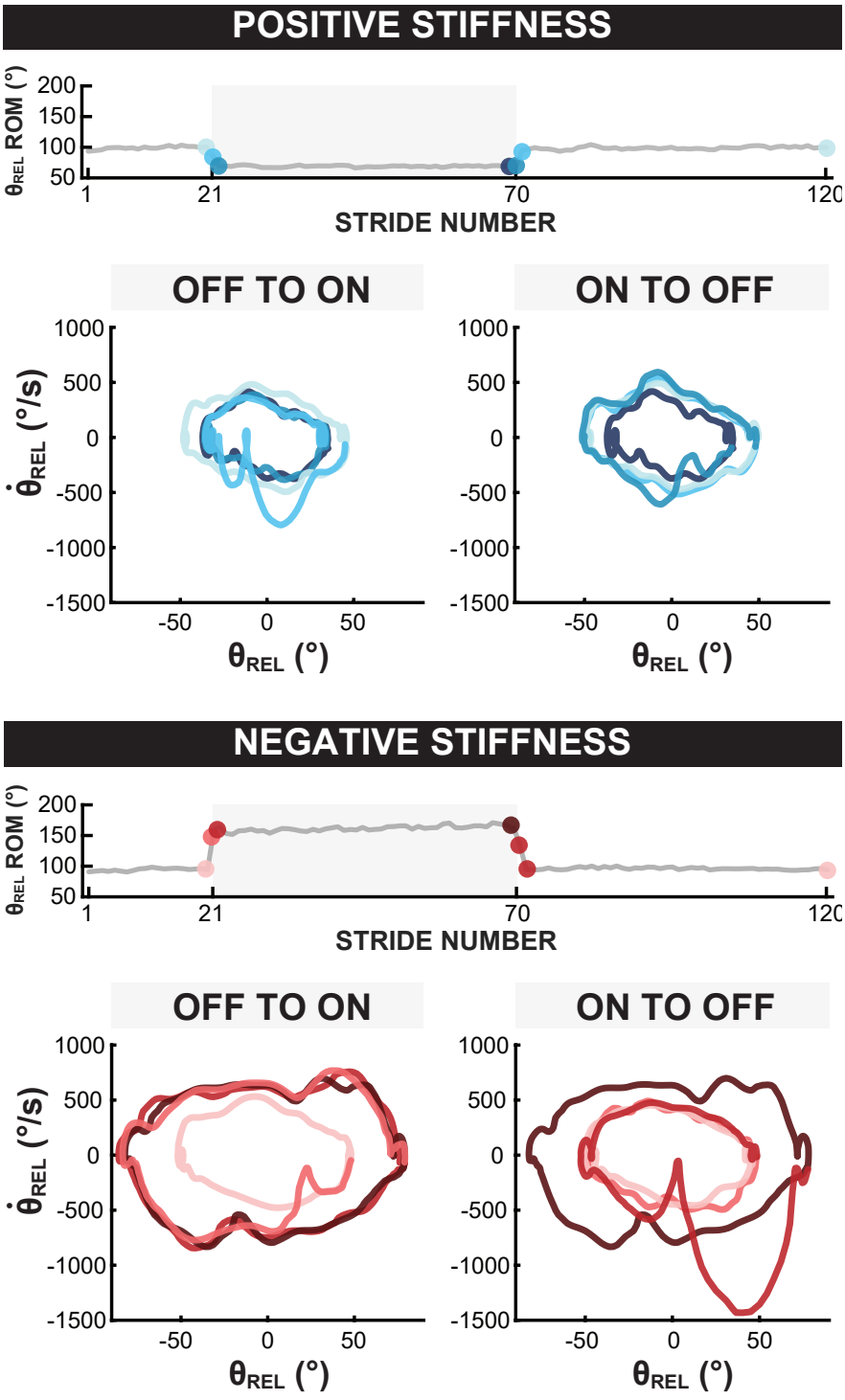

Figure 4-4: Phase plane trajectories of strides at the controller state transitions (ON-to-OFF and OFF-to-ON) from a representative subject during a positive stiffness trial (top) and a negative stiffness trial (bottom).

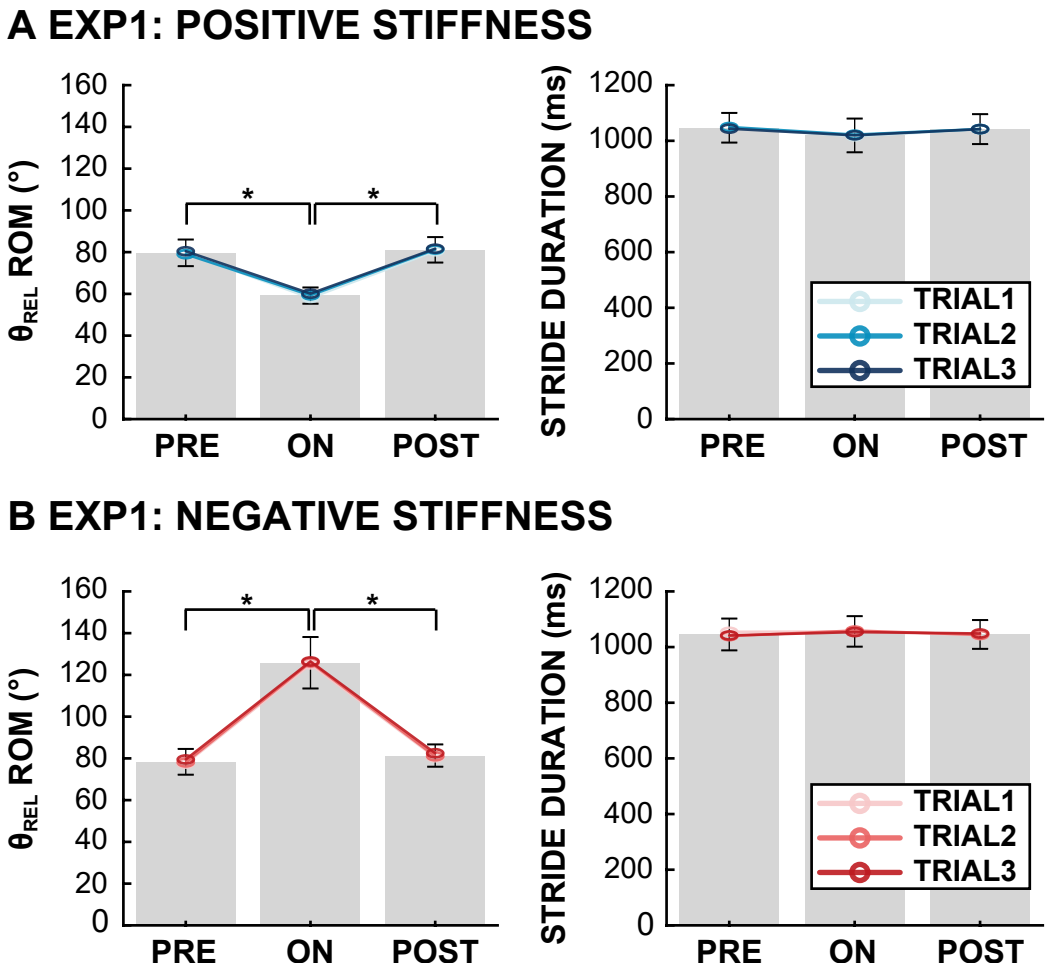

Figure 4-5: Experiment 1 results. Mean dependent measures for all subjects for each condition (PRE, ON, POST) for each experimental trial (trial 1, trial 2, trial 3) for positive stiffness **A** and negative stiffness **B**. All three trials are plotted on top of one another. Shaded bar graphs and error bars represent the mean of all trials for each condition and 1 standard error across subjects. * indicates a significant effect of condition with $p < 0.05$, revealed by planned comparisons.

Effects of applied stiffness on kinematics

The main effect 'Condition (PRE vs. ON vs. POST)' was significant for mean ROM for both positive and negative stiffness (Fig. 4-5A, Table 4.1). The 'Condition' for mean stride duration was barely significant for positive stiffness ($p = 0.05$); however, planned comparisons did not reveal significant differences between levels. Thus, even though the effect was statistically significant, it was weak. Moreover, the differences between the conditions on mean stride duration for positive stiffness (below 30 ms) were on par with the typical variability observed in normal walking (3 % of mean stride

duration [70]). The difference between PRE and POST condition were insignificant, indicating that the behavior returned to baseline after removal of the intervention.

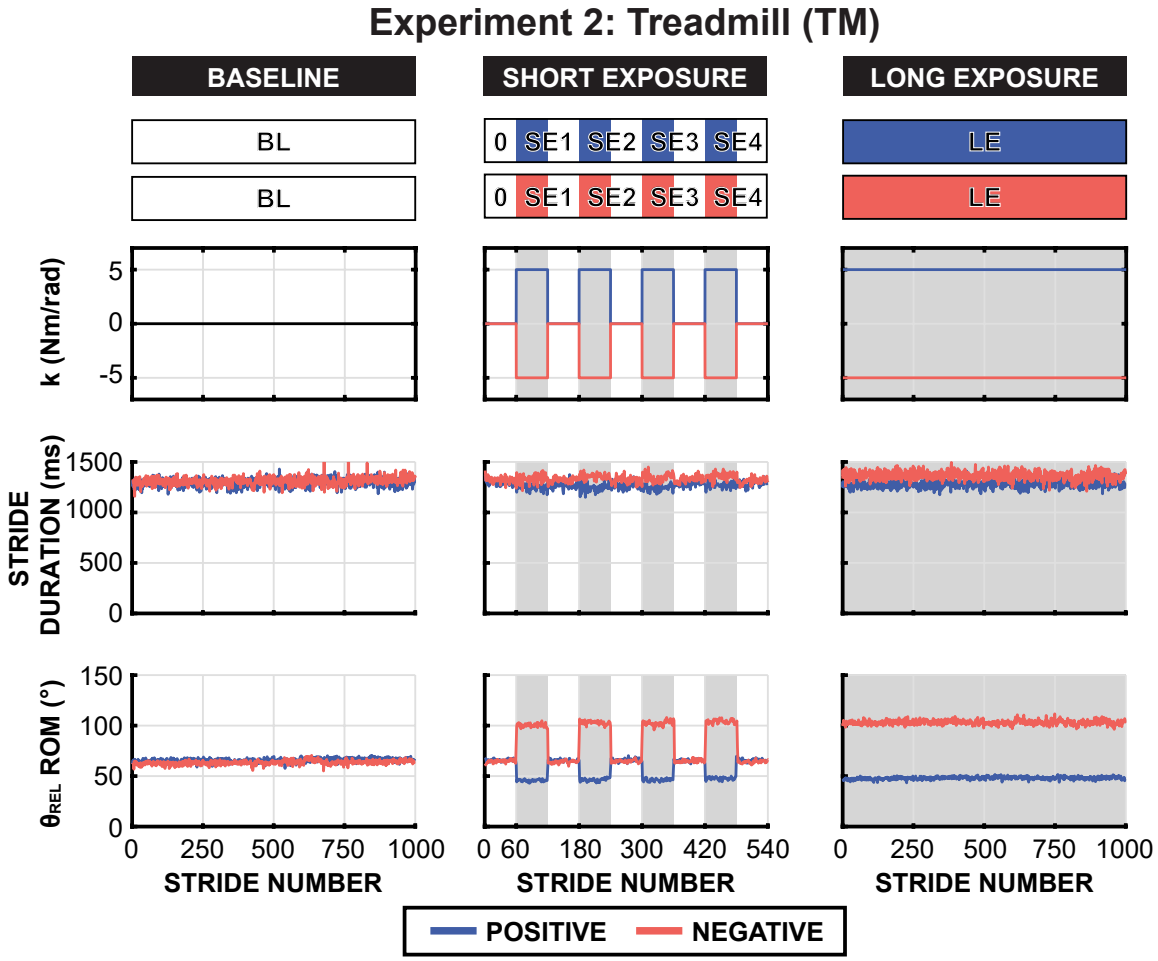

Figure 4-6: Representative subject data of experiment 2. Stride duration and θ_{REL}RoM during baseline (left), short-exposure (middle), and long-exposure (right) trials in the positive (blue) and negative stiffness (red) conditions are shown. Shaded regions represent when the controller was on.

4.3.2 Experiment 2

Fig. 4-6 exemplifies how the gait patterns of a representative subject changed over strides in three different stiffness conditions. As in experiment 1, the change of θ_{REL} was immediate and significant when the robot controller was turned ON and OFF, and the response was similar over repeated short exposures (SE) for both positive and negative stiffness. Moreover, the ROM was maintained over 1000 strides for both

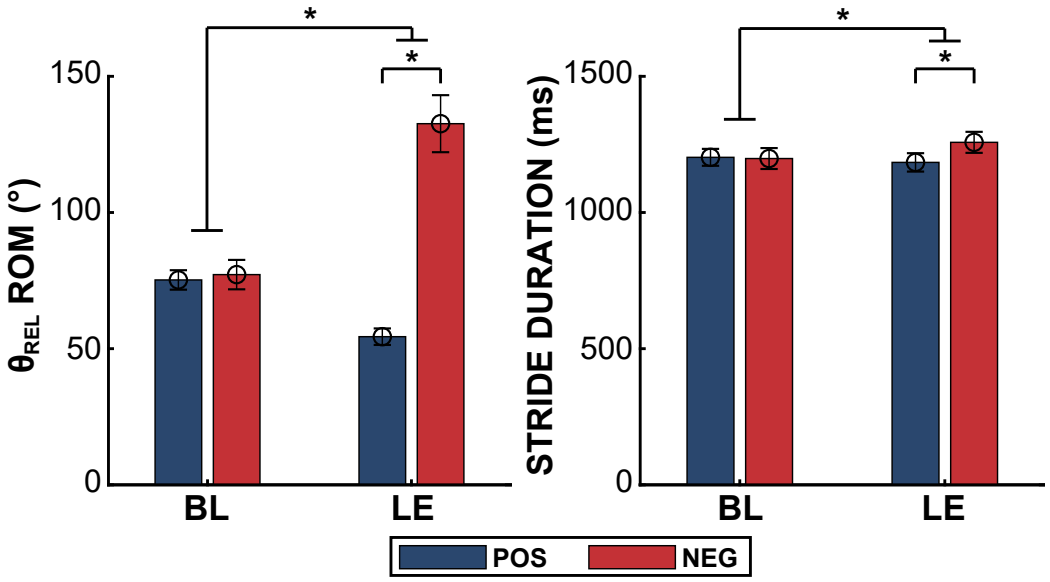

Figure 4-7: Experiment 2 results. Mean dependent measures of all subjects for each condition (BL, LE) for positive (POS) and negative (NEG) stiffness. Error bars represent 1 standard error of the mean across subjects. * indicates a statistically significant difference ($p < 0.05$).

positive and negative stiffness (LE). However, stride durations were not as consistent as in Experiment 1. In particular, in the negative stiffness condition, where the magnitude of kinematic change was larger, stride duration showed larger variability.

Effects of applied stiffness on kinematics

Both main effects (stiffness: positive vs. negative and condition: BL vs. LE) and their interaction had a significant effect on the mean ROM (Fig. 4-7, Table 4.2). Condition and interaction had a significant effect on stride duration (although the effect of condition was marginal; $p = 0.048$) while stiffness did not (Fig. 4-7, Table 4.2). Planned comparisons revealed that the mean θ_{REL}ROM and the mean stride duration of the LE condition between positive and negative stiffness were significantly different ($p = 0.0024$ and $p = 0.027$, respectively), while those of the BL condition were not. This significant interaction occurred because positive and negative stiffness affected ROM and stride duration in opposite ways; for example, applying negative stiffness increased ROM while positive stiffness decreased it.

Effects were similar across short, repeated exposures

The controller state (ON vs. OFF) had a significant effect on mean ROM for both positive and negative stiffness (Fig 4-8, Table 4.3). It had a significant effect on mean stride duration for negative stiffness only. Block (SE1 vs. SE2 vs. SE3 vs. SE4) had a significant effect on mean ROM for negative stiffness only (Fig 4-8, Table 4.3). However, planned comparisons did not reveal significant differences between levels. Thus, even though the effect was statistically significant, it was weak. Moreover, the differences between mean stride duration for negative stiffness (less than 16 ms) were far less than the typical variability observed in normal walking.

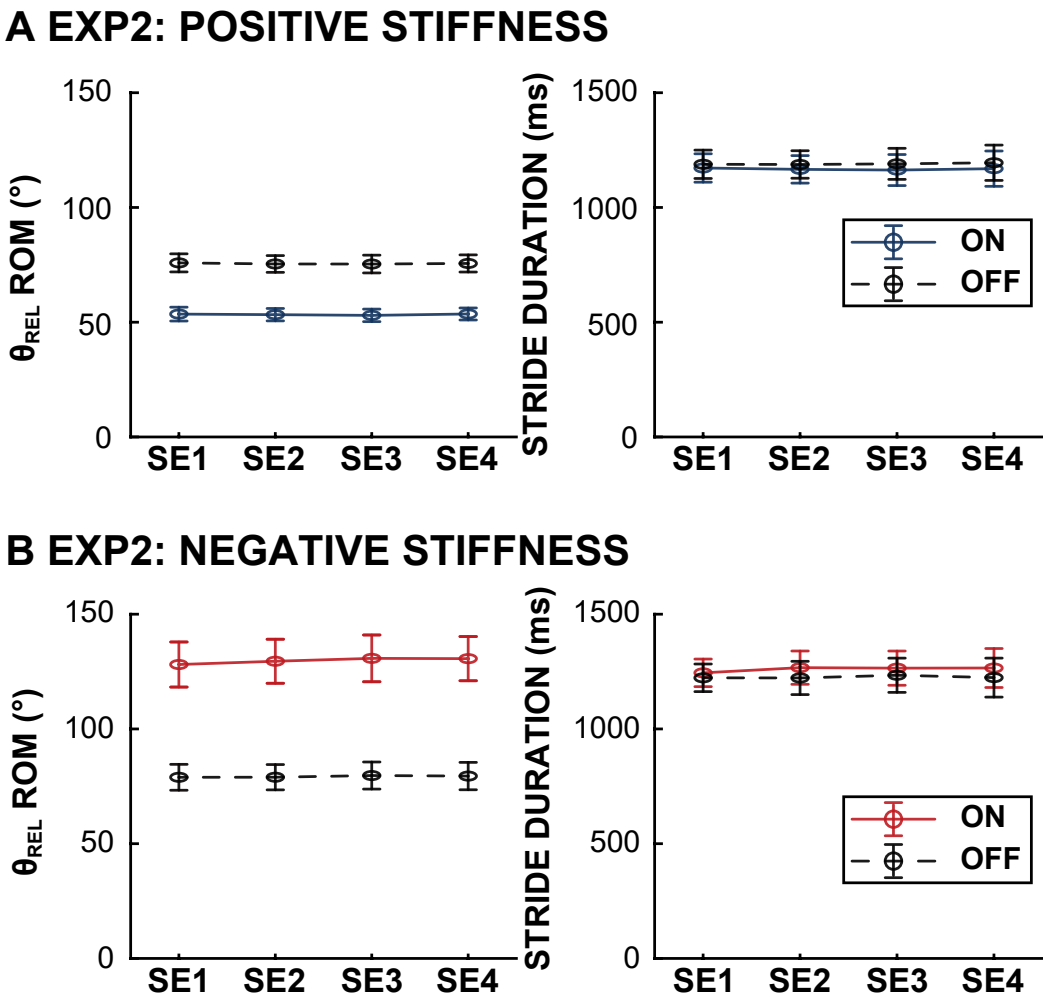

Figure 4-8: Experiment 2 results for short exposure trials. Mean dependent measures of all subjects for each block (SE1, SE2, SE3, SE4) and for each controller state (ON, OFF) for positive **A** and negative stiffness **B**. Error bars represent 1 standard error of the mean across subjects.

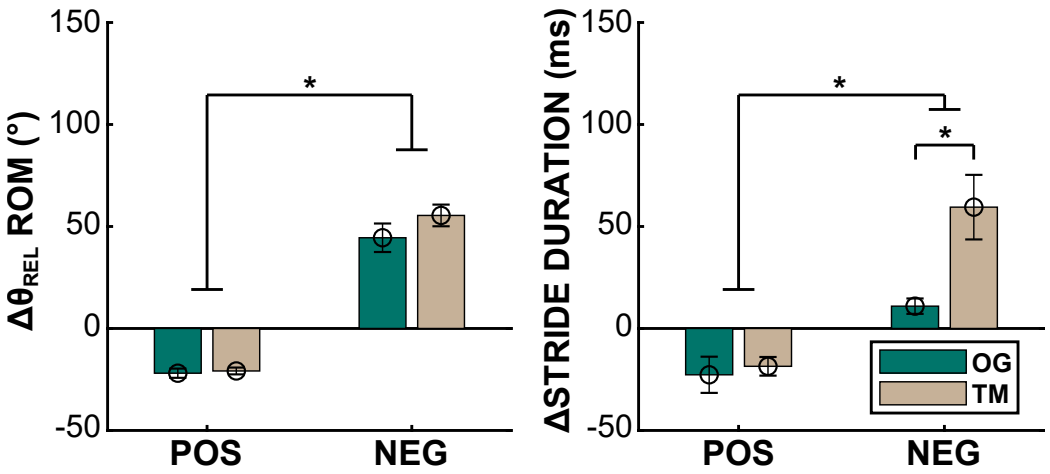

Figure 4-9: Experimental results comparing walking overground (Experiment1) and on treadmill (Experiment2). Mean changes in the dependent measures from controller state on to off for each walking condition. Error bars represent 1 standard error across subjects. * indicates a statistically significant difference ($p < 0.05$).

Difference between overground (Experiment1) and treadmill (Experiment2) walking

The effect of stiffness (positive vs. negative) on both $\Delta\theta_{\text{REL}}$ROM and Δstride duration was statistically significant (Fig. 4-9, Table 4.4). The effect of terrain (OG vs. TM) was statistically significant on stride duration only.

4.3.3 Experiment 3

Fig. 4-10 exemplifies how the gait patterns of a representative subject changed over strides while the subject was walking on the treadmill (TM) or overground (OG) while stiffness decreased (DEC) or increased (INC). In all trials, when the exoskeleton stiffness value changed, Mean θ_{REL}ROM was immediately altered and remained unchanged over subsequent strides. Fig. 4-11 shows mean $\Delta\theta_{\text{REL}}$ROM values averaged across subjects, for different conditions. Note that responses in DEC and INC trials are almost identical.

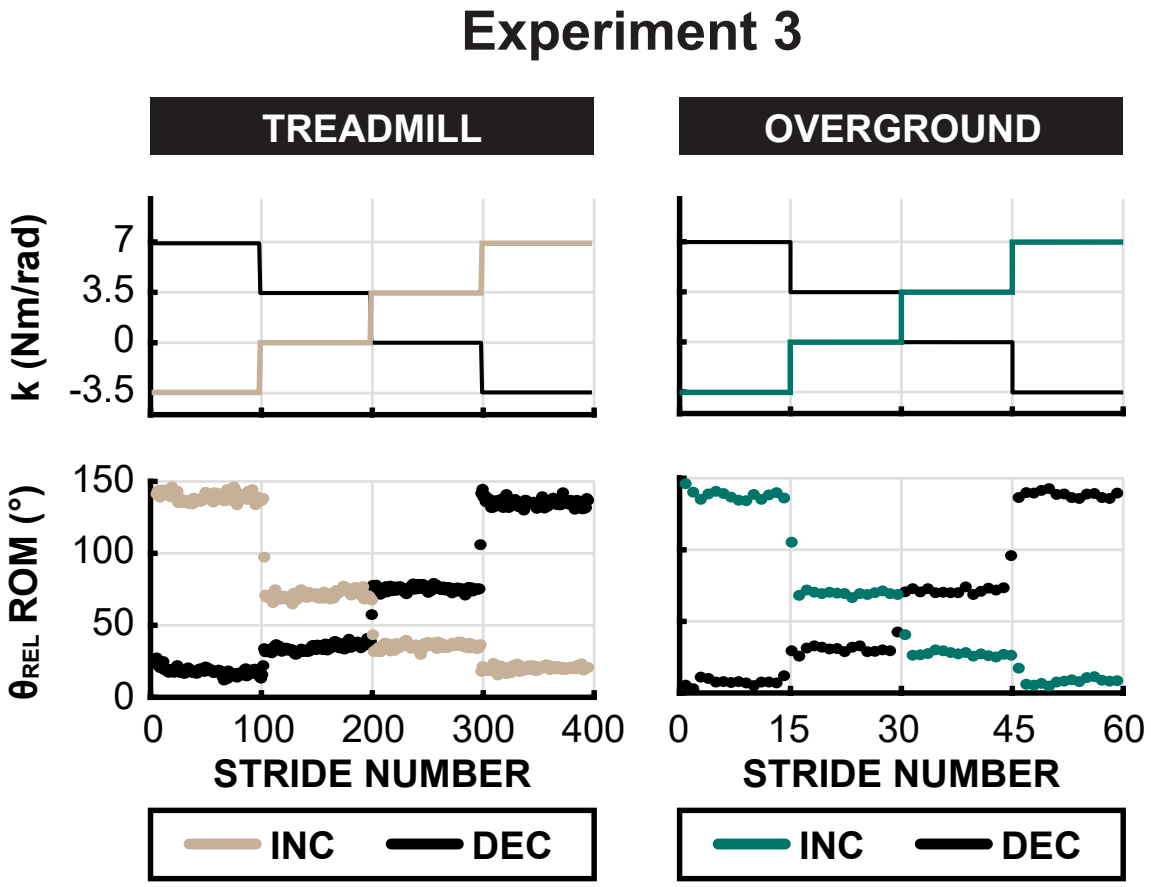

Figure 4-10: Representative subject data of experiment 3. Each trial was performed either on the treadmill (TM) or overground (OG). The robot applied stiffness k that changed from positive to negative values (decrease, DEC) or from negative to positive (increase, INC).

Does increasing and decreasing stiffness account for observed differences?

Stiffness (-3.5 Nm/rad vs. +3.5 Nm/rad vs. +7 Nm/rad) had a significant effect on mean $\Delta\theta_{\text{REL}}$ROM, but order (INC vs. DEC) or terrain (TM vs. OG) did not (Fig. 4-11, Table 4.5).

4.4 Discussion

This study characterized unimpaired human subjects' responses to stiffness applied between the thighs during walking. With a view to applications in locomotor rehabilitation, either to provide assistance or promote recovery, this study aimed to assess

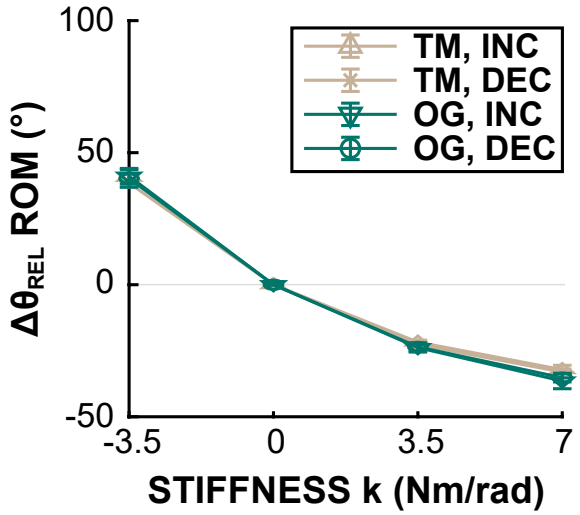

Figure 4-11: Mean $\Delta\theta_{\text{REL}}$ROM at each stiffness value, averaged across all subjects. Error bars represent 1 standard error across subjects.

whether imposed stiffness induced changes in the gait pattern (which is required for assistance); and whether any changes persisted, which would indicate changes in central neuro-motor control (necessary to promote recovery).

Both positive and negative stiffness significantly affected kinematics (Fig. 4-2-Fig. 4-11) as represented by the changes in θ_{rel}ROM. However, the experimental results showed little, if any, evidence of changes in neuro-motor control, inconsistent with previous studies that observed adaptation in response to imposed stiffness [20] or damping [103]. Changes in thigh kinematics due to imposed stiffness persisted over 50 strides (Experiment1, Fig. 4-2) or 1000 strides (Experiment2: LE, Fig. 4-6). They were consistent across multiple trials (Experiment1, Fig. 4-2) or repeated short-term exposures (Experiment2: SE, Fig. 4-6). The presence of time-varying behavior often signals change in the neuro-motor system (e.g., learning or adaptation); we did not observe this.

The existence of transients (e.g., aftereffects) and changes in transient behavior (e.g., savings) when switching between conditions also reflect changes in neuro-motor control. Neither was observed. Changes in kinematics occurred within a single stride, both when the controller transitioned from OFF to ON and ON to OFF. The applied stiffness also did not affect steady-state baseline behavior. For example, there was

no difference between PRE and POST in experiment 1. Moreover, neither repeated transitions between ON and OFF (Experiment2: SE, Fig. 4-6) nor changing the order of stiffness values (Experiment3: INC and DEC, Fig. 4-10) induced significant differences, which implied that even short-lived after-effects were absent.

While the effect of applied hip stiffness on the spatial aspects of gait was immediate and pronounced, its effect on the temporal aspects was minimal. During overground walking, stride duration was essentially unaffected. Changes in stride duration were greater during treadmill walking. Such a differential effect on treadmill and overground walking is not surprising [12, 145]. It might be attributed to the constraints on speed and admissible foot placements that the treadmill imposed. Practically speaking, changes in stride duration were small given the natural variance observed during walking [70].

4.4.1 Limitations of the Present Study

Robot-embedded Hip Measurement

In this study, robot-embedded encoder measurements were post-processed to compute temporal and spatial measures of gait. Because the robot did not perfectly conform to each individual, the hip joint angles measured by the robot-embedded encoders may have differed from the human hip joint angles. Nonetheless, our conclusion that changes in gait pattern due to applied stiffness did not reflect adaptation are still valid because they rely on the trend of changes rather than exact values. It is also possible that knee, ankle, or other body parts may have exhibited adaptive changes that we did not measure. However, normal subjects exhibit robust intra-limb coordination [169, 220], hence it would be remarkable indeed if the knee and/or ankle joints exhibited adaptive changes while the hip joint did not. Nonetheless, measurements based on whole-body kinematics (e.g., stride length) would be useful to confirm and further illuminate our results. In addition, direct measurements of muscle activity (e.g., surface electromyography; sEMG) would be useful to identify neuro-muscular mechanisms associated with the behavioral changes.

Robot Torque/power Transfer

The robot actuators transmitted power and/or torque through a thigh frame and belt assembly that was tightly coupled to the human subject. Due to actuator friction and elasticity in tissues and/or the thigh frame, torque transmission may have been imperfect. The difference between torque estimated from on-board sensors and external force-sensitive resistor (FSR) sensors was presented in [38]. However, even if the actual applied torques differed from those commanded, their effect on kinematics was unambiguous. Inaccurate torque application cannot dismiss our results.

Subject Population

We only studied young, healthy individuals, and it is possible that impaired subjects may show different responses.

4.4.2 Rehabilitation: Recovery or Compensation?

Technologies for compensation and recovery should be distinguished. An exoskeletal technology may be programmed to behave in many different ways to provide therapy or assistance (or both). A therapeutic intervention for recovery should not just temporarily enhance performance, but also lead to long-lasting improvements in performance under normal conditions. Such longer-term persistence implies that the intervention affected central neural control [80]. In other words, an intervention that does not evoke any changes in central neuro-motor control does not hold promise for long-term recovery.

On the other hand, interventions that do not evoke neuro-motor changes may productively compensate for human capability. Sometimes long-term, permanent behavioral improvement cannot be achieved; in that case, compensation without recovery is still valuable. For locomotion, an assistive intervention that did not evoke adaptation might still be beneficial; for example, it might improve balance immediately [79], augment load-carrying performance, improve economy, and may allow those with abnormal kinematics to walk with longer strides and faster speed, which might have

positive cardio-vascular effects as well. Assistive and therapeutic interventions both have their roles in rehabilitation.

In this study, we did not observe any evidence of changes in central neural control needed for neuro-recovery. Current therapeutic paradigms for rehabilitation are based on principles of motor learning and neuroplasticity [97,149,168]. Motor learning refers to a process associated with long-term practice or experience leading to relatively permanent changes in behaviors (Fig. 4-12A) [168,200]. Motor adaptation is a relatively short-term process of correcting an initial abrupt change in behavior due to a novel intervention (Fig. 4-12B) [18,168,191,200]. The presence of negative after-effects upon removal of the intervention implies the central neuro-motor controller was adjusted. Some interventions that elicited locomotor adaptation in healthy humans [21,59,103] also improved neurologically impaired gait kinematics [104, 229, 230, 235]. While it is still controversial whether repeated adaptations result in learning (hence recovery) [18,168,228] or whether they involve different forms of neuroplasticity [200], both indicate that the CNS makes adjustments to the feedforward motor plan [103, 168], which is necessary for neuro-motor recovery.

Another form of behavioral change is reactive [79, 103, 168]. These responses are immediate reactions necessary to accommodate the intervention. They persist throughout the intervention but then immediately disappear when it is removed, without any evidence of gradual adjustment or aftereffects (Fig. 4-12C) [168]; moreover, those changes do not affect or transfer to subsequent tasks [79]. This type of response indicates that the intervention may have limited benefit for neuro-recovery, but may compensate for inadequate motor behavior by assisting performance; and it is consistent with our data.

4.4.3 Practical Implication

The results of this study, in particular of experiment 3, imply that a (nonlinear) mapping function or a lookup table that can predict changes in kinematics from applied stiffness could be obtained easily and quickly, which would facilitate customizing the proposed intervention to each individual. This is actually a very important property

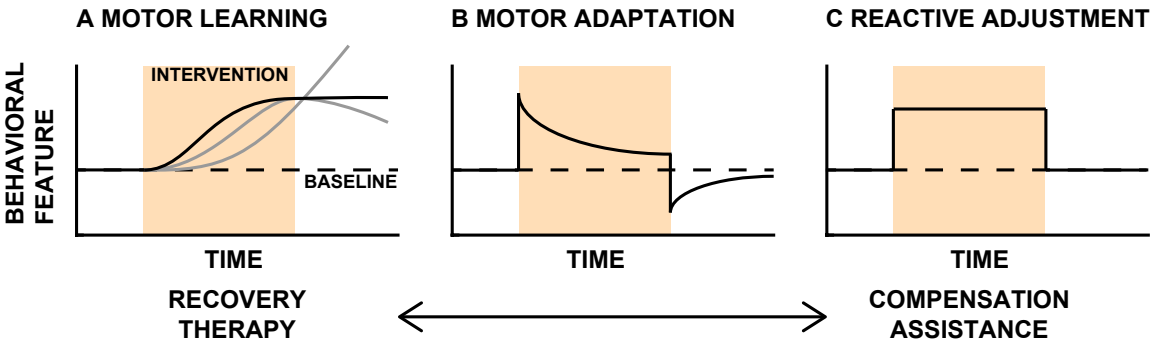

Figure 4-12: Schematic illustration of **A** motor learning, **B** motor adaptation, and **C** reactive adjustment. Motor learning results in a persistent deviation from baseline behavior. Actual patterns may differ from the idealized exemplary graphical illustrations. Motor adaptation exhibits abrupt initial change, gradual correction, and negative after-effects. Reactive adjustment shows immediate and persistent changes in behavior but no aftereffects. Motor learning or adaptation are signatures of changes in neuro-motor control, hence hold promise for recovery. An intervention that evokes only reactive adjustment is more suitable for compensation.

for an exoskeletal technology because the behavior of human individuals are extremely variable [183].

Depending on the value of stiffness, the robot may provide assistance or resistance. In this study, the robot provided assistance (positive work) during half of the gait cycle and resistance (negative work) during the other half. This actually means that the proposed intervention can be realized by purely passive mechanisms, or low-power variable stiffness actuators [27, 28]. Passive exoskeleton technologies have obvious advantages such as low mass, low power, and low cost. On the other hand, using the programmability of a technology such as GEMS-H, modulating stiffness values based on the phase of the gait cycle may achieve always-assisting or always-resisting intervention that might be useful for augmenting or challenging (i.e., “exercising") users while walking.

Despite the lack of evidence of motor adaptation in the current study, it is possible that other forms of virtual impedance may elicit different neural responses. Further studies are encouraged to evaluate the bio-mechanical impact of such interventions on healthy and impaired gait kinematics.

4.4.4 Neural Control of Walking: Insights Gained

This study provides important insight into the complexity of human locomotion control that involves both spinal and supraspinal structures. We found it quite surprising that imposing stiffness between the thighs did not evince any evidence of motor learning or adaptation, whereas many previous studies have shown evidence of locomotor adaptation to various types of interventions during walking [5, 18, 20, 21, 59, 103, 145, 169–171]. Moreover, in upper-limb studies, unstable stiffness applied to the hand evoked motor adaptation that changed hand stiffness to compensate while performing a reaching task [32]. Why did we not see any evidence of neuro-motor adaptation to applied positive / negative stiffness between the thighs?

Motor adaptation is an error-driven calibration process that adjusts motor commands when exposed to a novel intervention [18]. There is some evidence that neuromotor adaptation to a mechanical perturbation is predominantly due to descending drive from supra-spinal levels [91]. For example, an intact cerebellum and motor cortex appear to be critical for motor adaptation [190]. Therefore, the lack of neuromotor adaptation we observed implies that the supra-spinal level of locomotor control did not detect any error to correct despite large changes in kinematics. θ_{REL}ROM is an indicator of stride length. If stride length was a primary concern of the controller, subjects would have adapted to regulate the θ_{REL}ROM during walking. However, they did not, as evidenced by the immediate change with no after-effect, implying that an increase or decrease in θ_{REL}ROM due to applied stiffness was not detected as an error to correct.

A symmetric gait pattern minimizes the net change in angular momentum over a stride and might be important for stability; conversely, an asymmetric gait pattern may negatively impact balance during walking at moderate speed. Notably, the intervention introduced in this study did not affect symmetry between the two legs. The (virtual) spring applied equal magnitude but opposite direction torques to both thighs during the entire gait cycle. In contrast, those interventions that induced locomotor adaptation, e.g., torque pulses [5, 108, 145], forces on a single leg [20, 21, 53,

59, 103], or split-belt treadmills with asymmetric speed [169, 170], all interfered with inter-leg coordination. The requirement 'not-to-fall while moving forward' might be the primary functional objective of walking. In that sense, the neuro-muscular controller might be biased towards producing symmetric patterns of walking. As long as they are symmetric, the supra-spinal nervous system may not perceive even large changes in gait kinematics (e.g., θ_{REL}ROM) as errors to be corrected. Consequently, we suggest that the supra-spinal human walking controller is less sensitive to step length / stride length within broad limits, but sensitive to inter-leg coordination.

The different responses observed in θ_{REL}ROM and stride duration suggest that at least two dissociable control layers exist in the neuro-motor control of human walking. Changes in hip kinematics due to applied stiffness were similar to the changes in behavior observed when humans walked on a narrow beam while wearing rigid soles [79], which could be attributed to mechanical interaction between the periphery and environment [109]. In contrast, in our study, stride duration did not deviate substantially from the normal baseline pattern during overground walking. This suggests the existence of a separate layer controlling the rhythm of walking, which was not affected by the applied stiffness nor by the resultant changes in kinematics.

In sum, we suggest that human locomotion control is organized as a hierarchy with at least three layers: a supra-spinal nervous system that is associated with motor adaptation, an intermediate layer that controls stride duration, and a lower layer that may deal with mechanical interaction between the periphery and the environment (e.g., gravity, ground, etc.) to determine kinematics (e.g., stride length or θ_{REL}ROM). This organization is also consistent with a neuro-mechanical control architecture consisting of a rhythmic pattern generator and a reflex-based neuro-muscular structure as suggested previously [52, 205]. Of course, there may be further layers of control and coordination, e.g. to project affective state or mood (probably a 'high-level' concern) or reduce discomfort (probably a 'low-level' concern), but our data are silent on this possibility.

Here, the supra-spinal nervous system intervenes in the detailed control of the lower-level system only when need arises, e.g., when a symmetric gait pattern is dis-

rupted by mechanical interventions, but not when stiffness is applied between the thighs, slowly correcting descending signals to the lower-level systems. This slow feedback loop is associated with locomotor adaptation that shows gradual changes in gait pattern over more than tens of strides. If descending signals from the supra-spinal layer to the lower layers remain the same (i.e. there is no adaptation or learning), the frequency of walking also remains the same. Applied hip stiffness is autonomously handled by the (lowest-level) peripheral neuro-mechanics without changing timing, resulting in immediate changes of limb kinematics. Of course, whether these speculations have merit requires further investigation.

4.5 Conclusion

This study characterized unimpaired human subjects' responses to rotational stiffness applied about the hip joints during walking. Imposed stiffness evoked significant and reproducible kinematic changes but subjects showed no evidence of neuro-motor adaptation. The lack of neuro-motor adaptation suggests that, within broad limits, the CNS is surprisingly unaware of (or indifferent to) the details of lower limb kinematics. It also suggests that alternative interventions may be required to promote recovery. However, the immediate, significant and reproducible changes in kinematics suggest that applying hip stiffness with an exoskeleton may be an effective assistive technology for compensation.

4.6 Appendix: Statistical Analyses Details

Table 4.1: Two-way 3 (Condition: PRE vs. ON vs. POST) x 3 (Trial: 1 vs. 2 vs. 3) within-subject ANOVA results

		Positive Stiffness				Negative Stiffness			
		Mean ROM		Mean stride duration		Mean ROM		Mean stride duration	
	$[df_{num}, df_{den}]$	F-value	p	F-value	p	F-value	p	F-value	p
Condition	[2, 6]	73.84	**0.0001***	5.4	**0.046***	47.08	**0.0002***	1.63	0.27
Trial	[2, 6]	1.49	0.30	0.09	0.92	4.25	0.071	0.65	0.56
Condition x Trial	[4, 12]	1.05	0.42	0.22	0.92	0.18	0.94	1.8	0.19

Table 4.2: Two-way 2 (Stiffness: positive vs. negative) x 2 (Condition: BL vs. LE) within-subject ANOVA results

		Mean ROM		Mean stride duration	
	$[df_{num}, df_{den}]$	F-value	p	F-value	p
Stiffness	[1, 3]	65.33	**0.004***	10.02	0.051
Condition	[1, 3]	57.1	**0.0048***	10.5	**0.048***
Stiffness x Condition	[1, 3]	141.5	**0.0013***	15.88	**0.028***

Table 4.3: Two-way 2 (Controller state: ON vs. OFF) x 4 (Block: SE1 vs. SE2 vs. SE3 vs. SE4) within-subject ANOVA results

		Positive Stiffness				Negative Stiffness			
		Mean ROM		Mean stride duration		Mean ROM		Mean stride duration	
	$[df_{num}, df_{den}]$	F-value	p	F-value	p	F-value	p	F-value	p
Block	[3, 9]	0.34	0.80	0.56	0.66	8.5	**0.0054***	0.67	0.60
State	[1, 3]	442.5	**0.0002***	6.1	0.090	135.66	**0.0014***	67.17	**0.0038***
Block x State	[3, 9]	0.27	0.85	1.54	0.27	2.96	0.091	1.47	0.29

Table 4.4: Two-way 2 (Terrain: TM vs. OG) x 2 (Stiffness: positive vs. negative) mixed ANOVA results

		Mean ΔROM		Mean Δstride duration	
	$[df_{num}, df_{den}]$	F-value	p	F-value	p
Terrain	[1, 6]	3.23	0.12	9.65	**0.021***
Stiffness	[1, 6]	162.6	**0.000014***	28	**0.0018***
Terrain x Stiffness	[1, 6]	0.77	0.41	4.47	0.079

Table 4.5: Three-way 2 (Order: INC vs. DEC) x 2 (Terrain: TM vs. OG) x 3 (Stiffness (Nm/rad): -3.5 vs. +3.5 vs. +7) within-subject ANOVA

		Mean ΔROM	
	$[df_{num}, df_{den}]$	F-value	p
Order	[1, 3]	0.21	0.68
Terrain	[1, 3]	1.26	0.34
Stiffness	[3, 6]	509.14	**0***
Order x Terrain	[1, 3]	5.3	0.10
Order x Stiffness	[2, 6]	1.55	0.29
Stiffness x Terrain	[2, 6]	0.95	0.44
Order x Stiffness x Terrain	[2, 6]	0.16	0.85

Chapter 5

Walking Model

This work was supported by the Global Research Outreach program of Samsung Advanced Institute of Technology and a Samsung scholarship.

5.1 Introduction

In Chapter 3 and Chapter 4, we quantified changes in gait patterns when different interventions were applied by a hip exoskeleton. To develop effective interventions for human locomotion, it is important to understand underlying neuro-mechanical processes that gives rise to such differences. The goal of this chapter was to identify essential mechanisms to reproduce both experimental observations to enhance our understanding of neuromotor control of human walking.

To develop models, one should first determine the degree of complexity. Indeed, the same behavior can be accounted for by different models with different complexities (Fig. 5-1). The state-of-the-art high-fidelity models have been used to understand underlying control mechanisms of normal walking and to predict human joint mechanics and muscle activities in responses to novel interventions [35, 52, 194]. However, even the high-fidelity models often do not exactly reproduce experimental observations, requiring appropriate modifications to the models. When using those overly complex models, gaining insight is hindered rather than promoted, because there are too many parameters that are often more than the required number of variables to reproduce

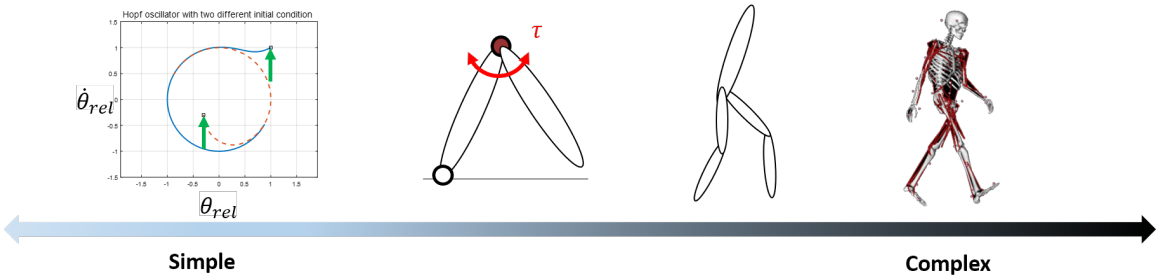

Figure 5-1: Descriptive models of walking may have different level of complexity. A single degree-of-freedom oscillator may serve as an abstract and conceptual model of walking, as well as a high-fidelity models with hundreds of bones and muscles. Rightmost image is obtained from https://simtk.org/projects/opensim.

observations.

In this chapter, we focus on simple models to understand the necessary mechanism to qualitatively explain experimental results. We first identify the key experimental observations to be accounted for by the model. Next, the key challenges and the essential mechanisms to reproduce experimental observations are investigated using conceptual models. Finally, a simple but competent model of walking is presented.

5.2 Target Experimental Phenomena to Model

In the previous Chapters, it was characterized how human walking was altered by two different interventions: periodic torque pulses (Chapter 3) and stiffness between the thighs (Chapter 4).

Among many different features evoked by those interventions, we identified a *conflicting* feature: stride frequency. The stiffness intervention resulted in essentially no change in stride duration, which implied existence of a dissociable control layer that governs the temporal pattern of walking. On the other hand, the pulse interventions evoked entrainment, implying that the phase dynamic was somehow influenced by the intervention.

Table 5.1 summarizes why the two features are difficult to be reproduced simultaneously. In short, if the stride frequency is emergent, then stride frequency will change when stiffness is applied; conversely, if the stride frequency is controlled, en-

Table 5.1: Conflicting features of experimental observations.

Intervention	Stiffness Intervention	Pulse Intervention
Features	**Invariant stride period**	**Stride period → pulse period**
Implication	Period (frequency) is controlled	Period (frequency) is emergent

trainment to torque pulses will not be observed. Developing models for each result might be straightforward, but developing a simple unifying model for both is not.

5.3 Insights Gained from Coupled Oscillators

The conflict can be more clearly elaborated by using simple oscillator models. To illustrate the concept, we adopt the examples presented in [222]. First, consider a pair of one-way (unidirectional) coupled identical oscillators (Fig. 5-2a):

$$\begin{cases} \dot{\mathbf{x}}_\mathbf{1} &= \mathbf{f}(\mathbf{x}_1, t) \\ \dot{\mathbf{x}}_\mathbf{2} &= \mathbf{f}(\mathbf{x}_2, t) + \mathbf{u}(\mathbf{x_1}) - \mathbf{u}(\mathbf{x_2}) + \mathbf{d}(\mathbf{x_1}, \mathbf{x_2}, t) \end{cases} \tag{5.1}$$

where $\mathbf{x_1}, \mathbf{x_2}$ are state vectors, $\mathbf{f}(\mathbf{x}, t)$ the dynamics of the uncoupled oscillators, $\mathbf{u}(\mathbf{x_1}) - \mathbf{u}(\mathbf{x_2})$ the coupling forces, and $\mathbf{d}$ the perturbation. If $\mathbf{d} = \mathbf{0}$ and the systems meet certain conditions, the two systems in (5.1) will synchronize.

On the other hand, consider two-way coupled identical oscillators of the form (Fig. 5-2b):

$$\begin{cases} \dot{\mathbf{x}}_\mathbf{1} &= \mathbf{f}(\mathbf{x}_1, t) + \mathbf{u}(\mathbf{x_2}) - \mathbf{u}(\mathbf{x_1}) \\ \dot{\mathbf{x}}_\mathbf{2} &= \mathbf{f}(\mathbf{x}_2, t) + \mathbf{u}(\mathbf{x_1}) - \mathbf{u}(\mathbf{x_2}) + d(\mathbf{x_1}, \mathbf{x_2}, t) \end{cases} \tag{5.2}$$

Again, if $\mathbf{d} = \mathbf{0}$ and the coupled systems meets certain conditions, the two systems in (5.2) can synchronize[1].

The difference becomes evident when nonzero perturbation $\mathbf{d} \neq \mathbf{0}$ is applied to system 2. In the two-way coupling, the perturbation indirectly affects system 1. If certain conditions are met, the two oscillators can maintain synchrony. In this

[1]Readers are referred to [222] to learn the contraction and partial contraction analyses, which are a simple yet general method to analyze networks of coupled oscillators.

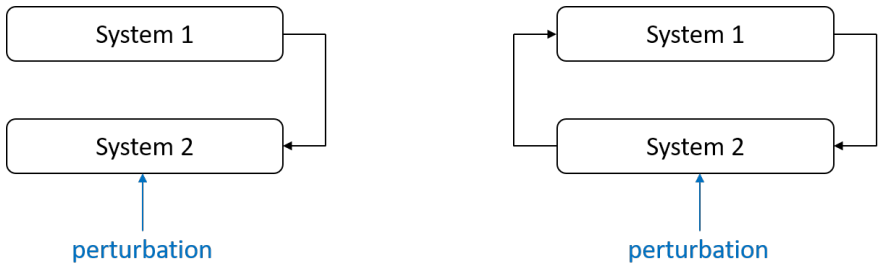

(a) One-way coupling (b) Two-way coupling

Figure 5-2: Coupled oscillators with two different configurations.

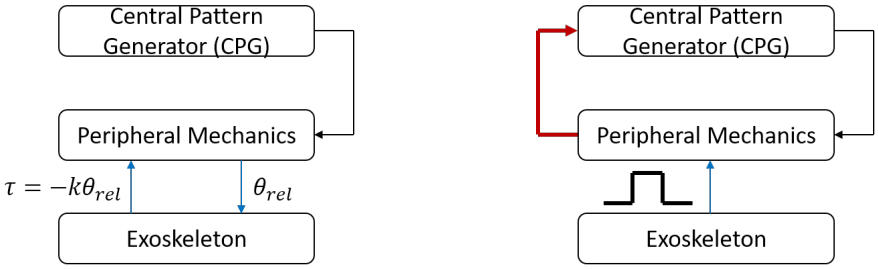

(a) Stiffness intervention (b) Pulse intervention

Figure 5-3: Rhythmic oscillator (central pattern generator), peripheral mechanics, and exoskeletons as a coupled system.

case, the frequency of the coupled oscillators with the perturbation can be different from that without the perturbation if perturbation frequency is different from natural frequency of the coupled system.[2]

On the other hand, if the oscillators are coupled in a one-way coupling configuration, the perturbation does not affect the system 1 and the frequency of oscillation of the coupled system will remain the same (as long as the synchrony is not broken by the perturbation). While this mathematical example is based on coupled identical oscillators, the analyses can be generalized to the coupling of nonidentical systems.

If we model human walking based on this reasoning as illustrated in Fig. 5-3, the model can demonstrate the effect of both interventions summarized in Table 5.1; invariant gait frequency to stiffness and adaptive frequency to periodic pulses. Suppose we replace the 'system 1' with some neural oscillator that generates rhythm, e.g., a central pattern generator (CPG) that appears frequently in the literature of

[2]For example, consider the coupled system as a single limit cycle oscillator with augmented state-space, and it is under periodic perturbation [63].

animal and human locomotion [52,102,129,172,173,204,205], and system 2 with some peripheral neuro-musculo-skeletal mechanics, interacting with the environment (e.g., gravity and ground). The experimental observations evoked by the stiffness intervention require one-way coupling (Fig. 5-3a) and those by the pulse intervention require two-way coupling (Fig. 5-3b). A convenient way to model human walking is that the afferent feedback (coupling from system 2: peripheral mechanics to system 1: CPG) was active with the pulse intervention and inactive with the stiffness intervention.

5.4 Competent Walking Model

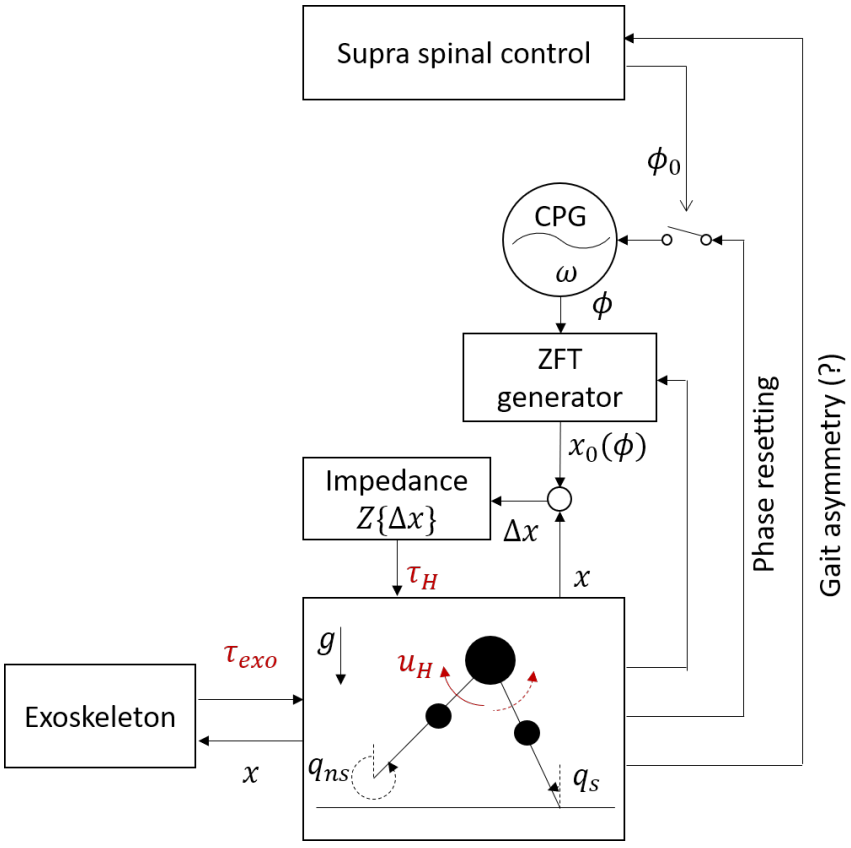

Figure 5-4: Schematic of a model of human walking. The model consists of a central pattern generator (CPG), zero-force trajectory (ZFT) generator, impedance controller, compass gait walking model as a mechanical system, a hip exoskeleton robot as a perfect torque source, and hypothetical supra-spinal control.

5.4.1 Model Structure

As our experiments showed that at least two dissociable levels were required, we formulated a multi-level model. For the lowest level we used a well-established 'compass gait walker', which competently describes the biomechanical relation between walking speed and step length [100]. At the spinal level we assumed a phase oscillator to model a biologically-plausible rhythmic Central Pattern Generator (CPG). Between those levels we inserted a Norton equivalent network [72, 74] to account for the relation between neuro-muscular mechanical impedance (to manage contact and physical interaction) and oscillatory nominal motion generated by the CPG. The highest level supra-spinal control determines activation of phase resetting mechanism which influences phase dynamic of the system.

The schematic of the mathematical model is illustrated in Fig. 5-4. The model structure is consistent with several previous walking models [14–16, 81, 196, 204, 205].

Central Pattern Generator

We assumed a phase oscillator to model a CPG:

$$\dot{\phi} = \omega + \pi\delta(t - t_c), \tag{5.3}$$

where ϕ is the phase variable, ω is the natural frequency of oscillation, and t_c is time when swing leg makes contact with the ground. $\delta(\cdot)$ is the Dirac delta function. The second term is to cope with the fact that the stance leg and swing leg change.[3]

If the phase-resetting mechanism is activated, this becomes

$$\dot{\phi} = \omega + (\phi_0 - \phi_c)\delta(t - t_c), \tag{5.4}$$

where ϕ_c is the phase value at swing leg - ground collision. In effect, this mechanism resets the value of phase to ϕ_0. The effect of phase resetting mechanism for stability of walking was presented in [14–16] and its relevance to actual human walking can be

[3]One may alternatively assign a phase oscillator to each leg to avoid discrete jump of states in the phase dynamics.

found in [142] and its references.

Mechanical System: Compass Gait Walker

We adopted a well-established compass gait walker [100] which has two degrees-of-freedom (DoF) with coordinates $\mathbf{q} = [q_{ns}, q_s]^T$. q_{ns} and q_s are the angle of non-stance (swing) leg and stance leg, respectively. When the non-stance leg makes contact with the ground, the stance and non-stance leg instantaneously switches without double stance phase and the system states undergoes a discrete jump, i.e., the system has hybrid dynamics.

The total torque applied to the system is $u_H = \tau_H + \tau_{exo}$, where τ_H is the human control and τ_{exo} is the exoskeleton torque. Details of its equations of motion can be found in the Appendix 5.7.

Dynamic Motor Primitives

The neuro-motor peripheral mechanics may be successfully described as a composition of dynamic motor primitives, which consists of a motion command (zero-force trajectory; ZFT) and mechanical impedance managing physical interaction. Dynamic motor primitives are behavioral patterns that robustly emerge from dynamic systems, i.e. humans [73, 74].

The phase variable ϕ from CPG is mapped to the zero force trajectory (ZFT) of the relative angle between the legs $q_{rel} = q_s - q_{ns}$ and its velocity,

$$\dot{q}_{rel,0}(\phi) = -r\omega \sin\phi \tag{5.5}$$

$$q_{rel,0}(\phi) = \int \dot{q}_{rel,0}(\phi)dt = r\cos(\phi) + r - S. \tag{5.6}$$

Here, S is a fixed parameter that represents step length, and r is a parameter that is updated at each step: $r^+ = \frac{2S - r^-(1+\cos\phi_c^-)}{1+\cos\phi(t_c^+)}$. Superscript $-$ and $+$ denote the values right before and after swing leg makes contact with the ground. Details of the rationale can be found in [16].

Mechanical impedance is a dynamic operator, $Z\{\cdot\} : \Delta\mathbf{x} \rightarrow \mathbf{f}$, that determines

the generalized force $\mathbf{f}$, evoked by an imposed generalized displacement $\Delta\mathbf{x} = \mathbf{x} - \mathbf{x_0}$, which is the deviation of the actual trajectory $\mathbf{x}$ from the zero-force trajectory $\mathbf{x_0}$.

Here, impedance control determines the hip joint torque τ_H:

$$\tau_H = -K(q_{rel} - q_{rel,0}) - B(\dot{q}_{rel} - \dot{q}_{rel,0}) \tag{5.7}$$

where K and B are effective stiffness and damping.

Exoskeleton

The Samsung GEMS-H exoskeleton was modeled as a perfect torque source. When the stiffness intervention is tested, the exoskeleton torque is simply

$$\tau_{exo} = -kq_{rel}, \tag{5.8}$$

where k is the stiffness of the virtual spring.

When the pulse intervention is tested,

$$\tau_{exo} = \begin{cases} \tau_M & \text{if } \mathrm{mod}(t, T_p) < T_d \text{ \& right leg is in swing} \\ -\tau_M & \text{if } \mathrm{mod}(t, T_p) < T_d \text{ \& left leg is in swing} \\ 0 & \text{otherwise} \end{cases} \tag{5.9}$$

when the periodic pulse intervention is applied, where τ_M, T_p, T_d are pulse magnitude, pulse period, and pulse duration, respectively.

Supra-spinal Control

The activity of the afferent feedback to evoke a phase resetting mechanism was determined by whether the intervention was a (virtual) spring or a sequence of pulses. The context-based switching of feedback is biologically plausible but it should be tested in further work.

5.5 Simulation Result

The model was implemented in MATLAB R2018b(Mathworks, Natick, MA, USA). Fig. 5-5 presents that the model simulation results could provide a competent description of our experiments. The stiffness intervention changed range of motion of the walking model but not stride duration (Fig. 5-5a), and the pulse intervention evoked gait entrainment of the model. When entrained, pulse phase (ϕ_P) converged to a consistent value such that the robot could provide positive work per stride (E_p).

5.6 Discussion

5.6.1 Summary of the Results

As the experiments showed that at least two dissociable levels were required, we formulated a multi-level model. This model could successfully reproduce our main experimental findings: (1) imposed stiffness changed thigh range of motion but not stride duration; (2) periodic perturbations evoked gradual entrainment, such that the exoskeleton provided maximum positive work.

This work showed that even though we grossly simplified the complexity of the neuro-bio-mechanical system, the simple model was quite successful to describe human behaviors at least qualitatively. Moreover, it provides insight to understand the possible mechanisms behind the significantly different behavioral responses.

5.6.2 Limitation of the Model

While several features of the experiments were reproduced, the model transient response may need improvement. Stiffness transiently affected model stride duration while experiments showed no influence. This may be improved by proper low-level parameter update rules, or may be masked by biological 'noise'; the model is deterministic. It is also expected that introducing stochasticity will better reproduce the progress of pulse phase when the model is close to the basin of entrainment.

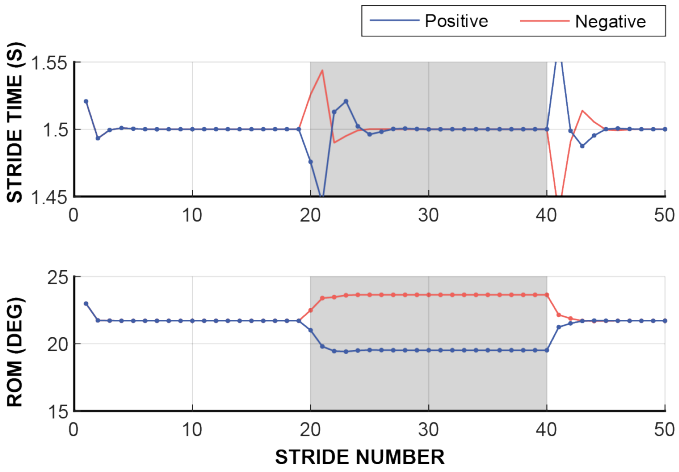

(a) Stiffness intervention. Positive ($k = 5$Nm/rad) and negative stiffness ($k = -5$Nm/rad) were tested. The model could reproduce significant changes in the range of motion with essentially no change in stride duration.

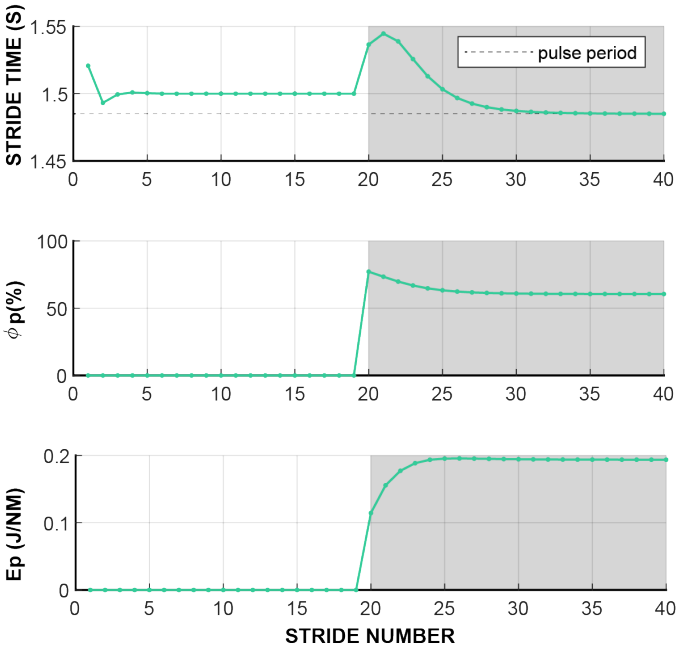

(b) Pulse intervention. The model could reproduce frequency adaptation and convergence of pulse phase such that the exoskeleton provide positive mechanical energy per stride. Tested pulse parameters were $\tau_M = 2.5$ Nm, $T_p = T_o - 0.015$ s, $T_d = 0.2$ s. Resetting phase $\phi_0 = 0.32$ rad was obtained from steady-state walking without interventions, which is dependent on the model parameters such as impedance.

Figure 5-5: Simulation results. Shaded region indicates when the exoskeleton intervention was simulated.

Selective response to a certain type of intervention is biologically plausible. However, the mechanism that triggers the activation of the afferent feedback (phase resetting) was not implemented in the simulation. We will discuss possible mechanism in the following.

5.6.3 Gait Asymmetry May Evoke Frequency Adaptation

As discussed in Chapter 3 and Chapter 4, our data implies that gait asymmetry may be the key factor that evoked motor adaptation in the experiments. Fig. 5-6 presents the trajectory of thigh relative motion of the representative subjects of the two experiments. The key difference between interventions that evoked adaptation and those that did not appears to be whether they induced gait asymmetry: entrainment did; stiffness did not.

Symmetric gait pattern seems relevant to controlling balance during walking. It is as yet unclear whether the CNS monitors gait asymmetry directly, or other measures that would be influenced by gait symmetry (e.g. net moment applied to the torso). In fact, phase resetting mechanism and fall risk seem closely related in human walking [142].

If humans detect gait asymmetry, how it is detected is also in question. One approach could be continuously monitoring the difference between phase of the oscillator and phase of walking somehow computed from peripheral mechanics. Alternative way is to evaluate gait symmetry at the end of each stride.

While the requirements for successful rehabilitation continue to be a matter of debate, an intervention that evokes adaptation would appear to be necessary (though perhaps not sufficient by itself). We believe addressing this question will provide critical information for future exoskeletal applications to promote neuro-recovery.

5.6.4 State-dependent and Time-periodic Interventions

Another distinct difference between the stiffness intervention and the pulse intervention is the way they influence the peripheral dynamics. The stiffness intervention is

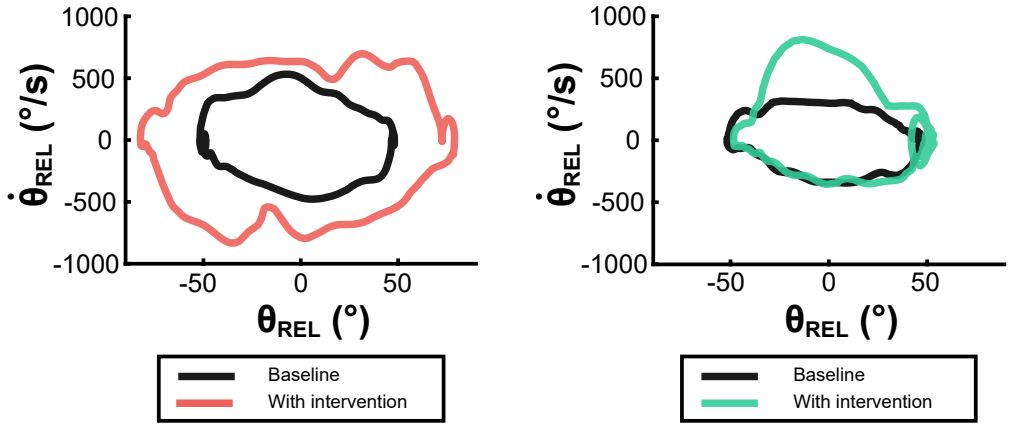

(a) Stiffness intervention (b) Pulse intervention

Figure 5-6: Stiffness intervention did not disrupt gait symmetry, while pulse intervention evoked asymmetric gait pattern. Black: baseline behavior. Colored: steady-state trajectory. When stiffness intervention was applied, despite large change, the symmetric gait pattern was preserved. On the other hand, applying torque pulses disrupted symmetric gait pattern. Note that $\theta_{\text{rel}} = \theta_{\text{L}} - \theta_{\text{R}}$.

state-dependent, while the pulse intervention is time-periodic and unaffected by the state of the system.

Assuming the peripheral mechanics of human walking can be described as a semi-autonomous system [4], its dynamics can be fully described by the flow field in its state-space. If this is correct, when applying a state-dependent intervention such as stiffness, the shape of the flow field is altered. On the other hand, applying pulses does not change the flow field itself but relocates the state vector without following the autonomous dynamics of the system [63, 150, 221]. Regarding pulse duration as instantaneous, this introduces a discrete 'jump' dynamics to the system, similar to how instantaneous foot-ground collision is modeled in walking [100, 224]. This might be a critical difference detected by the CNS but this speculation warrants further experimental studies.

5.6.5 Net Mechanical Energy from the Exoskeleton

The other difference between the stiffness intervention and the pulse intervention is the net mechanical energy flow between the exoskeleton robot and human subjects. When the stiffness intervention was applied with either positive or negative

spring constant, the net mechanical work done by the robot is zero in theory. On the other hand, the robot with the pulse intervention certainly generates or absorbs mechanical energy. The frequency adaptation we observed in the experiments may have been a consequence of finding an energetically-optimal gait pattern that maximizes mechanical work done by the robot. Many previous works have suggested that energy optimality explains many aspects of healthy human walking [100, 198, 199]. Furthermore, recent works suggested energy optimality may explain locomotor adaptation [188]. However, with the current data, we do not know the energetic cost of the altered gait pattern compared to the original pattern because for example the target muscles may benefit from exoskeletons while other muscles might be loaded. Therefore, this speculation invites further experimental and modeling studies.

5.6.6 Scope of the Model

Importantly, while this model explains the key observations of the data presented in this thesis, there may be other possible (even better) models that can exhibit the behaviors. Moreover, this model may not explain other experimental results obtained by using different hip exoskeleton robot controllers. As emphasized elsewhere, a simple model deliberately simplifies complex phenomena - to explain a particular observation(s). Applying this model to other phenomena beyond the scope of the current experimental data requires care.

5.7 Appendix: Compass Gait Walker Equations of Motion

Fig. 5-7 illustrates model parameters and joint coordinates. The model has hybrid dynamics consisting of continuous swing dynamics and discrete collisional dynamics [100].

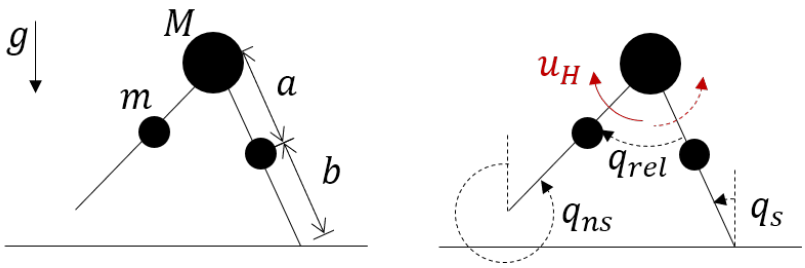

Figure 5-7: Compass gait walker

5.7.1 Continuous Dynamics

The equations of motion of the model are expressed as

$$\mathbf{M}(\mathbf{q})\ddot{\mathbf{q}} + \mathbf{C}(\mathbf{q}, \dot{\mathbf{q}})\dot{\mathbf{q}} + \mathbf{G}(\mathbf{q}) = \mathbf{B}\boldsymbol{\tau}$$

where $\mathbf{q} = [q_{ns}, q_s]^T$ are non-stance (swing) and stance leg angle and $\boldsymbol{\tau} = [\tau_H, \tau_A]$ are hip and angle torques, respectively. We assumed zero ankle torque to simplify the model, i.e. $\tau_A = 0$.

The mass matrix, Coriolis and centrifugal torques, gravitational torques, and the input matrix are detailed as follows:

$$\mathbf{M}(\mathbf{q}) = \begin{bmatrix} mb^2 & -mbl\cos(q_s - q_{ns}) \\ -mbl\cos(q_s - q_{ns}) & ma^2 + (M+m)l^2 \end{bmatrix}$$

$$\mathbf{C}(\mathbf{q}, \dot{\mathbf{q}}) = mlb\sin(q_s - q_{ns}) \begin{bmatrix} 0 & \dot{q}_s \\ -\dot{q}_{ns} & 0 \end{bmatrix}$$

$$\mathbf{G}(\mathbf{q}) = g \begin{bmatrix} mb\sin(q_{ns}) \\ -(Ml + ma + ml)\sin(q_s) \end{bmatrix}$$

$$\mathbf{B} = \begin{bmatrix} -1 & 0 \\ 1 & 1 \end{bmatrix}$$

5.7.2 Discrete Dynamics

When the non-swing leg makes contact with the ground, the system state $\mathbf{x} = [\mathbf{q}, \dot{\mathbf{q}}]^{\mathrm{T}}$ undergoes a discrete change. This change can be calculated using the inter-leg angle at the event, $\alpha = \frac{1}{2}(q_{ns}^{-} - q_{s}^{-})$ based on momentum conservation. Superscript $^{-}$ and $^{+}$ denote states right before and after the collision.

$$\mathbf{x}^{+} = \mathbf{W}\mathbf{x}^{-}$$

where

$$\mathbf{W} = \begin{bmatrix} \mathbf{J} & \mathbf{0} \\ \mathbf{0} & \mathbf{H} \end{bmatrix}$$

$$\mathbf{J} = \begin{bmatrix} 0 & 1 \\ 1 & 0 \end{bmatrix}$$

$$\mathbf{H} = (\mathbf{Q}^{+})^{-\mathbf{1}}\mathbf{Q}^{-}$$

$$\mathbf{Q}^{-} = \begin{bmatrix} -mab & -mab + (Ml^2 + 2mal)\cos(2\alpha) \\ 0 & -mab \end{bmatrix}$$

$$\mathbf{Q}^{+} = \begin{bmatrix} mb(b - l\cos(2\alpha)) & ml(l - b\cos(2\alpha)) + ma^2 + Ml^2 \\ mb^2 & -mbl\cos(2\alpha) \end{bmatrix}$$

Model parameters are listed in Table 5.2.

Table 5.2: Walking model parameters.

Symbol	Parameter	Value (units)
M	body mass	10 (kg)
m	leg mass	5 (kg)
$l = a + b$	leg length	1 (m)
a	leg mass position	0.5 (m)
g	gravitational acceleration	9.81 (m/s^2)
T_o	stride duration	1.5 (s)
$\omega(= 2\pi\frac{1}{T_o})$	CPG frequency	4.19 (rad/s)
S	reference step length	12 (deg)
K	hip stiffness	15 (Nm/rad)
B	hip damping	5 (Nms/rad)

Chapter 6

Discussion

6.1 Summary

The overall goal of this work was to explore novel applications of a hip exoskeleton robot to overcome gait deficits by providing assistance (e.g. to healthy elders) or treatment (e.g. to stroke survivors). To inform more effective approaches to overcome gait deficits, it is important to understand the neuro-mechanical dynamics and control of unimpaired locomotion, and how it interacts with robotic interventions.

We developed two fundamentally different robotic interventions using Samsung GEMS-H, one time-based, i.e. a periodic sequence of brief pulses, and one state-based, i.e. emulating a virtual spring between the thighs.

The most striking result of these studies was that the behavioral changes depended strongly on the type of mechanical intervention, even when it was applied by the same device. When periodic torque pulses were applied (Chapter 3), we frequently observed gradual entrainment—a change of stride period to match the perturbation period. When converged, the torque pulse was located at a gait phase where it provided mechanical assistance to swing leg motion. Finally, an after-effect when the perturbations were discontinued (slow drift of stride period back to its preferred value) showed clear evidence of adaptation.

In contrast, when stiffness was applied (Chapter 4) an immediate change of hip range-of-motion occurred, with no change of stride duration. There was no evidence

of adaptation.

While the requirements for successful rehabilitation continue to be a matter of debate, an intervention that evokes adaptation would appear to be necessary (though perhaps not sufficient by itself) [97, 149, 168]. The adaptation evoked by entrainment meets this requirement and shows promise for rehabilitation therapy. Entrainment might serve as a treatment to encourage faster gait or improve gait symmetry (e.g. by assisting a stroke survivor's paretic leg). In contrast, the absence of adaptation to imposed stiffness indicates that it is not a promising approach to therapy. However, the immediate response to imposed stiffness suggests that it may be applicable to maintain wellness in healthy elders, e.g., to encourage larger strides (negative stiffness) or provide resistive exercise (positive stiffness).

To encapsulate the results of both studies, we developed a mathematical model and simulation (Chapter 5). Our approach was to shun complexity and find the simplest model that was competent to account for our observations. The steady-state response of this deterministic model successfully reproduced our main experimental findings: (1) imposed stiffness changed thigh range of motion but not stride duration; (2) periodic perturbations evoked gradual entrainment, with an after-effect when perturbations were discontinued. That said, the model would benefit from further development, but that is beyond the scope of this work.

The key difference between interventions that evoked adaptation and those that did not appears to be whether they induced gait asymmetry: entrainment did; stiffness did not. Symmetric or asymmetric changes of gait appear to be the key factor in developing robot-aided interventions intended to change locomotor behavior. Whether this hypothesis is valid or not should be tested with further experiments and modeling studies. This study will contribute to finding a sufficient condition for locomotor adaptation and rehabilitation.

Part II

Balancing on a Beam with Mechanical Interventions

Chapter 7

Overview

Maintaining balance is important for human locomotion. While the task of standing balance seems tedious, it is actually remarkable how humans can coordinate a multi-degree-of-freedom inherently unstable skeletal system in a stable manner, without requiring much attention.

Assisting or retraining balancing requires fundamental understanding of human motor control and how it is altered by the mechanical interventions. One way to facilitate insights is to investigate the effects of interventions on healthy humans while they balance on a challenging environment. This would help us (1) understand balancing skills that humans have, and (2) analyze the effects of the interventions on human control - and these insights may be relevant to humans with impaired balance.

In this part, we studied how humans balance on a beam; how humans balance on a beam was affected by simple and passive mechanical interventions; and how we could understand such behaviors via human experiments and mathematical models. In Chapter 8, we analyzed the behavior of humans balancing on a narrow beam to understand how they coordinated their whole-body to accomplish this challenging task. Then we investigated changes in human behavior when they maintained balance on a narrow beam with bare feet and with wearing rigid soles. We will show that this simple change of mechanical interface between foot and beam substantially influenced balancing. Simple models were developed and investigated to identify possible mechanisms to account for experimental observations.

Numerous studies showed that postural balance improves through light touch, highlighting the importance of haptic information, seemingly downplaying the contribution of mechanical support. Chapter 9 examined the effects of canes, which are the most frequently prescribed mobility-assistive devices. In particular, the experiment was designed to focus on the mechanical effects of canes on human balancing.

Chapter 8

Balancing on a beam with rigid soles

This work was conducted in collaboration with Dr. Meghan E Huber (Newman Lab for Biomechanics and Human Rehabilitation, MIT; now Prof. Meghan E Huber at Human Robot Systems Laboratory, University of Massachusetts). Experimental data was collected at Eberhard-Karls-Universität of Tübingen, Germany, in collaboration with Prof. Martin Giese (Hertie Institute for Clinical Brain Research and University Clinic Tübingen, Germany), Dr. Enrico Chiovetto (the same), and Prof. Dagmar Sternad (Action Lab, Northeastern University).

This work was supported by a Samsung scholarship. This work was also supported by NIH-R01-HD087089, R01-HD081346, NSF-NRI 1637854, NSF-EAGER-1548514, and NSF-CRCNS-1723998 awarded to Prof. Dagmar Sternad, by the Eric P. and Evelyn E. Newman fund and NIH-R01-HD087089, NSF-NRI 1637824, NSF-EAGER-1548501, and NSF-CRCNS-1724135 awarded to Prof. Neville Hogan, by BMBF FKZ 01GQ1704, BW Stiftung NEU007/1 KONSENS-NHE, EC H2020 ICT-23-2014 /644727 CogIMon, and HFSP RGP0036/2016 awarded to Prof. Martin Giese.

This work was partially presented in [109, 112].

8.1 Introduction

Despite low bandwidth and long latencies in the neuromuscular system, humans have a remarkable ability to maintain balance across a variety of terrains and conditions.

When humans lose this ability, either due to age [185] or injury [213], it has a profound impact on their quality of life. The use of robotic devices is one promising approach to assist or or retrain balance, but how to control these robotic devices for impaired balance ability remains a critical open question [236].

Walking and standing on a narrow beam, or even simply with feet in tandem, is challenging. Compared to normal stance, humans are less stable in the mediolateral direction under these conditions due to the reduced base of support [146]. Hence, balance beam standing and walking are ideal paradigms to study how humans maintain balance and how the balance ability can be improved, which would inform the development of robotic devices for enhancing and retraining balance.

Recent results suggest that our understanding of how healthy humans control mediolateral balance may not yet be sufficient to deliver effective robotic assistance. Domingo and Ferris attempted to enhance learning of a balance beam walking task by providing physical assistance [48] and augmenting error [47]. Counter to their predictions, practice with these interventions led to *worse* performance compared to practicing without any assistance in a beam walking task [47,48]. This was surprising as robotic guidance and error augmentation have previously been shown to enhance learning of a variety of other motor skills [156, 167]. One possible explanation for these unexpected results is that the interventions did not lead subjects to adopt the imposed balance behavior. This begs the question: what is the natural and desired balance control strategy of humans? What interventions can improve balance?

In this study, we first examined inter-limb coordination of healthy subjects while they maintained balance on a narrow beam. Specifically, we examined the spatio-temporal patterns in the angular momenta generated by individual body segments in the mediolateral direction (i.e. frontal plane). To truly capture the whole body coordination, we did not restrict arm movements as in the previous narrow-beam-walking experiments [47, 48, 181]. In the previous study [181], Sawers et al. showed that experts (trained ballet dancers) use more muscle synergies or modules compared to novices, suggesting that experts have finer coordination when balancing during walking on a beam. To understand the difference between 'good' and 'bad' balance

strategies, we also assessed whether the inter-limb coordination patterns differed with balance performance.

Next, we tested whether mechanical change in the foot-beam interface would influence human balancing when standing on a beam, by comparing whole-body behavior with "bare" feet and "rigid" feet. The width of the beam and thus the maximum range of the center of pressure were identical in both conditions. Hence, the behavior should be similar in both conditions unless the mechanics of the foot-beam interface was influential.

Developing a simple yet competent model facilitates understanding the experimental observation. We first examined whether existing balance controllers used in robotics could adequately describe the coordination pattern observed in the experiment with bare feet condition. Then we investigated whether a simplified model of foot-beam interface could qualitatively account for differences between bare feet and rigid feet conditions.

The remainder of the chapter is organized as follows. Section 8.2 details the human experiments conducted to examine human mediolateral balance when standing on a narrow beam with and without wearing rigid soles. Section 8.3 examines a simplified model of human balance that accounts for experimental observations. Section 8.4 follows with points of discussion. Section 8.5 presents concluding remarks.

8.2 Human Balancing Experiment

The purpose of this experiment was to characterize how humans with different skill levels coordinate their entire body to maintain mediolateral balance on a narrow beam. We expected that the experienced subject would have better mediolateral balance compared to the novice subject. We further predicted that the novice and expert would exhibit differences in inter-limb coordination, reflecting the use of different control strategies to maintain balance in this challenging task.

We also characterized how wearing rigid soles influences mediolateral balance on a narrow beam. Regardless of whether the task was performed with bare feet or with

rigid soles, the width of the beam was the same. Thus, we expected that balance behavior would be similar across the two conditions.

8.2.1 Methods

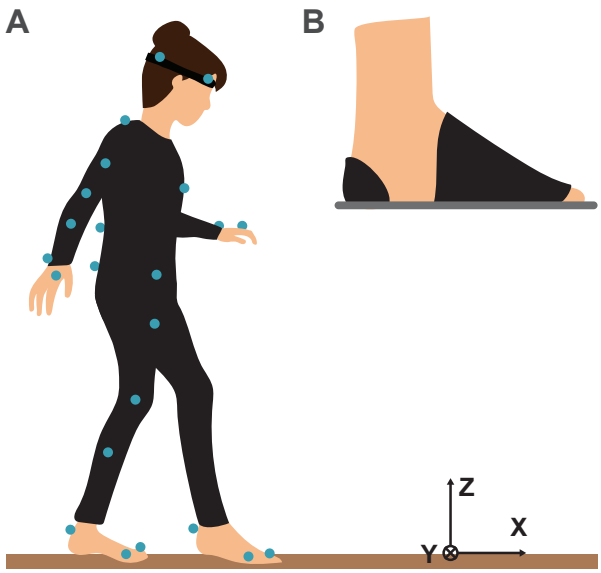

Figure 8-1: Experimental Task. (A) Subjects were instructed to maintain balance on a narrow beam (3.4cm) for as long as possible without stepping off the beam. Subjects performed the task under two conditions: bare feet and "rigid feet". (B) To simulate rigid feet on human subjects, rigid plastic platforms were attached to the bottom of the subjects' feet using Velcro straps and tape.

Subjects

Seven subjects (gender: 2 females, 5 males; age: $M = 29.8\text{yo}, SD = 2.0\text{yo}$) participated in the experiment. The experiment conformed to the Declaration of Helsinki, and written informed consent was obtained from all subjects according to a protocol approved by the ethical committee at the Medical Department of the Eberhard-Karls-Universität of Tübingen, Germany where the experiment was conducted.

Experimental Procedure

In each trial, subjects were instructed to stand on a narrow beam (3.4cm width) for as long as possible with their feet in tandem (Fig. 8-1A). Subjects initially placed their left (front) foot on the beam. The trial started when they subsequently placed their right (hind) foot on the beam. The trial ended when one of their feet lost contact with the beam.

Each subject performed 5 trials without wearing footwear (Bare Feet condition) followed by another 5 trials wearing flat, rigid soles attached to the bottom of their feet (Rigid Feet condition). Note that the rigid soles were attached such that ankle inversion/eversion and plantarflexion/dorsiflexion range of motion were unimpeded (Fig. 8-1B).

Immediately prior to performing the two standing conditions, all subjects completed 20 trials walking across the beam in each foot condition as part of a larger study [79]. Thus, all subjects were sufficiently familiar with both experimental conditions.

Kinematic Data Recording

Kinematic data were collected using a 10-camera Vicon motion capture system (Oxford, UK) at a sampling rate of 100Hz. As illustrated in Fig. 8-1A, the x-axis of the lab coordinate frame was aligned with the beam. Reflective markers were placed on the subjects' bodies following Vicon's Plug-In Gait marker set (Fig. 8-1A). For each subject, the Plug-In Gait model, which consists of 15 rigid body segments, was fit to the kinematic data using Vicon Nexus and C-Motion Visual3D software (Germantown, MD). See Table 8.1 for list of body segments.

Signal Processing

For each trial, we calculated the following output signals from the model-fitted data processed in Visual3D to quantify and characterize human balance ability.

The linear velocity of the whole body's center of mass in the mediolateral (i.e.,

Table 8.1: Segments of Human Rigid Body Model

Segment Number, i	**Segment Name**	**Body Region**
1	Head	Upper
2	Thorax/Abdomen	Upper
3	Right Upper Arm	Upper
4	Right Forearm	Upper
5	Right Hand	Upper
6	Left Upper Arm	Upper
7	Left Forearm	Upper
8	Left Hand	Upper
9	Pelvis	Lower
10	Right Thigh	Lower
11	Right Shank	Lower
12	Right Foot	Lower
13	Left Thigh	Lower
14	Left Shank	Lower
15	Left Foot	Lower

y) direction at each time t, $v_{\mathrm{wb,y}}(t)$ was calculated by backward finite difference on $c_{\mathrm{wb,y}}(t)$, the whole body center of mass position, with $T_s = 0.01$s as step size. The v_y was subsequently smoothed with a moving average filter.

The angular momentum of i-th body segment about the axis of the balance beam (i.e., the x-axis) at each time t, $L_{i,x}(t)$, was calculated by

$$L_{i,x}(t) = m_i(c_{i,y}(t)v_{i,z}(t) - c_{i,z}(t)v_{i,y}(t)) + j_{i,x}\omega_i(t), \tag{8.1}$$

where $c_{i,y}$ and $c_{i,z}$ were the positions of the center of mass in y and z direction, m_i was the mass, $v_{i,y}$ and $v_{i,z}$ were the linear velocities in y and z direction, and $j_{i,x}\omega_i$ was the x component of the angular momentum about its center of mass in the lab coordinate frame, respectively.

The total angular momentum of all upper body segments about beam axis at each time t, $L_{\mathrm{ub}}(t)$ was calculated by

$$L_{\mathrm{ub}}(t) = \sum_{i=1}^{8} L_{i,x}(t). \tag{8.2}$$

The total angular momentum of all lower body segments about beam axis at each time t, $L_{\mathrm{lb}}(t)$ was calculated by

$$L_{\mathrm{lb}}(t) = \sum_{i=9}^{15} L_{i,x}(t). \tag{8.3}$$

The total angular momentum of the whole body (i.e., of all body segments) about beam axis at each time t, $L_{\mathrm{wb}}(t)$ was calculated by

$$L_{\mathrm{wb}}(t) = \sum_{i=1}^{15} L_{i,x}(t). \tag{8.4}$$

The torque about x-axis at the foot-beam interface was estimated by

$$\tau_{\mathrm{ext,x}}(t) = \dot{L}_{\mathrm{wb}}(t) + mgc_{\mathrm{wb,y}}(t) \approx \frac{L_{\mathrm{wb,x}}(t) - L_{\mathrm{wb},x}(t - T_s)}{T_s} + mgc_{\mathrm{wb},y}(t) \tag{8.5}$$

where $m = \sum_{i=1}^{15} m_i$ is the total mass of the subject and g is the gravitational acceleration constant.

To accommodate differences in body size across subjects, the signals of $v_{\mathrm{wb},y}$, $L_{\mathrm{wb},x}$, and $\tau_{\mathrm{ext},x}$ at time t were normalized to obtain $\hat{v}_{\mathrm{wb},y}$, $\hat{L}_{\mathrm{wb},x}$, and $\hat{\tau}_{\mathrm{ext},x}$ at time $\hat{t} = \frac{t}{\left(\frac{h}{g}\right)^{1/2}}$, respectively, as follows:

To accommodate differences in body size across subjects, the outputs $v_{\mathrm{wb},y}$, $L_{\mathrm{wb},x}$, and $\tau_{\mathrm{ext},x}$ at time t were normalized to obtain $\hat{v}_{\mathrm{wb},y}$, $\hat{L}_{\mathrm{wb},x}$, and $\hat{\tau}_{\mathrm{ext},x}$ at time $\hat{t} = \frac{t}{\left(\frac{h}{g}\right)^{1/2}}$, respectively, as follows:

$$\hat{v}_{\mathrm{wb},y} = \frac{v_{\mathrm{wb},y}}{h\left(\frac{h}{g}\right)^{-1/2}}, \hat{L}_{\mathrm{wb},x} = \frac{L_{\mathrm{wb},x}}{mh^2\left(\frac{h}{g}\right)^{-1/2}}, \hat{\tau}_{\mathrm{ext},x} = \frac{\tau_{\mathrm{ext},x}}{mgh} \tag{8.6}$$

where h was the height of each subject.

Dependent Measures

For each subject, the dependent measures were calculated for the longest trial in each condition. Data from the first and the last 25% of each trial were omitted to minimize

any possible transients or fatigue effects.

- Trial time, quantified as the amount of time the subject stood with both feet on the beam, served as the first gross measure of balance ability.
- The root-mean-square (RMS) of $\hat{v}_{\mathrm{wb,y}}$ and $\hat{L}_{\mathrm{wb,x}}$ also characterized balance proficiency.
- The correlation coefficient between the angular momenta of the upper and lower body, 'Corr-AM' was used to characterize the coordination between the different body segments.
- The RMS of $\hat{\tau}_{\mathrm{ext,x}}$ was used to assess foot-beam interaction torque.

Statistical Analysis

In order to test if wearing rigid soles affected balance performance and whole-body coordination, pairwise t-tests were conducted on the dependent measures calculated for the longest trial in each condition. The significance level was set to $\alpha = 0.05$. Statistical analyses were performed using MATLAB, Version 2016b (The Mathworks, Natick, MA).

8.2.2 Human Balance on a Beam: Representative Subjects

Two representative subjects were selected to investigate differences between 'novice' and 'expert'. The 'Novice' subject (28yo male, 180cm height, 80kg weight) did not have any formal balance training. The 'Expert' subject (26yo female, 163cm height, 58kg weight) was a trained gymnast.

Gross Assessment of Balance Ability

As expected, the Novice, who had no prior balance training, had worse balance performance than the Expert, who was a trained gymnast. As summarized in Table 8.2, the Novice was only able to maintain balance for approximately 23 s, whereas the

Table 8.2: Representative subjects balance performance

	Novice	Expert
Trial time [s]	23.3	421.2
RMS of $c_{\mathrm{wb,y}}$ [cm]	1.06	0.69
RMS of $v_{\mathrm{wb,y}}$ [cm/s]	0.017	0.015
CorrAM [a.u.]	-0.95	-0.91
RMS of L_{ub}[kg·m^2/s]	5.54	2.00
RMS of L_{lb}[kg·m^2/s]	1.58	0.70
RMS of L_{wb}[kg·m^2/s]	4.07	1.43

Expert was able to maintain balance for just over 7 minutes. Novice also had greater center of mass motion compared to the Expert.

Patterns in Angular Momenta Across Body Segments

Fig. 8-2 depicts the time profiles of angular momenta from a representative portion (10 seconds) of each subject's trial. Note that the magnitude of angular momenta generated by the individual segments depended on the height and weight of subject. Despite clear differences in body stature and balance ability as indicated by trial time, the pattern of angular momenta generated by body segments was consistent across both subjects, which ran counter to our prediction. As illustrated in Fig. 8-2, the angular momenta of the individual upper body segments consistently acted opposite to the lower body segments.

Calculation of the cross correlation function between the total angular momentum of upper body segments, L_{ub}, and the lower body segments, L_{lb} confirmed this visual observation. The most negative cross correlation coefficient (Corr-AM) was -0.95 for Novice and -0.91 for Expert, indicating that the two signals were highly anti-correlated.

While L_{ub} and L_{lb} were highly anti-correlated, they did not cancel each other out. For both subjects, magnitude of L_{ub} was generally greater than the magnitude of L_{lb} over the course of each trial as described in Table 8.2. As a result, there was significant whole body angular momentum L_{wb} about the beam axis throughout the

entirety of each trial. Note that this same behavior was observed during balance beam walking as well [37].

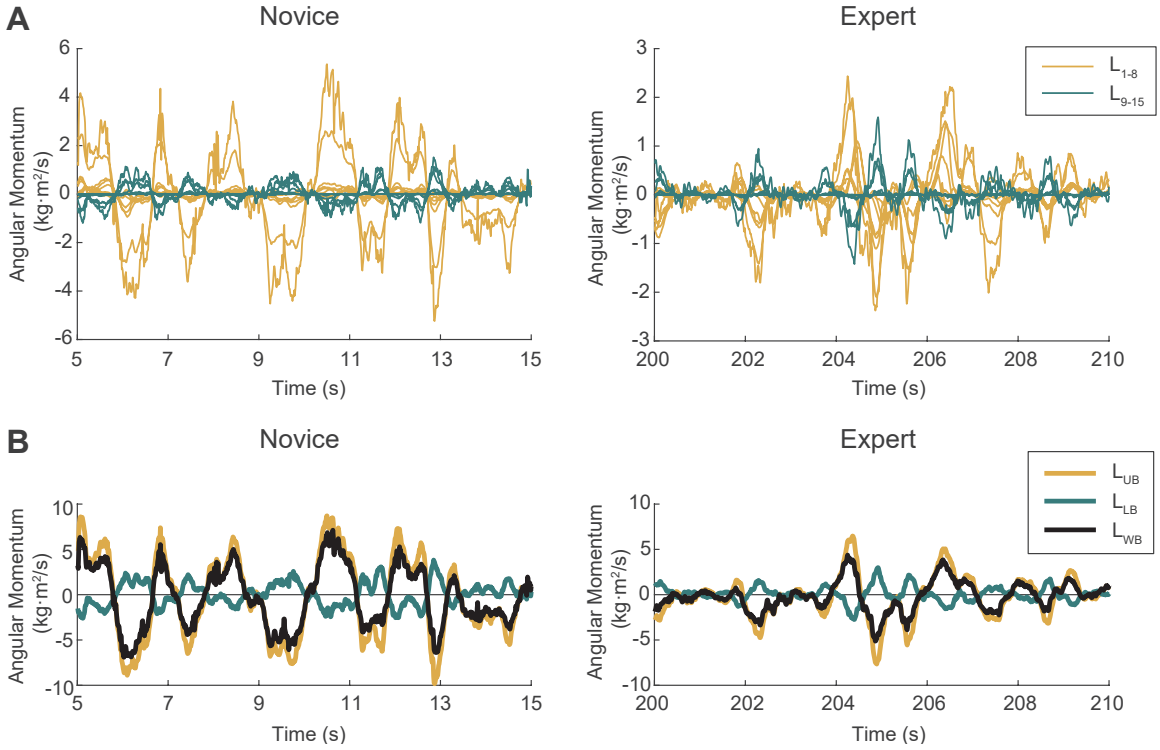

Figure 8-2: Human experimental results. Profiles of angular momentum generated by **A** individual segments and **B** lumped upper body, lower body, and whole body segments. To visualize the observed patterns in angular momenta, data from only a representative segment (10 s) of each trial are shown.

8.2.3 Effects of Rigid Feet on Balance on a Beam

Rigid Feet Improved Task Balance Ability

Subjects stood on the beam significantly longer in the rigid feet condition ($M = 236.0\text{s}, SD = 119.4\text{s}$) than in the bare feet condition ($M = 103.1\text{s}, SD = 158.3\text{s}$), ($t_6 = -2.59, p = 0.041$; Fig. 8-3A).

The RMS of $\hat{v}_{\text{wb},y}$ was significantly reduced in the rigid-feet condition ($M = 0.0024, SD = 0.0005$) compared to the bare-feet condition ($M = 0.0052, SD = 0.0032$), ($t_6 = 2.46, p = 0.049$; Fig. 8-3B). The RMS of $\hat{L}_{\text{wb},x}$ was also significantly lower in the rigid feet condition ($M = 0.0026, SD = 0.0010$) compared to the bare-feet

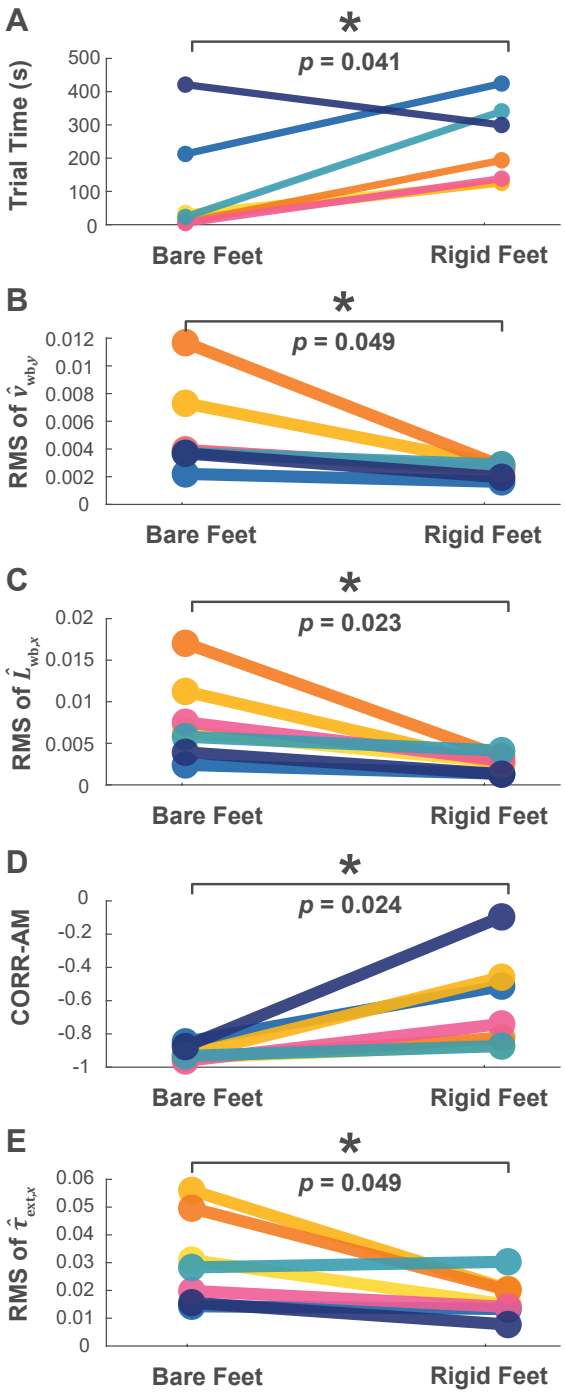

Figure 8-3: Experimental Results. (A) Trial time, (B) RMS of center of mass velocity in the mediolateral direction ($\hat{v}_{\mathrm{wb},y}$), (C) RMS of whole body angular momentum ($\hat{L}_{\mathrm{wb},x}$), (D) correlation of upper and lower body angular momentum (Corr-AM), (E) RMS of external foot-beam interaction torque ($\hat{\tau}_{\mathrm{ext},x}$). Individual subjects are represented by colors. An asterisk represents a significant within-subject difference in the two conditions ($p < 0.05$).

condition ($M = 0.0078, SD = 0.0050$), ($t_6 = 3.02, p = 0.023$; Fig. 8-3C).

Together, these results indicate that balance performance was improved when subjects wore rigid soles.

Rigid Feet Altered Whole-body Coordination

Not only the aforementioned representative subjects, all subjects exhibited strong anti-correlation between upper body and lower-body angular momenta in the bare-feet condition (Corr-AM; $M = -0.92, SD = 0.04$). Even though it was also negative in the rigid-feet condition, ($M = -0.62, SD = 0.29$), the value was significantly increased (i.e., less anti-correlated) compared to the bare-feet condition ($t_6 = -3.00, p = 0.024$; Fig. 8-3C).

Rigid Feet Reduced Estimated Foot-beam Interaction Torque

The RMS of $\hat{\tau}_{\text{ext},x}$ was significantly reduced in the rigid feet condition ($M = 0.0172, SD = 0.0072$) compared to the bare-feet condition ($M = 0.0306, SD = 0.0164$), ($t_6 = 2.47, p = .049$; Fig. 8-3C).

8.3 Modeling Human Balance on a Beam

8.3.1 Double Inverted Pendulum Model

To account for anti-correlation between the upper- and the lower-body angular momentum, the double inverted pendulum model was chosen for simulations as illustrated in Fig. 8-4. The equations of motion is

$$\mathbf{M(q)}\ddot{\mathbf{q}} + \mathbf{C(q,\dot{q})}\dot{\mathbf{q}} + \mathbf{G(q)} = \boldsymbol{\tau}, \tag{8.7}$$

where $\mathbf{M(q)} \in \mathbb{R}^{2\times 2}$ is the inertia matrix, $\mathbf{C(q,\dot{q})}\dot{\mathbf{q}} \in \mathbb{R}^{2\times 1}$ are the Coriolis and centrifugal terms, and $\mathbf{G(q)} \in \mathbb{R}^{2\times 1}$ are the gravitational torques. The relative joint angles $\mathbf{q} = [q_1, q_2]^{\mathrm{T}} \in \mathbb{R}^{2\times 1}$ were chosen as generalized coordinates to describe the

model. $\boldsymbol{\tau} = [\tau_1, \tau_2]^{\mathrm{T}} \in \mathbb{R}^{2\times 1}$ is the associated torque vector. The model parameters used for simulation are listed in Table 8.3, which were obtained from [82, 119].

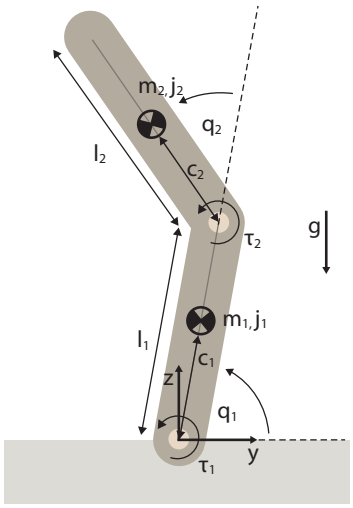

Figure 8-4: Double Inverted Pendulum Model.

Table 8.3: Double Inverted Pendulum Model Parameters

Parameter	**Meaning**	**Value [unit]**
m_1	mass of link 1	28.36 [kg]
l_1	length of link 1	0.6960 [m]
c_1	center of mass of link 1	0.3480 [m]
j_1	moment of inertia of link 1 about its com	1.145 [kg·m^2]
m_2	mass of link 2	42.54 [kg]
l_2	length of link 2	1.044 [m]
c_2	center of mass of link 2	0.5220 [m]
j_2	moment of inertia of link 2 about its com	3.864 [kg·m^2]
g	gravitational acceleration	9.810 [m/s^2]

8.3.2 Model of Human Balance with Bare Feet

Developing balance control algorithms for bipedal robots has been a major research interest of the robotics community, and many of them have been implemented on complex real robotic platforms with demonstrated success. We adopted several balance controllers from robotics literature that are compatible with the simple double inverted pendulum model. A subset of controllers was identified that produced bal-

ance behavior similar to what we observed in humans, i.e. the angular momenta generated by the upper and lower body segments were anti-correlated.

Joint Impedance Controller (JIC)

The simplest balancing controller is to implement virtual compliance either in joint (configuration) space or in the Cartesian (task) space. The joint impedance controller is defined as

$$\mathbf{u} = \mathbf{K_{pj}}(\mathbf{q_0} - \mathbf{q}) - \mathbf{K_{dj}}\dot{\mathbf{q}}, \tag{8.8}$$

where $\mathbf{K}_{\mathrm{pj}}, \mathbf{K}_{\mathrm{dj}} \in \mathbb{R}^{2\times 2}$ are positive definite joint stiffness and damping matrices, respectively, and the rest position $\mathbf{q}_0 = [\frac{\pi}{2}, 0]^{\mathrm{T}}$ corresponds to the upright posture. $\mathbf{u} \in \mathbb{R}^{2\times 1}$ is the commanded joint torque vector.

Cartesian Impedance Controller (CIC)

Alternatively, a virtual linear spring-damper supporting the center of mass of the model can also maintain balance,

$$\mathbf{u} = \mathbf{J^T}(\mathbf{K_{px}}(\mathbf{c}_{\mathrm{wb},0} - \mathbf{c}_{\mathrm{wb}}) - \mathbf{K_{dx}}\mathbf{v}_{\mathrm{wb}})), \tag{8.9}$$

where $\mathbf{K}_{\mathrm{px}}, \mathbf{K}_{\mathrm{dx}} \in \mathbb{R}^{2\times 2}$ are positive definite Cartesian stiffness and damping matrices, respectively, and $\mathbf{c}_{\mathrm{wb}}, \mathbf{c}_{\mathrm{wb},0}$ are the center of mass position and rest position of the virtual spring, respectively. $\mathbf{v}_{\mathrm{wb}} = \frac{d}{dt}\mathbf{c}_{\mathrm{wb}}$ is the center of mass velocity.

Linear Quadratic Regulator (LQR)

By defining the state variables as $\mathbf{x} := [\mathbf{q}^{\mathrm{T}}, \dot{\mathbf{q}}^{\mathrm{T}}]^{\mathrm{T}}$, one can linearize the nonlinear equations of motion (8.7) about its equilibrium point, $\mathbf{x}_*$ and $\mathbf{u}_*$, corresponding to the resting upright posture,

$$\dot{\bar{\mathbf{x}}} = \mathbf{A}_{\mathrm{lin}}\bar{\mathbf{x}} + \mathbf{B}_{\mathrm{lin}}\bar{\mathbf{u}}, \tag{8.10}$$

where $\bar{\mathbf{x}} = \mathbf{x} - \mathbf{x}_*$ and $\bar{\mathbf{u}} = \mathbf{u} - \mathbf{u}_*$ and $\mathbf{A}_{\text{lin}}$ and $\mathbf{B}_{\text{lin}}$ are linearized state and input matrices, respectively. Since $\mathbf{x}_*$ is singular configuration, required joint torque $\mathbf{u}_* = 0$. Hence, the bar is omitted for the input.

The full-state linear quadratic regulator (LQR) takes advantage of the dynamic model of the system, and the choice of costs on deviation of states and actuation affects the controller gain $\mathbf{K}_{\text{LQR}}$ [197].

$$\mathbf{u} = -\mathbf{K}_{\text{LQR}}\bar{\mathbf{x}}. \tag{8.11}$$

Natural Posture Recovery (NPR)

The natural posture recovery (NPR) method presented by Abdallah and Goswami [1] is another simple, yet powerful, nonlinear controller for balance. Noting that upright posture corresponds to maximum potential energy that the system can have, one can design a control law to maximize the potential energy as below, with a positive gain k.

$$\dot{\mathbf{q}}^{\text{ref}} = k\mathbf{G}(\mathbf{q}) \tag{8.12}$$

$$\mathbf{u} = \mathbf{K}_{\text{dj}}(\dot{\mathbf{q}}^{\text{ref}} - \dot{\mathbf{q}}) \tag{8.13}$$

Here, the property that $\mathbf{G}(\mathbf{q}) = \frac{\partial V(\mathbf{q})}{\partial \mathbf{q}}^{\text{T}}$ is used, where $V(\mathbf{q})$ is the potential energy of the system. This control law leads the potential energy of the system towards global maximum, with some inevitable oscillation.

Angular Momentum Based Controller (AMBC)

The last controller tested in this work is the angular momentum based balance controller (AMBC) recently presented by Featherstone [57]. The controller assumes that only the hip is actuated to balance ($u = 0$). Let us denote the angular momentum of the total system about the supporting point as L_{wb}. As the ankle torque is zero, the

following relation holds.

$$L_{\mathrm{wb}} = \mathbf{SM}\dot{\mathbf{q}} \tag{8.14}$$

$$\dot{L}_{\mathrm{wb}} = -mgc_{\mathrm{wb,y}} = -\mathbf{SG} \tag{8.15}$$

$$\ddot{L}_{\mathrm{wb}} = -mg\dot{c}_{\mathrm{wb,y}} = -\mathbf{S}\frac{\partial \mathbf{G}}{\partial \mathbf{q}}\dot{\mathbf{q}} \tag{8.16}$$

where $\mathbf{S} = [1 \quad 0]$ is the selection matrix and $c_{\mathrm{wb,y}}$ is the horizontal component of center of mass position. Consider the following control law:

$$\dddot{L}_{\mathrm{wb}} = k_{dd}\ddot{L}_{\mathrm{wb}} + k_d\dot{L}_{\mathrm{wb}} + k_L L_{\mathrm{wb}} + k_q(q_2 - q_2^{\mathrm{d}}). \tag{8.17}$$

By taking the time derivative of (8.16), one can get $\dddot{L}_{\mathrm{wb}} = -mg\ddot{c}_{\mathrm{wb,y}}$ and the control torque u_2 is computed by solving the inverse dynamics. The controller gains (k_{dd}, k_d, k_L, and k_q) are chosen following the rule described in [57] which guarantees stability.

Simulation Results

Each controller was implemented on the same double inverted pendulum model with the same initial conditions. Furthermore, random ankle torque noise $\tau_{1,\mathrm{pert}}$ was added to simulate the variability observed in the human balancing experiment, i.e. $\boldsymbol{\tau} = \mathbf{u} + [\tau_{1,\mathrm{pert}}, 0]^{\mathrm{T}}$. The perturbation torque was assumed to follow a uniform distribution on the interval $\tau_{1,\mathrm{pert}} \in [-10, 10]$N·m. This interval was chosen based on the RMS value of estimated torque seen at the point of foot-beam contact from the Novice subject. The simulations were conducted using MATLAB (Mathworks, Inc., MA) `ode45` with default options.

The gains of each controller were empirically, but carefully, chosen such that the resultant center of pressure (CoP) deviation remained within ± 2cm. This width was chosen to be close to the width of the beam (3.4cm).

The simulation results are shown in Fig. 8-5. For the six controllers tested, the time course of angular momentum about the support of whole body (L_{wb}), upper

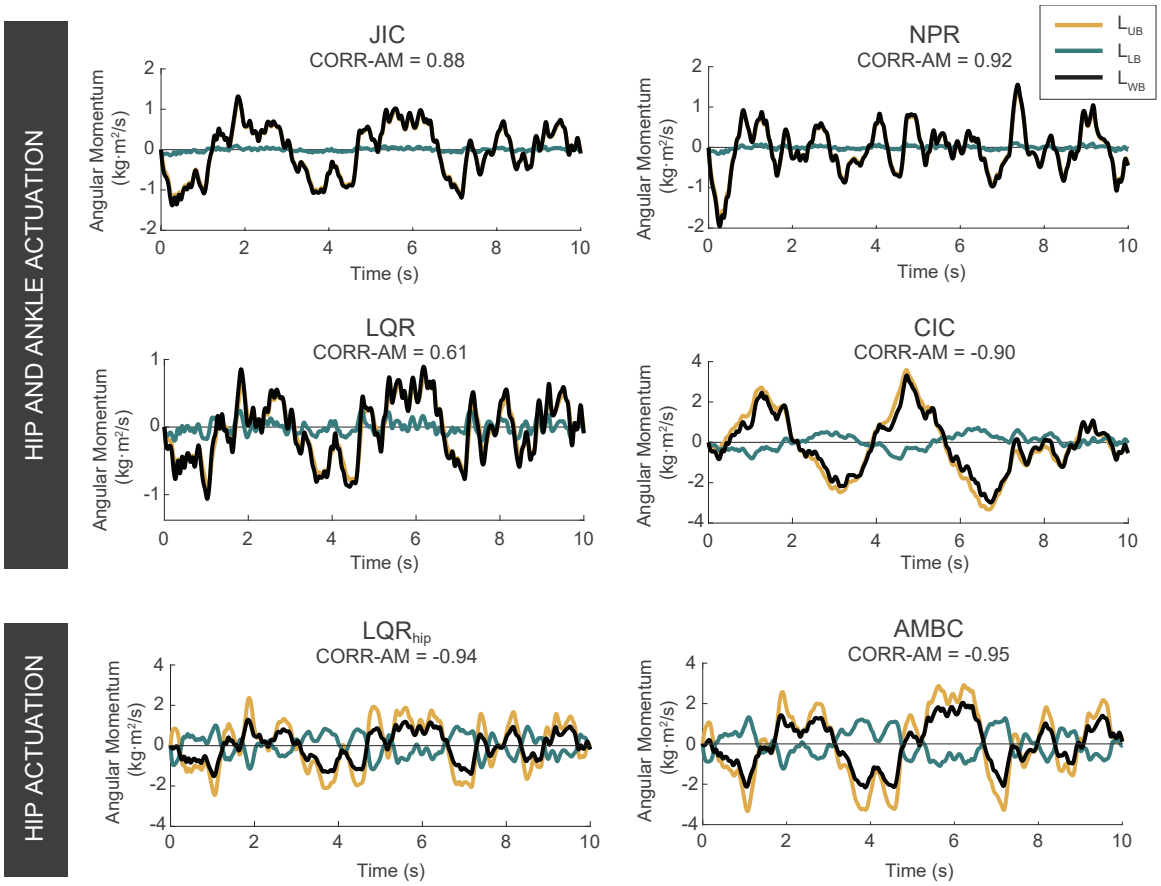

Figure 8-5: Simulation results. Time course of angular momentum about the support of whole body (black), upper body (yellow), and lower body (green) for different six different balance controllers. The cross correlation coefficient between L_{ub} and L_{lb} of each system are denoted as well.

body (L_{ub}), and lower body (L_{lb}) is plotted and the most negative/positive cross correlation coefficient between L_{ub} and L_{lb} is noted. In the LQR controller, ankle and hip actuation were equally penalized, whereas in the LQR_{hip} controller, ankle actuation was largely penalized to suppress use of the ankle. Three controllers showed positive cross correlation (JIC: 0.88, LQR: 0.61, and NPR: 0.92). The other three controllers showed high anti-correlation with cross correlation coefficient less than -0.90 (CIC: -0.90, LQR_{hip}: -0.94, and AMBC: -0.95).

Table 8.4 summarizes the dependent measures of interest. The controllers that showed high anti-correlation of upper and lower body angular momentum are in bold font.

8.3.3 Modeling the Effect of Changing Foot-beam Interface

We developed a simple model to describe the effect of altering the foot-beam interaction dynamics on overt balance behavior observed in the human experiment (Fig. 8-3), by extending the double inverted pendulum model. While AMBC reproduced the observed anti-correlation of upper- and lower-body angular momentum, it imposed zero RMS ankle torque as shown in Table 8.4, which was not observed in human behavior. The LQR controller exhibited more robust performance than the CIC controller. Therefore, we decided to use the LQR controller for a competent model of human balancing, when investigating the effect of changing mechanical interface between the feet and the beam (Fig. 8-6).

The full-state LQR determined the control (commanded) torques, $\mathbf{u} = [u_1, u_2]^{\mathrm{T}} = -\mathbf{K}_{\mathrm{LQR}}\mathbf{x}$. The controller gain is determined by solving the following infinite-horizon optimal problem:

$$\mathbf{u} = \underset{\mathbf{u}}{\operatorname{argmin}} \int_0^\infty \mathbf{x}^T\mathbf{Q}\mathbf{x} + \mathbf{u}^T\mathbf{R}\mathbf{u} = -\mathbf{K}_{\mathrm{LQR}}\mathbf{x}, \tag{8.18}$$

with the penalty matrices $\mathbf{Q}$ and $\mathbf{R}$ were parameterized as ,

$$\mathbf{Q} = \mathbf{I}_4, \mathbf{R} = \begin{bmatrix} \beta & 0 \\ 0 & \frac{1}{\beta} \end{bmatrix}, \tag{8.19}$$

such that $\mathbf{Q}$ equally penalize the state errors and $\mathbf{R}$ penalized ankle and hip actuation while allowing the parameter β to control the relative contribution between control actions. Changing the parameter β does not change the determinant of $\mathbf{R}$ so the

Table 8.4: Summary of Simulation Results

	CIC	**LQR$_{\mathbf{hip}}$**	**AMBC**	JIC	LQR	NPR
Corr-AM	**-0.90**	**-0.94**	**-0.95**	0.88	0.61	0.92
RMS of τ_1, [N· m]	**6.49**	**0.967**	**0**	4.94	4.11	4.50
RMS of τ_2 [N· m]	**32.0**	**17.1**	**28.3**	2.39	1.41	2.20
RMS of CoP [cm]	**1.0**	**0.70**	**0.72**	0.80	0.75	0.80

relative penalty between state errors and actuation were maintained at a similar level. $\mathbf{I}_n$ is the identity matrix with dimension n. In this model, the control torques represent the joint torques generated by human neural controller.

Foot-beam Interface Model

With a flat, stationary foot on a large support surface, the ankle torque and the ground reaction moment may be equal. When standing on a narrow beam, however, the commanded ankle torque may not be directly transmitted to the ground due to the foot-beam interaction dynamics. In double inverted pendulum model, τ_1 is the actual torque acting between the human body and the beam.[1] To describe discrepancy between the ankle control torque, u_1, and the applied torque at the interface, τ_1, the foot-ankle complex was represented as a torque transmission, with an efficiency factor $\eta \in [0, 1]$:

$$\tau_1 = \eta u_1 + \tau_{1,\text{pert}} \tag{8.20}$$

$$\tau_2 = u_2 \tag{8.21}$$

where $\tau_{1,\text{pert}}$ is the noise applied to the model in order to reproduce the variability in humans.

This foot-beam interface model was introduced to describe the change in human behavior across feet conditions without altering the controller. When balancing on the ground, the feet may be regarded as an ideal transmission with $\eta = 1$. Due to foot-beam interactive dynamics, the bare feet and rigid feet on a beam could be described as an imperfect transmission with $\eta < 1$. In simulation, we tested whether humans performed better with rigid feet because they acted as more efficient transmission mechanisms than bare feet.

[1] τ_1 of the model is equivalent to $\tau_{\text{ext,x}}$ of the human data.

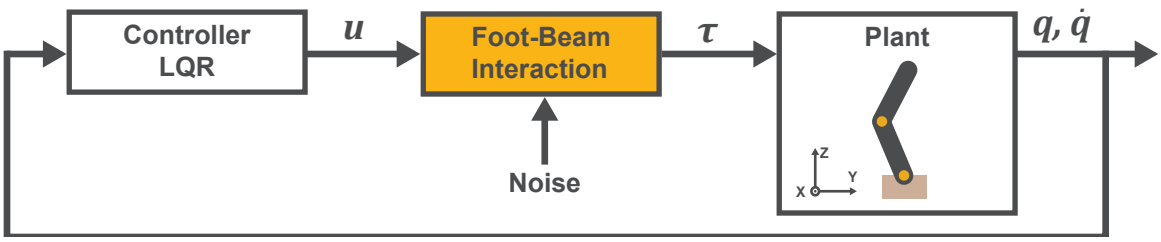

Figure 8-6: Block Diagram of the Proposed Human Balance Model

Simulation Details

The double inverted pendulum model with LQR was simulated with rest at upright posture as its initial condition. The random perturbation torque was drawn from a uniform distribution on the interval $\tau_{1,\text{pert}} \in [-10, 10]$ N·m as in the previous section. The simulations were conducted using the MATLAB `ode45` function with default options. The solutions were evaluated at 100Hz using the MATLAB `deval` function to compute angular momentum, joint torques, and center of mass velocity. The dependent measures were also normalized as in human data processing (8.6), using the model mass and height.

In the simulation, the analysis was carried out by changing parameters β and η, as follows:

- β values from 3 to 5 (step size of 0.5);
- η values from 0.0 to 1.0 (step size of 0.05).

The pairs of parameters resulting in physically infeasible behavior (e.g., negative vertical reaction force, center-of-pressure excursion larger than beam width) or that did not reproduce human behavior (e.g., positive instead of negative correlation between upper and lower body angular momenta) were discarded.

Simulation Results

The RMS of the horizontal velocity of the center of mass, $\hat{v}_{\text{wb},y}$, RMS of whole body angular momentum, $\hat{L}_{\text{wb},x}$, correlation coefficient between upper and lower body angular momenta, Corr-AM, and RMS of ankle torque, $\hat{\tau}_1$, for different values of η and β are presented in Fig. 8-7.

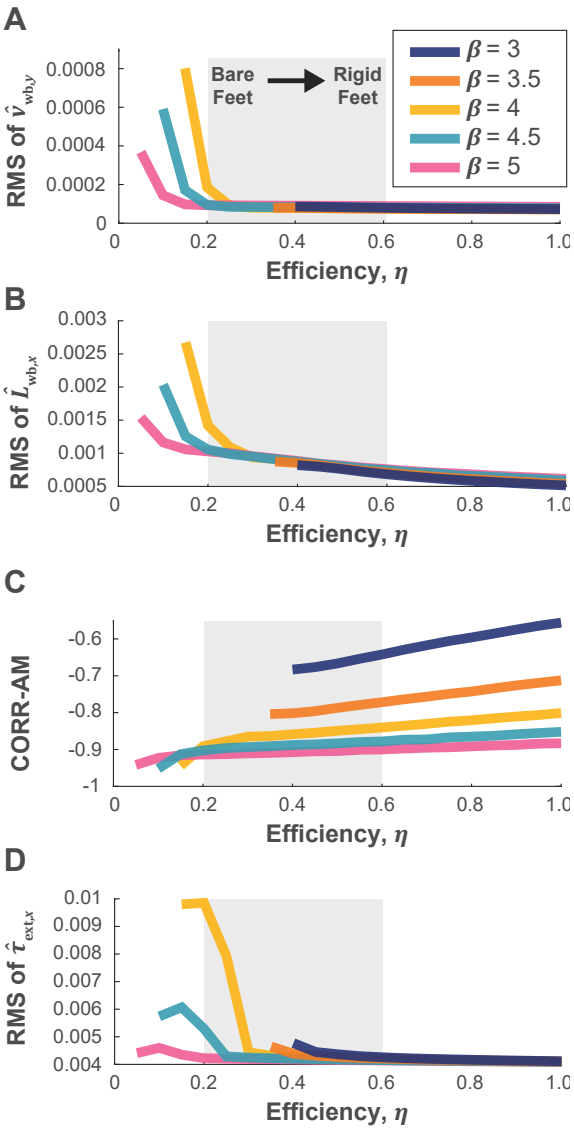

Figure 8-7: Simulation Results. (A) RMS of the horizontal velocity of the center of mass ($\hat{v}_{\mathrm{wb},y}$), (B) RMS of whole body angular momentum ($\hat{L}_{\mathrm{wb},x}$), (C) correlation of upper and lower body angular momentum (Corr-AM), (D) RMS of actual torque acting at the foot-beam interface ($\tau_1 \equiv \hat{\tau}_{\mathrm{ext},x}$). Simulations with different values of the parameter β are represented with colors. The light shaded region indicates the range of $\eta \in [0.2, 0.6]$ that best represents the behavior observed in the bare feet and rigid feet conditions of the human experiment.

Given the range of tested parameters, the model with larger β showed smaller Corr-AM and smaller RMS of $\hat{\tau}_1$. On the other hand, it was hard to find consistent trends on $\hat{v}_{\mathrm{wb,y}}$ and $\hat{L}_{\mathrm{wb,x}}$ across all values of β.

Given the range of tested parameters, the model with smaller η showed smaller

Corr-AM, larger RMS of $\hat{\tau}_1$, larger RMS of $\hat{v}_{\mathrm{wb},y}$, and larger RMS of $L_{\mathrm{wb},x}$.

The behavior of the model in the range of $\eta \in [0.2, 0.6]$ (shaded region in Fig. 8-7) was comparable to that observed in the human experiment. Model behavior with small η resembled human behavior in the bare feet condition, and model behavior with large η resembled human behavior in the rigid feet condition. Even though the model could capture the qualitative result, it could not accurately capture the quantitative results. Within the range of parameters tested, the magnitude of change in the dependent measures was smaller than that observed in the human experiment.

8.4 Discussion

For robotic devices designed to assist humans with balance, it is necessary that the assistance they provide does not interfere with the humans' intended behavior. Along the same vein, robotic devices used for rehabilitating or retraining balance ability need to guide users towards a desirable balance strategy. Hence, we sought to further characterize the intended and desired human behavior during balance such that future devices can be controlled to provide effective assistance.

Summary of the Experimental Results

The behavior observed from humans standing on the beam revealed several important characteristics of mediolateral balance. First, while we did not constrain the subjects' arms, they generated angular momentum correlated with the thorax/abdomen such that the behavior of the upper body could be lumped into one segment. Second, the lumped upper body and lower body angular momenta were highly anti-correlated, meaning they acted in the opposite directions. The contribution of the upper body was significantly higher such that the overall whole-body angular momentum was non-zero. Moreover, the sum of the time derivative of the whole-body angular momentum $\dot{L}_{\mathrm{wb}}$ and the moment due to gravity was also non-zero. This finding indicated the existence of non-zero external torque applied to the body about the beam axis (see 8.5), despite of the very narrow beam that constrained base of support.

The results of this study also revealed that foot-beam interaction mechanics significantly influenced human behavior when standing on a narrow support surface. When the contact between the foot and beam was altered by wearing rigid soles, subjects significantly improved their ability to maintain mediolateral balance. It also altered inter-limb coordination. While the angular momenta of the upper and the lower body were anti-correlated with both bare feet and rigid feet conditions, there was less anti-correlation when the contact was rigid. In addition, the foot-beam interaction torque was reduced with rigid contact; however, it is less clear whether this indicates changes in balance controls strategy or was merely due to improved balance.

Modeling human balancing on a beam without footwear

Among the balance controllers we tested, three could reproduce the behavior we observed in the human experiment. Simulations with the $\mathrm{LQR}_{\mathrm{hip}}$, AMBC, and CIC generated behavior with high anti-correlation between L_{ub} and L_{lb}. In these controllers, there was either no or little contribution of the ankle compared to the hip (Table 8.4).

The remaining controllers we tested could not reproduce the high anti-correlation between L_{ub} and L_{lb}. Instead, the correlation was positive, meaning the double inverted pendulum only exhibited in-phase modes. In these controllers, the contribution of ankle actuation was comparable to or larger than hip actuation.

Note that, in all simulations, the internal noise was identical and the CoP of the model remained in a reasonable range (Table 8.4). This may indicate that the observed human behavior was not as trivial as one might think; a narrow base of support of the beam constrains the range of mediolateral CoP, but it *does not* necessarily limit the ability to actively use ankle nor enforce humans to exhibit strong anti-correlation between upper and lower body angular momentum. The consistent whole-body coordination pattern we observed was not an obvious consequence of biomechanical constraint but should be attributed to the neuro-mechanical balance controller.

Simplified Model of the Foot-beam Interface

In a companion study [79], it was found that the effects of wearing rigid soles on human walking on a beam was immediate but did not persist upon removal of the soles. This suggested that human subjects did not adapt their neural control strategy during several trials and practice with the rigid soles. Instead, it is likely that the change of the mechanical interface was responsible for the altered human behavior.

The differences between the bare feet and the rigid feet condition could be reproduced by modeling the *foot-ankle complex* as a transmission mechanism between the commanded ankle torque and the actual torque that acted between the foot and the ground. By considering the ankle-foot complex simply as a transmission mechanism parameterized by η, we modeled that the transmission of the ankle torque to the ground was less efficient (smaller η, i.e., lower torque transmission efficiency) in the bare feet condition compared to the rigid feet condition.

For an arbitrary control torque, u_1, a smaller η yields a smaller applied torque, τ_1. Over time, however, a smaller η results in a greater accumulation of state errors, which causes an increase in control torque u_1. Thus, simulation of the model with a smaller η actually resulted in greater τ_1, as well as worse balance performance (Fig. 8-7D). Because τ_2 was unaffected by η, a smaller η reduced the contribution of ankle torque relative to hip torque, resulting in a more negative Corr-AM.

In the simulation, the same LQR control strategy with different values of parameter β was tested to account for possible differences in behavior across individual subjects. For all β values that we tested, the effect of the parameter η was consistent. The model could qualitatively reproduce the changes in balance performance observed with rigid soles: improved balance (decreased RMS CoM velocity and RMS whole-body angular momentum) and altered whole-body coordination (less negative anti-corrleation Corr-AM).

Simple but Competent model Provides Insight

We emphasize that the purpose of the model is not to precisely predict human behavior nor to suggest how the human neuromuscular system controls balance. Rather, the model was developed to facilitate insights by identifying possible mechanisms that can describe human behavior we observed. This is a subtle, yet important distinction. The human system is vastly complex. For instance, there are both passive and active compliance at the joints, significant time delays within the neuromotor system, and noise both in sensing and actuation. Even though none of these were considered in the models tested here, we were nevertheless able to identify controllers that adequately captured the anti-correlation of upper- and lower-body behavior. Moreover, the effect of wearing rigid soles on human balancing on a beam could be reproduced without changing the controller but by introducing mechanical changes.

Importantly, these novel models not only provide explanations of the human data, but also generate more research questions that should be further discerned.

Future Works

While we limited our investigation to specific forms of controllers, other control architectures found in biomechanical studies or robotics could be also investigated (see [147]). For example, intermittent control [34, 62], optimal control with constraints, or treating the problem as a linear-quadratic-Gaussian synthesis might yield further insights.

The torque transmission loss was lumped into a single parameter η. Biomechanically and physiologically plausible explanation of this model should be illuminated.

8.5 Conclusions

This study quantified whole body coordination of human balancing on a beam, and quantified how it was altered by changing the foot-beam mechanical interface, simply wearing a rigid sole. A highly-simplified model could reproduce several features of human beam balancing. Importantly, it demonstrated that the difference in hu-

man behavior between the bare feet and rigid feet conditions could be explained by accounting for foot-beam mechanical interface rather than a change in the controller.

Chapter 9

Balance on a beam with canes

This work was conducted in collaboration with Dr. Marta Russo (Northeastern University, Action Lab) and Prof. Dagmar Sternad (the same). We would like to thank Christian Moses for his help in collecting the data. We would also like to thank Dr. Randy Trumbower for lending us torque sensors.

This work was supported by a Samsung scholarship. This work was also supported by NSF CRCNS-1723998 awarded to Prof. Dagmar Sternad and by NSF CRCNS-1724135 awarded to Prof. Neville Hogan.

Publication of this work is in preparation [179].

9.1 Introduction

In the last century neuroscientists thought that maintaining postural balance was achieved by spinal reflexes, triggered by visual, vestibular and somatosensory inputs [124]. However, in the more recent past, a large number of studies accumulated evidence that balancing is a complex skill and should be understood as the interaction of multiple dynamic sensorimotor processes [75,76]. While the effects on postural control were mainly evaluated in terms of the fluctuations of the ground reaction forces, several studies also examined body kinematics and muscle activation. For example, Ting and Macpherson suggested that to maintain upright balance, muscle synergies are activated in service of the desired biomechanical output [209]. Based on mea-

sured ankle torque and muscle activity, Loram and collaborators showed that the neuromotor system that controls balance relies on motor planning and processing of sensorimotor information [120]. Morasso and colleagues have demonstrated with a computational model that postural balance is an intricate control processes involving forward and inverse internal models [134]. Recent work proposed an optimal feedback control model to account for the fluctuations of the center of pressure location [118].

Many researchers also focused their attention on the role of sensory information for postural control. Not surprisingly, visual input together with vestibular and proprioceptive information is strongly involved [154, 158]. Less intuitive is the role of haptic information, such as through touching a surface or holding the hand of another person. A seminal study has shown that light touch of the fingertip on an earth-fixed surface significantly reduced sway [86]. Increasing the amount of force applied on the surface had minimal effect on the sway. Indeed, blind individuals who rely on haptic information from the 'white cane' reported that force levels significantly below those that provided physical support presented useful stabilization [85]. Jeka and collaborators confirmed that touch with a cane was effective in reducing postural sway, indicating that even haptic information from indirect contact with a fixed surface reduced postural sway. When balance was challenged, for example when standing on a beam elevated above ground, light touch reduced sway both with and without visual input [122]. The same study also tested the effect of bimanual light touch under conditions of increased risk, i.e., greater heights of the beam. Those results showed that bimanual touch improved postural balance, especially when standing on a high beam when fear of falling became an issue.

The force levels that have been investigated in the studies on light touch typically ranged from < 1 N to about 10 N. At such low force levels, benefits derived from the touch were mainly perceptual and mechanical changes were subordinate. Hence, this previous set of studies highlighted the perceptual role of support for spatial orientation. In addition, these light touch studies tested participants' ability to balance using earth-fixed supports that were stationary; even one study of cane use by Jeka and colleagues examined the role of a cane that was fixed onto the ground [85]. Such

a scenario is uncommon when relying on a supporting device. Typically, a cane or holding the hand of another person does not present a stable or stationary support. Yet, as seen in the frequent use of sticks or poles in hiking, such nonstationary devices appear to provide stability.

The aim of the present study was to investigate the mechanical contribution to postural balance of support through hand-held canes. This study tested the role of support with two canes, one held in each hand and placed on the ground. In many activities where balance is challenged, humans rely on both hands for support, for example using poles when skiing or hiking. To challenge postural stability, participants were asked to stand on a narrow beam in tandem stance. In that configuration, the base of support was strictly limited by the beam dimensions, in particular its width. For reference, we also included two control conditions: standing on the beam without canes, and standing on the ground, also in tandem stance. The first question was to what degree standing on the beam with cane support would improve with respect to standing on the beam without canes and standing on the ground. While cane support should evidently decrease postural sway compared to free standing on the beam, we expected that using canes when balancing on a beam would remain more variable than standing on the ground without canes (Hypothesis 1).

To explore the influence of forces applied to the canes, participants were asked to apply minimal, preferred, and maximum levels of force on the two canes, where the maximal force condition should significantly exceed the force levels studied in earlier work. We reasoned that greater forces applied on the canes would have significant mechanical effects on postural stability, and expected that the variability of the center of mass motion and the center of pressure would be reduced (Hypothesis 2).

Participants were instructed to place the canes in two different configurations. In the first 'planar' condition, participants held the canes symmetrically with their arms extended to their sides, extending the base of support in the medio-lateral direction, but confining support to the frontal plane only. In the second 'tripod' condition, canes were placed in front of the body, with both arms at 45deg angle with the frontal plane. We reasoned that the tripod condition would significantly increase the

base of support as mechanical support is provided in both medio-lateral and anterior-posterior directions. We therefore hypothesized that the tripod condition would yield more stability and that postural variability in center of pressure and center of mass would decrease (Hypothesis 3).

Nevertheless, these canes presented an additional challenge: a cane is an inverted pendulum that is inherently unstable. When applying force, its variability (noise) may increase proportionally as it is regarded as signal-dependent [89]. Moreover, it was shown that exerting a force on an inherently unstable system can induce mechanical instability, i.e. the cane may fall over [163, 164]. Hence, higher forces can have the opposite effect and destabilize posture (Hypothesis 4).

To sensitively evaluate the intricate mechanical effects, ground reaction force was measured both at the feet and at the canes. The beam was placed on a force plate and 6-DOF force sensors measured forces applied on the canes. The latter allowed separate quantification of the center of pressure at the canes and at the feet. Based on 3D kinematic recordings, we also assessed the center of mass motion. Remarkably, we found that the controller exploits the novel mechanics of the canes allowing for more variability in task-irrelevant dimensions and reducing unnecessary force activation.

9.2 Methods

9.2.1 Participants

16 participants (7 females, 9 males, between 19 and 36 years) with no history of neurological conditions and normal or corrected-to-normal vision took part in the experiments upon signing an informed consent form. The study was approved by the Institutional Review Board of Northeastern University.

9.2.2 Experimental Apparatus

Participants stood on a narrow wooden beam (width 3.65 cm, height 7.62 cm) that was placed on the floor on top of a force plate (AMTI, Watertown, MA, Fig. 9-1).

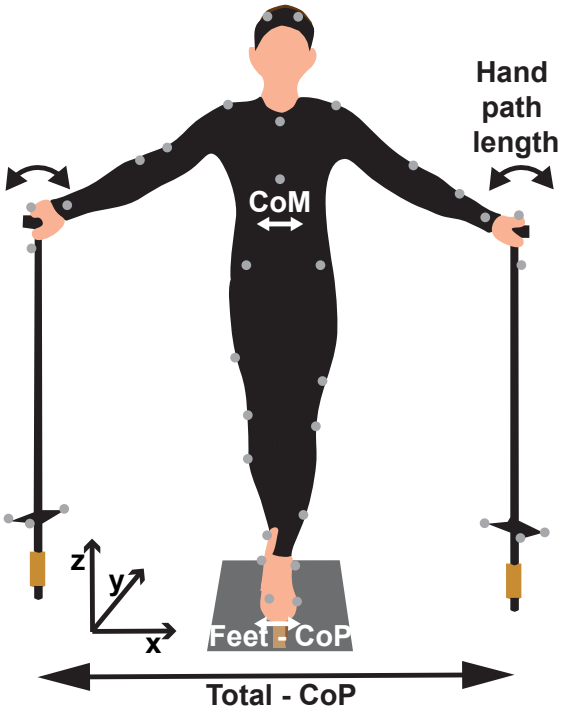

Figure 9-1: Experimental setup. Participants stood on a beam that was placed in a fixed position on a force plate, holding a cane in each hand. A set of 43 light-reflective markers measured displacements of the full body and the canes in 3D. The canes were instrumented with two 6D torque sensors at the bottom of each cane. The sketch shows the planar cane configuration where the two canes were placed to be on one line with the feet. In the tripod configuration, the canes were placed 0.50 m further to the front to form a triangle with the feet.

They held two aluminum canes, one in each hand, to support themselves (length 117 cm, mass 680 g). The two canes were instrumented with a 6-DOF load cell at the bottom of each cane to measure the forces applied to the canes (MCW-500 Walker Sensors, AMTI Watertown, MA). All force data were recorded at 500 Hz sampling rate. To record the participants' movements in 3D space, whole-body kinematics were recorded by 12 optoelectronic cameras at a sampling rate of 100 Hz (Qualisys AB, Göteborg, Sweden). Each participant was equipped with a standard biomechanical set of 43 reflective markers, following the C-Motion Plug-In Gait marker set. To track the orientation of the canes in 3D space, 4 additional markers were attached to each cane.

9.2.3 Experimental Protocol

Participants were asked to stand in tandem stance on the narrow beam without stepping on the ground. They could choose which foot was at the front of their stance and they kept the same foot in front in all trials. For all experimental conditions, participants supported themselves with two canes, one held in each hand, their arms comfortably extended. Participants were asked to apply one of three levels of force on the canes: minimum (Min), i.e., as little as they could, preferred (Pref), i.e., as much as they liked, maximum (Max), i.e., as much as possible. They performed the same three force conditions in two arm configurations: their arms extended out horizontally in the frontal plane (Planar), and stretched out forward forming approximately a 45deg angle at the shoulder with the frontal plane (Tripod). In one additional control condition participants stood on the beam without the cane support. In this difficult condition they were allowed to move their arms freely to help maintain balance on the beam. We further recorded a baseline condition in which participants stood on the ground in the same tandem stance without holding canes (Off Beam vs On Beam). Each combination of arm configurations and force on the canes was repeated three times, performed in blocks. Each block presented all experimental conditions once (3 force levels: Min vs. Pref vs. Max in 2 arm configurations: Planar vs. Tripod). Each trial lasted 30 s; the entire recording session lasted approximately one hour, including placing the markers on the body.

9.2.4 Data Preprocessing

All analyses were carried out with custom software written in Matlab (The Mathworks Inc., Natick, MA). All kinematic and kinetic data were filtered with a zero-lag 3rd-order low-pass Butterworth filter at 10 Hz (functions: butter, filtfilt). In order to exclude any transient or fatigue effects, data from the first 10% and last 10% of each trial were excluded from the analysis. The weight of the cane was subtracted from the vertical component of the force measured at the canes, to estimate the effective force applied by participants. In trials with cane support, participants did not step off the

beam during the trial, hence no further action was necessary. In the control condition where participants stood on the beam without cane support, they occasionally lost balance and stepped off the beam. These trials were excluded from the analysis.

As the feet of participants were not in direct contact with the force plate but with the beam, the center of pressure recorded by the force plate (Ground-CoP) was different from that resultant from the feet-beam interaction (Beam-CoP). The discrepancy was evaluated by the following equations,

$$\text{Beam} - \text{CoP}_x = \text{Ground} - \text{CoP}_x + h\frac{F_x^g}{F_z^g} \tag{9.1}$$

$$\text{Beam} - \text{CoP}_y = \text{Ground} - \text{CoP}_y + h\frac{F_y^g}{F_z^g} \tag{9.2}$$

where h is the height of the beam and $F^g = \left[F_x^g, F_y^g, F_z^g\right]$ is the ground reaction force recorded by the force plate. The x-axis corresponded to the ML direction, the y-axis to the AP direction, and the z-axis to the vertical direction, as illustrated in Fig. 9-1.

As $F_z^g >> F_{x,y}^g$, the additional term on the right side of equation (1) and (2) was negligible. Thus, in the following only the Ground-CoP was considered. For the sake of clarity, the CoP on the ground was referred to as the Feet-CoP.

When two canes touched the floor, the participant had three points of contact with the ground: the feet on the beam, and the tips of the two canes. The feet were on the beam, which was located on the force platform, thus measuring the ground reaction force and the center of pressure. Information about the force applied on the canes was provided by the load cells at the tip of the canes. The center of pressure of each cane was computed by the ratio between the moments, m_x, and m_y, and the forces, f_z, measured by the load cells.

$$cop_x = \frac{m_y}{f_z} cop_y = \frac{m_x}{f_z} \tag{9.3}$$

The spatial positions of the tips of the canes were determined from the markers attached to the canes. With all variables in the laboratory coordinate frame, the total center of pressure (Total-CoP) was computed as the ratio of the total moments,

$M_{x,y}$, and the total force, F_z. The total moments were defined as the sum of the product of the vertical force at each point of contact with the respective moment arm. The moment arm at each point was computed as the sum of the center of pressure with the relative position $a = [a_x, a_y, 0]$, which in turn is the vector from the origin of the coordinate frame to the point of contact. As it was desirable to compute the CoP in the medio-lateral (ML) and antero-posterior (AP) directions, the total moments in the AP and ML directions were determined, respectively, as shown in (9.4), (9.5).

$$M_x = \sum_{i=1}^{3} (a_y^i + cop_y^i) f_z^i \tag{9.4}$$

$$M_y = \sum_{i=1}^{3} (a_x^i + cop_x^i) f_z^i \tag{9.5}$$

The index i indicates the current point of contact ($i = 1$: feet, $i = 2$: left cane, $i = 3$: right cane). Following the rule applied previously, the total CoP was determined as

$$\text{Total} - \text{CoP}_x = \frac{M_y}{F_z} \tag{9.6}$$

$$\text{Total} - \text{CoP}_y = \frac{M_x}{F_z} \tag{9.7}$$

where $F_z = \sum_{i=1}^{3} f_z^i$.

For each participant a kinematic model of 15 rigid body segments (head, trunk, pelvis, left and right upper arms, forearms, hands, thighs, shanks and feet) was fit to the kinematic data using C-Motion Visual3D (Germantown, MD). The whole-body center of mass (CoM) was computed in Visual3D.

9.2.5 Dependent Measures

To obtain a metric for postural sway, the fluctuations of the CoP were summarized by the standard deviations of the CoP in two orthogonal directions, AP and ML. These two directions were calculated separately, because of the anisotropic constraints of the beam, i.e., the base of support on the beam was larger in the AP direction

than in ML. Another measure of postural sway was defined as the area of the 95% tolerance ellipse. The same metrics were computed for both Feet-CoP and Total-CoP. In addition, the fluctuations of the center of mass (CoM) were quantified by the area of the 95% tolerance ellipse. This area was calculated in the horizontal $(x-y)$ plane to make it comparable to the areas of the CoPs. Note that movements in the vertical (z) direction were negligible. To quantify movements of the hand at the tip of the cane, the path length of the hand movement was calculated as the integral of the root mean squared sum of the derivatives of the x-, y- and z-components.

$$\text{pathlength} = \int_{\text{start}}^{\text{end}} \sqrt{\left(\frac{\text{dx}}{\text{dt}}\right)^2 + \left(\frac{\text{dy}}{\text{dt}}\right)^2 + \left(\frac{\text{dz}}{\text{dt}}\right)^2}\,\text{dt} \tag{9.8}$$

9.2.6 Statistical Analysis

A linear mixed model was used to evaluate the differences in the sway of the center of mass and the center of pressure between the three levels of force applied to the canes and the two cane configurations. The mixed model compared the experimental conditions (fixed effects), i.e., beam, force and cane configuration conditions, which were consistent across participants, and accounted for the effects of normally distributed variability between participants (random effects). In equation (10) Y is the latent response variable for each participant i and each trial j, B is the beam condition (On the Beam or On the Ground); F is the force condition (three levels: Min, Pref, Max), C is the arm configuration (two levels: Planar and Tripod), are the fixed-effects coefficients, S are the random-effects coefficients.

$$Y_{ij} = \beta_0 + S_{0i} + \beta_b\, B_j \;+ (\beta_F + S_{Fi})\, F_j + \beta_c\, C_j \;+ \epsilon_{ij} \tag{9.9}$$

To better compare the force conditions in which participants were standing on the beam with the canes on the ground, a second model (see (9.10)) was tested on a subset of the data, excluding trials in the control conditions.

$$Y_{ij} = \beta_0 + S_{0i} + (\beta_F + S_{Fi})\, F_j + \beta_c\, C_j \;+ \epsilon_{ij} \tag{9.10}$$

Additional multiple comparisons were conducted across experimental conditions by pairwise t-tests with Bonferroni correction. All statistical analyses were carried out in R, with packages `stats`, `lme4` and `lmerTest` [162].

9.3 Results

This study examined the mechanical effect of cane support for maintaining standing balance. Specifically, the experiment aimed to identify the mechanical effects of two canes on the control of balance when standing on a narrow beam. Participants supported themselves by holding two canes placed either on their side or in a tripod configuration (Fig. 9-1). In the latter placement, the arms formed a 45 deg angle and the canes were in front of the body, forming a triangle with the feet. Participants were asked to exert three levels of force onto the canes: minimum (Min), preferred (Pref), and maximum (Max). We measured the displacements of the center of pressure on the beam, the forces on the canes, the body's center of mass, and the displacements of the hands at the cane. To provide a baseline measure, both the center of pressure and the center of mass were quantified when participants stood on the ground, in the same tandem foot position as on the beam. Another reference measure was obtained when participants stood on the beam without cane support. The overarching question of this study was how different forces applied to the canes and two arms configurations affected the mechanics and, hence, the control of postural balance.

9.3.1 Forces Applied on the Canes

The first test verified that participants indeed followed instructions and applied different forces on the canes. Table 9.1 shows the summed forces applied on the two canes averaged over the duration of the trial. For the three force instructions and for the two cane placements the applied forces ranged between 4 and 50 N for each cane. The linear mixed model confirmed the difference between the three force instructions with a significant main effect ($\beta = 10.1 \pm 2.6, p < 0.001$). All three force conditions were larger than those examined in previous studies and the preferred force differed

from both the maximum and the minimum forces. The two cane configurations did not elicit different forces in the three force conditions ($\beta = -0.7 \pm 4.3, p = 0.86$). The preferred force applied on both canes was reliably around 33 N in both arm configurations, corresponding to the weight of a 3.36 kg mass. Assuming the weight of the arm is 5% of total body weight, this force approximated the weight of the arm for an average body mass of 67 kg (3.35 kg) [42, 225]. As the weight of the arm was distributed across hand and shoulder, each cane supported about half of the weight of the arm, and this significantly offset the need to support the arms against gravity.

9.3.2 Variability of Center of Pressure and Center of Mass

Fig. 9-2 displays exemplary trials of Feet-CoP (colored lines), Total-CoP (grey lines) and also of the center of mass CoM (black lines) for each experimental condition. When standing on the ground (Fig. 9-2A), the fluctuations of CoM and CoP were considerably reduced compared to standing on the beam without canes, especially in the AP direction (Fig. 9-2B), which was not surprising. When standing on the beam without canes, both CoP and CoM showed visibly larger excursions, both in the AP and ML directions, again as expected.

The six panels in Fig. 9-2C show exemplary data from the same participant standing on the beam with the canes on the ground (yellow shading represents the beam width). The excursions of both CoPs and CoM were significantly reduced compared to those when standing on the beam without cane support and were similar to those measured when standing on the ground (Fig. 9-2A,B). The planar cane configuration led to visibly smaller sway in the AP direction than the tripod configuration,

Table 9.1: Sum of forces applied on the canes. Means and standard deviations across participants of the sum of the forces applied on the two canes in the three force conditions and in the two postures. Forces were averaged across the duration of the trial.

	min (M ± SD)	pref (M ± SD)	max (M ± SD)
planar	8.25 ± 10.08 N	33.21 ± 11.97 N	91.20 ± 36.82 N
tripod	9.64 ± 12.15 N	32.87 ± 12.28 N	85.60 ± 31.71 N

especially in the maximum force condition. In the minimum force condition, ML variability was similar in both Feet-CoP and Total-CoP, in both cane configurations. With increasing forces applied on the canes, the Feet-CoP decreased its ML amplitude. In contrast, the Total-CoP went beyond the width of the beam, indicating that the participants were moving their weight away from the feet and actively relying on the canes. Lastly, the fluctuations of the CoM, shown by the black lines, followed the changes of the Total-CoP across different forces and cane placements and presented additional evidence that participants shifted their weight beyond the base of support on the beam towards that provided by the canes.

The exact CoP location along the beam changed between trials, even within the same participant. This effect resulted from changing the distribution of body weight from the front to the back foot, even without stepping off the beam between trials.

9.3.3 Comparison of Postural Sway On and Off the Beam

To first evaluate the difference between balancing on the beam supported by canes with the two control conditions, the area of the CoM served as a collective measure of balance performance. Fig. 9-3A shows the CoM in the three force conditions contrasting with the two control conditions; the data combined the two cane configurations to focus on the comparison with the two control conditions. The figure makes it evident that standing on the beam without canes had the highest degree of variability ($\beta = 1682.1 \pm 290.2, p < 0.001$). The variability of the CoM on the beam with canes declined to levels similar to the variability on the ground. While pairwise post-hoc comparisons revealed a significant but small difference for the minimum force condition, the two higher force conditions did not differ from standing on the ground (Min: $p = 0.02$, Pref: $p = 0.08$, Max: $p = 0.1$). Interestingly, when applying increasing force on the canes, the variability of the CoM did not change ($p = 1$). This was counter to the expectation that balancing on the beam would remain more variable even with cane support (Hypothesis 1).

Fig. 9-3B shows participant averages of the 95% confidence interval of CoP for all force conditions to compare with the two control conditions without cane support

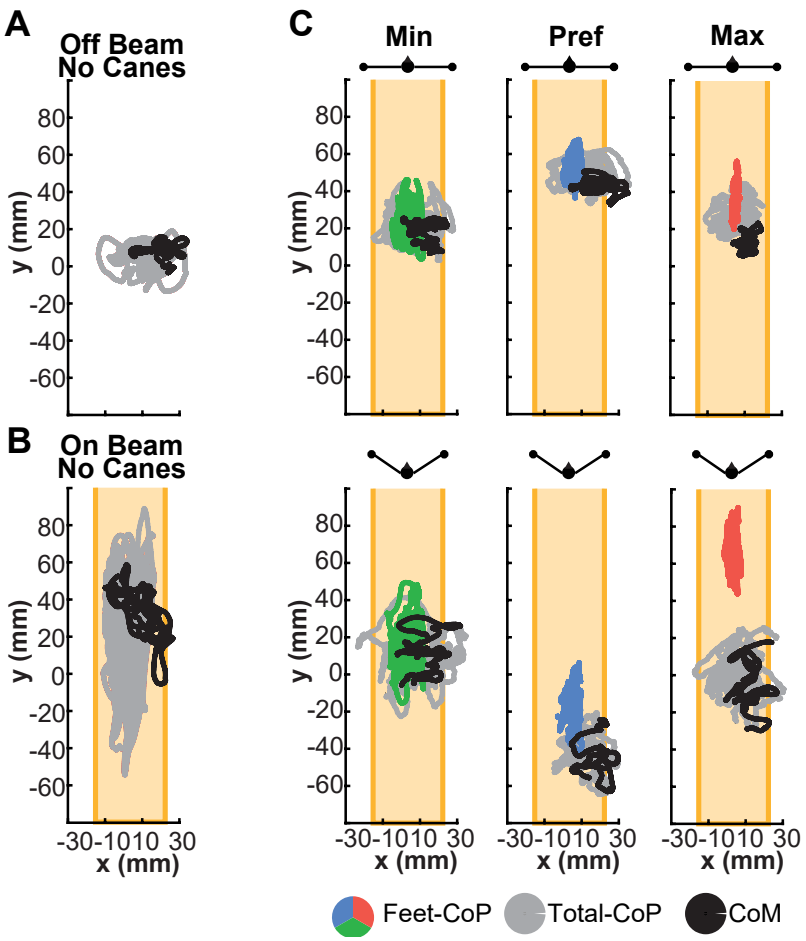

Figure 9-2: Representative paths of the center of pressure (CoP) and of the center of mass (CoM) in the horizontal plane. The two CoPs and CoM for one trial for each of the different force instructions and the two postures are shown in a top-down view. **A**. Exemplary trial when standing on the ground. The grey line represents the CoP and the black line the CoM. **B**. CoP and CoM of one trial of the same participant are shown when standing on the beam without canes. C. Each panel shows both the CoP at the feet (colored) and the total CoP (grey) for the three force conditions: minimum (green), preferred (blue), maximum (red); black lines show the center of mass (CoM). The two postures are identified by the drawings at the top of each panel. The beam is the light yellow area bounded by thin lines for visibility. For all conditions on and off the beam, the participant stood in tandem stance with the same foot in the front.

(white bars). To take into account the different nature of Total-CoP and Feet-CoP when participants used canes, the results were separated. Again, the data were pooled for the two cane configurations to facilitate comparison. As expected, standing on the beam without cane support significantly increased the CoP excursions with respect to standing on the ground by a factor of 10 ($\beta = 2953.6 \pm 236.2, p < 0.001$). However,

when participants used the canes for support, the Total-CoP returned to values similar to standing on the ground, as confirmed by the pairwise post-hoc comparisons ($p = 1$). The Feet-CoP showed even smaller values than the Total-CoP with canes and the CoP on the ground without canes ($p < 0.001$). While surprising at first, participants had three points of contact with the floor that allowed them to rely less on foot-beam interaction and more on canes. Taken together, these findings confirmed expectations that standing on the beam increased sway. However, counter to Hypothesis 1, both CoM and CoP variabilities were not higher than when standing on the beam, but approached the same level of variability as standing still on the ground. Given the mechanical instability when balancing without canes, this gives first evidence of the significant mechanical effect of the canes.

9.3.4 Effect of Forces on Postural Balance in the ML Direction.

This first analysis focused on the variability in the ML direction as it is the most relevant direction for maintaining balance on a beam. Fig. 9-4A shows the ML sway of Total-CoP against the average force applied on the canes; the data points represent all individual trials of all participants with force condition differentiated by color. Fig. 9-4B shows the same data averaged across the different force and cane conditions and pooled over all participants. There was no evidence of any change with increasing force ($\beta = -0.000015 \pm 0.0001, p = 0.87$). The Total-CoP was affected by the canes showing a slightly larger ML sway in the tripod condition ($\beta = 0.0006 \pm 0.0002, p < 0.001$). While different from what we expected in Hypothesis 2, this finding was consistent with previous results: ML variability was significantly attenuated by small forces at the support, and increasing force levels did not further affect sway of the Total-CoP (9, 10).

In contrast, the ML standard deviation of the Feet-CoP decreased with the average force for each trial, as shown in Fig. 9-4C. Fig. 9-4D shows the pooled data of all participants for each experimental condition. For both cane configurations the same

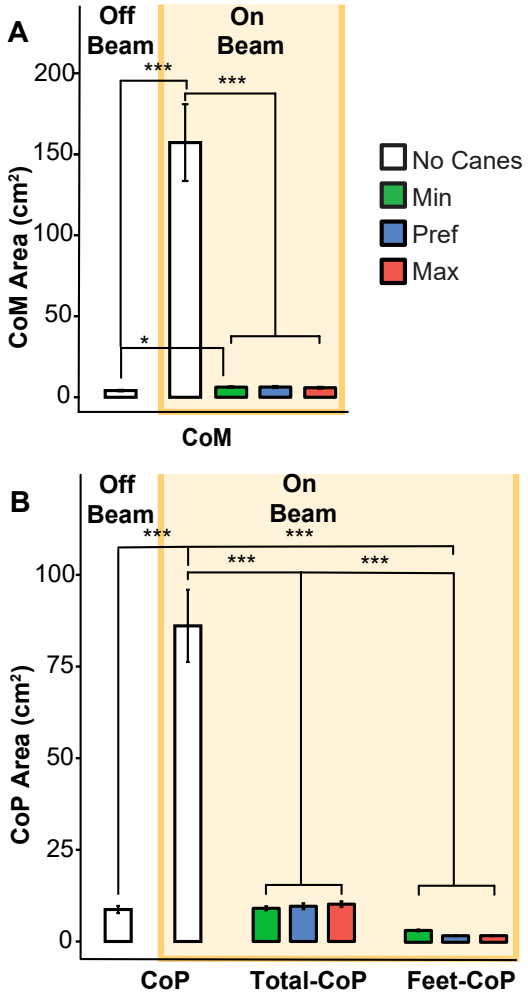

Figure 9-3: Postural sway metrics for the center of pressure (CoP) and center of mass (CoM) for all experimental conditions. The light yellow background indicates metrics for standing on the beam, while the white background on the left shows results for standing on the ground. The colored bars show the metrics when the participants used canes; green, blue and red differentiate the three force conditions. **A**: Area of the center of mass (CoM) quantified by the 95% tolerance ellipse. Each bar shows the mean and standard error (n=16) for the different experimental conditions, pooled over all participants. The white bars on the left show the CoM area when participants stood on the ground and on the beam, without canes; the green, blue and red bars represent the three force conditions. **B**: Area of the center of pressure (CoP, Total-CoP and Feet-CoP) quantified by the 95% tolerance ellipse. Each bar shows the mean and standard error (n=16) for the different experimental conditions, pooled over all participants. The two white bars show the CoP area when participants did not use canes. The lower value of CoP on the left represents the participants standing on the ground; the white bar shows the CoP area when participants stood on the beam. The colored bars show the Total-CoP and the Feet-CoP when the participants used canes. (significance levels: ***: $p < 0.001$; *: $p < 0.05$)

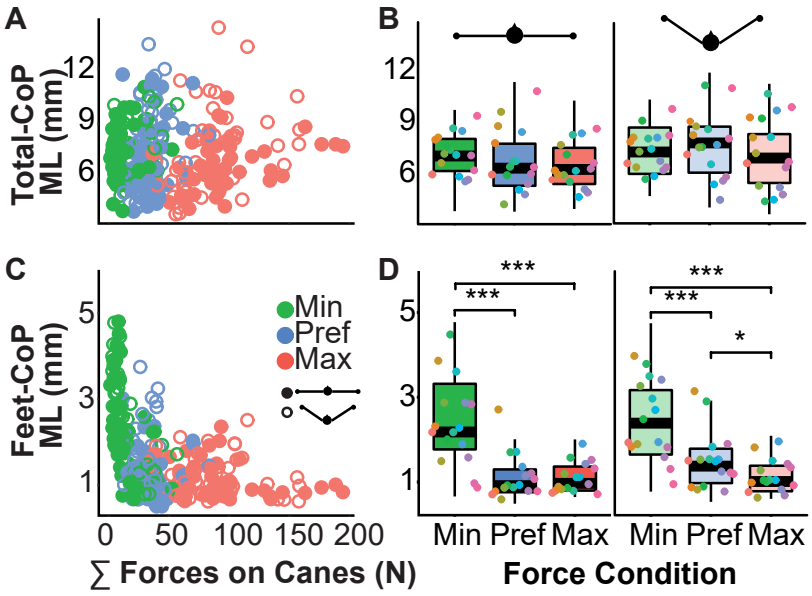

Figure 9-4: Total center of pressure (Total-CoP) and center of pressure at the feet (Feet-CoP) in the medio-lateral (ML) direction for different force conditions. **A**: Mediolateral (ML) component of the Total-CoP motion with respect to the sum of the forces applied on the canes; each data point is the average of one trial. Filled circles represent the planar posture, empty circles the tripod posture. **B**: Standard deviations of the ML-component of the Total-CoP motion for the two postures. Each data point represents one participant; different colors indicate different participants. **C**: ML-Feet-CoP against the sum of the forces applied on the canes for each trial. **D**: The ML component of the Feet-CoP for each force condition and for the two postures. Each data point represents one participant, different colors indicate different participants. (significance levels: ***: $p < 0.001$; *: $p < 0.05$)

trend was observed: applying a force larger than minimum force reduced the sway at the feet ($\beta = -0.0008 \pm 0.00015, p < 0.001$). This indicates that increasing force applied on the canes let subjects rely less on foot-beam interaction and more on canes. The variability in the ML direction for the Feet-CoP was not affected by cane configuration ($\beta = -0.00016 \pm 0.0002, p = 0.45$), indicating that the spatial configuration of the arms was not relevant for the ML direction of the Feet-CoP. This set of results on Feet-CoP is in line with Hypothesis 2, although the Total-CoP did not show any effect on sway variability with force.

9.3.5 Effect of Forces on Postural Balance in the AP Direction

The standard deviations of both Feet-CoP and Total-CoP were also compared in the AP direction, i.e., along the beam length. Fig. 9-5 shows that applying different levels of force did not affect AP variability neither in Feet-CoP ($\beta = 0.0003 \pm 0.0002, p = 0.29$) nor Total-CoP ($\beta = 0.0002 \pm 0.0002, p = 0.37$). However, AP variability was larger in the tripod condition than the planar condition, both for Feet-CoP and Total-CoP (Feet-CoP: $\beta = 0.002 \pm 0.0007, p < 0.01$; Total-CoP: $\beta = 0.002 \pm 0.0004, p < 0.001$). This confirmed that the tripod cane condition allowed for more variability along the length of the beam and that participants actually exploited this extended base of support (Hypothesis 3).

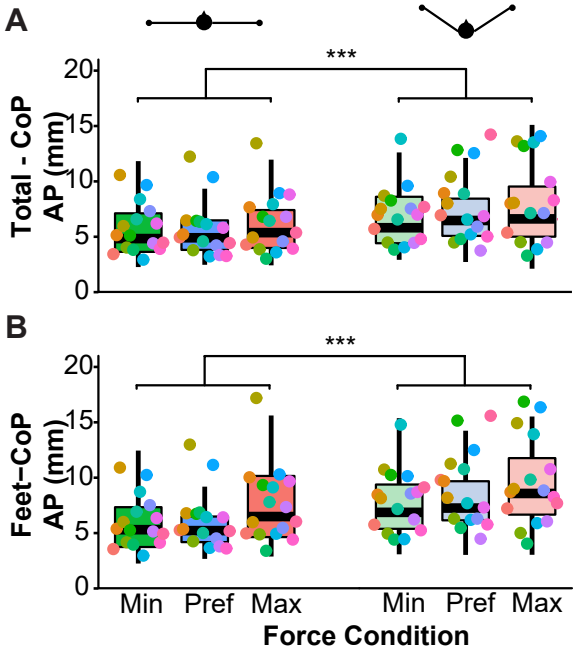

Figure 9-5: Total center of pressure (Total-CoP) and center of pressure at the feet (Feet-CoP) in the Antero-Posterior (AP) direction for different cane conditions. **A**: Standard deviations of the AP-component of the Total-CoP motion for the two cane configurations. Data are pooled together within each force condition. Each data point represents one participant; different colors indicate different participants. **B**: The AP component of the Standard Deviation of the Feet-CoP for each force condition and for the two cane conditions. Each data point represents one participant, different colors indicate different participants (*** indicates significance of $p < 0.001$).

9.3.6 Effect of Forces on Variability of Cane Motion

Even though participants were instructed to stand still, some small movements in the body, arms, and hands were always present [55]. This noise inevitably transferred from the hand to the cane handle, deflecting the cane from the vertical position. As a cane is an inverted pendulum, small lateral deflections destabilize the vertical cane. To quantify these deflections, the path length of the hand on the cane handle was computed for each trial. Fig. 9-6A shows the paths traveled by the right and left hands of one participant over the course of one trial in each force condition (marked by color). The path length of the hand increased when more force was applied (right cane: $\beta = 0.006 \pm 0.001, p < 0.001$; left cane: $\beta = 0.006 \pm 0.001, p < 0.001$). Fig. 9-6B shows path lengths of all participants, plotted against the average force applied on the respective cane; each point represents the path length traveled by the right or left hand during one trial. It shows that the path length increased with the amount of force applied. Path length in the minimum force condition was significantly different from the maximum force condition for both hands (right hand: $p < 0.001$, left hand: $p < 0.001$). The preferred force condition was not significantly different from the minimum force condition for the right hand ($p = 0.09$) and only barely significant for the left hand ($p < 0.05$). These results suggest that higher forces indeed had a destabilizing side-effect as expected (Hypothesis 4).

9.4 Discussion

The present study tested the mechanical effects of cane support in a challenging balance task. While standing on a narrow beam, the use of canes improved postural balance as evidenced by the reduced variability of the center of pressure (CoP) and the center of mass (CoM); these fluctuations declined to the same level as when standing on the floor. This reduction of sway was observed for all force levels, even for relatively small forces applied to the two canes. When subjects exerted higher forces on the canes, the fluctuations of both the CoM and the total center of pressure (Total-CoP) did not decrease any further. Comparing the two cane configurations,

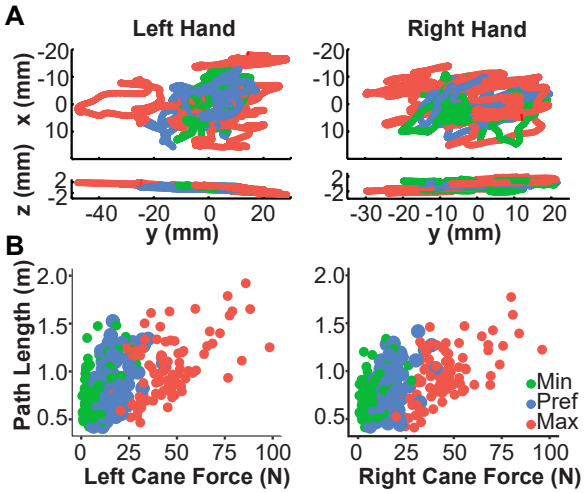

Figure 9-6: Paths and path lengths of the left and right hands for different force instructions differentiated by color. **A**: Exemplary paths of the movements of the left and right hands from two point of view: x-y at the top, z-y below. Each colored line shows one trial in the three force conditions. **B**: Path lengths for the left and right hands per trial are plotted against the average force applied to the cane.

participants clearly used the larger base of support when canes and feet formed a tripod. However, higher forces also destabilized the canes as evidenced by longer hand paths.

9.4.1 Perceptual Benefits of Canes

Numerous previous studies investigated the effect of light touch on postural control and showed that increasing forces applied on a support surface did not provide further benefit to reduce sway [84–87,122,201]. However, the touch condition in previous studies by Jeka and colleagues required subjects to apply a target force of 1 N and in the free force condition they exerted on average 5 N. As the present study wanted to further probe into the mechanical effects of canes on control, our study tested forces from 5 N to 100 N that extended well above the previously tested force conditions. Our results on variability of the Total-CoP and the CoM showed again that, while canes were generally helpful for balance, exerting the maximum level of force on the canes did not provide any further stabilizing effect. In addition, when free to use their preferred force, participants did not choose a high level of force to maintain bal-

ance, presumably because there was no further benefit. Rather, they stayed within a force level that reduced the need to support their arms against gravity. Taken together, these findings corroborated previous studies and supported the widely accepted conclusion that even very light touch provides perceptual information that enhances balance performance, similar to how visual information stabilizes postural sway [158]. Hence, at first blush, these results seem to support the conclusion that the mechanical effect of the support was negligible. And yet, from a mechanical perspective, canes on the ground do increase the base of support and that inherently changes the mechanics of the system.

9.4.2 Mechanical Benefits of Canes on Postural Sway

Intuitively, canes should facilitate balance, and evidently they do. What are these mechanical effects and how do they affect demands on postural control? Our data gave several indications that cane support went beyond being purely perceptual support and afforded mechanical benefits. First, as the additional contacts with the floor enlarged the base of support, CoP and CoM went outside the beam width, which limits the base of support without the canes. Therefore, humans indeed used the available larger base of support. Second, while the extent of the fluctuations in CoP and CoM did not depend on the magnitude of forces applied to the canes, they did depend on the placement of the canes. The standard deviations of the Total-CoP and Feet-CoP in the tripod condition were significantly larger than in the planar configuration, indicating that the triangular contact points had a significant influence on control. Third, the Feet-CoP significantly decreased with increasing force on the canes, indicating that the more force applied on the canes, the more did control rely on their support to balance. Fourth, the preferred force applied on each cane corresponded to the weight of the participant's arm; the preferred force corresponded to 5% of average body weight [42]. Hence, this choice of support reduced the effort required to hold one's arms, while exploiting the new mechanical support provided by the additional devices.

9.4.3 Mechanical Challenge due to Instability of the Canes

Applying forces on the vertical canes is an isometric task with potential instability. Unlike in previous studies that tested forces applied on a fixed surface, the canes were not inherently stable; rather, mechanically they presented an inverted pendulum at its unstable equilibrium point. Hence, the inherent noise in the human sensorimotor system can introduce displacements that immediately destabilize the inverted pendulum, and with it, destabilize postural balance. Assuming that noise increases with force, this destabilizing effect increases with higher forces. It was also shown that applying larger force on an unstable mechanical system induced more mechanical instability [163–165]. On the other hand, human joint stiffness also increases with increasing force which probably counteracted this perturbing effect to maintain postural balance [117]. However, as the observed path lengths of the hand increased with the applied force, the stiffness at the shoulder joint may have been limited and did not fully compensate for the displacements of the hands and canes. And yet, the variability of the CoM and the Total-CoP did not vary with increasing force, indicating that the larger displacements at the hand may have been compensated at the torso. Hence, these findings reveal that the cane support not only facilitated balance, but also created complex control demands across the multi-segmented body.

9.4.4 Underlying Control Mechanisms

All together, these results present an intricate picture of how the canes significantly affected the control of postural stability, some effects even cancelling each other. What are the potential control mechanisms underlying these observations? To begin, when standing on the beam with canes, the variability of the CoM and Total-CoP in the ML or task-relevant direction were essentially identical to those when standing on the ground. If the measured fluctuations when standing on the ground are regarded as a measure of the noise level (as participants were asked to stand as still as possible), then the use of canes enabled participants to minimize sway all the way to this lower bound. That could also be the reason why the different force levels did not lead to

further reductions in sway. Second, when the canes formed a tripod, the fluctuations of the CoP were larger than in the planar condition, making use of the larger base of support. Especially, the higher variability in the AP direction suggested that the controller did not constrain fluctuations, i.e., allowing more variability in this task-irrelevant direction. Allowing variability in directions orthogonal to what affects the task is usually interpreted as a reduction of control effort [3, 45]. Third, control took advantage of the additional devices, evidenced in the preferred force level that just off-set the weight of the arms while staying away from higher forces that potentially introduced destabilizing effects. In summary, we speculate that the controller avoids high forces not only because they require more effort without any obvious benefit, but also because they introduce additional demands on neuro-muscular stiffness to counteract destabilizing forces. The controller also allows fluctuations as long as the CoM stays within a certain region, whose limits are defined by the margin of the base of support and by the noise of the system.

9.4.5 Limitations and Outlook

In the present study participants used canes to balance on a narrow beam holding them with the arms extended. While this presented a clean geometric body configuration, different mechanisms might be manifest if the canes were held with flexed arms or when walking with one or two canes. Our metrics, ML and AP standard deviations and the total area of sway, could capture interesting features of the task, but they were scalar measures of data distributions. Additional analyses could characterize the temporal evolution of the forces and their relative centers of pressure. Further, recent work went beyond analyzing the point of application of the force vector, and examined the orientation of the ground reaction force with respect to the center of mass. This analysis revealed interesting information about the relative role of biomechanics and control [24, 192]. Applying these methods to the more challenging task of standing on a narrow beam with canes could provide further information about the strategy adopted by the controller when using canes.

9.4.6 Appendix: Intervention for Recovery or Compensation

Fig. 9-7 shows how balance performance (measured by the center of mass sway in medio-lateral (ML) direction, averaged over three trials per condition) varied in each condition. Importantly, pairwise t-tests identified no significant difference ($p > 0.05$) in the balance performance before and after using canes, while subjects were allowed to 'practice' to balance using canes with different force levels. This implies that the improved performance may not be attributed to changes in the neural controller, rather, mainly mechanical effects [79]. This behavioral change is consistent with what observed in Chapter 8, when humans balancing on a beam with wearing rigid soles. In sum, the canes may not be useful for promoting neuro-recovery, but may be useful for compensating for impaired balance.

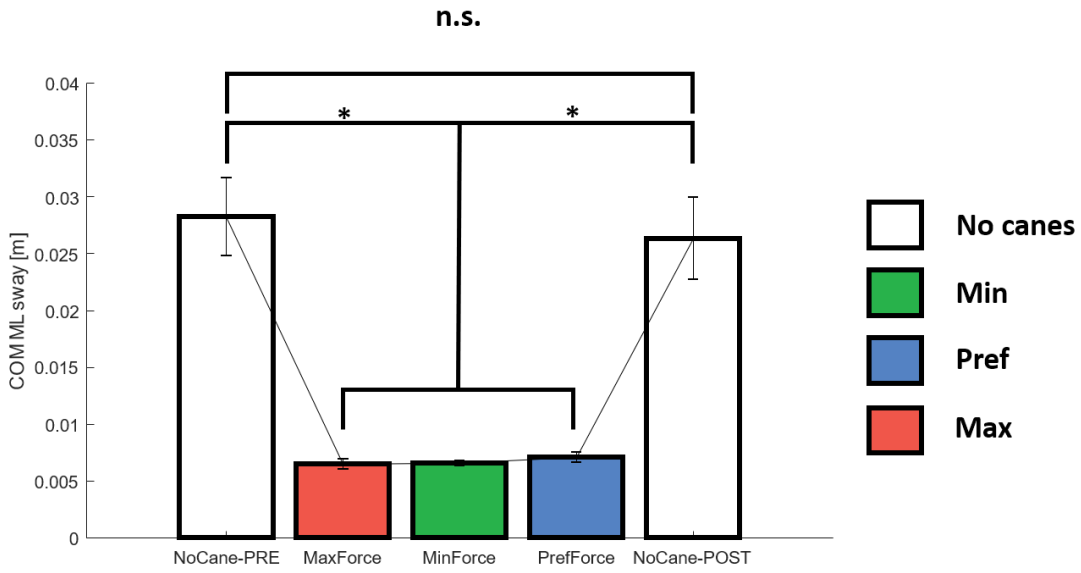

Figure 9-7: No behavioral change before (PRE) and after (POST) using canes. * indicates significant difference between conditions ($p < 0.05$).

Chapter 10

Conclusion

10.1 Summary

We investigated human whole-body coordination during balancing in challenging conditions, analyzed how several passive mechanical interventions altered human balance, and attempted to understand the neuro-mechanical origins of the changes in behavior.

The results found a consistent coordination pattern of humans balancing on a beam, represented by a high anti-correlation between lumped upper- and lower-body angular momentum. Despite differences in gross measures of balance, the coordination pattern was consistent between the novice and expert subjects, suggesting that both performances could be described with the same balance controller. By simulating a double inverted pendulum model utilizing different balancing controllers described in the robotics literature, we identified that the whole-body behavior observed from humans standing on a beam was best replicated with controllers that predominantly utilized hip actuation.

When wearing rigid soles, human balance significantly and immediately improved. Importantly, results suggested that differences in human balancing behavior across different support surfaces may not solely result from changes in their neural control strategy, rather it was largely due to mechanical changes at the foot-ground interface. A simplified model of foot-beam interface was inserted to a double inverted pendulum model for human balancing. This extended model could capture the several aspects

of changes in human behavior across different foot contact conditions (bare feet vs. rigid feet) at least qualitatively.

Similarly, canes significantly reduced the variability of center of pressure and center of mass to the same level as when standing on the ground. Increasing the exerted force beyond the preferred level yielded no further benefits, in fact had a destabilizing effect on the canes: the displacement of the hand on the cane handle increased with the force, consistent with the known effect that pushing destabilizes an inverted pendulum. In the preferred condition, participants exploited the altered mechanics by resting their arms on the canes and, in the tripod configuration, allowing for larger sway. These results suggest that the controller minimizes effort keeping the center of mass and center of pressure within the task-allowed region, whose upper limit is defined by the base of support and lower limit by the noise of the system. Despite the challenge of a statically unstable system, these results show that, in addition to augmenting perceptual information, using canes can provide mechanical benefits.

10.2 Discussion

While both simple and passive mechanical interventions could significantly and immediately improve balance, there was little evidence of behavioral signatures that central neural processes were involved. That is, practice with the devices did not affect performance over time and without the devices. This implies that the tested interventions may not be suitable for training for long-term neuro-recovery, but for compensation, consistent with what we observed and discussed in Chapter 4, when humans walking with a stiffness intervention.

Part III

Quantifying Balance Mechanism without Perturbation

Chapter 11

Overview

Objective and quantitative assessments of human balance is critical to design and follow-up personalized balance training; however, it is as yet largely missing among current clinical methods [147].

In human balance control research community, input-output system identification methods are the most frequently used to identify and estimate human balance models. Despite their mathematical rigor, humans may substantially change their behavior when perturbation is applied - and it is hard to predict how each intervention would change the balance dynamics, as extensively demonstrated in Part I and Part II. The input-output system identification methods require to apply external perturbations - thus they may accurately identify human *reactive* balance, but not normal and daily standing balance.

In this Part, we present two different methods to quantify the normal balancing mechanisms of humans without applying perturbation.

In Chapter 12, we developed a systematic method for identifying dynamics and control of human standing based on force-plate data, motivated by a consistent pattern observed in healthy humans, presented in [24]. Aiming to develop the simplest, competent, and neuromechanically justifiable dynamic model that could account for the pattern, we first explored the minimum number of degrees of freedom required for the model. Then, we exploited the structure of a well-established optimal control theory that was parameterized to maximize physiologically-relevant insight.

In Chapter 13, we explored a mathematically rigorous system identification method to identify the dynamics of human standing based on a time-series of joint motion data. With a biomechanically reasonable model of the multi-joint human body, the method could reliably estimate the state feedback controller. The method was validated using numerical simulations, which established a foundation for experimental studies to identify human balance mechanisms without applying perturbation and without exact information about internal biological noise.

Chapter 12

Frequency-Dependent Force Direction Elucidates Neural Control of Balance

This work was conducted in collaboration with Kaymie Shiozawa (MIT, Newman Lab for Biomechanics and Human Rehabilitation), Prof. Dagmar Sternad (Northeastern University, Action Lab), and Dr. Marta Russo (the same), with insightful input from Prof. Kreg Gruben (University of Wisconsin, Neuromuscular Coordination Laboratory). Kaymie Shiozawa conducted numerical simulation and analyzed the numerical data. I mentored Kaymie, developed simulations, and performed mathematical analysis of the intersection point. Dr. Marta Russo and Prof. Sternad helped frequency analysis and statistical analyses, and provided insightful comments throughout the work.

This work was supported by a Samsung scholarship. This work was also supported by NSF-CRCNS 1724135 awarded to Prof. Neville Hogan and by NSF-CRCNS-1723998 awarded to Prof. Dagmar Sternad.

This work was published in [192].

12.1 Background

Controlling balance during standing and walking is a fundamental necessity for human mobility. Although maintaining upright posture involves little overt movement, its

inherently unstable nature poses an interesting sensorimotor control problem [11, 76, 147, 158].

While many recent studies have investigated reactive balance by applying perturbations to the individual [64, 94, 158, 215], it is also important to understand how humans maintain their balance without external perturbations, i.e., during quiet standing. In particular, the center of pressure and the fluctuations of the center of mass have been commonly used to evaluate balance performance during quiet standing [39, 131]. However, studying the center of mass and/or the center of pressure trajectories alone is insufficient to describe the complex dynamics and control of the multi-segmented human body. Insights can be gained by investigating how humans use the direction of their foot-ground interaction force, which is the outcome of a complex sensorimotor control process that involves timed muscle activity, biomechanical constraints, and sensory feedback from multiple pathways. Importantly, the ground reaction force directly contributes to the centroidal dynamics of the human body [148]. The orientation of the ground reaction force vector and where its line-of-action lies relative to the center of mass may give further insight into how human subjects control the translational motion of the center of mass and net angular motion of the body.

Recently, Gruben and colleagues suggested a new method to study the relation between the orientation of the ground reaction force vector and the center of pressure in human subjects during quiet standing [24, 232]. Net ground reaction forces at different times, which have different orientations and points of application (centers of pressure), intersect at some point in space. The authors defined this point as the intersection point and examined its relation to the center of mass of the standing individual. Because the height of the intersection point relative to the center of mass determines the translational and angular components of centroidal accelerations, it provides a compact geometric representation that is useful for understanding the dynamics and control of human standing balance. When analyzing the force vectors in the frequency domain, this previous study [24] found that the vertical position of the intersection point exhibited a consistent pattern across subjects. With this

observation, the authors suggested that the frequency-dependent intersection point characterizes the neural controller of human balance. However, the biomechanics of upright posture might account for some of the variation of intersection point height across different frequency bands.

This study therefore aimed to elucidate the extent to which the frequency-dependent variation of the intersection point could be attributed to neural control strategies or to biomechanics. To that end, the first objective was to develop the simplest, competent, and neuromechanically justifiable dynamic model that could account for the consistent pattern observed across multiple subjects [24]. Second, we examined the hypothesis that the neural control strategies in standing balance would economize control effort [94]. To test this hypothesis, we took advantage of the Linear Quadratic Regulator (LQR) [197], a well-established optimal control method, that enabled a systematic search of physiologically-plausible controller parameters [76, 99, 210, 211]

12.2 Methods

12.2.1 Human Experiment

Experimental Procedure

In the previous study [24], ten unimpaired, young participants (24.2 ± 10.3 years) were asked to stand quietly while viewing a mark at head height 1 m away. Each participant completed one 50 s trial standing on a 6-axis force-plate measuring at 1000 Hz. The subjects' average mass and height were 71 kg and 1.75 m, respectively.

Intersection Point

The intersection point was defined as a point in space where the net ground reaction force vectors at adjacent time-steps intersect [24], as illustrated in Fig. 12-1. The intersection point is a geometric representation of the relation between the ground reaction force and the center of pressure in human subjects. This point was originally identified with the goal to understand how humans maintain balance during

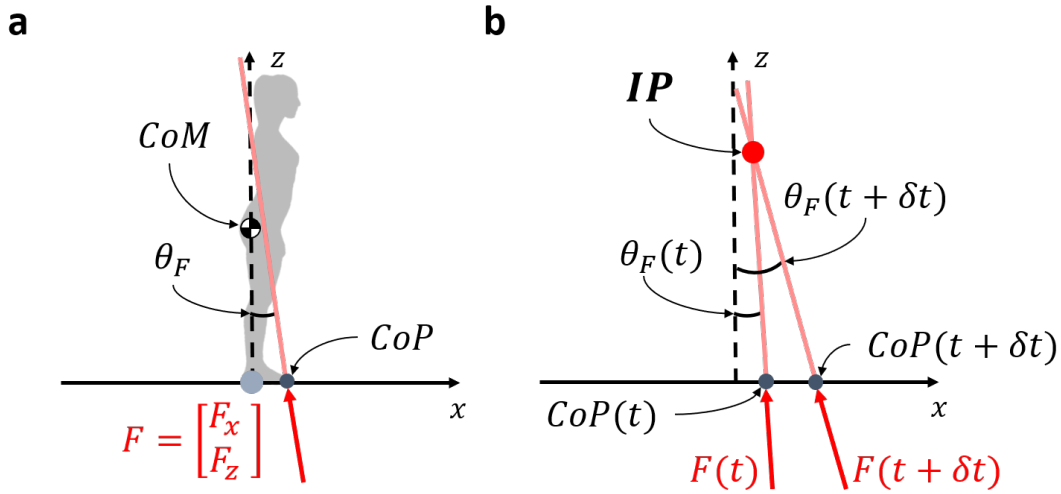

Figure 12-1: **a** A net ground reaction force, F, made up of horizontal and vertical components, F_x and F_z, acts at the center of pressure, CoP, and has an orientation θ_F. The center of mass, CoM, is also shown. **b** Two force vectors from two different time points, which are defined by their respective θ_F and CoP, intersect at the intersection point, IP.

walking [66, 125]; Gruben and colleagues were the first to apply it to understand the mechanics of standing balance [24].

Assuming subtle movements of the body and small variations in ground reaction force orientations, the orientation of the ground reaction force (θ_F) can be approximated as

$$-\frac{F_x}{F_z} = \tan\theta_F \approx \theta_F, \tag{12.1}$$

where F_x and F_z are the horizontal and vertical components of the *net* ground reaction force, respectively.

The height of the intersection point (IP) of two forces at adjacent times ($F(t), F(t+\delta t)$) is

$$IP(t) = \frac{\mathrm{CoP(t)} - \mathrm{CoP(t+\delta t)}}{\theta_F(t) - \theta_F(t+\delta t)},$$

where CoP(t) is the center of pressure at time t.

Frequency-Dependence of the Intersection Point

Investigating the system response in the frequency domain often yields insight into the structure of a dynamic system. To parse the time series into frequency bands, a Hamming window with the length of the entire data set was first applied to both θ_F and CoP signals. θ_F and CoP signals were then bandpass-filtered (zero-lag, 2nd-order Butterworth) and parsed into bands of 0.2 Hz width centered on frequencies from 0.5 to 7.9 Hz (38 nominally non-overlapping bands). Finally, the principal eigenvector of the best-fit covariance matrix of θ_F plotted against CoP (both signals detrended to have zero-mean) was extracted for each band. Its slope is equivalent to the inverse of the intersection point, as illustrated in Fig. 12-2. This is because, assuming small variation between the forces,

$$\theta_F(t + \delta t) \approx \theta_F(t) + \delta\theta_F(t),$$
$$\mathrm{CoP(t + \delta t)} \approx \mathrm{CoP(t)} + \delta\mathrm{CoP(t)},$$

the lower-order component of the intersection point height (IP) can be approximated as

$$IP \approx \frac{d\mathrm{CoP}}{d\theta_F}, \tag{12.2}$$

and re-arranging (12.2) results in

$$d\theta_F = \frac{1}{IP} d\mathrm{CoP}. \tag{12.3}$$

Gruben and colleagues [24] found that the vertical position of the intersection point exhibited a consistent pattern across subjects: it was above the center of mass at low frequencies and decreased as frequency increased, reaching an asymptote below the center of mass at higher frequencies as shown in Fig. 12-4a in the results section.

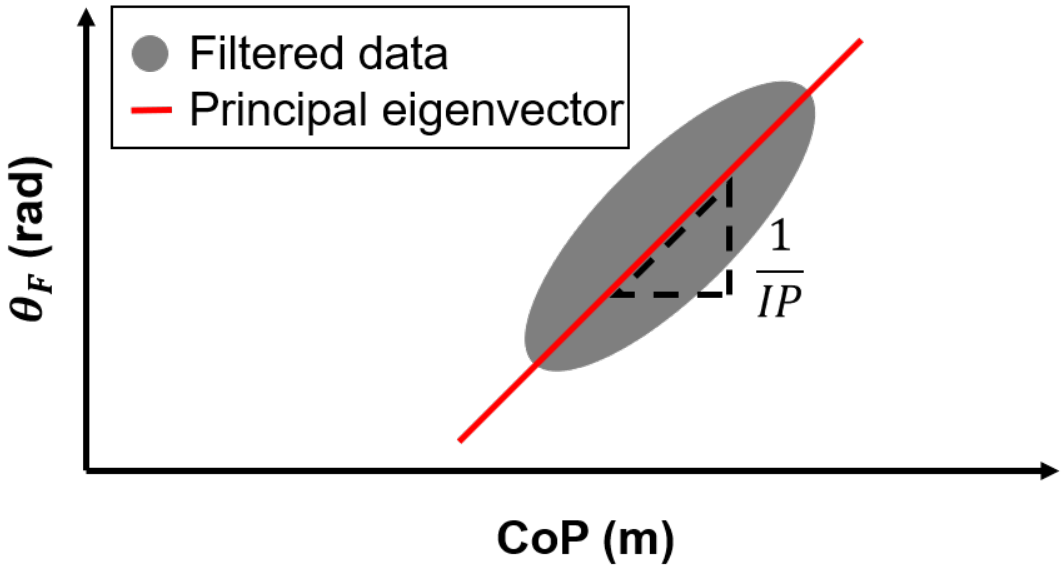

Figure 12-2: Relation between θ_F and CoP for one simulation trial. The data were processed by filtering the CoP and θ_F signals using a 2nd-order bandpass filter with a 0.2 Hz wide frequency band. The principal eigenvector of the covariance matrix of the filtered data was extracted. The intersection point (IP) was computed as the inverse of the angle of the principal eigenvector. Note that the time series of the data was approximated as an ellipse in this schematic illustration.

12.2.2 Simulation

Single Inverted Pendulum Model

We first investigated whether a single inverted pendulum, which is a widely accepted model for human quiet standing [147], could reproduce the experimental observations. Theoretical analysis showed that the model could not adequately reproduce the experimental observation in [24], because the intersection point height of the single inverted pendulum was always above the center of mass (Appendix 12.6). Hence, a multi-degree-of-freedom model was required.

Double Inverted Pendulum Model

The double inverted pendulum model that was used to simulate a multi-segmented human body is illustrated in Fig. 12-3. The lumped model parameters summarized in Table 12.1 used the anthropometric distribution of male subjects in the sagittal

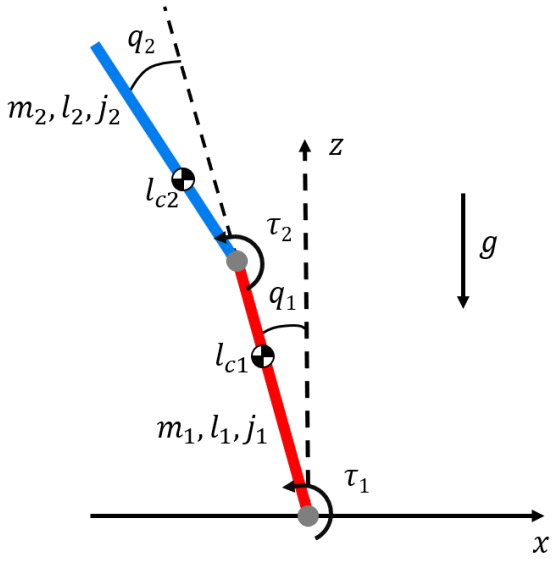

Figure 12-3: Double inverted pendulum model with angle (q_i) and torque (τ_i) conventions and parameter values for mass (m_i), length (l_i), center of mass (l_{ci}), and moment of inertia about the center of mass (j_i). The direction of gravity (g) is also defined.

plane [42] based on the average height and weight of the subjects from [24]. Any mass and length below the ankle was neglected, as the simulation assumed the ankle to be a pin joint. The center of mass positions were measured with respect to the ankle joint for link 1 and the hip joint for link 2. The moments of inertia were calculated about the center of mass of each link.

Table 12.1: Lumped Model Parameters

Symbol	**Parameter (units)**	**Value**	
		Link 1 Lower Body	**Link 2** Upper Body
m	**Mass** (kg)	26.30	42.88
l	**Length** (m)	0.867	0.851
l_c	**Center of mass**(m)	0.589	0.332
j	**Moment of inertia** (kgm^2)	1.400	2.227
g	**Gravitational acceleration** (m/s^2)	9.81	

The equations of motion of the double inverted pendulum were

$$\mathbf{M}(\mathbf{q})\ddot{\mathbf{q}} + \mathbf{C}(\mathbf{q}, \dot{\mathbf{q}})\dot{\mathbf{q}} + \mathbf{G}(\mathbf{q}) = \boldsymbol{\tau}, \tag{12.4}$$

where $\mathbf{M}(\mathbf{q}) \in \mathbb{R}^{2\times2}$ is the inertia matrix, $\mathbf{C}(\mathbf{q}, \dot{\mathbf{q}}) \in \mathbb{R}^{2\times2}$ contains the Coriolis and centrifugal terms, $\mathbf{G}(\mathbf{q}) \in \mathbb{R}^{2\times1}$ are gravitational torques, and $\boldsymbol{\tau} = [\tau_1, \tau_2]^T \in \mathbb{R}^{2\times1}$ is the joint torque vector (see Appendix 12.7 for full symbolic inertia, centrifugal, and gravitational matrices). Generalized coordinates are $\mathbf{q} = [q_1, q_2]^T \in \mathbb{R}^{2\times1}$ as defined in Fig. 12-3. These variables represent the sagittal plane angular displacements of the ankle and hip joints respectively.

Defining the state vector as $\mathbf{x} = [\mathbf{q}^T, \dot{\mathbf{q}}^T]^T$, (12.4) can be rewritten in state-determined form as

$$\dot{\mathbf{x}} = \begin{bmatrix} \dot{\mathbf{q}} \\ -\mathbf{M}(\mathbf{q})^{-1}(\mathbf{C}(\mathbf{q}, \dot{\mathbf{q}})\dot{\mathbf{q}} + \mathbf{G}(\mathbf{q})) + \boldsymbol{\tau} \end{bmatrix}. \tag{12.5}$$

The internal perturbations that cause persistent sway in quiet standing were simulated by additive noise,

$$\boldsymbol{\tau} = \boldsymbol{u} + \mathbf{w}, \tag{12.6}$$

where $\boldsymbol{u} = [u_1, u_2]^T$ are the ankle and hip torques that stabilize the body. In this study, we assumed the noise $\mathbf{w} \in \mathbb{R}^{2\times1}$ was white, mutually uncorrelated, and followed a zero-mean Gaussian distribution with covariance matrix $E\{\mathbf{w}\mathbf{w}^T\} = diag\{\sigma_1^2, \sigma_2^2\}$. The relative strength of the two noise sources was defined as $\sigma_r = \sigma_1/\sigma_2$, where σ_1 and σ_2 are the noise at the ankle and hip, respectively.

F_x and F_z, the horizontal and vertical components of the ground reaction force, were computed as follows

$$F_x = m\ddot{r}_{CoM,x}, \quad F_z = m(\ddot{r}_{CoM,z} + g),$$

where $m = m_1 + m_2$ is the total mass of the body, $\ddot{r}_{CoM,x}$ and $\ddot{r}_{CoM,z}$ are the horizontal and vertical components of the center of mass acceleration. The center of pressure

was then computed as

$$\text{CoP} = \frac{\tau_1}{\text{F}_z}. \tag{12.7}$$

Linear Quadratic Regulator

This study used a nonlinear model with a linear controller. Hence, the nonlinear equations of motion (12.5) were first linearized about the upright balancing posture at rest ($\mathbf{x}_* = \mathbf{0}$ and $\boldsymbol{\tau}_* = \mathbf{0}$) as follows

$$\dot{\bar{\mathbf{x}}} = \mathbf{A}_{lin}\bar{\mathbf{x}} + \mathbf{B}_{lin}\bar{\boldsymbol{u}} + \mathbf{B}_{lin}\mathbf{w}, \tag{12.8}$$

where $\bar{\mathbf{x}} = \mathbf{x} - \mathbf{x}_* = \mathbf{x}$, $\bar{\boldsymbol{u}} = \boldsymbol{u} - \boldsymbol{u}_* = \boldsymbol{u}$, and $\mathbf{A}_{lin}$ and $\mathbf{B}_{lin}$ are linearized state and input matrices, respectively (see Appendix 12.8 for the linearized state-space matrices).

As normal human standing is evidently stable in the upright position, the LQR method was chosen as it guarantees a stable closed-loop system[1]. The LQR is an optimal linear state-feedback controller that minimizes the quadratic cost function

$$J = \int_0^\infty [\mathbf{x}^T(t)\mathbf{Q}\mathbf{x}(t) + \boldsymbol{u}^T(t)\mathbf{R}\boldsymbol{u}(t)]dt \tag{12.9}$$

to determine control torques

$$\boldsymbol{\tau}_{\text{ctl}} = -\mathbf{K}_{LQR}\mathbf{x}, \tag{12.10}$$

where $\mathbf{K}_{LQR}$ is the optimal control gain matrix found via the LQR procedure. The matrices $\mathbf{Q}$ and $\mathbf{R}$ in (12.9) weight the state and input deviations from zero.

[1]To ensure stability, the state-space matrices $\mathbf{A}_{lin}$ and $\mathbf{B}_{lin}$ must be a controllable pair, the $\mathbf{Q}$ matrix must be symmetric positive semi-definite, and the $\mathbf{R}$ matrix must be symmetric positive definite.

We parameterized the input weighting matrix[2] as

$$\mathbf{R} = \alpha \begin{bmatrix} \beta & 0 \\ 0 & 1/\beta \end{bmatrix}, \tag{12.11}$$

to facilitate exploration of two important features: the relative cost between state deviation and control effort, determined by the parameter α, and the relative magnitude of hip and ankle effort, determined by the parameter β.

When α is large, control effort is reduced to a minimum value required for stability. Thus, with this choice of α, the need to add joint torque limits to the model was eliminated. Additionally, with large α, the resulting closed-loop system has a well-defined behavior (placing its poles at the mirror images of the unstable open-loop poles) that is independent of the state weighting matrix $\mathbf{Q}$. To evaluate the working hypothesis that humans economize effort, the minimal-effort solution was of interest. Consequently, the choice of the state weighting matrix was not critical, and $\mathbf{Q} = I_4$, the identity matrix with dimension 4, was chosen to equally penalize each state's deviation from equilibrium.

When $\beta > 1$, the ankle torque is penalized more heavily than the hip, and vice versa when $\beta < 1$. Since the LQR controller minimizes a quadratic cost function (12.9) to achieve stability, only the symmetric components of $\mathbf{R}$ affect the result. The diagonal values of $\mathbf{R}$ were selected such that the size of the matrix (i.e., the product of its eigenvalues) was always equal to 1 and only the components' ratio affected the results. This choice of parameters also allowed for conclusions to be drawn about the relative penalty on the ankle and hip joints.

[2]The off-diagonal elements were deliberately set to zero to reduce the number of parameters to fit. In human, there is no muscle that spans over the hip and ankle simultaneously, justifying the choice. It is possible that active neural feedback control may yield non-zero off-diagonal terms. If this parameterization fails to reproduce human experimental data, one may add coupling terms to the matrix $\mathbf{R}$.

Simulation Protocol

The simulation was conducted using semi-implicit Euler integration. The initial condition was set to $\mathbf{x}_0 = [0, 0, 0, 0]^T$. Replicating the experimental protocol of Gruben and colleagues [24], each simulation was run for 50 s at 1000 Hz. All simulations were conducted in MATLAB 2020a (Mathworks, Natick MA).

To observe the effect of altering the LQR parameters on the frequency-dependence of the intersection point and to find the simplest model that could reproduce the human data, various parameters were tested using the following procedure. First, the parameter that weights the relative cost of the control input, α, was set to a large value to ensure minimal control ($\alpha > 10^4$). This design choice effectively reduced the number of parameters to two (β and σ_r) as the essential intersection point frequency-dependence (above the center of mass at low frequencies, below at high frequencies) varied little as long as α was sufficiently large. Then the noise ratio, σ_r, was adjusted to produce the best fit at high frequencies while setting $\beta = 1$. Lastly, β was varied to produce the best fit in the frequency range where the intersection point height was approximately equal to the center of mass height. At the same time, it was ensured that the asymptotic behavior and the fit at high frequencies were maintained.

40 trials were conducted for each tested parameter set to enable statistical analysis of the simulated dependence of the intersection point height on frequency.

12.2.3 Comparison of Simulation and Human Experimental Results

When determining the goodness of fit across different model parameter conditions, the average difference of the simulated data and the human subject data from [24] was computed over selected frequency bands by

$$\text{average difference} = \frac{\sum_{i=1}^{N} \text{Human Data}_i - \text{Simulation Data}_i}{N_{band}}, \quad i = 1, 2, ...N_{band}.$$

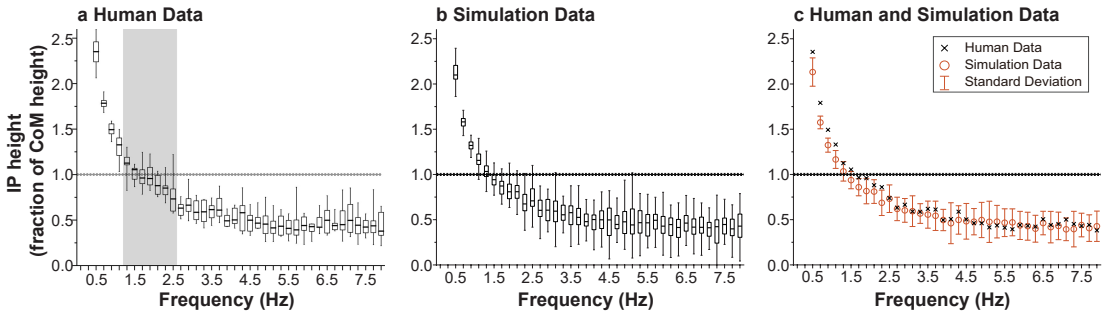

Figure 12-4: Comparison of the intersection point's frequency-dependence from: **a** Human experimental data (reproduced from [24] with permission) and **b** Simulation data with best-fit parameters. **c** The mean of the best-fit simulation data overlaid on the median of the human data from [24]. Within the frequency band from 1.2 – 2.6 Hz for the human data, there was no significant difference (with 95% confidence) between the mean of the intersection point height and the center of mass height. This frequency band is marked by the shaded region. The high-frequency asymptote (3 – 8 Hz range) of the intersection point was 0.479 ± 0.028 and 0.468 ± 0.021 for the human and simulation data, respectively (with 95% confidence).

where Human Data$_i$ is the median of the intersection point height as a fraction of the center of mass height reported by Gruben and colleagues [24] at each frequency band; Simulation Data$_i$ is the average intersection point height as a fraction of the center of mass height across 40 trials of the simulation data in a given frequency band; N_{band} is the number of frequency bands for which the difference in the data was computed. Because balance is characterized by only small motions, a constant center of mass height was assumed.

To identify the onset of the high-frequency asymptote, the human data were fit to an exponential function. The best-fit decay constant was $T \cong 1$ Hz. Assuming the curve reached its asymptote at frequency $\cong 3T$, the asymptote started at 3 Hz. Therefore, the difference between the simulated and experimental asymptote was evaluated at frequencies from 3 to 8 Hz ($N_{band} = 25$). To evaluate the effect of different controller parameters on the frequency range in which the experimentally observed intersection point height crossed the center of mass height, the average difference between simulation and human data was evaluated at frequencies from 1.2 - 2.6 Hz ($N_{band} = 7$). This range encompassed the frequencies in which the observed intersection point height was not statistically different from the center of

mass height in human subject experiments [24]. One-sample t-tests were used to evaluate the difference between the center of mass height and the simulated mean intersection point height. The 95% confidence interval of the mean of the difference was computed as well.

12.3 Results

12.3.1 Minimum Required Model Complexity

Theoretical analysis showed that a single-degree-of-freedom inverted pendulum model could not reproduce the experimental observation in [24]. The intersection point height of a single inverted pendulum model was always above the center of mass for any selection of parameters (Appendix 12.6). Hence, we proceeded with a double inverted pendulum, i.e. with two degrees of freedom, to approximate the multi-segmented human body.

12.3.2 Best-Fit Model Parameter Set

The simulated center of mass height did not deviate far from 0.97 m, the height of the center of mass when perfectly upright, justifying the assumption of small angular displacement. In what follows, the center of mass height was therefore assumed to be constant.

The simulated frequency-dependent intersection point response for the parameter set, $\alpha = 10^6$, $\beta = 0.3$, $\sigma_r = 0.9$, best matched the human subject data from [24] as shown in Fig. 12-4. Both simulations and human experimental results show that the intersection point height crossed the center of mass height in similar frequency bands (1.2 – 2.6 Hz) and had similar asymptotes at higher frequencies. The difference compared to human data for this parameter set was 0.101 ± 0.040 in the 1.2 – 2.6 Hz range and 0.011 ± 0.019 in the 3 – 8 Hz range (both within the 95% confidence interval).

12.3.3 Varying Model Parameters

Varying the simulation parameters affected both the frequency at which the intersection point crossed the height of the center of mass and the high-frequency asymptote. The effect of changing parameter values is presented in Fig. 12-5a, 12-5b, and 12-5c. The differences between simulation and human data for certain parameter sets are shown in Fig. 12-5d and 12-5e.

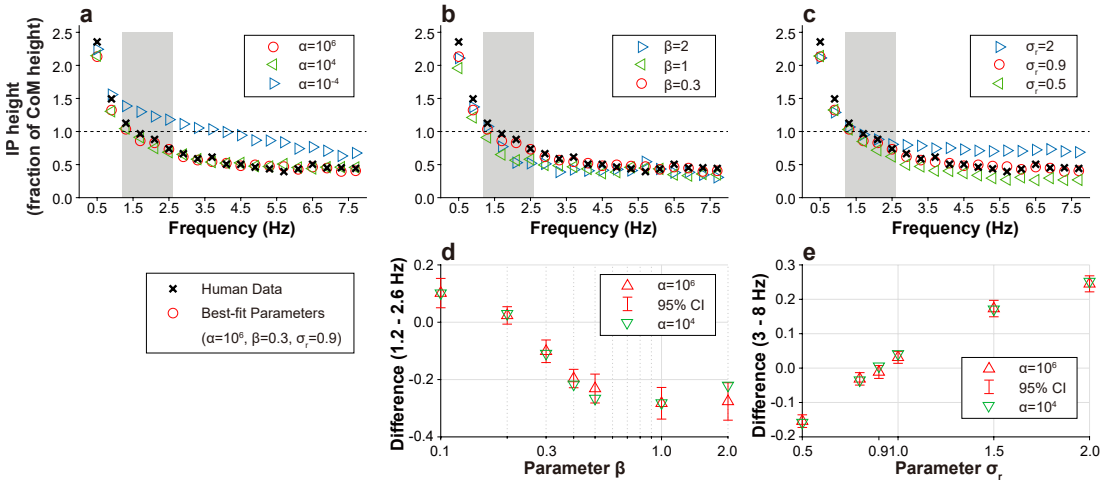

Figure 12-5: Effect of varying parameter values on the frequency-dependence of the intersection point. Each model parameter was varied with respect to the "best-fit" parameter set that closely resembled human subject data observed in [24] ($\alpha = 10^6$, $\beta = 0.3$, $\sigma_r = 0.9$). The height of the center of mass is indicated by a dashed line. The shaded region, based on human experiments, indicates the frequency band in which the mean of the intersection point height was not significantly different from the center of mass height in [24]. **a** The parameter α determined the cost of the overall magnitude of the control effort relative to state deviation from equilibrium. When varying α, the other parameters were set to $\beta = 0.3$ and $\sigma_r = 0.9$. **b** The parameter β determined the relative cost of ankle and hip torque. When $\beta > 1$, there was more penalty on ankle torque. When varying β, the other parameters were set to $\alpha = 10^6$ and $\sigma_r = 0.9$. **c** The parameter σ_r determined the relative strength of noise in the ankle and the hip. When $\sigma_r > 1$, ankle noise was greater than hip noise. When varying σ_r, the other parameters were set to $\alpha = 10^6$ and $\beta = 0.3$. **d** The difference of the intersection point in the 1.2 – 2.6 Hz frequency range of the simulated data compared to the human subject data [24] with respect to β. The parameter σ_r was kept at 0.9. **e** The difference of the intersection point in the 3 – 8 Hz frequency range of the simulated data compared to the human subject data [24] with respect to σ_r. The parameter β was kept at 0.3. In both cases, the effect of varying α is also shown. The error bars indicate the 95% confidence interval of the mean of difference when $\alpha = 10^6$.

Effect of α

As shown in Fig. 12-5a, when α, the weighting of control effort relative to state deviation, was increased, the intersection point crossed the center of mass at lower frequencies. For example, when α was varied from 10^{-4} to 10^{6}, the frequency at which the intersection point crossed over the center of mass moved from 3.9 Hz to 1.5 Hz. As expected from theory, when α was relatively large ($\alpha > 10^{4}$), there was little effect of varying its value on the difference between human and simulation data for different model parameter sets, as shown in Fig. 12-5d and 12-5e.

Effect of β

As in Fig. 12-5b, when β was decreased, i.e. when hip control was penalized more than ankle control, the intersection point crossed the center of mass at higher frequencies. For example, when β was varied from 1 to 0.3, the frequency at which the intersection point crossed over the center of mass moved from 1.1 Hz to 1.5 Hz. In Fig. 12-5d, $\beta = 0.2$ was shown to be the parameter with the smallest difference (0.024) in the 1.2-2.6 Hz range when $\alpha = 10^{6}$. However, both the selection of $\beta = 0.2$ and $\beta = 0.1$ sacrificed the high-frequency fit, increasing the absolute value of the difference in that range by 0.102 and 0.292, respectively, compared to $\beta = 0.3$ when $\alpha = 10^{6}$. As β deviated from $\beta = 0.3$, the absolute value of the difference in the 1.2 – 2.6 Hz range increased by 0.181 when $\beta = 1$ and $\alpha = 10^{6}$.

Effect of σ_r

Adjusting σ_r shifted the high frequency asymptote (3 – 8 Hz) of the intersection point, as shown in Fig. 12-5c. Variation of the high-frequency asymptote of the intersection point height was predicted by the analysis presented in Appendix 12.9. Here, the two extremes, zero noise in the ankle ($\sigma_r = 0$) and the hip ($\sigma_r = \infty$), provided lower and upper bounds for the high frequency asymptote. When compared to the best-fit height of the intersection point at high frequencies, the asymptote was 55% higher when $\sigma_r = 2$ (more noise in the ankle) and 30% lower when $\sigma_r = 0.5$ (more noise

in the hip). In Fig. 12-5e, $\sigma_r = 0.9$ is shown to be the best-fit parameter with the smallest difference value, at -0.011 when $\alpha = 10^6$. As σ_r deviated from the best-fit value, the difference increased to 0.245 when $\sigma_r = 2$ and to -0.154 when $\sigma_r = 0.5$, when $\alpha = 10^6$.

12.4 Discussion

This study analyzed a deliberately simplified model of human quiet standing with a stabilizing linear optimal controller to better understand the origin of the frequency-dependent intersection point reported by Boehm et al [24].

The simplest competent model required two degrees of freedom (ankle and hip) with a stabilizing controller that used minimal control effort and more ankle torque than hip torque. We successfully identified a narrow range of parameters that provided not only a quantitative reproduction of experimental observations, but also qualitative insight.

12.4.1 Neural Control or Biomechanics?

Despite the biomechanical constraints that limit the admissible center of mass accelerations and the centers of pressure [99, 101], the ground reaction force options to comply with these constraints are infinite [50, 66]. Beyond the obvious fact that the musculo-skeletal system is inherently unstable without a neural controller, we should not expect mechanics alone to determine the intersection point's frequency dependence. When Gruben and colleagues [24] analyzed the frequency dependence of the intersection point, they observed a consistent trend across multiple subjects and suggested that this consistency was the signature of a neural controller employed by humans during balance.

The results of our simulations replicated the frequency dependence of the intersection point reported for human standing in the sagittal plane—the intersection point was above the center of mass at low frequencies and below the center of mass at high frequencies, as shown in Fig. 12-4.

To understand the general frequency-dependent trend of the intersection point, first consider an extreme case at very low frequencies where the two-degree-of-freedom pendulum behaves similar to a single rigid body: its intersection point would be above the center of mass, like that of the single inverted pendulum (Appendix 12.6). A double inverted pendulum can also be stabilized solely by hip torque, i.e. zero ankle torque. In the latter case, the system would exhibit higher frequency behavior while maintaining the intersection point height to be zero (from (12.7) and (12.2) with $\tau_1 = 0$). This indicates that the general trend for the intersection point to be above the center of mass at low frequencies and below at high frequencies may be a consequence of biomechanics, i.e. a double inverted pendulum stabilized about upright posture.

However, biomechanics cannot account for the specific details of the frequency variation of the intersection point height. Somewhere between the low-frequency and high-frequency regimes, the intersection point must cross from above to below the center of mass height; this particular crossing point is not specified by biomechanics. Similarly, biomechanics does not dictate the asymptote to which the intersection point height converges at high frequencies. In fact, both the intersection point's asymptote and the frequency at which the intersection point height crossed that of the center of mass varied substantially across the tested parameter values. Only a small set of model parameters could replicate human behavior. Therefore, we conclude that the details of the profile of intersection point height with frequency reflect a neural control strategy used by humans during quiet stance.

12.4.2 Physiologically-Plausible Best-Fit Parameters

The main contribution of this work is to deploy a deliberately-simplified mathematical analysis to elucidate how experimental observations of the frequency-dependence of the intersection point may inform the neural control of balance. To conduct this quantitative analysis, the model parameters were systematically varied such that the simulated intersection point frequency-dependent response closely replicated human data. To facilitate analysis, we took advantage of the LQR procedure and its well-

known properties.

Selecting $\alpha = 10^6$ yielded the best-fit result compared to human data, suggesting that a double inverted pendulum model with minimal control effort can successfully account for the frequency-dependent intersection point response observed in humans. Though it is widely assumed that humans generally minimize effort, supporting evidence during quiet standing has been sparse. Our results show that the observed variation of intersection point height with frequency implies that humans minimize control effort rather than reduce state deviation during quiet standing. This is consistent with the conclusion of a previous study reporting that the nervous system does not exert more control effort than necessary to stabilize upright balance [94].

Long transmission delays in the neural system pose a risk to stability of the balance controller. To account for this, the continuous feedback loop gain must be effectively zero at high frequencies regardless of variations in other model parameters. However, muscle mechanical impedance is not limited in this way; it can respond essentially instantaneously. Behavior in the high frequency range is therefore not likely to depend on neural feedback (defined by α and β), but instead on neuromuscular impedance and noise (defined by σ_r). Hence, the noise ratio, σ_r, was adjusted to fit the high-frequency range before fitting the low-frequency range with β.

Altering the relative noise magnitude in the ankle and the hip torques (σ_r) shifted the high-frequency asymptote of the intersection point height. The simulation result most similar to human experimental data had a $0.9 : 1$ ankle-to-hip noise ratio.

The β value that best described human data [24], 0.3, penalizes hip control effort more than ankle control effort. That is, the system is more likely to use the ankle to maintain upright posture than hip. This is consistent with previous findings that humans primarily use the "ankle strategy" during quiet standing [75, 99, 139, 178].

12.4.3 Single vs. Multi-Joint Model

The observed trend that the intersection point varied with frequency in humans requires multi-segment mechanics (Appendix 12.6). Although the single inverted pendulum model has been widely used to model quiet human standing [93, 133, 135, 147,

158, 226], our finding that a single-segment model cannot adequately describe quiet standing is also consistent with recent literature [68, 94, 159, 176, 180].

Why no more than two degrees of freedom? It is patently obvious that the standing human body has many more degrees of freedom. However, although adding a knee joint [233] or multiple segments of the spine might more accurately replicate human biomechanics, it is unclear whether this would improve the insight to be gleaned from experimental observations. In fact, as shown in Appendix 12.9, the two-segment model yields a high-frequency asymptote for the intersection point height that must lie between zero (corresponding to zero noise at the ankle) and below the center of mass height (corresponding to zero noise at the hip). These two extremes bracket the experimental observations reported by Gruben and colleagues [24]. Thus, the two-segment model used in this study was the simplest that could competently reproduce the experimental results observed by Boehm et al [24].

12.4.4 Intersection Point: A Target Variable of Control or an Emergent Consequence?

In this study, the feedback signal was the state error (joint angles and velocities) rather than the intersection point height. Even so, the control model was able to replicate the frequency dependence of the intersection point found in humans. Hence, it appears that the intersection point may be an emergent consequence of stabilization rather than a variable explicitly regulated by the controller. Consistent with this hypothesis, a previous study suggested that the force direction pattern observed in human walking might be an emergent property rather than a target variable of control [138]. However, further experimentation would be required to test this hypothesis.

12.4.5 Limitations

The simulations conducted in this study assumed simple mechanics. The joint torques in the model are net joint torques that summarize the contributions of various elements, from passive muscle properties to complex neural control. Known features of

neuromuscular physiology such as muscle mechanical impedance, neural transmission delay, or sensory noise were omitted. While these features are unquestionably present, our goal was to identify the simplest model competent to reproduce experimental observations. Despite the lack of muscle- and nerve-level detail, our simulations were able to articulate subtle differences between control parameters that influence the frequency-dependence of the intersection point. Nevertheless, including those neurophysiological features might yield further insight; that is deferred to future work.

This study employed a linear full-state feedback controller with a constant gain matrix (proportional feedback of angle and angular velocity) even though the central nervous system comprises many nonlinear neural elements. This decision was motivated by the observation that the body generates only small motions about the upright posture, justifying the use of a linearized model to obtain feedback controller gains. This observation also justified the choice of additive noise, as higher-order terms that characterize nonlinear noise processes are negligible. We therefore modeled the noise as white. However, some studies have indicated that biological noise may be better described by 'pink' or Brownian noise [216]. Since the low-pass filter property of inertial mechanics suppresses high-frequency components of the spectrum, this noise model proved to be a convenient and viable option.

Finally, the model employed in this study assumed a perfect state estimator. Future studies might assess the effect of including sensory information into the motor controller by employing other control architectures, for instance, using an adaptive [215] or optimal state estimator [99] instead of perfect full-state measurements.

Another important point to highlight is that we do not presume that the central nervous system actually implements the linear regulator used in our model. The LQR design procedure was simply a tool to generate stabilizing controllers while simultaneously analyzing the influence of factors like the cost of control on balance performance.

12.5 Conclusion

This study showed that a double inverted pendulum stabilized by a linear minimal-effort controller could account for the ground reaction force pattern observed in human quiet standing. Numerical simulations also informed the contribution of neural control and biomechanics in generating the pattern observed in human data, i.e. the frequency-dependence of the intersection point. The results suggest that the intersection point conveys quantitative information about human balance control strategies.

This study introduced a method to select optimal control and noise parameters that best reproduced human data. This method might be extended to study human neural control strategies in different contexts, e.g., balance in the frontal plane, balance on a beam, balance with and without assistive devices, or in other populations such as aged or neurologically impaired subjects.

12.6 Appendix 1: Intersection Point of the Single Inverted Pendulum

The intersection point below center of mass at high frequencies observed in human data cannot be reproduced by a single inverted pendulum model. Consider a single inverted pendulum with mass m, center of mass position from the pivot l_c, moment of inertia about pivot j', gravitational acceleration g, and actuated by ankle torque τ. The equation of motion is

$$j'\ddot{q} - mgl_c \sin q = \tau = u + w, \tag{12.12}$$

where q is the angular displacement of the ankle joint with respect to the upright equilibrium posture, u is the control torque, and w is the additive actuation noise. For small motion typical of quiet standing, linearization of (12.12) is well justified:

$$j'\ddot{q} - mgl_c q = \tau.$$

As introduced in (12.3), the intersection point is defined in terms of the orientation of the force, θ_F, and the center of pressure, CoP:

$$\theta_F = -\frac{F_x}{F_z} \approx \frac{ml_c\ddot{q}}{mg} = \frac{l_c}{g}\ddot{q}, \quad CoP = \frac{\tau}{F_z} \approx \frac{\tau}{mg} = \frac{j'}{mg}\ddot{q} - l_c q.$$

Taking the Laplace transform:

$$\Theta_F(s) = \frac{l_c}{g}s^2 Q(s), \quad COP(s) = (\frac{j'}{mg}s^2 - l_c)Q(s),$$

where s is a complex variable, $Q(s)$, $\Theta_F(s)$, and $COP(s)$ are the Laplace transforms of q, θ_F, and CoP, respectively. Denote $H(s) = Q(s)/W(s)$, the transfer function from input noise to output motion, where $W(s)$ is the Laplace transform of w. To investigate the intersection point at high frequency, consider $s = i\Omega$ where $i^2 = -1$ and $\Omega \to \infty$. As the first term of $COP(s)$ dominates, $\Theta_F(s)$ and $COP(s)$ have the same phase. Then, the variation of two output variables will be linear at high frequencies and the intersection point can be determined from the ratio of magnitudes of the two outputs:

$$IP(\Omega) = \frac{|COP(i\Omega)|}{|\Theta_F(i\Omega)|} = \frac{\frac{j'}{mg}\Omega^2 + l_c}{\frac{l_c}{g}\Omega^2} = \frac{j'\Omega^2 + mgl_c}{ml_c\Omega^2}.$$

As $\Omega \to \infty$,

$$IP(\Omega) \to \frac{j'}{ml_c} = \frac{j + ml_c^2}{ml_c^2} = l_c + \frac{j}{ml_c} > l_c.$$

Note that the centroidal moment of inertia is $j = j' - ml_c^2$. Therefore, the intersection point height must be greater than the center of mass height. The single inverted pendulum model cannot explain the intersection point behavior observed in human studies.

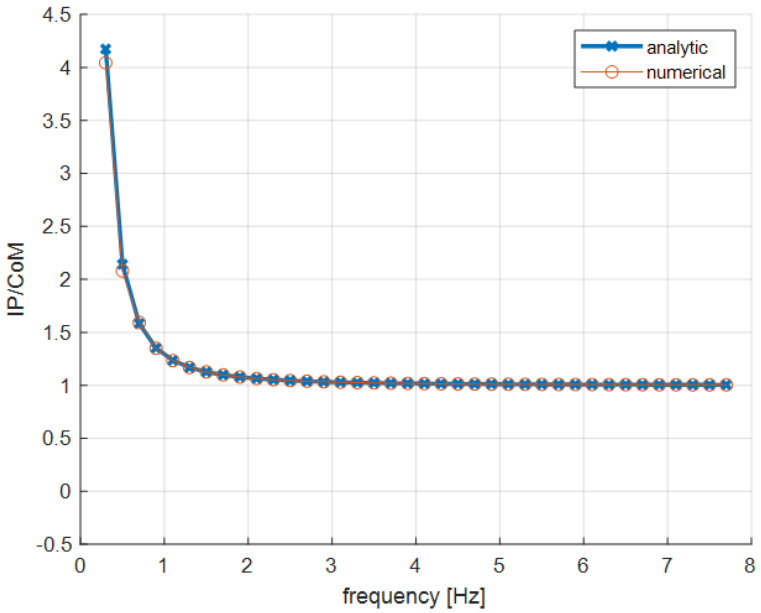

Figure 12-6: Single DoF model cannot have IP below CoM at any frequency.

12.7 Appendix 2: Nonlinear Model Equations

The equations of motion of the double inverted pendulum are expressed in (12.4). Note that the choice of generalized coordinates, q_1, q_2, are consistent with the generalized forces (torques) that are applied. The following details each component of the matrices in terms of the variables in Table 12.1. j_1' and j_2' denote moment of inertia taken about ankle and hip joints, respectively. l_{c1} is the distance from the ankle joint to the center of mass of link 1, and l_{c2} is the distance from the hip joint to the center of mass of link 2. $\cos(q_i)$ and $\sin(q_i)$ are replaced with c_i and s_i, respectively. Setting $\theta_2 = q_1 + q_2$, $\cos(\theta_2)$ and $\sin(\theta_2)$ are replaced with c_{θ_2} and s_{θ_2}, respectively.

$$\mathbf{M}(\mathbf{q}) = \begin{bmatrix} j_1' + j_2' + m_2(l_1^2 + 2l_1 l_{c2} c_2) & j_2' + m_2 l_1 l_{c2} c_2 \\ j_2' + m_2 l_1 l_{c2} c_2 & j_2' \end{bmatrix}$$

$$\mathbf{C}(\mathbf{q}, \dot{\mathbf{q}}) = m_2 l_1 l_{c2} s_2 \begin{bmatrix} -2\dot{q}_2 & -\dot{q}_2 \\ \dot{q}_1 & 0 \end{bmatrix}$$

$$\mathbf{G}(\mathbf{q}) = -g \begin{bmatrix} m_1 l_{c1} s_1 + m_2(l_1 s_1 + l_{c2} s_{\theta_2}) \\ m_2 l_{c2} s_{\theta_2} \end{bmatrix}$$

The ground reaction forces are computed from the motion of the center of mass, $\mathbf{r}_{CoM}(\mathbf{q}) \in \mathbb{R}^{2\times 1}$. The acceleration of the center of mass was computed as

$$\ddot{\mathbf{r}}_{CoM} = [\ddot{r}_{CoM,x}, \ddot{r}_{CoM,z}]^T = \begin{bmatrix} \dot{\mathbf{J}}_{CoM} & \mathbf{J}_{CoM} \end{bmatrix} \dot{\mathbf{x}}. \tag{12.13}$$

$\mathbf{J}_{CoM} \in \mathbb{R}^{2\times 2}$ is the Jacobian of the center of mass with respect to the joint angles $\mathbf{q}$ and $\mathbf{x} = [\mathbf{q}, \dot{\mathbf{q}}]^T$ is the state vector.

The Jacobian matrix and its derivative are given as follows:

$$\mathbf{J}_{CoM} = - \begin{bmatrix} \mathbf{J}_{CoM,1} & \mathbf{J}_{CoM,2} \end{bmatrix}$$

and

$$\dot{\mathbf{J}}_{CoM} = \begin{bmatrix} \dot{J}_{CoM,(1,1)} & \dot{J}_{CoM,(1,2)} \\ \dot{J}_{CoM,(2,1)} & \dot{J}_{CoM,(2,2)} \end{bmatrix},$$

where

$$\mathbf{J}_{CoM,1} = \begin{bmatrix} M_1 l_{c1} c_1 + M_2(l_1 c_1 + l_{c2} c_{\theta_2}) \\ M_1 l_{c1} s_1 + M_2(l_1 s_1 + l_{c2} s_{\theta_2}) \end{bmatrix},$$

$$\mathbf{J}_{CoM,2} = \begin{bmatrix} M_2 l_{c2} c_{\theta_2} \\ M_2 l_{c2} s_{\theta_2} \end{bmatrix},$$

$$\dot{J}_{CoM,(1,1)} = M_1 l_{c1} \dot{q}_1 s_1 + M_2(l_1 \dot{q}_1 s_1 + l_{c2} \dot{\theta}_2 s_{\theta_2}),$$
$$\dot{J}_{CoM,(1,2)} = M_2 l_{c2} \dot{\theta}_2 s_{\theta_2},$$
$$\dot{J}_{CoM,(2,1)} = -M_1 l_{c1} \dot{q}_1 c_1 - M_2(l_1 \dot{q}_1 c_1 + l_{c2} \dot{\theta}_2 c_{\theta_2}),$$
$$\dot{J}_{CoM,(2,2)} = -M_2 l_{c2} \dot{\theta}_2 c_{\theta_2},$$

and $M_1 = \frac{m_1}{m_1+m_2}$ and $M_2 = \frac{m_2}{m_1+m_2}$.

12.8 Appendix 3: Linearized State-Space Matrices

Linearizing the equations of motion about the stable upright position, we are left with (12.8). The state-space matrices are

$$\mathbf{A}_{lin} = \begin{bmatrix} \mathbf{0} & \mathbf{I} \\ \mathbf{M}^{-1}\frac{\partial \mathbf{G}}{\partial \mathbf{q}} & \mathbf{0} \end{bmatrix}_{\mathbf{x}=\mathbf{x}_*, \boldsymbol{\tau}=\boldsymbol{\tau}_*}$$

$$\mathbf{B}_{lin} = \begin{bmatrix} \mathbf{0} \\ \mathbf{M}^{-1}\mathbf{B} \end{bmatrix}_{\mathbf{x}=\mathbf{x}_*, \boldsymbol{\tau}=\boldsymbol{\tau}_*},$$

where

$$\left.\frac{\partial \mathbf{G}}{\partial \mathbf{q}}\right|_{\mathbf{x}=\mathbf{x}_*} = -g \begin{bmatrix} m_1 l_{c1} + m_2(l_1 + l_{c2}) & m_2 l_{c2} \\ m_2 l_{c2} & m_2 l_{c2} \end{bmatrix}$$

and $\mathbf{B} = \mathbf{I}_2$.

12.9 Appendix 4: Intersection Point of the Linearized Double Inverted Pendulum

Noting (12.1) and (12.7), consider two outputs $\mathbf{y} = [y_1, y_2]^T$: $y_1 = -F_x = -m\ddot{r}_{CoM,x}$, $y_2 = \tau_1$. From (12.13), $y_1 = -m[1,0]\ddot{\mathbf{r}}_{CoM} = -m[1,0][\dot{\mathbf{J}}_{CoM}, \mathbf{J}_{CoM}]\dot{\mathbf{x}} \triangleq \mathbf{J}_{y_1}\dot{\mathbf{x}}$. Then, linearized output equations can be obtained as

$$\mathbf{y} = \mathbf{C}\mathbf{x} + \mathbf{D}\boldsymbol{\tau} = \begin{bmatrix} \mathbf{C}_1 \\ \mathbf{C}_2 \end{bmatrix} \mathbf{x} + \begin{bmatrix} \mathbf{D}_1 \\ \mathbf{D}_2 \end{bmatrix} \boldsymbol{\tau},$$

where $\mathbf{C}_1 = \mathbf{J}_{y_1}\mathbf{A}_{lin}, \mathbf{D}_1 = \mathbf{J}_{y_1}\mathbf{B}_{lin}$, evaluated at $(\mathbf{x}, \boldsymbol{\tau}) = (\mathbf{x}_*, \boldsymbol{\tau}_*)$, and $\mathbf{C}_2 = \mathbf{0}, \mathbf{D}_2 = [1, 0]$. With controller $\boldsymbol{\tau} = -\mathbf{K}\mathbf{x} + \mathbf{w}$ as in (12.6) and (12.10), the closed-loop linear

system can be constructed as

$$\begin{cases} \dot{\mathbf{x}} = (\mathbf{A_{lin}} - \mathbf{B_{lin}}\mathbf{K})\mathbf{x} + \mathbf{B_{lin}}\mathbf{w} = \mathbf{A}_{\text{cl}}\mathbf{x} + \mathbf{B_{lin}}\mathbf{w} \\ y_1 = (\mathbf{C}_1 - \mathbf{D}_1\mathbf{K})\mathbf{x} + \mathbf{D}_1\mathbf{w} = \mathbf{C}_{\text{cl},1}\mathbf{x} + \mathbf{D}_1\mathbf{w} \\ y_2 = (\mathbf{C}_2 - \mathbf{D}_2\mathbf{K})\mathbf{x} + \mathbf{D}_2\mathbf{w} = \mathbf{C}_{\text{cl},2}\mathbf{x} + \mathbf{D}_2\mathbf{w}. \end{cases} \tag{12.14}$$

The multi-input, multi-output (MIMO) transfer function can be obtained

$$\mathbf{Y}(s) = \mathbf{H}(s)\mathbf{W}(s), \quad \mathbf{H}(s) = \begin{bmatrix} H_{11}(s) & H_{12}(s) \\ H_{21}(s) & H_{22}(s) \end{bmatrix}$$

where $\mathbf{Y}(s)$ and $\mathbf{W}(s)$ are the Laplace transforms of $\mathbf{y}$ and $\mathbf{w}$, respectively. The intersection point at each frequency can be obtained by the procedure outlined in the methods section, as the inverse of the slope of the principal eigenvector. If $y_1(t)$ and $y_2(t)$ are harmonic, this procedure is equivalent to finding the slope of the major axis of an ellipsoid that the two signals form.

Assuming two harmonic signals $y_i(t)$ with magnitude ν_i and phase ϕ_i at frequency Ω,

$$y_1(t) = \nu_1 \sin(\Omega t + \phi_1), \quad y_2(t) = \nu_2 \sin(\Omega t + \phi_2),$$

and an implicit formula for the ellipsoid can be written in quadratic form,

$$\sin^2\phi = [y_2, y_1] \begin{bmatrix} \frac{1}{\nu_2^2} & -\frac{\cos\phi}{\nu_1\nu_2} \\ -\frac{\cos\phi}{\nu_1\nu_2} & \frac{1}{\nu_1^2} \end{bmatrix} \begin{bmatrix} y_1 \\ y_2 \end{bmatrix}$$

where $\phi = \phi_1 - \phi_2$.

The eigenvector corresponding to the smaller eigenvalue is the major axis and its slope is the inverse of the intersection point as in Fig 12-2.

Consider two extreme cases where the ankle noise is zero ($w_1 = 0$ and $\sigma_r = 0$) and the hip noise is zero ($w_2 = 0$ and $\sigma_r = \infty$). For example, when hip noise is zero,

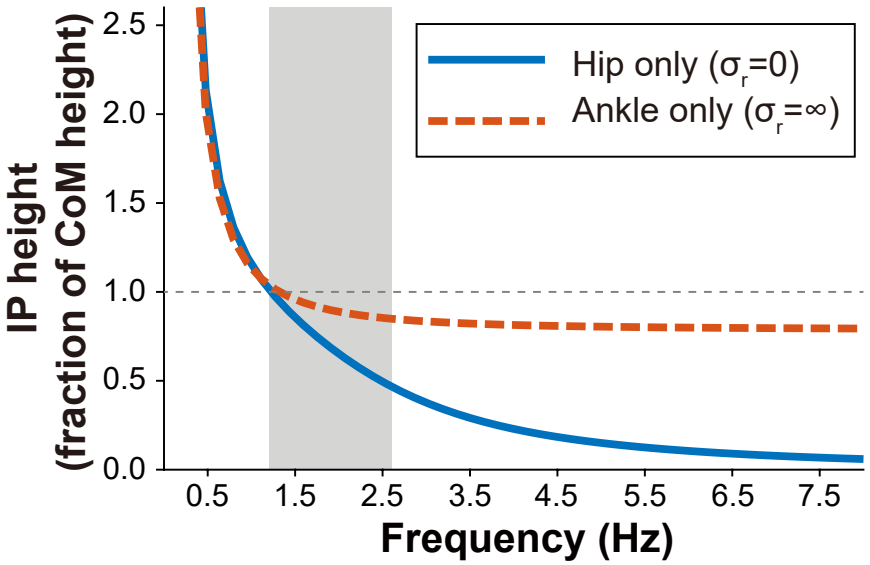

Figure 12-7: Height of the intersection point of the linearized double inverted pendulum model with two extreme σ_r values: $\sigma_r = 0$ (hip noise only) and $\sigma_r = \infty$ (ankle noise only).

substituting $s = i\Omega$,

$$\frac{y_1}{w_1}(i\Omega) = H_{11}(i\Omega), \frac{y_2}{w_1}(i\Omega) = H_{21}(i\Omega)$$

and

$$\nu_1 = |H_{11}(i\Omega)|, \phi_1 = \angle H_{11}(i\Omega),$$
$$\nu_2 = |H_{21}(i\Omega)|, \phi_2 = \angle H_{21}(i\Omega).$$

The intersection point height can be calculated using this method at different frequencies as shown in Fig. 12-7. We numerically validated that the system response with any σ_r is bounded by these two extreme responses. It seems possible to analytically derive the shape of the intersection point, given a feedback controller gain and given noise ratio σ_r, but this is left for future study.

Chapter 13

Identifying human postural dynamics and control from unperturbed balance

This work was conducted in collaboration with Kuangen Zhang (co-affiliated with Southern University of Science and Technology, China and University of British Columbia, Canada; a visiting student at Newman Lab for Biomechanics and Human Rehabilitation, MIT). We worked together to formulate the problem, develop the method, refine the mathematics, and analyze the simulation results.

This research was supported by a Samsung scholarship. This was also supported by the MIT-SUSTech centers for mechanical engineering research and education. Kuangen Zhang was supported in part by funding from the University of British Columbia.

This work was published in [113].

13.1 Background

13.1.1 Previous Studies to Identify Balance

Identifying Dynamics by Perturbing Balance

Studies of human postural control can be broadly classified into two different experimental paradigms: perturbed balance and unperturbed balance [22, 217]. In per-

turbed balance, external perturbations are applied to challenge participants' balance, e.g. by applying pushing/pulling forces or translating/rotating a platform on which they stand. Those perturbations have traditionally been regarded as necessary to identify the dynamics of human postural control, because the input (external perturbation) and output (motion in response to the perturbation) are directly measured, allowing application of well-established closed-loop system identification techniques to obtain a robust and reliable input-output dynamic relation [54, 64, 94, 217]. While insights into sensorimotor control of balance may be gained in this way, it should be noted that humans are notoriously adaptive and are likely to change behavior in response to the applied perturbations [22]. For example, Park et al. [152] showed that postural feedback gains scaled with the magnitude of the applied disturbance. Hence, the closed-loop dynamics and control estimated in this way may not well represent those of daily activity.

Understanding Natural Balance without Perturbations

In contrast, unperturbed balance studies do not apply external perturbation. Instead, the only challenges to individuals' balance arise from internal biological noise in motor and / or sensory systems. The response to this biological noise may be used to investigate humans' natural postural control. Unperturbed balance also includes studies to understand humans' remarkable balance ability in challenging environments, such as on a narrow beam [37, 79, 112, 182]. In these environments, applying external perturbation is often avoided because the environment itself is so challenging that participants may lose balance before enough data has been collected.

Consistent behavioral patterns observed across individuals, represented by descriptive measures such as center of mass or center of pressure motion, suggest strategies to manage complex whole-body balancing in a coordinated manner [24, 37, 39, 79, 112, 131]. While there is no doubt that characterizing behavioral patterns is important, it does not define the postural control strategy [77]. Identifying the controller solely from behavioral features is quite difficult since different controllers may reproduce the same features observed in experiments [112]. On the other hand, it is quite difficult

to apply the system identification techniques which have been widely-employed for perturbed balancing, because the inputs to the system (biological noise) that induce output motion (e.g., sway) in unperturbed balance are *internal* and inaccessible to direct measurement [217]. A reliable system identification method for unperturbed balance would be highly desirable.

13.1.2 Existing Methods

Recently, Ahn and Hogan [7] and Ahn et al. [9] have shown that it is possible to estimate parameters of a noisy, scalar (first-order) dynamical system without external perturbation. Noting that a time series of the dynamical system output can be represented as an autoregressive model of order one, they quantified the bias in estimation based on conventional linear regression methods, then proposed how to compensate for it. Equipped with this revised method, they assessed the gait stability of a model that simulated human walking [7] and, using experimental data, estimated the error-correction gain of a model of human motor learning [9]. Other more classical theories relevant to linear, stationary, white stochastic processes with unknown noise strength have also treated multi-dimensional system parameter identification [13,126,212,234].

13.1.3 Main Contribution

The main contribution of this chapter is to develop and validate a systematic method to identify the closed-loop dynamics of a multi-joint model of unperturbed human balancing. We formulate this problem as identifying a stochastically-excited, linear, finite-dimensional, discrete-time dynamic system. We exploit auto-correlation matrices of the measurements with non-zero time lags to estimate the parameters of the model. The strengths of the noise processes are not required, which is especially important when identifying unperturbed balance which is driven by unknown internal noise. To better understand the key properties of the new method, we first consider a simple scalar dynamic model. Then we present a numerical example of a model that simulates human upright balancing and show that its dynamics can

be identified accurately. Assuming the dynamic structure of a stochastically-excited double-inverted-pendulum model, a state feedback controller can also be identified. Conversely, comparable parameters estimated using conventional least squares methods exhibit large errors.

The method is largely inspired by similar approaches developed to identify human gait stability [7], human motor learning dynamics [9], and brain activity from electroencelphalogram (EEG) signals [13]. While those studies did not consider measurement noise separately from biological noise, we show that measurement noise can cause significant bias in estimation. We also present a way to mitigate the problem. With this method, natural human postural dynamics and control can be studied in depth without concerning adaptation or possible reflex responses evoked by external perturbations. Reliable quantitative identification of the dynamics and control of human balance would enable diagnosis and treatment of individuals with impaired balance, and the development of safe and effective assistive and / or rehabilitative technologies.

13.2 Methods

13.2.1 Identifying a General System from autocorrelation matrices

Consider a discrete-time stochastic finite-dimensional linear time-invariant dynamic system

$$\begin{cases} \mathbf{x}_{t+1} = \mathbf{A}\mathbf{x}_t + \mathbf{G}\mathbf{w}_t \\ \mathbf{z}_t = \mathbf{H}\mathbf{x}_t + \mathbf{v}_t, \end{cases} \tag{13.1}$$

where $\mathbf{x} \in \mathbb{R}^{n_x}, \mathbf{z} \in \mathbb{R}^{n_z}$ are state and measured output vectors, respectively, at time t.

We assume that process noise, $\mathbf{w} \in \mathbb{R}^{n_w}$, and measurement noise, $\mathbf{v} \in \mathbb{R}^{n_v}$, are

white and uncorrelated:

$$\begin{aligned} E\{\mathbf{w}_t\} = \mathbf{0}, \quad & E\{\mathbf{w}_t \mathbf{w}_s^T\} = \mathbf{\Sigma}_{\mathbf{w}} \delta_{ts} \\ E\{\mathbf{v}_t\} = \mathbf{0}, \quad & E\{\mathbf{v}_t \mathbf{v}_s^T\} = \mathbf{\Sigma}_{\mathbf{v}} \delta_{ts} \\ E\{\mathbf{w}_t \mathbf{v}_s^T\} = \mathbf{0} \quad & \forall t, s \end{aligned}$$

The objective is to estimate the $n_x \times n_x$ system matrix $\mathbf{A}$. We first compute the auto-correlation matrix of the output $\mathbf{z}$ with non-zero lag $k > 0$ as

$$\begin{aligned} \mathbf{R}_{\mathbf{zz}}(k) &= E\{\mathbf{z}_t \mathbf{z}_{t-k}^T\} \\ &= E\{(\mathbf{H}\mathbf{x}_t + \mathbf{v}_t)(\mathbf{H}\mathbf{x}_{t-k} + \mathbf{v}_{t-k})^T\} \\ &= E\{\mathbf{H}\mathbf{x}_t \mathbf{x}_{t-k}^T \mathbf{H}^T + \mathbf{H}\mathbf{x}_t \mathbf{v}_{t-k}^T + \mathbf{v}_t \mathbf{x}_{t-k}^T \mathbf{H}^T + \mathbf{v}_t \mathbf{v}_{t-k}^T\} \\ &= \mathbf{H} E\{\mathbf{x}_t \mathbf{x}_{t-k}^T\} \mathbf{H}^T = \mathbf{H} \mathbf{R}_{\mathbf{xx}}(k) \mathbf{H}^T \end{aligned} . \tag{13.2}$$

$\mathbf{R}_{\mathbf{zz}}(0)$ can be obtained as

$$\begin{aligned} \mathbf{R}_{\mathbf{zz}}(0) &= E\{\mathbf{z}_t \mathbf{z}_t^T\} \\ &= E\{(\mathbf{H}\mathbf{x}_t + \mathbf{v}_t)(\mathbf{H}\mathbf{x}_t + \mathbf{v}_t)^T\} \\ &= E\{\mathbf{H}\mathbf{x}_t \mathbf{x}_t^T \mathbf{H}^T + \mathbf{H}\mathbf{x}_t \mathbf{v}_t^T + \mathbf{v}_t \mathbf{x}_t^T \mathbf{H}^T + \mathbf{v}_t \mathbf{v}_t^T\} \\ &= \mathbf{H} E\{\mathbf{x}_t \mathbf{x}_t^T\} \mathbf{H}^T + E\{\mathbf{v}_t \mathbf{v}_t^T\} = \mathbf{H} \mathbf{R}_{\mathbf{xx}}(0) \mathbf{H}^T + \mathbf{\Sigma}_{\mathbf{v}} \end{aligned} \tag{13.3}$$

An expression for $\mathbf{R}_{\mathbf{xx}}(k)$ for the dynamic system (13.1) can easily be obtained. Noting that $E\{\mathbf{x}_t \mathbf{w}_s^T\} = \mathbf{0}$ for $t \leq s$,

$$\begin{aligned} \mathbf{R}_{\mathbf{xx}}(k) &= E\{\mathbf{x}_t \mathbf{x}_{t-k}^T\} \\ &= E\{(\mathbf{A}^k \mathbf{x}_{t-k} + \sum_{j=1}^{k} \mathbf{A}^{j-1} \mathbf{G} \mathbf{w}_{t-j}) \mathbf{x}_{t-k}^T\} = \mathbf{A}^k E\{\mathbf{x}_{t-k} \mathbf{x}_{t-k}^T\} = \mathbf{A}^k \mathbf{R}_{\mathbf{xx}}(0) \end{aligned} \tag{13.4}$$

where $\mathbf{R_{xx}}(0)$ can be obtained as

$$\begin{aligned}\mathbf{R_{xx}}(0) &= \mathbf{P} = E\{\mathbf{x}_t\mathbf{x}_t^T\} \\ &= E\{(\mathbf{A}\mathbf{x}_{t-1} + \mathbf{G}\mathbf{w}_{t-1})(\mathbf{A}\mathbf{x}_{t-1} + \mathbf{G}\mathbf{w}_{t-1})^T\} \\ &= E\{\mathbf{A}\mathbf{x}_{t-1}\mathbf{x}_{t-1}^T\mathbf{A}^T + \mathbf{G}\mathbf{w}_{t-1}\mathbf{w}_{t-1}^T\mathbf{G}^T\} \\ &= \mathbf{A}\mathbf{R_{xx}}(0)\mathbf{A}^T + \mathbf{G}\mathbf{\Sigma_w}\mathbf{G}^T = \mathbf{A}\mathbf{P}\mathbf{A}^T + \mathbf{G}\mathbf{\Sigma_w}\mathbf{G}^T\end{aligned} \tag{13.5}$$

From (13.2) and (13.4), it readily follows that

$$\mathbf{R_{zz}}(k) = \mathbf{H}\mathbf{A}^k\mathbf{P}\mathbf{H}^T, \forall k > 0 \tag{13.6}$$

If $\mathbf{H}^{-1}$ exists, one can derive the matrix A from autocorrelation matrices as

$$\mathbf{A} = \mathbf{H}^{-1}\mathbf{R_{zz}}(k+1)\mathbf{R_{zz}}(k)^{-1}\mathbf{H}, \tag{13.7}$$

Note that (13.7) holds for all $k > 0$.

We now turn to the estimation problem. Using the ergodic property of $\mathbf{z}_t$, $\mathbf{R_{zz}}(k)$ can be estimated as $\frac{1}{N-k}\sum_{t=k+1}^{N}\mathbf{z}_t\mathbf{z}_{t-k}^T$ for $k \geq 0$, where N is the length of the time series. As long as the process is ergodic, it has been shown that $\hat{\mathbf{R}}_{\mathbf{zz}}(k)$ provides an asymptotically unbiased, normal, and consistent estimate [153]. The estimation can be improved by either increasing the trial duration (N) or combining multiple-trial data of each participant. In practice, the trial duration cannot be arbitrarily extended because participants' dynamics may vary over time due to fatigue. Denoting n_T as the total number of trials per participant and $\hat{\mathbf{R}}_{\mathbf{zz}}^{(i)}(k)$ as the estimated autocorrelation matrix for i-th trial, we can re-define $\hat{\mathbf{R}}_{\mathbf{zz}}(k)$ as

$$\hat{\mathbf{R}}_{\mathbf{zz}}(k) = \frac{1}{n_T}\sum_{i=1}^{n_T}\hat{\mathbf{R}}_{\mathbf{zz}}^{(i)}(k) = \frac{1}{n_T}\frac{1}{N-k}\sum_{i=1}^{n_T}\sum_{t=k+1}^{N}\mathbf{z}_t^{(i)}\mathbf{z}_{t-k}^{(i)T}.$$

where $\mathbf{z}^{(i)}$ is the measured output of i-th trial. From (13.7), we obtain an expression

for the estimate of $\mathbf{A}$ as

$$\hat{\mathbf{A}}_{\mathrm{CR}} = \mathbf{H}^{-1}\hat{\mathbf{R}}_{\mathbf{zz}}(k+1)\hat{\mathbf{R}}_{\mathbf{zz}}(k)^{-1}\mathbf{H}, \forall k > 0, \tag{13.8}$$

where the subscript CR stands for correlation.

In practice, since $\mathbf{R}_{\mathbf{zz}}(k) = \mathbf{H}\mathbf{R}_{\mathbf{xx}}(k)\mathbf{H}^T = \mathbf{H}\mathbf{A}^k\mathbf{R}_{\mathbf{xx}}(0)\mathbf{H}^T$, for a stable system with $\|\mathbf{A}\| < 1$, too large a value of k will cause $\mathbf{R}_{\mathbf{zz}}(k)$ to have a large condition number, which may amplify numerical error and degrade the quality of estimate. To alleviate this performance degradation, by noting that the relation $\mathbf{A}\mathbf{H}^{-1}\mathbf{R}_{\mathbf{zz}}(k) = \mathbf{H}^{-1}\mathbf{R}_{\mathbf{zz}}(k+1)$ holds for all $k > 0$, (13.8) can be improved

$$\hat{\mathbf{A}}_{\mathrm{CR(m)}} = \mathbf{H}^{-1}[\hat{\mathbf{R}}_{\mathbf{zz}}(2), ..., \hat{\mathbf{R}}_{\mathbf{zz}}(m+1)] \times [\hat{\mathbf{R}}_{\mathbf{zz}}(1), ..., \hat{\mathbf{R}}_{\mathbf{zz}}(m)]^{+}\mathbf{H} \tag{13.9}$$

for a hyperparameter m, where $\cdot^+$ denotes a pseudo-inverse operator.

13.2.2 Identifying Controller Gain

In order to apply (13.9) to identify human postural control, consider a controllable system

$$\begin{cases} \mathbf{x}_{t+1} = \mathbf{A}\mathbf{x}_t + \mathbf{B}\mathbf{u}_t + \mathbf{G}\mathbf{w}_t \\ \mathbf{z}_t = \mathbf{H}\mathbf{x}_t + \mathbf{v}_t \end{cases}, \tag{13.10}$$

where $\mathbf{u} \in \mathbb{R}^{n_u}$ is control input and $\mathbf{B}$ is input weighting matrix. If a balancing human is modeled as a set of kinematically coupled rigid segments, with an appropriate choice of generalized coordinates the structure of $\mathbf{A}$ and $\mathbf{B}$ may be determined from equations of motion using standard methods. For example, if relative joint angles and angular velocities are chosen as the state vector $\mathbf{x}$ and joint torques as the input vector $\mathbf{u}$, the system matrix $\mathbf{A}$ and input matrix $\mathbf{B}$ are constrained by the dynamic structure. In particular, if joint angles comprise the first elements of $\mathbf{x}$, $\mathbf{B}$ must have $[\mathbf{0}]$ as its top $n_x/2$ rows. The corresponding rows of $\mathbf{A}$ have a a unity block $[\mathbf{I}]$ in the first $n_x/2$ columns. The second half of the matrix is determined by the continuous-to-discrete time conversion rule and sampling frequency, as the first rows

of the corresponding matrix in continuous-time consist of a [**0**] block and a unity block [**I**]; see Appendix 13.8. The dimensions and precise meaning of the rest of **A** and **B** depend on the system configuration, state vector, and control input. For instance, modeling a human as a planar inverted pendulum with two joints (ankle and hip), one may assume the pendulum is controlled either by joint torque actuators (**u**: joint torques) or muscle actuators (**u**: muscle forces), depending on the purpose of the model. While these assumptions may be restrictive, they are biomechanically reasonable and establish the structure of **A** and **B**.

Next, suppose the system is equipped with a feedback controller that stabilizes the system about its operating point $\mathbf{x} = \mathbf{0}$,

$$\begin{cases} \mathbf{y}_t = \mathbf{C}\mathbf{x}_t + \mathbf{D}\mathbf{u}_t + \mathbf{e}_t \\ \mathbf{u}_t = -\mathbf{K}\mathbf{y}_t + \boldsymbol{\eta}_t \end{cases} \tag{13.11}$$

where $\mathbf{y} \in \mathbb{R}^{n_y}, \mathbf{e} \in \mathbb{R}^{n_e}, \boldsymbol{\eta} \in \mathbb{R}^{n_\eta}$ are sensory signals fed back to a stabilizing controller, sensory noise, and motor noise, respectively. $\mathbf{K}$ is the $n_u \times n_y$ gain matrix. Without loss of generality and for simplicity, we can assume $\mathbf{D} = \mathbf{0}$ [1]. The closed-loop system equipped with the controller (13.10)-(13.11) is reduced to

$$\begin{cases} \mathbf{x}_{t+1} = \mathbf{A_{cl}}\mathbf{x}_t + \mathbf{G}_{cl}\tilde{\mathbf{w}}_t \\ \mathbf{z}_t = \mathbf{H}\mathbf{x}_t + \mathbf{v}_t \end{cases} \tag{13.12}$$

where $\mathbf{A_{cl}} = \mathbf{A} - \mathbf{BKC}$, $\quad \mathbf{G_{cl}} = [\mathbf{G}, -\mathbf{BK}, \mathbf{B}]$, and $\tilde{\mathbf{w}} = [\mathbf{w^T}, \mathbf{e^T}, \boldsymbol{\eta}^T]$. We assume that the noise sources $\mathbf{w}, \mathbf{e}$, and $\boldsymbol{\eta}$ are white, mutually uncorrelated, and with covariance matrices $\boldsymbol{\Sigma}_\mathbf{w}, \boldsymbol{\Sigma}_\mathbf{e}, \boldsymbol{\Sigma}_\eta$, respectively. An asymptotically unbiased and consistent estimate $\hat{\mathbf{A}}_\mathbf{cl}$ can be obtained using the procedure of (13.9).

One can further estimate the gain matrix $\mathbf{K_x} = \mathbf{KC}$ of the state-feedback con-

[1] Extension of the method to non-zero **D** would be straightforward, but is left for future work.

troller (13.11) by solving the following linear regression problem,

$$\hat{\mathbf{K}}_{\mathbf{x}} = \mathbf{B}^{+}(\mathbf{A} - \hat{\mathbf{A}}_{\mathbf{cl}}) \tag{13.13}$$

Note that for $n_u < n_x$, this is an over-determined problem and its unique solution can be obtained. Note also that the controller gain can be estimated in the continuous-time domain using a proper discrete-to-continuous time model conversion, as described in Appendix 13.8.

This method requires *a priori* knowledge of $\mathbf{A}$ and $\mathbf{B}$ but those are determined by the mechanical physics of the model assumed to describe experimental human balancing data. Note especially that if joint angles and angular velocities are chosen as the state vector $\mathbf{x}$ and joint torques (with zero mechanical impedance) as the input vector $\mathbf{u}$, constructing $\mathbf{A}$ and $\mathbf{B}$ for the open-loop (uncontrolled) system only requires knowledge of kinematics and gravito-inertial mechanics. Geometric and inertial properties of limb segments are quite well quantified in the literature, for example see [42]. In this way, the method presented here 'fills in' the missing data about mechanical impedance.

This approach is well-justified and enough to model apparent mechanical behavior of human balancing. However, if one pursues to develop a model that encapsulate complex details of human body such as muscle dynamics and neural transmission, a more sophisticated method will be needed.

13.3 Results

13.3.1 Numerical Simulation: Scalar Dynamic System

Model

To gain insight, consider a simple stable dynamic system,

$$\begin{cases} x_{t+1} = ax_t + gw_t \\ z_t = hx_t + v_t, \end{cases} \tag{13.14}$$

where a, g, h are unknown scalar system parameters. Unknown noise processes are drawn from zero-mean Gaussian distributions, $w_t \sim \mathcal{N}(0, \sigma_w^2), v_t \sim \mathcal{N}(0, \sigma_v^2)$. We assume $|a| < 1$, i.e., the system is stable. It can readily be obtained from (13.2) - (13.5) that

$$\begin{cases} R_{xx}(0) = P = a^2P + g^2\sigma_w^2 = \frac{1}{1-a^2}g^2\sigma_w^2 \\ R_{xx}(k) = a^kP, \forall k \geq 0 \\ R_{zz}(0) = h^2P + \sigma_v^2 = \frac{1}{1-a^2}g^2h^2\sigma_w^2 + \sigma_v^2 \\ R_{zz}(1) = ah^2P \\ R_{zz}(k+1) = aR_{zz}(k), \forall k \geq 1 \end{cases}$$

Simulation Setup

For this simple system, we compared the new method (13.9), $\hat{a}_{\mathrm{CR(m)}}$ with different m-values ($m = 1$ and $m = 10$), with the ordinary least-squares method (OLS), $\hat{a}_{\mathrm{OLS}}$. The ordinary least-squares method is detailed in Appendix 13.6; note that the estimate yielded by OLS is equivalent to that yielded by the Yule-Walker equations, which are widely used [7, 13]. In the following numerical example, we simulated the dynamic system (13.14) with $h = g = 1$ for different system parameters $a \in (-1, 1)$ with a finite resolution of 0.1. The estimates $\hat{a}_{\mathrm{CR(m)}}$ and $\hat{a}_{\mathrm{OLS}}$ were computed from five different trials ($n_T = 5$) and each trial consisted of a time series with length $N = 3000$. This corresponds to 30s of simulation with a sampling rate of 100Hz, typical for studies of human behavior. The noise strengths σ_w, σ_v were also varied such that the relative strength $\sigma_r = \sigma_v/\sigma_w$ was 0, 1/2, 1, and 2. Finally, to understand the statistical properties of the estimation methods, we iterated the above procedure 100 times and obtained the mean and standard deviation of the error of estimation,

$\hat{a}_{(\cdot)} - a$. All simulations and computations were conducted in MATLAB R2018b (Mathworks, MA).

Simulation Result

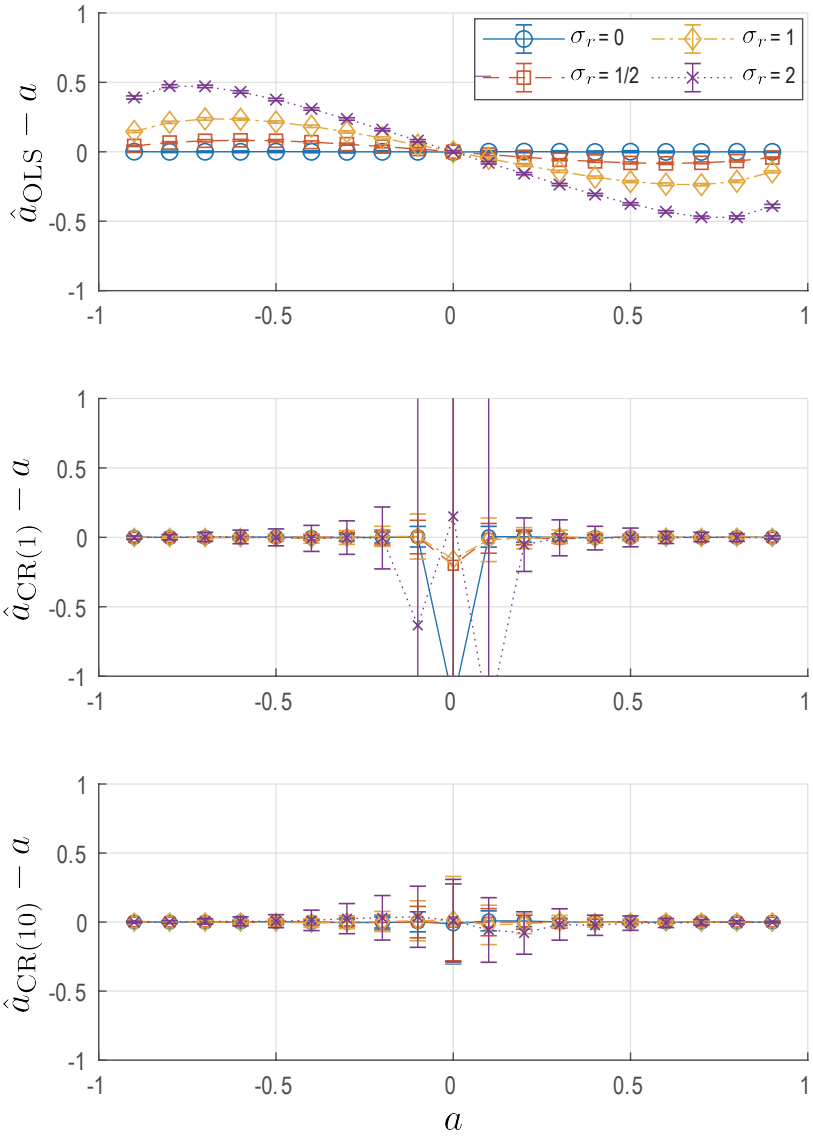

Figure 13-1: Comparison of estimation methods with different process and measurement noise strengths. Each estimate was obtained from 5 different trials. Each trial consisted of a time series with length N = 3000. The mean and standard deviation of the error of estimation $(\hat{a} - a)$ for each plot were obtained from 100 iterations of the whole process.

Fig. 13-1 compares the performance of different estimation methods. The ordinary least-squares estimate $\hat{a}_{\mathrm{OLS}}$ shows small variance but non-zero bias. The mean error of the estimate is zero at $a = 0$, but the bias at large $|a|$ is considerable and probably unacceptable. On the other hand, $\hat{a}_{\mathrm{CR(m)}}$ is not biased when the system parameter a is non-zero and large. However, when $|a| \sim 0$, its performance is degraded. In general, the variance and mean error of all methods decrease as relative noise strength σ_r increases, i.e., with more accurate measurements and larger internal perturbation.

To understand the difference between $\hat{a}_{\mathrm{OLS}}$ and $\hat{a}_{\mathrm{CR(1)}}$, it is convenient to derive analytic expressions. The ordinary least squares method is given as

$$\hat{a}_{\mathrm{OLS}} = \frac{\hat{R}_{zz}(1)}{\hat{R}_{zz}(0)} \approx \frac{R_{zz}(1)}{R_{zz}(0)} \tag{13.15}$$

and $\hat{a}_{\mathrm{CR(1)}}$ is given as

$$\hat{a}_{\mathrm{CR(1)}} = \frac{\hat{R}_{zz}(2)}{\hat{R}_{zz}(1)} \approx \frac{R_{zz}(2)}{R_{zz}(1)} \tag{13.16}$$

where

$$\frac{R_{zz}(1)}{R_{zz}(0)} = \frac{ah^2P}{h^2P + \sigma_v^2} = \frac{a}{1 + (1-a^2)\frac{\sigma_v^2}{h^2 g^2 \sigma_w^2}} \tag{13.17}$$

$$\frac{R_{zz}\,(2)}{R_{zz}\,(1)} = \frac{a^2h^2P}{ah^2P} = a \tag{13.18}$$

It is clear that even if autocorrelation is perfectly estimated, e.g., $\hat{R}_{zz}(k) = R_{zz}(k)$, $\hat{a}_{\mathrm{OLS}}$ has bias which depends on both the system parameters a, g, h and the unknown noise strengths σ_w^2, σ_v^2, while $\hat{a}_{\mathrm{CR(1)}}$ provides an unbiased estimate without requiring any information about the noise strengths. In particular, the bias in $\hat{a}_{\mathrm{OLS}}$ increases as the relative noise σ_v/σ_w increases. On the other hand, $\hat{a}_{\mathrm{CR(1)}}$ is not well defined for $|a| \sim 0$ because its denominator contains a. These properties are well represented in Fig. 13-1. While $\hat{a}_{\mathrm{OLS}}$ has smaller variance for all a values, the error due to bias is substantial for non-zero a. $\hat{a}_{\mathrm{CR(1)}}$ has relatively large variance in general but provides quite an accurate estimate unless a is close to 0. When true a is close to 0, $\hat{a}_{\mathrm{CR(1)}}$ is quite imprecise.

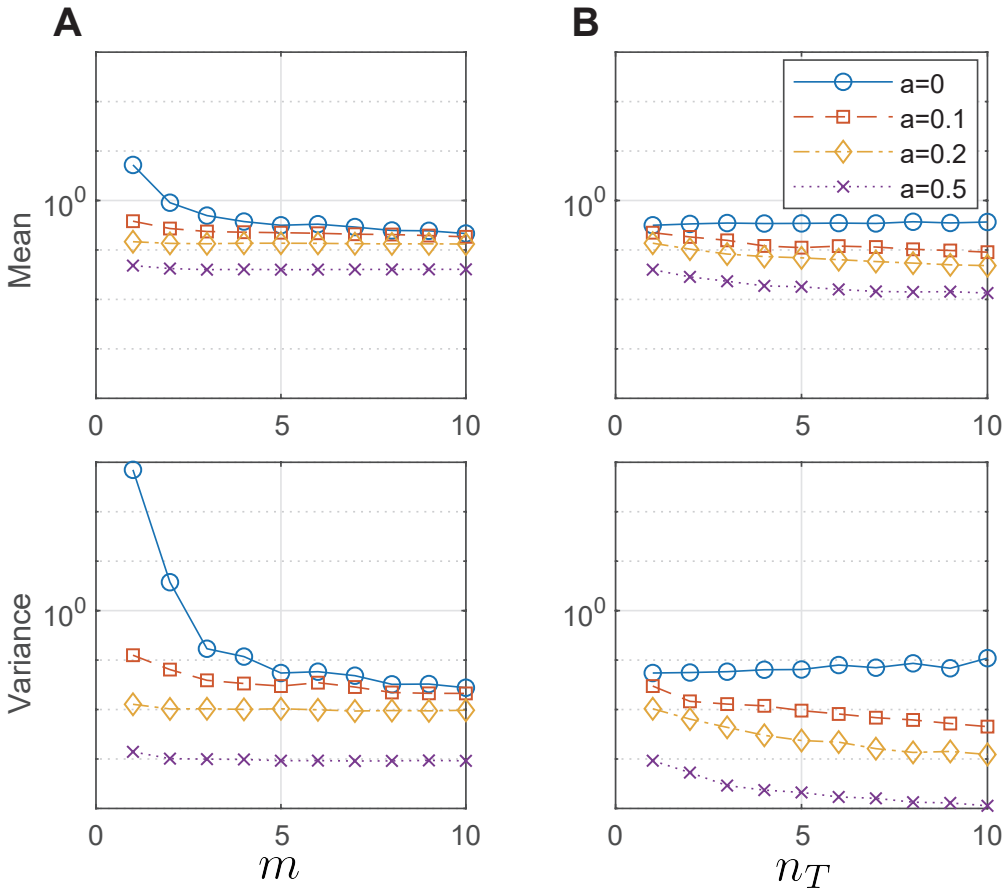

Figure 13-2: The effect of hyper-parameters m, the maximum time lag of the autocorrelation function used to estimate $\hat{a}$, and n_T, the total number of trials, on $|\hat{a}_{\mathrm{CR(m)}} - a|$. Noise strengths were fixed as $\sigma_w = \sigma_v = 1$. **A** $n_T = 5$ was fixed and m was varied. **B** $m = 5$ was fixed and n_T was varied.

This drawback can be overcome if we use $\hat{a}_{\mathrm{CR(10)}}$. This estimate for large true a is as accurate and exhibits as little bias as $\hat{a}_{\mathrm{CR(1)}}$. More importantly, it is remarkable that $\hat{a}_{\mathrm{CR(10)}}$ substantially improves accuracy and variance even when $|a| \sim 0$. While its variance is still larger than $\hat{a}_{\mathrm{OLS}}$, the accuracy of its mean value is comparable.

We also tested the effect of hyper-parameters m, the maximum time lag in autocorrelation to estimate $\hat{a}$, and n_T, the total number of trials, on the error of estimation and present the result in Fig. 13-2. The absolute value of the error of estimation, $|\hat{a}_{\mathrm{CR(m)}} - a|$ was computed, then the average and variance of the absolute error were computed from 100 iterations. As shown in Fig. 13-2, in general both hyper-parameters monotonically improved the reliability of estimation by reducing

both mean error and its variance. As might be expected, increasing the number of trials had more effect than m. This is because increasing m means more $\hat{R}_{zz}(k)$ are recruited for $\hat{a}$, while increasing the number of trials helps to better estimate $R_{zz}(k)$ and consequently reduces the errors that propagate in estimating $\hat{a}$. Thus it is always recommended to use as large as n_T as possible, i.e., collect as many data as possible from each participant.

The performance improvement with increasing m quickly reached a plateau, and thus a sufficiently large value of m, for instance $m = 10$ can be chosen to improve the estimation. As can be seen in Fig. 13-1 and Fig. 13-2, the variance when $|a| \sim 0$ is still quite large. Therefore one may first compute $\hat{a}_{\text{OLS}}$ to estimate a, then compute $\hat{a}_{\text{CR(m)}}$ when $|\hat{a}_{\text{OLS}}|$ is larger than a threshold, e.g., 0.1. For higher dimensional systems, one may instead use the norms of $\mathbf{R_{zz}}(k)$ and $\mathbf{R_{zz}}(1)$ to determine the value of m.

13.3.2 Numerical Simulation: Balance Model

Double inverted pendulum model

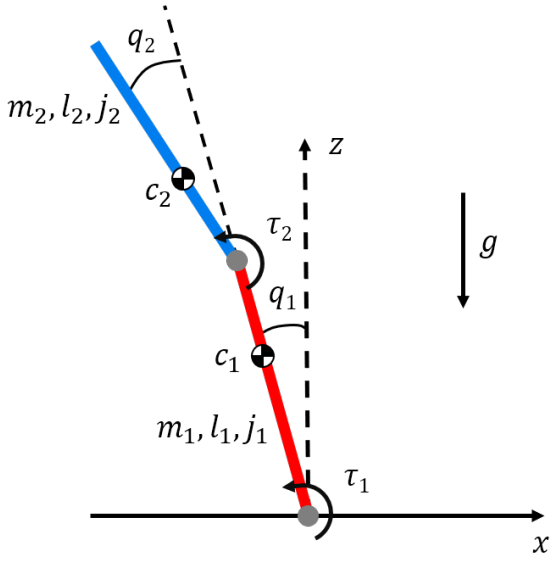

Figure 13-3: Double inverted pendulum model with angle (q_i) and torque (τ_i) sign conventions and parameter values for mass (m_i), length (l_i), center of mass (c_i), and moment of inertia about center of mass (j_i). The direction of gravity (g) is also defined.

Human quiet standing is often modeled as an inverted pendulum with single [119], double [112], or more than two joints [99]. To establish how the new method performs for a multi-joint case, we adopted a double inverted pendulum model of human quiet standing. Lumped model parameters including mass, center of mass position from joint, length, moment of inertia about center of mass of each link, and gravitational acceleration are listed in Table 13.1. They were computed based on the anthropomorphic distribution of males [42], with weight and height of 73 kg and 1.73 m. We assumed that the foot is not moving during standing and regarded the ankle as a pin joint; any mass and length below the ankle was neglected in the double-inverted pendulum model. Fig. 13-3 illustrates joint angles and torques for ankle (q_1, τ_1) and hip (q_2, τ_2). As in (13.11), it was assumed that each joint torque is a sum of control input torque and actuation error, $\tau_i = u_i + \eta_i$. The state vector $\mathbf{x} = [q_1, q_2, \dot{q}_1, \dot{q}_2]^T$ and input vector $\mathbf{u} = [u_1, u_2]^T$ were defined accordingly.

Stabilizing Controller

We used an infinite-horizon linear quadratic regulator (LQR) to stabilize the double inverted pendulum. The LQR is a state-feedback controller in which gain $\mathbf{K_x}$ is determined such that a quadratic cost is minimized:

$$\mathbf{K_x} = \underset{\mathbf{K_x}}{\operatorname{argmin}} \int_0^\infty [\mathbf{x}^T(t)\mathbf{Q}\mathbf{x}(t) + \mathbf{u}^T(t)\mathbf{R}\mathbf{u}(t)]\mathrm{dt},$$

Table 13.1: double inverted pendulum model parameters

Symbol	Parameter meaning (units)	Value
m_1	Mass of link 1 (kg)	25.89
l_1	Length of link 1 (m)	0.857
c_1	Center of mass of link 1 (m)	0.582
j_1	Moment of inertia of link 1 (kgm^2)	1.350
m_2	Mass of link 2 (kg)	42.20
l_2	Length of link 2 (m)	0.841
c_2	Center of mass of link 2 (m)	0.328
j_2	Moment of inertia of link 2 (kgm^2)	2.547
g	Gravitational acceleration (m/s^2)	9.81

where $\mathbf{u} = -\mathbf{K}_\mathbf{x}\mathbf{x}$ [197]. Two sets of parameters of the LQR were tested:

- Case 1:

$$\mathbf{Q} = \mathbf{I}_4, \quad \mathbf{R} = \begin{bmatrix} 5 & 0 \\ 0 & 1/5 \end{bmatrix}.$$

- Case 2:

$$\mathbf{Q} = \mathbf{I}_4, \quad \mathbf{R} = 10^6 \begin{bmatrix} 0.3 & 0 \\ 0 & 10/3 \end{bmatrix}.$$

The parameters used in Case 1 are those which were reported as well-representing human balancing and similar to the 'hip strategy' [109, 112]. Case 2 was intended to test a different type of controller which encouraged more use of the 'ankle', similar to the 'ankle strategy', but minimized control effort.

Finally, the torque controller was perturbed by internal sensory noise $\mathbf{e}$ and motor noise $\boldsymbol{\eta}$ with $\boldsymbol{\Sigma}_\mathbf{e} = \sigma_e^2\mathbf{I}_4$ and $\boldsymbol{\Sigma}_\eta = \sigma_\eta^2\mathbf{I}_2$ such that

$$\boldsymbol{\tau} = \mathbf{u} + \boldsymbol{\eta} = -\mathbf{K}_\mathbf{x}(\mathbf{x} + \mathbf{e}) + \boldsymbol{\eta}.$$

Model Linearization

While we used the full nonlinear equations of motion to simulate human balance, when stabilized by the LQR and perturbed by small internal noise, the resultant motion of the double inverted pendulum is subtle, consistent with experimental observations of quiet standing [64, 233]. For small motion, the nonlinear system can be well-approximated as a linear system (13.10), as described in the previous chapter. From the linearized model, $\mathbf{A}_{\text{cl}} = \mathbf{A} - \mathbf{B}\mathbf{K}_\mathbf{x}$ was obtained.

Simulation Setup

We used the new method to estimate the closed-loop system matrix $\mathbf{A}_{\text{cl}}$ and controller gain matrix $\mathbf{K}_\mathbf{x}$. Because the model was developed in continuous-time, we

first estimated discrete-time model parameters using (13.9), then converted them into continuous-time model parameters by following the method described in Appendix 13.8. The size of the error between true and estimated matrices were computed as below

$$e_A = (\|\mathbf{A}_{\text{cl}} - \hat{\mathbf{A}}_{\text{cl}}\|_2)/\|\mathbf{A}_{\text{cl}}\|_2 \tag{13.19}$$

$$e_K = (\|\mathbf{K}_{\mathbf{x}} - \hat{\mathbf{K}}_{\mathbf{x}}\|_2)/\|\mathbf{K}_{\mathbf{x}}\|_2 \tag{13.20}$$

Note that from the choice of the state vector $\mathbf{x}$, the first two rows of $\mathbf{A}_{\text{cl}}$ are constrained to $[\mathbf{0}, \mathbf{I}]$. Therefore, we replaced the first two rows of $\hat{\mathbf{A}}_{\text{cl}}$ with $[\mathbf{0}, \mathbf{I}]$ to obtain the controller gain using (13.13) and compute errors.

Similar to the example presented in 13.3.1, the errors obtained from the new method and from the ordinary least squares method were compared for different combinations of noise strengths. Note that sensory and motor noise are essentially equivalent in this setup, e.g., $\mathbf{u}_t = -\mathbf{KCx}_t - \mathbf{Ke}_t + \boldsymbol{\eta}_t = -\mathbf{KCx}_t + \tilde{\boldsymbol{\eta}}_t$. Thus, in the following simulation we fixed σ_η and varied σ_e. The tested parameters are summarized in Table 13.2.

$\hat{\mathbf{A}}_{\text{cl}}$ was computed from five different trials ($n_T = 5$). In each trial, a semi-implicit Euler integrator was used to simulate forward dynamics of the model for 90 s with a time step of 0.01 s (100Hz sampling rate, $N = 9000$). Finally, in order to understand the statistical properties of each estimation method, we iterated the above procedure 10 times and obtained the mean and standard deviation of $e_{A,(\cdot)}$ and $e_{K,(\cdot)}$. All simulations and computations were conducted in MATLAB 2018b (Mathworks, MA).

Table 13.2: Range of noise strengths tested

Symbol	Parameter meaning	Range
σ_e	Sensory noise strength	[1e-02, 3e-02]
σ_η	Motor noise strength	1e-02
σ_v	Measurement noise strength	[1e-03, 5e-03]

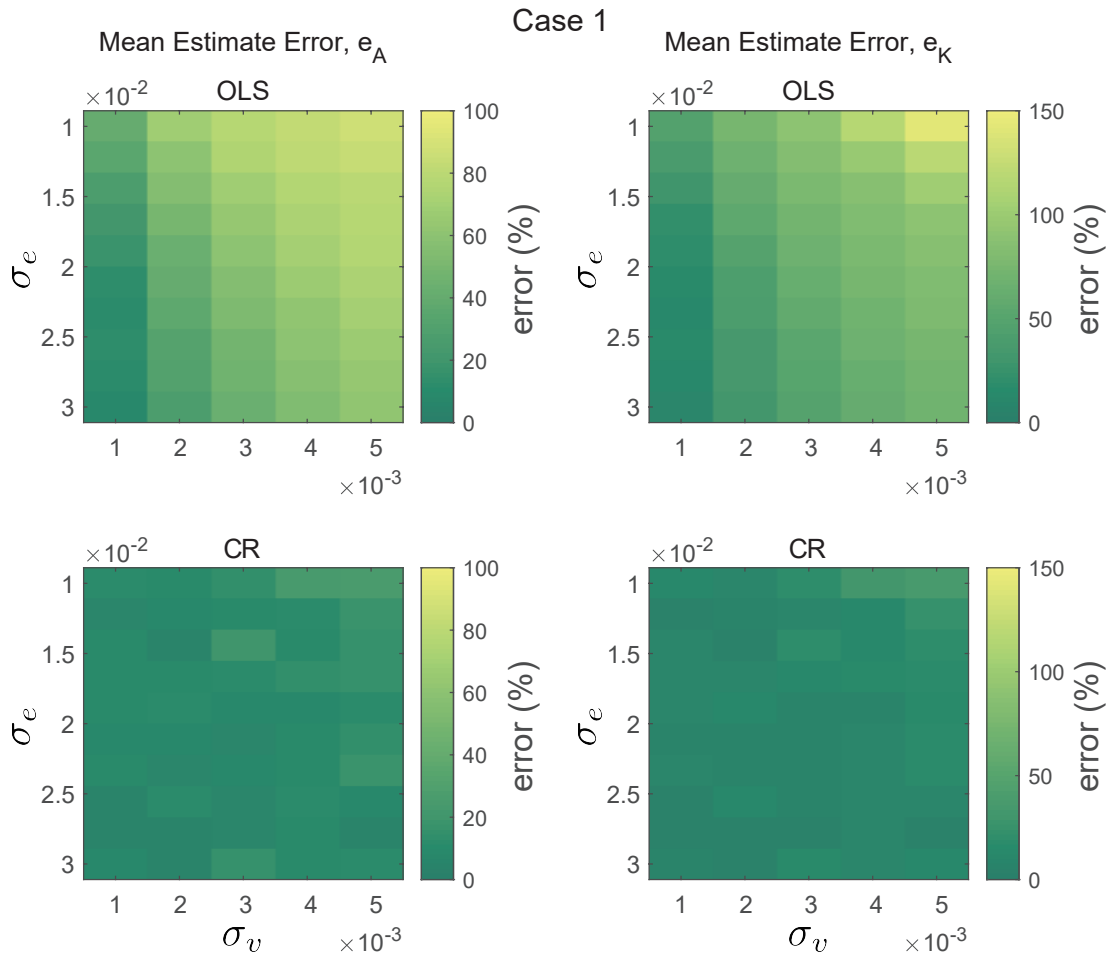

Figure 13-4: Mean estimated error of the system matrix e_A(%, left) and the control gain e_K(%, right) from 10 iterations for different noise combinations. Errors of the ordinary least squares method (OLS, top) and the new method (CR, bottom) are shown. For both cases, motor noise was fixed as $\sigma_\eta = 0.01$. The double inverted pendulum model was simulated with the Case 1 controller parameters.

Results

Fig. 13-4 and Fig. 13-5 present the mean error of estimation of the system matrix e_A and the controller gain e_K obtained from $\hat{\mathbf{A}}_{\text{cl,OLS}}$ and $\hat{\mathbf{A}}_{\text{cl,CR}}$ for various combinations of noise strengths and for two different controllers. In general, increasing measurement noise degraded performance estimation. For example, in Case 1, when $\sigma_e = 0.01$ and $\sigma_\eta = 0.01$, the mean $e_{A,\text{OLS}}$ was 40.5% with $\sigma_v = 0.001$ but 86.9% with $\sigma_v = 0.005$. Increasing sensory noise improved the estimate of the ordinary least squares method, yet its performance remained much worse than that obtained from the new method.

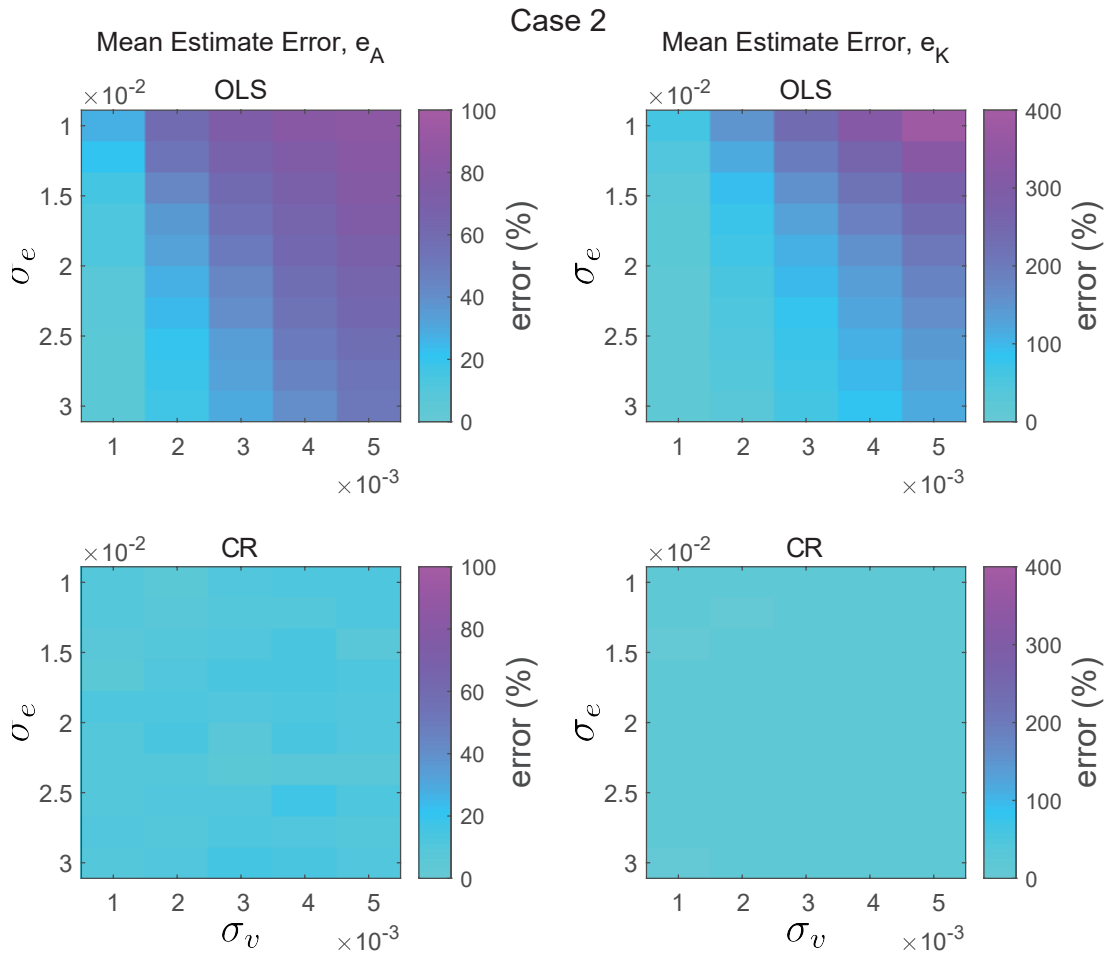

Figure 13-5: Mean estimated error of the system matrix e_A(%, left) and the control gain e_K(%, right) from 10 iterations for different noise combinations. Errors of the ordinary least squares method (OLS, top) and the new method (CR, bottom) are shown. For both cases, motor noise was fixed as $\sigma_\eta = 0.01$. The double inverted pendulum model was simulated with the Case 2 controller parameters.

The performance gap between the ordinary least squares method and the new method was even larger when estimating controller gain. For example, the mean error of estimation e_K from the ordinary least squares method reached about 150%.

Within the range of parameters tested, the error of estimation from the new method was slightly affected by different levels of noise. The mean and standard deviation of the error of estimation for all conditions were about 10% and 9% for e_A and 11% and 10% for e_K, respectively.

The performance gap between the ordinary least squares method and the new method was even larger in Case 2, as shown in Fig. 13-5. For example, the mean

error of estimation e_K from the ordinary least squares method reached over 400% (note the scale of the color bar), while the mean and standard deviation of the error of estimation from the new method for all conditions were about 10% and 7% for e_A and 9% and 6% for e_K, respectively.

13.4 Discussion

13.4.1 Summary of the Work

In this work, we presented an unbiased parametric system identification method that enables estimating the dynamics of human postural control using recorded joint trajectories without external perturbation. While the physical world is in the continuous-time domain, our digital measurement systems provide us signals in the discrete-time domain. Hence, we investigated a method to identify a discrete-time model. With a biomechanically reasonable model of the multi-joint human body, the gain matrix of a state-feedback controller can also be estimated. We first examined the properties of the new method using a simple scalar dynamic system. While the ordinary least squares method showed bias due to unknown noise in the system, the new method did not show bias even without information about the system's noise strengths. The variance of the new method was substantially reduced by employing multiple trials to improve the estimate of autocorrelation with non-zero time lags. The new method was then validated using a double inverted pendulum model stabilized by two different state-feedback controllers and perturbed by internal noise, a reasonable model of human balancing which can describe the widely-reported 'ankle' and 'hip' strategies [75]. In particular, compared to the ordinary least squares method, the controller gain identified by the new method was considerably more accurate, yielding errors of $\sim$10% or less. The numerical simulation examples indicate that the new method can be used to identify human postural dynamics from experimental data. Given a biomechanically plausible model of the relevant gravito-inertial mechanics, the net multi-joint impedance, whether due to intrinsic mechanics or feedback control, may

also be identified.

13.4.2 Caveats of Parametric Model Fitting

Like other parametric system identification techniques, the new method relies heavily on the model which determines the structure of $\mathbf{A}$ and $\mathbf{B}$. It should also be noted that $\mathbf{K_x}$ identified from the method is the gain matrix of a linear full-state feedback controller. Consequently, several trade-offs must be considered when developing models and interpreting results. As presented in this study, one may model a human as a double inverted pendulum with joint positions and velocities as its states and joint torques as its control input. With this model, the gain $\mathbf{K_x}$ should be interpreted as the apparent impedance seen at the ankle and the hip, i.e., stiffness and damping at each joint as well as coupling between them. Depending on the order of the model and the physical meaning of the state and input vectors, the precise meaning of $\mathbf{K_x}$ will vary. Therefore, the state vector and the model order should be carefully determined, based on the purpose of modeling. Moreover, the method does not draw any conclusions about underlying neural processes but only their products; it only identifies the net contributions from all control components such as intrinsic mechanical impedance and neural feedback control.

Significant time delay due to limited neural signal transmission rate is another important factor that makes human motor control challenging. However, the current work did not incorporate this aspect of human postural control. To identify time delay in the system, more sophisticated methods are required. In recent literature, the limitation of neural transmission has often been modeled as a pure time-delay in state feedback control [17, 64, 217]. This would essentially increase the order (or the maximum lag) of the model (13.12). Neglecting measurement noise, that model is equivalent to the widely studied auto-regressive models with order larger than one, and there exist a number of papers treating such models with scalar [238] and multi-dimensional state variables [13]. Both the unknown model order (equivalent to the unknown time delay) and the model parameters can be estimated, as briefly presented in Appendix 13.7. Augmenting the present methods with such features is

left for future work.

13.4.3 Important Assumptions

The new method requires a number of modeling assumptions including 1) the stochastic dynamics of human balancing is linear and time-invariant (stationary), 2) the number of independent measurements equals the order of the system (hence $\mathbf{H}^{-1}$ exists), and 3) the process and measurement noises are white and mutually uncorrelated.

Linear and Stationary Processes

A mechanical system with any controller (nonlinear, discontinuous, or higher order) must yield at least the lower-order behavior modeled here. Musculo-skeletal mechanics acts to smooth out discontinuities. The remaining nonlinearities would either be differentiable or resemble noise, and small motions would justify a linearized representation. Indeed it has been widely reported that unperturbed human balancing exhibits only subtle movement [131, 233].

The stationarity of human balance is debatable [22, 143, 187]; due to fatigue or change in control strategy (e.g., transitioning between an 'ankle strategy' and a 'hip strategy' [75]) during balancing, the system may exhibit time-varying dynamics. Stationarity should be established before applying the new method to identify human postural control.

Existence of H

Whether $\mathbf{H}^{-1}$ exists or not depends on the model. If one develops a joint-level human balance model, joint angular positions and velocities can be measured with combination of reasonably high accuracy with available technologies, e.g., motion capture systems (MOCAP), inertial measurement units (IMUs), accelerometers, gyroscopes, and goniometers. In general it becomes harder to obtain full measurement of states as more complex features of postural control are included in the model (e.g., muscle dynamics or neural time delay). On the other hand, [126, 212, 234] have shown that

an appropriate system order and parameters may be identified from partial measurements for single-input systems. Further investigation and application of such methods to the analysis of human postural control is left for future work.

White and Mutually Uncorrelated Noise

The new method relies heavily on the assumption that all noise processes in (13.10) are white and uncorrelated with each other. However, some studies have indicated that biological noise may best be described by 'pink' noise or Brownian noise [216]. Moreover, linear models lump all the higher-order and nonlinear terms of a real human system into process noise, which might not be white. However, it should be noted that the purpose of system identification is to parameterize a model which may provide mechanically feasible explanations of observations and guide experiments to test hypotheses. In that sense, any model is wrong, and white noise may be wrong, but it is a convenient and useful approximation.

13.4.4 Strength of the New Method Compared to the Ordinary Least Squares Method

We used a scalar stochastic dynamic system to analyze properties of the new method. In Fig. 13-1, it was shown that the variance and bias of the new method are sensitive to the size of the true system parameters. The method's performance degraded when a was close to 0 (in the 1D model). In the multi-joint model, it would correspond to the case when $\|\mathbf{A}_{\text{cl}}\|$ is close to 0. However, such a case is quite rare in biological systems. In particular, $\|\mathbf{A}_{\text{cl}}\| = 0$ implies that the neural controller rejects any perturbation within one sampling interval.

It was also shown that the quality of the estimate is sensitive to the size of measurement noise, or more precisely, the size of measurement noise relative to process noise (internal biological noise), σ_r. Both the ordinary least squares method and the new method performed better as measurement noise decreased. When $\sigma_r = 0$, the ordinary least squares method provided a very accurate estimate of the system

parameter a as shown in Fig. 13-1 and it outperformed the new method. However, as σ_r became larger, error in the ordinary least squares method increased rapidly. In contrast, the new method showed consistent performance across a range of σ_r values. Moreover, recruiting multiple auto-correlation matrices with different time lags ($m = 10$) substantially improved the precision of the new method and provided accurate estimates for values of $\|a\| \sim 0$. The improvement can easily be extended to the multi-dimensional case as it does not require any difficult operations. The performance difference between the new method and the conventional ordinary least squares method was even more pronounced in the double inverted pendulum example as shown in Fig. 13-4 and Fig. 13-5.

Furthermore, with the known parameters $\mathbf{A}$ and $\mathbf{B}$ based on the gravito-inertial model, the controller gain matrix could be estimated. The mean error of estimation of controller gain obtained from the new method was much smaller than that from the ordinary least squares method (Fig. 13-4 and Fig. 13-5), especially when measurement noise was large. Sensitivity to measurement noise is an important practical consideration. It has been reported that the variability of joint angles during quiet standing is on the order of 0.1 deg [64, 233]. The measurement errors of state-of-the-art IMUs, 0.2 - 0.3 deg, [231] is comparable to and perhaps larger than sway motion during quiet standing. This work showed that when measurement noise was comparable to process noise, the ordinary least squares method can be substantially biased, while our method was unbiased for even larger noises.

The practical implication is quite striking. While measurement noise can be further reduced by setting up high-precision MOCAP in the lab, such high-precision measurement systems are usually expensive and require large space. If clinicians are to diagnose patients remotely in at-home settings, they may not have access to accurate measurement systems (e.g., MOCAP or high-precision IMUs). In that case, our method would be an effective alternative to the conventional ordinary least squares method because it does not require such high-precision sensors.

13.4.5 Wider Application

The method proposed in this work is applicable to any linear, discrete-time stochastic system, thus relevant to a broad range of human system studies. For example, the new method appears to be applicable to the study of rhythmic movements, another important field in human motor control [73,74]. For example, it is possible to quantify the degree of stability of walking [7] or rhythmic arm movement [240]. The relevance of the proposed framework to rhythmic movement is detailed in Appendix 13.9. In a recent study, Ahn and Hogan [7] have shown how to obtain accurate assessment of gait stability by correcting the bias due to the short duration of experimental time series. However, that method was limited to a scalar human walking model and not easily extensible to the multi-joint models which are typical of human systems. Moreover, significant error in human motion measurement systems was not accounted for. Combining the strength of the new method with the results of Ahn and Hogan [7] may improve the state-of-the-art in stability assessment of human walking [30]. The same technique may also improve experimental stability assessment of legged robots.

Another interesting field of application is motor learning [9,69]. In motor learning studies, how humans learn a task from observing errors in each trial is often modeled as a linear discrete-time system with some feedback mechanism as in (13.10). Typical human motor learning models assume measurement noise and process noise are the same ($\mathbf{v} = \mathbf{w}$ in (13.1)). Due to this assumption, the least squares estimate requires additional correction as shown in [9] while our new method can readily be applied. Recent studies [9, 69] have examined a scalar dynamic model which assumes that a task error can be represented by a scalar variable. A method for multi-dimensional systems, as presented in the current study, would enable studies of how humans learn complex tasks in which error cannot be simply represented by a single number.

13.5 Conclusion

This study presented a mathematically rigorous system identification method for identifying dynamics of unperturbed balance. With a biomechanically reasonable

model of the multi-joint human body, the gains of a state-feedback controller can also be estimated without any information about the system's noise strength. A numerical example with a double inverted pendulum model of human quiet standing validated the method.

Methods to assess human motor control have significant practical importance. They may allow quantitative diagnosis of individual patients and development of customized treatment plans. With an aging population, technology-assisted human mobility is a growing need. The methods presented here may allow better assessment of technology-assisted mobility, which may eventually lead to development of customized assistive and / or rehabilitative technologies.

This work established that system identification of unperturbed balance is possible with several testable assumptions. Application of the proposed method to the real-world experimental data is on-going, led by Rika Sugimoto-Dimitrova.

13.6 Appendix: Ordinary Least Squares

For the zero-mean discrete timeseries $\{\mathbf{z}_t\}_1^N$ obtained from the system (13.1),

$$\begin{aligned}
\mathbf{z}_{t+1} &= \mathbf{H}\mathbf{x}_{t+1} + \mathbf{v}_{t+1} \\
&= \mathbf{H}(\mathbf{A}\mathbf{x}_t + \mathbf{G}\mathbf{w}_t) + \mathbf{v}_{t+1} \\
&= \mathbf{H}\mathbf{A}\mathbf{H}^{-1}(\mathbf{z}_t - \mathbf{v}_t) + \mathbf{H}\mathbf{G}\mathbf{w}_t + \mathbf{v}_{t+1} \\
&= \mathbf{H}\mathbf{A}\mathbf{H}^{-1}\mathbf{z}_t - \mathbf{H}\mathbf{A}\mathbf{H}^{-1}\mathbf{v}_t + \mathbf{H}\mathbf{G}\mathbf{w}_t + \mathbf{v}_{t+1},
\end{aligned}$$

one can form the over-determined system

$$\underbrace{\begin{pmatrix} \mathbf{z}_2^T \\ \mathbf{z}_3^T \\ \vdots \\ \mathbf{z}_N^T \end{pmatrix}}_{\mathbf{T}} = \underbrace{\begin{pmatrix} \mathbf{z}_1^T \\ \mathbf{z}_2^T \\ \vdots \\ \mathbf{z}_{N-1}^T \end{pmatrix}}_{\mathbf{W}} \underbrace{(\mathbf{H}\mathbf{A}\mathbf{H}^{-\mathbf{1}})^T}_{\mathbf{\Phi}}$$

or succinctly

$$\mathbf{T} = \mathbf{W}\mathbf{\Phi}$$

which can be readily solved using the usual least-squares estimator

$$\begin{aligned}
\hat{\mathbf{\Phi}}_{\text{OLS}} &= (\mathbf{W}^T\mathbf{W})^{-1}\mathbf{W}^T\mathbf{T} \\
&= (\mathbf{z}_1\mathbf{z}_1^T + \cdots + \mathbf{z}_{N-1}\mathbf{z}_{N-1}^T)^{-1}(\mathbf{z}_1\mathbf{z}_2^T + \cdots + \mathbf{z}_{N-1}\mathbf{z}_N^T) \\
&= \hat{\mathbf{R}}_{\mathbf{zz}}(0)^{-1}\hat{\mathbf{R}}_{\mathbf{zz}}(1) \\
&= (\mathbf{H}\hat{\mathbf{A}}_{\text{OLS}}\mathbf{H}^{-1})^T
\end{aligned}$$

Rearranging, the ordinary least squares estimate is obtained as

$$\hat{\mathbf{A}}_{\text{OLS}} = \mathbf{H}^{-1}\hat{\mathbf{R}}_{\mathbf{zz}}(1)\hat{\mathbf{R}}_{\mathbf{zz}}(0)^{-1}\mathbf{H} \tag{13.21}$$

which is equivalent to (13.8) with $k = 0$.

13.7 Appendix: Yule-Walker Equations for Multivariate Autoregressive Models

If one assumes a zero-mean discrete timeseries $\{\mathbf{z}_t\}_1^N$ is an autoregressive process, a method to estimate the appropriate order p of the model

$$\mathbf{z}_t = \mathbf{A}_1\mathbf{z}_{t-1} + \mathbf{A}_2\mathbf{z}_{t-2}\cdots + \mathbf{A}_p\mathbf{z}_{t-p} + \mathbf{e}(t)$$

and the corresponding coefficients $\mathbf{A}_j$ can be established. By multiplying $\mathbf{z}_{t-k}^T$ to each side of equation, taking expectation, and noting that $E\{\mathbf{e}(t)\mathbf{z}(t-k)^T\} = \mathbf{0}$, one can obtain

$$\mathbf{R}_{\mathbf{zz}}(k) = \mathbf{A}_1\mathbf{R}_{\mathbf{zz}}(k-1) + \mathbf{A}_2\mathbf{R}_{\mathbf{zz}}(k-2) + \mathbf{A}_p\mathbf{R}_{\mathbf{zz}}(k-p), \forall k > 0$$

Substituting $k = 1, 2, \cdots, p$ in the above equation, with $\mathbf{R_{zz}}(k)^T = \mathbf{R_{zz}}(-k)$, one can obtain the set of equations referred to as the Yule-Walker equations [13, 238]:

$$\begin{aligned}
\mathbf{R_{zz}}(1) &= \mathbf{A}_1\mathbf{R_{zz}}(0) + \mathbf{A}_2{\mathbf{R_{zz}}}^T(1) + \mathbf{A}_p{\mathbf{R_{zz}}}^T(p-1) \\
\mathbf{R_{zz}}(2) &= \mathbf{A}_1\mathbf{R_{zz}}(1) + \mathbf{A}_2\mathbf{R_{zz}}(0) + \mathbf{A}_p{\mathbf{R_{zz}}}^T(p-2) \\
&\vdots \\
\mathbf{R_{zz}}(p) &= \mathbf{A}_1\mathbf{R_{zz}}(p-1) + \mathbf{A}_2\mathbf{R_{zz}}(p-2) + \mathbf{A}_p\mathbf{R_{zz}}(0)
\end{aligned}$$

which can also be written as

$$\underbrace{\Big(\mathbf{R_{zz}}(1), \mathbf{R_{zz}}(2), \cdots, \mathbf{R_{zz}}(p)\Big)}_{\tilde{\mathbf{r}}}$$

$$= \underbrace{\Big(\mathbf{A}_1, \mathbf{A}_2, \cdots, \mathbf{A}_p\Big)}_{\mathbf{\Phi}} \underbrace{\begin{pmatrix} \mathbf{R_{zz}}(0) & \mathbf{R_{zz}}(1) & \cdots & \mathbf{R_{zz}}(p-1) \\ {\mathbf{R_{zz}}}^T(1) & \mathbf{R_{zz}}(0) & \cdots & \mathbf{R_{zz}}(p-2) \\ \vdots & & & \\ {\mathbf{R_{zz}}}^T(p-1) & \mathbf{R_{zz}}(p-2) & \cdots & \mathbf{R_{zz}}(0) \end{pmatrix}}_{\tilde{\mathbf{R}}}$$

or succinctly

$$\tilde{\mathbf{r}} = \mathbf{\Phi}\tilde{\mathbf{R}}$$

Note that this is a well-posed system with the same number of equations as unknowns. The matrix $\tilde{\mathbf{R}}$ is full-rank and symmetric, so that invertibility is guaranteed. Therefore the coefficients or the system parameters $\mathbf{\Phi}$ can be estimated by

$$\hat{\mathbf{\Phi}} = \tilde{\mathbf{r}}\tilde{\mathbf{R}}^{-1}$$

There are various ways to determine the order of the system p. For example, the proper order p can be determined by minimizing the Akaike information criterion

(AIC). Readers are referred to [13] for more details. Note that for the model with order $p = 1$, the resultant parameter estimate of $\hat{\mathbf{A}}_1$ is the same as the ordinary least squares method, i.e., $\hat{\mathbf{A}}_1 = \mathbf{R_{zz}}(1)\mathbf{R_{zz}}(0)^{-1}$

13.8 Appendix: Discrete-to-Continuous Conversion

The method described in this work is based on discrete-time system model, but sometimes continuous-time models are more convenient. In such cases, the discrete-time system parameters obtained using the new method should be properly converted to continuous-time approximation.

In the example in **Balance Model**, we used semi-implicit Euler integrator to integrate forward dynamics. Therefore the conversion from the continuous-time system parameters $\mathbf{A}_\mathrm{c}$ to its discrete-time counterpart $\mathbf{A}_\mathrm{d}$ becomes

$$\mathbf{A}_\mathrm{d} = \begin{bmatrix} \mathbf{I} & dt\mathbf{I} \\ \mathbf{0} & \mathbf{I} \end{bmatrix} + \begin{bmatrix} \mathbf{0} & dt^2\mathbf{I} \\ \mathbf{0} & dt\mathbf{I} \end{bmatrix} \mathbf{A}_\mathrm{c}$$

where dt is the sample time interval. If we assume that the top rows of $\mathbf{A}_\mathrm{c}$ are $[\mathbf{0}, \mathbf{I}]$,

$$\mathbf{A}_\mathrm{d} = \begin{bmatrix} \mathbf{I} & \mathbf{0} \\ \mathbf{0} & \mathbf{I} \end{bmatrix} + \begin{bmatrix} dt\mathbf{I} & dt^2\mathbf{I} \\ \mathbf{0} & dt\mathbf{I} \end{bmatrix} \mathbf{A}_\mathrm{c}$$

therefore the discrete-time to continuous-time conversion is obtained as

$$\mathbf{A}_\mathrm{c} = \frac{1}{dt} \begin{bmatrix} \mathbf{I} & -dt\mathbf{I} \\ \mathbf{0} & \mathbf{I} \end{bmatrix} \left(\mathbf{A}_\mathrm{d} - \begin{bmatrix} \mathbf{I} & \mathbf{0} \\ \mathbf{0} & \mathbf{I} \end{bmatrix} \right)$$

13.9 Appendix: Stability Assessment of Rhythmic Movement

Orbital stability of a limit cycle in state-space has one-to-one correspondence to the stability of a discrete return map, or Poincarè map. The eigenvalues of the linearized

Poincaré map are called characteristic or Floquet multipliers [202, 224].

The Poincarè map $\mathbf{x} \mapsto P(\mathbf{x})$ relates the state of a system after one cycle ($\mathbf{x}_{t+1}$) and its current state ($\mathbf{x}_t$): $\mathbf{x}_{t+1} = P(\mathbf{x}_t)$. It follows that limit cycle trajectories correspond to the fixed point ($\mathbf{x}^*$) of the map, $\mathbf{x}^* = P(\mathbf{x}^*)$, and the (local) orbital stability of the limit cycle is equivalent to the stability of the corresponding fixed point of the map on the Poincarè section. To evaluate the effects of small perturbations on $\mathbf{x}^*$, the Poincarè map can be linearized:

$$\mathbf{x}_{t+1} - \mathbf{x}^* = \frac{\partial P}{\partial \mathbf{x}}|_{(\mathbf{x}=\mathbf{x}^*)}(\mathbf{x}_t - \mathbf{x}^*)$$

Denoting $\mathbf{A_p} = \frac{\partial P}{\partial \mathbf{x}}|_{(\mathbf{x}=\mathbf{x}^*)}$ and assuming $\mathbf{x}^* = \mathbf{0}$ without loss of generality, also assuming white process and measurement noise, we obtain the following expression,

$$\begin{cases} \mathbf{x}_{t+1} = \mathbf{A_p}\mathbf{x}_t + \mathbf{G}\mathbf{w}_t \\ \mathbf{z}_t = \mathbf{H}\mathbf{x}_t + \mathbf{v}_t \end{cases}$$

to which (13.9) can be readily applied to obtain $\hat{\mathbf{A}}_\mathbf{p}$. The maximum Floquet multiplier is the eigenvalue of $\hat{\mathbf{A}}_\mathbf{p}$ with the largest modulus.

Chapter 14

Concluding Remarks

14.1 Summary and Discussion

In this part, two complementary methods to quantify normal balance control were presented. Quantifying normal balance control without applying perturbations is not a trivial problem. A major challenge is that we can only measure the output sway and the driving signals, the internal biological noise, are not directly measurable without invasion. This prevents using typical optimization or machine learning techniques to find optimal model parameters that minimize RMS time-domain errors between actual and simulated trajectories. Both of the two methods we developed resolved this challenge. Further improvements of the methods and application of the methods to the various data sets are already on-going by my colleagues Kaymie Shiozawa and Rika Sugimoto-Dimitrova.

One of the major accomplishments of Chapter 12 is that we analytically proved that a single inverted pendulum model could not reproduce the ground reaction force pattern observed in experiments, no matter what controller was used. This is not at all an 'obvious' result. Note that we investigated human balance in sagittal-plane standing, which has been modeled as a single inverted pendulum in a vast number of previous studies - by far this is the most common biomechanical model used in the literature [147]. As demonstrated, developing a simple model may seem trivial, but developing a *simple but competent* model is not at all obvious and requires (and

facilitates) keen insight.

While human behaviors are largely complex with their internally complicated neuro-musculo-skeletal structures, their apparent behaviors can be simple. The small number of parameters required to estimate simple models is advantageous and practical to quantify individual human data. Moreover, the quantified data of young and healthy individuals will serve as a reference to assess balance control of older and/or neurologically impaired populations. The severity of impaired balance can be quantified by calculating its deviation from normal. The methods provided here hence would be useful to design and follow-up personalized training.

Fall-related injuries due to loss of balance, frequently observed in the elderly population, pose a significant threat to life [177]. Both methods presented in this work hence have significant practical importance. Both methods do not require expensive, high-precision in-lab systems (e.g., systems to apply external perturbations, motion capture system requiring a number of built-in cameras and markers). A single force plate (Chapter 12) or a modest-precision motion measurement system (Chapter 13) are deemed enough. This is advantageous to develop human balance diagnosis systems, perhaps outside the lab. With the rapid development of motion measurement technologies e.g. wearable sensors (goniometers or IMUs) or inexpensive and machine-learning based image processing technologies, this seems promising.

Part IV

Conclusion

Chapter 15

Discussion and Conclusion

15.1 Summary

In this thesis, I designed, conducted, and / or participated in healthy human experiments to investigate how simple mechanical interventions alter human locomotion (balance and walking), quantified behavioral changes to understand their neuro / mechanical origins, developed simple models to account for experimental observations and gain insight, and developed methods to quantitatively assess human balance without applying perturbations.

15.2 Human Adaptation to Mechanical Interventions: Significant, but Not Known a Priori

The most important lesson we learned is that different interventions may evoke very different behavioral responses; and the results are unknown a priori. In Part I, we showed that different interventions based on the same device (Samsung GEMS-H) may evoke quite different behavioral responses. Applying periodic pulses evoked motor adaptation; on the other hand, applying stiffness evoked immediate changes, implying that only peripheral neuro-mechanics was involved. In Part II, we showed that altering mechanical interfaces by wearing rigid soles or using canes significantly

altered human balancing, but they did not seem to evoke changes in central neural processes.

None of these results were able to be precisely predicted before conducting human experiments. The quantification and modeling conducted in these studies will serve as foundation to understand neuro-mechanical behavior of human locomotion and to understand the effects of the mechanical interventions on human balance. Understanding how humans alter their behavior due to mechanical interventions will provide significant information for developing effective devices and interventions for assisting, augmenting, and restoring human locomotion.

To make progress, neither just theory nor just experiment would work; experiments and theories must complement each other. Falsifiable predictions made by theories should be validated by experiments and extensive data require theories and descriptive models for proper interpretation [10]. Experiments should guide models, and theories and models should inspire new experiments. In this iterative process, simple models play a powerful role.

15.3 Simple Models Promote Insights

While complex theoretical models and data-driven computational approaches are prevalent, the importance of simple models should not be dismissed. Recently, high-fidelity human models with anatomical and physiological details (with all the bones, muscles, muscular dynamics, and some of reflex responses) have made substantial progress [43, 194]. Those complex models are used to not only analyze observation but also to predict and understand human locomotion with interventions [35, 52, 128, 195, 196]. With advanced computational techniques and machine learning tool-boxes, and with the rise in computing power, using high-fidelity models seems more promising than ever. However, in this thesis, we heavily used simple models. Why are we still investigating simple models? Aren't they too simple to correctly predict details of experimental data?

In fact, it is challenging even for the most complex existing models to precisely

predict the effects of a novel intervention on human locomotion. For example, our recent study showed that computational models could not exactly reproduce how human walking changes with a hip exoskeleton robot [2], and it was hard to understand why; complex models often obscure insights due to their large number of tunable parameters. Even though not straightforward, one may add additional components to correct the model [35], but even this 'corrected' model is unlikely to reproduce 'all' testable human behaviors. Building a perfect human model faces fundamental limitation that humans are vastly complex biological systems and we do not have access to all levels of signals.

At this point we should admit that "all models are wrong, but some are useful" (by the statistician George Box [25, 26]). While no model (remember it is a model) can be 'true', a model can be useful if it properly encapsulates the phenomena of interest. Unnecessary details are rather to be removed than retained. This shares the philosophy of parsimony with the famous 'Occam's razor' and another famous aphorism "everything should be made as simple as possible, but not simpler" by Dr. Albert Eistein[1].

Simple models are simple, and due to their simplicity, they cannot predict all aspects of human behaviors. However, the goal of modeling is insight, not just prediction. The models developed or presented in this thesis *deliberately* did not address neuro-physiological details (e.g. individual muscle activities), but they still provide us with several important insights. So, what insight?

15.3.1 What Insights?

First, simple models are useful to identify essential features to reproduce a behavior, i.e., sufficient conditions. With this, we can sometimes reject a 'wrong necessary condition', even if they are a widely-accepted and dominant theory. For example, Ahn and Hogan showed that long-range correlations in stride intervals may not require

[1]It turned out that people have paraphrased his original (and long) statement into a 'simple as possible' form. See an interesting short blog article: `https://quoteinvestigator.com/2011/05/13/einstein-simple/#more-2363`

chaotic walking dynamics [6]. In this thesis, I identified that a context-based switching is required to reproduce two different exoskeleton experiment. This was not obvious before delving into the math.

This also helps to dissociate contribution of neural control and biomechanics when analyzing human behaviors. In Chapter 8 and Chapter 12, investigating simple models concluded that the observed human behaviors cannot be a mere consequence of mechanical constraints.

Second, simple models provide clear conceptual understanding of mechanisms to make testable predictions. For example, a 'necessary consequence' of limit cycle oscillators is that they are entrained when coupled to another oscillator. This understanding enabled us to design experiments to apply pulse torques to humans during walking to assess whether a limit cycle oscillator is a competent descriptive model for human walking [5, 108, 111].

Third, simple models allow for quantifying human behaviors with a handful of parameters, and the known structures of the simple models facilitate the parameter fitting process (for example, see 12). This would be important for diagnosis of individuals and to provide customized therapy in clinical studies.

Last but not least, simple models provide a perspective or framework to ask 'right questions' when interpreting experimental data. Another necessary consequence of nonlinear dynamics of coupled oscillators is that entrainment does not always occur. In general, coupling strength and frequency difference between two oscillators determine when entrainment would occur (the so-called Arnold's Tongue structure [63]). To those who have such conceptual understanding, it is not surprising that human subjects did not always synchronize their gait frequency to the robot. Rather, they would ask more interesting questions such as 'what are the parameters that determine the coupling strength for this intervention?', which would be useful to make progress.

15.3.2 Caveats

One important caveat should be emphasized. While simple models can reject 'wrong necessary conditions', rejecting 'alternative sufficient conditions' requires care. Using

the example of [6], this study cannot rule out the possibility that human walking dynamics may be chaotic. The simple *descriptive* models provided in this thesis also cannot rule out other possible mechanisms.

Another caveat is that there is no golden rule to determine how simple the model should be. For those who are interested in muscle activities, a double-inverted pendulum model for human balance is just too simple. It all depends on the phenomenon of interest, and the perspective of a researcher. For example, a walking model that reasonably described speed-step length relationship [100] predicted that applying stiffness between thighs would significantly affect gait frequency, which was not consistent with our experiments (Chapter 4). However, this is just because the purpose of the model was not to interpret human walking with exoskeleton robot.

15.4 Open Questions for Future Studies

There are several important questions to be addressed to advance the field.

First, the high-level control objective of human locomotion should be identified. When we simplify human motor control, identifying the right representation and control variables is important. For example, controlling a limb during walking can be done using a Cartesian impedance control rather than a joint impedance control. Humans may care about absolute angles rather than relative angles between limbs when balancing. Distinguishing controlled behavior and emergent behavior is difficult, but it can be done experimentally, supported by a careful modeling studies. For example, applying stiffness using a hip exoskeleton robot found that humans may be indifferent to changes in kinematics as long as inter-leg symmetric pattern is preserved.

Second, a unifying experimental and theoretical framework of human locomotion that integrates walking and balance should be developed. As deeply discussed in [11], there is a huge disciplinary divide in the investigation of balance and walking, while walking and balance are integrated motor behaviors required for locomotion. To fully understand the stability and versatility of human locomotion, and to develop systems to assist or augment human locomotion in the real-world, a unifying frame-

work is necessary. Moreover, transient behaviors should be more deeply investigated for assisting versatile human locomotion. For example, how humans accelerate and decelerate? How humans initiate and terminate walking?

Third, for practical and clinical purposes, we need to understand 'why' some interventions evoked central neural processes to adapt (promising for neuro-recovery), while others did not (promising for compensation). To generalize the scientific findings, we should keep asking 'what class of intervention' can be useful, rather than 'what particular intervention' can be. For example, does state-dependent intervention evoke qualitatively different behaviors than time-dependent intervention? Is inter-leg coordination a key to evoke motor adaptation? What characteristics of interventions can encapsulate all the interventions tested in this study that elicited immediate responses not adaptation?

15.5 Conclusion

Human behavioral experiments and modeling can be a complementary source of insight. Not only can models aid our understanding of how the behavioral observations arise, but they can also produce new predictions to inform the design of subsequent experiments. Advancing robotic technologies will allow for systematically testing different interventions in ecological context. With understanding of fundamentals of human locomotion and how they interact with robotic interventions, developing successful and effective devices for human locomotion that meet our demand will be possible.

Bibliography

[1] Muhammad Abdallah and Ambarish Goswami. A biomechanically motivated two-phase strategy for biped upright balance control. In Robotics and Automation, 2005. ICRA 2005. Proceedings of the 2005 IEEE International Conference on, pages 1996–2001. IEEE, 2005.

[2] Banu Abdikadirova, Jongwoo Lee, Neville Hogan, and Meghan Huber. Muscle-reflex model of human locomotion entrains to mechanical perturbations. In 2021 IEEE/RSJ International Conference on Intelligent Robots and Systems (IROS). IEEE, 2021 (Under Review).

[3] Masaki O Abe and Dagmar Sternad. Directionality in distribution and temporal structure of variability in skill acquisition. Frontiers in Human Neuroscience, 7:225, 2013.

[4] Jooeun Ahn and Neville Hogan. A simple state-determined model reproduces entrainment and phase-locking of human walking. PloS one, 7(11):e47963, 2012.

[5] Jooeun Ahn and Neville Hogan. Walking is not like reaching: evidence from periodic mechanical perturbations. PloS one, 7(3):e31767, 2012.

[6] Jooeun Ahn and Neville Hogan. Long-range correlations in stride intervals may emerge from non-chaotic walking dynamics. PloS one, 8(9):e73239, 2013.

[7] Jooeun Ahn and Neville Hogan. Improved assessment of orbital stability of rhythmic motion with noise. PloS one, 10(3), 2015.

[8] Jooeun Ahn, Tara Patterson, Hyunglae Lee, Daniel Klenk, Albert Lo, Hermano Igo Krebs, and Neville Hogan. Feasibility of entrainment with ankle mechanical perturbation to treat locomotor deficit of neurologically impaired patients. In Engineering in Medicine and Biology Society, EMBC, 2011 Annual International Conference of the IEEE, pages 7474–7477. IEEE, 2011.

[9] Jooeun Ahn, Zhaoran Zhang, and Dagmar Sternad. Noise induces biased estimation of the correction gain. PloS one, 11(7):e0158466, 2016.

[10] Robert Ajemian and Neville Hogan. Experimenting with theoretical motor neuroscience. Journal of motor behavior, 42(6):333–342, 2010.

[11] Jessica L. Allen and Lena H. Ting. Why is neuromechanical modeling of balance and locomotion so hard? In Boris I. Prilutsky and Donald H. Edwards, editors, Neuromechanical Modeling of Posture and Locomotion, pages 197–223. Springer, New York, 2016.

[12] F Alton, L Baldey, S Caplan, and MC Morrissey. A kinematic comparison of overground and treadmill walking. Clinical biomechanics, 13(6):434–440, 1998.

[13] Charles W Anderson, Erik A Stolz, and Sanyogita Shamsunder. Multivariate autoregressive models for classification of spontaneous electroencephalographic signals during mental tasks. IEEE Transactions on Biomedical Engineering, 45(3):277–286, 1998.

[14] Shinya Aoi, Poramate Manoonpong, Yuichi Ambe, Fumitoshi Matsuno, and Florentin Wörgötter. Adaptive control strategies for interlimb coordination in legged robots: a review. Frontiers in neurorobotics, 11:39, 2017.

[15] Shinya Aoi and Kazuo Tsuchiya. Locomotion control of a biped robot using nonlinear oscillators. Autonomous robots, 19(3):219–232, 2005.

[16] Shinya Aoi and Kazuo Tsuchiya. Stability analysis of a simple walking model driven by an oscillator with a phase reset using sensory feedback. IEEE Transactions on robotics, 22(2):391–397, 2006.

[17] Yoshiyuki Asai, Yuichi Tasaka, Kunihiko Nomura, Taishin Nomura, Maura Casadio, and Pietro Morasso. A model of postural control in quiet standing: robust compensation of delay-induced instability using intermittent activation of feedback control. PLoS One, 4(7):e6169, 2009.

[18] Amy J Bastian. Understanding sensorimotor adaptation and learning for rehabilitation. Current opinion in neurology, 21(6):628, 2008.

[19] Hamid Bateni and Brian E Maki. Assistive devices for balance and mobility: benefits, demands, and adverse consequences. Archives of physical medicine and rehabilitation, 86(1):134–145, 2005.

[20] Michaël Bertrand-Charette, Jens Bo Nielsen, and Laurent J Bouyer. A simple, clinically applicable motor learning protocol to increase push-off during gait: A proof-of-concept. Plos one, 16(1):e0245523, 2021.

[21] Andreanne Blanchette, Helene Moffet, Jean-Sébastien Roy, and Laurent J Bouyer. Effects of repeated walking in a perturbing environment: a 4-day locomotor learning study. Journal of neurophysiology, 108(1):275–284, 2012.

[22] Glen M Blenkinsop, Matthew TG Pain, and Michael J Hiley. Balance control strategies during perturbed and unperturbed balance in standing and handstand. Royal Society open science, 4(7):161018, 2017.

[23] Boualem Boashash. Estimating and interpreting the instantaneous frequency of a signal. i. fundamentals. Proceedings of the IEEE, 80(4):520–538, 1992.

[24] Wendy L. Boehm, Kieran M. Nichols, and Kreg G. Gruben. Frequency-dependent contributions of sagittal-plane foot force to upright human standing. Journal of biomechanics, 83:305–309, 2019.

[25] George EP Box. Science and statistics. Journal of the American Statistical Association, 71(356):791–799, 1976.

[26] George EP Box. Robustness in the strategy of scientific model building. In Robustness in statistics, pages 201–236. Elsevier, 1979.

[27] David J Braun, S Apte, Olzhas Adiyatov, Abhinav Dahiya, and Neville Hogan. Compliant actuation for energy efficient impedance modulation. In 2016 IEEE International Conference on Robotics and Automation (ICRA), pages 636–641. IEEE, 2016.

[28] David J Braun, Vincent Chalvet, Tze-Hao Chong, Salil S Apte, and Neville Hogan. Variable stiffness spring actuators for low-energy-cost human augmentation. IEEE Transactions on Robotics, 35(6):1435–1449, 2019.

[29] Forbes T Brown. Engineering system dynamics: a unified graph-centered approach. CRC press, 2006.

[30] SM Bruijn, OG Meijer, PJ Beek, and JH Van Dieën. Assessing the stability of human locomotion: a review of current measures. Journal of the Royal Society Interface, 10(83):20120999, 2013.

[31] Maria Federica Bruni, Corrado Melegari, Maria Cristina De Cola, Alessia Bramanti, Placido Bramanti, and Rocco Salvatore Calabrò. What does best evidence tell us about robotic gait rehabilitation in stroke patients: a systematic review and meta-analysis. Journal of Clinical Neuroscience, 48:11–17, 2018.

[32] Etienne Burdet, Rieko Osu, David W Franklin, Theodore E Milner, and Mitsuo Kawato. The central nervous system stabilizes unstable dynamics by learning optimal impedance. Nature, 414(6862):446–449, 2001.

[33] Joshua M Caputo and Steven H Collins. An experimental robotic testbed for accelerated development of ankle prostheses. In 2013 IEEE International Conference on Robotics and Automation, pages 2645–2650. IEEE, 2013.

[34] James R Chagdes, Shirley Rietdyk, Jeffrey M Haddad, Howard N Zelaznik, Michael E Cinelli, Luke T Denomme, Kaley C Powers, and Arvind Raman. Limit cycle oscillations in standing human posture. Journal of biomechanics, 49(7):1170–1179, 2016.

[35] Vaughn Chambers and Panagiotis Artemiadis. A model-based analysis of supraspinal mechanisms of inter-leg coordination in human gait: Toward model-informed robot-assisted rehabilitation. IEEE Transactions on Neural Systems and Rehabilitation Engineering, 29:740–749, 2021.

[36] Won Hyuk Chang and Yun-Hee Kim. Robot-assisted therapy in stroke rehabilitation. Journal of stroke, 15(3):174, 2013.

[37] Enrico Chiovetto, Meghan E Huber, Dagmar Sternad, and Martin A Giese. Low-dimensional organization of angular momentum during walking on a narrow beam. Scientific reports, 8(1):1–14, 2018.

[38] Hyundo Choi, Keehong Seo, Seungyong Hyung, Youngbo Shim, and Soo-Chul Lim. Compact hip-force sensor for a gait-assistance exoskeleton system. Sensors, 18(2):566, 2018.

[39] James J Collins and Carlo J De Luca. Open-loop and closed-loop control of posture: a random-walk analysis of center-of-pressure trajectories. Experimental brain research, 95(2):308–318, 1993.

[40] Loïc Damm, Déborah Varoqui, Valérie Cochen De Cock, Simone Dalla Bella, and Benoît Bardy. Why do we move to the beat? a multi-scale approach, from physical principles to brain dynamics. Neuroscience & Biobehavioral Reviews, 112:553–584, 2020.

[41] V Cochen De Cock, DG Dotov, P Ihalainen, V Bégel, F Galtier, C Lebrun, MC Picot, V Driss, N Landragin, C Geny, et al. Rhythmic abilities and musical training in parkinson's disease: do they help? NPJ Parkinson's disease, 4(1):1–8, 2018.

[42] Paolo De Leva. Adjustments to zatsiorsky-seluyanov's segment inertia parameters. Journal of biomechanics, 29(9):1223–1230, 1996.

[43] Scott L Delp, Frank C Anderson, Allison S Arnold, Peter Loan, Ayman Habib, Chand T John, Eran Guendelman, and Darryl G Thelen. Opensim: open-source software to create and analyze dynamic simulations of movement. IEEE transactions on biomedical engineering, 54(11):1940–1950, 2007.

[44] Ye Ding, Myunghee Kim, Scott Kuindersma, and Conor J Walsh. Human-in-the-loop optimization of hip assistance with a soft exosuit during walking. Science robotics, 3(15), 2018.

[45] Jonathan B Dingwell and Joseph P Cusumano. Re-interpreting detrended fluctuation analyses of stride-to-stride variability in human walking. Gait & posture, 32(3):348–353, 2010.

[46] Aaron M. Dollar and Hugh Herr. Lower extremity exoskeletons and active orthoses: Challenges and state-of-the-art. IEEE Transactions on Robotics, 24(1):144–158, 2008.

[47] Antoinette Domingo and Daniel P. Ferris. The effects of error augmentation on learning to walk on a narrow balance beam. Experimental Brain Research, 206(4):359–370, 2010.

[48] Antoinette Domingo and Daniel P. Ferris. Effects of physical guidance on short-term learning of walking on a narrow beam. Gait & Posture, 30(4):464—-468, 2010.

[49] Dobromir G Dotov, Valérie Cochen de Cock, Christian Geny, Petra Ihalainen, Bart Moens, Marc Leman, Benoît Bardy, and Simone Dalla Bella. The role of interaction and predictability in the spontaneous entrainment of movement. Journal of Experimental Psychology: General, 148(6):1041, 2019.

[50] Marcos Duarte and Dagmar Sternad. Complexity of human postural control in young and older adults during prolonged standing. Experimental Brain Research, 191(3):265–276, 2008.

[51] Pamela W Duncan, Katherine J Sullivan, Andrea L Behrman, Stanley P Azen, Samuel S Wu, Stephen E Nadeau, Bruce H Dobkin, Dorian K Rose, Julie K Tilson, Steven Cen, et al. Body-weight–supported treadmill rehabilitation after stroke. New England Journal of Medicine, 364(21):2026–2036, 2011.

[52] Florin Dzeladini, Jesse Van Den Kieboom, and Auke Ijspeert. The contribution of a central pattern generator in a reflex-based neuromuscular model. Frontiers in human neuroscience, 8:371, 2014.

[53] Jeremy L Emken, Raul Benitez, Athanasios Sideris, James E Bobrow, and David J Reinkensmeyer. Motor adaptation as a greedy optimization of error and effort. Journal of neurophysiology, 97(6):3997–4006, 2007.

[54] Denise Engelhart, Tjitske A Boonstra, Ronald GKM Aarts, Alfred C Schouten, and Herman van der Kooij. Comparison of closed-loop system identification techniques to quantify multi-joint human balance control. Annual reviews in control, 41:58–70, 2016.

[55] A Aldo Faisal, Luc PJ Selen, and Daniel M Wolpert. Noise in the nervous system. Nature reviews neuroscience, 9(4):292–303, 2008.

[56] Dominic James Farris and Gregory S Sawicki. The mechanics and energetics of human walking and running: a joint level perspective. Journal of The Royal Society Interface, 9(66):110–118, 2012.

[57] Roy Featherstone. A simple model of balancing in the plane and a simple preview balance controller. The International Journal of Robotics Research, 36(13-14):1489–1507, 2017.

[58] Valery L Feigin, Bo Norrving, and George A Mensah. Global burden of stroke. Circulation research, 120(3):439–448, 2017.

[59] Karine Fortin, Andreanne Blanchette, Bradford J McFadyen, and Laurent J Bouyer. Effects of walking in a force field for varying durations on aftereffects and on next day performance. Experimental brain research, 199(2):145, 2009.

[60] Xiang Gao, Jennie Si, Yue Wen, Minhan Li, and He Huang. Reinforcement learning control of robotic knee with human-in-the-loop by flexible policy iteration. IEEE Transactions on Neural Networks and Learning Systems, 2021.

[61] Roger Gassert and Volker Dietz. Rehabilitation robots for the treatment of sensorimotor deficits: a neurophysiological perspective. Journal of neuroengineering and rehabilitation, 15(1):1–15, 2018.

[62] Peter Gawthrop, Ian Loram, Martin Lakie, and Henrik Gollee. Intermittent control: a computational theory of human control. Biological cybernetics, 104(1-2):31–51, 2011.

[63] Leon Glass and Jiong Sun. Periodic forcing of a limit-cycle oscillator: Fixed points, arnold tongues, and the global organization of bifurcations. Physical Review E, 50(6):5077, 1994.

[64] Adam D Goodworth and Robert J Peterka. Identifying mechanisms of stance control: a single stimulus multiple output model-fit approach. Journal of neuroscience methods, 296:44–56, 2018.

[65] Keith E Gordon and Daniel P Ferris. Learning to walk with a robotic ankle exoskeleton. Journal of biomechanics, 40(12):2636–2644, 2007.

[66] Kreg G. Gruben and Wendy L. Boehm. Force direction pattern stabilizes sagittal plane mechanics of human walking. Human Movement Science, 31:649–659, 2012.

[67] Pierre A Guertin. Central pattern generator for locomotion: anatomical, physiological, and pathophysiological considerations. Frontiers in neurology, 3:183, 2013.

[68] Michael Günther, Sten Grimmer, Tobias Siebert, and Reinhard Blickhan. All leg joints contribute to quiet human stance: a mechanical analysis. Journal of biomechanics, 42(16):2739–2746, 2009.

[69] Christopher J Hasson, Zhaoran Zhang, Masaki O Abe, and Dagmar Sternad. Neuromotor noise is malleable by amplifying perceived errors. PLoS computational biology, 12(8):e1005044, 2016.

[70] Jeffrey M Hausdorff, CK Peng, ZVI Ladin, Jeanne Y Wei, and Ary L Goldberger. Is walking a random walk? evidence for long-range correlations in stride interval of human gait. Journal of applied physiology, 78(1):349–358, 1995.

[71] Joseph Hidler, Diane Nichols, Marlena Pelliccio, Kathy Brady, Donielle D Campbell, Jennifer H Kahn, and T George Hornby. Multicenter randomized clinical trial evaluating the effectiveness of the lokomat in subacute stroke. Neurorehabilitation and neural repair, 23(1):5–13, 2009.

[72] Neville Hogan. Physical interaction via dynamic primitives. In J.P. Laumond, N. Mansard, and J.B. Lasserre, editors, Geometric and numerical foundations of movements, pages 269–299. Springer, 2017.

[73] Neville Hogan and Dagmar Sternad. Dynamic primitives of motor behavior. Biological cybernetics, 106(11-12):727–739, 2012.

[74] Neville Hogan and Dagmar Sternad. Dynamic primitives in the control of locomotion. Frontiers in computational neuroscience, 7:71, 2013.

[75] F. B. Horak and L. M. Nashner. Central programming of postural movements: Adaptation to altered support-surface configurations. Journal of Neurophysiology, 55(6):1369–1381, 1986.

[76] Fay B. Horak. Postural orientation and equilibrium: What do we need to know about neural control of balance to prevent falls? In Age and Ageing, page ii7–ii11, 2006.

[77] Fay B Horak and Jane M Macpherson. Postural orientation and equilibrium. Comprehensive Physiology, pages 255–292, 2010.

[78] M. E. Huber, J. Lee, V. Agarwal, H. Warren, and N. Hogan. Overground gait patterns changed by modulating hip stiffness with a robotic exoskeleton. In 2020 8th IEEE RAS/EMBS International Conference for Biomedical Robotics and Biomechatronics (BioRob), pages 967–972, 2020.

[79] Meghan E Huber, Enrico Chiovetto, Martin Giese, and Dagmar Sternad. Rigid soles improve balance in beam walking, but improvements do not persist with bare feet. Scientific Reports, 10(1):1–17, 2020.

[80] Meghan E Huber and Dagmar Sternad. Implicit guidance to stable performance in a rhythmic perceptual-motor skill. Experimental brain research, 233(6):1783–1799, 2015.

[81] Fumiya Iida and Russ Tedrake. Minimalistic control of biped walking in rough terrain. Autonomous Robots, 28(3):355–368, 2010.

[82] Tamás Insperger, John Milton, and Gábor Stépán. Acceleration feedback improves balancing against reflex delay. Journal of the Royal Society Interface, 10(79):20120763, 2013.

[83] Arun Jayaraman, Megan K O'brien, Sangeetha Madhavan, Chaithanya K Mummidisetty, Heidi R Roth, Kristen Hohl, Annie Tapp, Kimberly Brennan, Masha Kocherginsky, Kenton J Williams, et al. Stride management assist exoskeleton

vs functional gait training in stroke: A randomized trial. Neurology, 92(3):e263–e273, 2019.

[84] John J Jeka. Light touch contact as a balance aid. Physical therapy, 77(5):476–487, 1997.

[85] John J Jeka, Randolph D Easton, Billie L Bentzen, and James R Lackner. Haptic cues for orientation and postural control. Perception & psychophysics, 58(3):409–423, 1996.

[86] John J Jeka and James R Lackner. Fingertip contact influences human postural control. Experimental brain research, 79(2):495–502, 1994.

[87] John J Jeka and James R Lackner. The role of haptic cues from rough and slippery surfaces in human postural control. Experimental Brain Research, 103(2):267–276, 1995.

[88] Matthew Johnson. Mixed (Between/Within Subjects) ANOVA. `https://www.mathworks.com/matlabcentral/fileexchange/27080-mixed-between-within-subjects-anova`. Retrieved January 20, 2021.

[89] Kelvin E Jones, Antonia F de C Hamilton, and Daniel M Wolpert. Sources of signal-dependent noise during isometric force production. Journal of neurophysiology, 88(3):1533–1544, 2002.

[90] Henrik S Jørgensen, Hirofumi Nakayama, Hans O Raaschou, and Tom S Olsen. Recovery of walking function in stroke patients: the copenhagen stroke study. Archives of physical medicine and rehabilitation, 76(1):27–32, 1995.

[91] Pei-Chun Kao, Cara L Lewis, and Daniel P Ferris. Short-term locomotor adaptation to a robotic ankle exoskeleton does not alter soleus hoffmann reflex amplitude. Journal of neuroengineering and rehabilitation, 7(1):1–8, 2010.

[92] H Stephen Kaye, Taewoon Kang, and Michell P LaPlante. Mobility Device Use in the United States. Disability Statistics Report 14. 2000.

[93] Tim Kiemel, Kelvin S. Oie, and John J. Jeka. Multisensory fusion and the stochastic structure of postural sway. Biological Cybernetics, 87(4):262–277, 2002.

[94] Tim Kiemel, Yuanfen Zhang, and John J Jeka. Identification of neural feedback for upright stance in humans: stabilization rather than sway minimization. Journal of Neuroscience, 31(42):15144–15153, 2011.

[95] Boudewijn Kollen, Gert Kwakkel, and Eline Lindeman. Longitudinal robustness of variables predicting independent gait following severe middle cerebral artery stroke: a prospective cohort study. Clinical rehabilitation, 20(3):262–268, 2006.

[96] Jeffrey R Koller, Daniel A Jacobs, Daniel P Ferris, and C David Remy. Learning to walk with an adaptive gain proportional myoelectric controller for a robotic ankle exoskeleton. Journal of neuroengineering and rehabilitation, 12(1):97, 2015.

[97] John W Krakauer. Motor learning: its relevance to stroke recovery and neurorehabilitation. Current opinion in neurology, 19(1):84–90, 2006.

[98] Hermano Igo Krebs, Jerome Joseph Palazzolo, Laura Dipietro, Mark Ferraro, Jennifer Krol, Keren Rannekleiv, Bruce T Volpe, and Neville Hogan. Rehabilitation robotics: Performance-based progressive robot-assisted therapy. Autonomous robots, 15(1):7–20, 2003.

[99] Arthur D. Kuo. An optimal control model for analyzing human postural balance. IEEE Transactions on Biomedical Engineering, 42:87–101, 1995.

[100] Arthur D Kuo. A simple model of bipedal walking predicts the preferred speed–step length relationship. J. Biomech. Eng., 123(3):264–269, 2001.

[101] Arthur D. Kuo and Felix E. Zajac. Human standing posture: Multi-joint movement strategies based on biomechanical constraints. Progress in Brain Research, 97:349–358, 1993.

[102] Francesco Lacquaniti, Yuri P Ivanenko, and Myrka Zago. Patterned control of human locomotion. The Journal of physiology, 590(10):2189–2199, 2012.

[103] Tania Lam, Martin Anderschitz, and Volker Dietz. Contribution of feedback and feedforward strategies to locomotor adaptations. Journal of neurophysiology, 95(2):766–773, 2006.

[104] Tania Lam, Katherine Pauhl, Amanda Ferguson, Raza N Malik, Andrei Krassioukov, and Janice J Eng. Training with robot-applied resistance in people with motor-incomplete spinal cord injury: Pilot study. Journal of Rehabilitation Research & Development, 52(1), 2015.

[105] E.A. Lauer, S.L. Boege, and A.J. Houtenville. Annual Disability Statistics Compendium: 2019. Durham, NH: University of New Hampshire, Institute on Disability, 2020. `https://files.eric.ed.gov/fulltext/ED605680.pdf`. [Accessed June 21, 2021].

[106] J. Lee, K. Seo, B. Lim, J. Jang, K. Kim, and H. Choi. Effects of assistance timing on metabolic cost, assistance power, and gait parameters for a hip-type exoskeleton. In 2017 International Conference on Rehabilitation Robotics (ICORR), pages 498–504, 2017.

[107] J. Lee, H. R. Warren, V. Agarwal, M. E. Huber, and N. Hogan. Modulating hip stiffness with a robotic exoskeleton immediately changes gait. In 2020 IEEE International Conference on Robotics and Automation (ICRA), pages 733–739, 2020.

[108] Jongwoo Lee, Devon Goetz, Meghan E Huber, and Neville Hogan. Feasibility of gait entrainment to hip mechanical perturbation for locomotor rehabilitation. In 2019 IEEE/RSJ International Conference on Intelligent Robots and Systems (IROS), pages 7343–7348. IEEE, 2019.

[109] Jongwoo Lee, Meghan E Huber, Enrico Chiovetto, Martin Giese, Dagmar Stemad, and Neville Hogan. Human-inspired balance model to account for foot-beam interaction mechanics. In 2019 International Conference on Robotics and Automation (ICRA), pages 1969–1974. IEEE, 2019.

[110] Jongwoo Lee, Meghan E Huber, and Neville Hogan. Applying hip stiffness with an exoskeleton to compensate gait kinematics. IEEE Transactions on Neural Systems and Rehabilitation Engineering, (Under Review).

[111] Jongwoo Lee, Meghan E Huber, and Neville Hogan. Gait entrainment to torque pulses applied by a hip exoskeleton. IEEE Transactions on Neural Systems and Rehabilitation Engineering, (Under Review).

[112] Jongwoo Lee, Meghan E Huber, Dagmar Stemad, and Neville Hogan. Robot controllers compatible with human beam balancing behavior. In 2018 IEEE/RSJ International Conference on Intelligent Robots and Systems (IROS), pages 3335–3341. IEEE, 2018.

[113] Jongwoo Lee, Kuangen Zhang, and Neville Hogan. Identifying human postural dynamics and control from unperturbed balance. Journal of NeuroEngineering and Rehabilitation, 18(1):1–15, 2021.

[114] Y. Lee, S. Roh, M. Lee, B. Choi, J. Lee, J. Kim, H. Choi, Y. Shim, and Y. Kim. A flexible exoskeleton for hip assistance. In 2017 IEEE/RSJ International Conference on Intelligent Robots and Systems (IROS), pages 1058–1063, 2017.

[115] Li-Ann Leow, Taylor Parrott, and Jessica A Grahn. Individual differences in beat perception affect gait responses to low-and high-groove music. Frontiers in human neuroscience, 8:811, 2014.

[116] Bokman Lim, Jusuk Lee, Junwon Jang, Kyungrock Kim, Young Jin Park, Keehong Seo, and Youngbo Shim. Delayed output feedback control for gait assistance with a robotic hip exoskeleton. IEEE Transactions on Robotics, 2019.

[117] David B Lipps, Emma M Baillargeon, Daniel Ludvig, and Eric J Perreault. Quantifying the multidimensional impedance of the shoulder during volitional contractions. Annals of biomedical engineering, 48(9):2354–2369, 2020.

[118] Daniel B Lockhart and Lena H Ting. Optimal sensorimotor transformations for balance. Nature neuroscience, 10(10):1329–1336, 2007.

[119] Ian D Loram and Martin Lakie. Direct measurement of human ankle stiffness during quiet standing: the intrinsic mechanical stiffness is insufficient for stability. The journal of physiology, 545(3):1041–1053, 2002.

[120] Ian D Loram, Constantinos N Maganaris, and Martin Lakie. Human postural sway results from frequent, ballistic bias impulses by soleus and gastrocnemius. The Journal of physiology, 564(1):295–311, 2005.

[121] Dennis R Louie and Janice J Eng. Powered robotic exoskeletons in post-stroke rehabilitation of gait: a scoping review. Journal of neuroengineering and rehabilitation, 13(1):1–10, 2016.

[122] Fernanda Lopes Magre, Thais Delamuta Ayres da Costa, Ana Clara de Souza Paiva, Renato Moraes, and Eliane Mauerberg-deCastro. Does the level of difficulty in balancing tasks affect haptic sensitivity via light touch? Journal of motor behavior, 2019.

[123] Clare C Maguire, Judith M Sieben, and Robert A de Bie. The influence of walking-aids on the plasticity of spinal interneuronal networks, central-pattern-generators and the recovery of gait post-stroke. a literature review and scholarly discussion. Journal of bodywork and movement therapies, 21(2):422–434, 2017.

[124] Jean Massion, Alexei Alexandrov, and Alexander Frolov. Why and how are posture and movement coordinated? Progress in brain research, 143:13–27, 2004.

[125] H. M. Maus, S. Lipfert, M. Gross, J. Rummel, and A. Seyfarth. Upright human gait did not provide a major mechanical challenge for our ancestors. Nature communications, 1(70):1–6, 2010.

[126] R Mehra. On-line identification of linear dynamic systems with applications to kalman filtering. IEEE Transactions on Automatic Control, 16(1):12–21, 1971.

[127] Jan Mehrholz, Simone Thomas, Joachim Kugler, Marcus Pohl, and Bernhard Elsner. Electromechanical-assisted training for walking after stroke. Cochrane Database of Systematic Reviews, (10), 2020.

[128] Matthew Millard, Manish Sreenivasa, and Katja Mombaur. Predicting the motions and forces of wearable robotic systems using optimal control. Frontiers in Robotics and AI, 4:41, 2017.

[129] Karen Minassian, Ursula S Hofstoetter, Florin Dzeladini, Pierre A Guertin, and Auke Ijspeert. The human central pattern generator for locomotion: Does it exist and contribute to walking? The Neuroscientist, 23(6):649–663, 2017.

[130] Franco Molteni, Eleonora Guanziroli, Michela Goffredo, Rocco Salvatore Calabrò, Sanaz Pournajaf, Marina Gaffuri, Giulio Gasperini, Serena Filoni, Silvano Baratta, Daniele Galafate, et al. Gait recovery with an overground powered exoskeleton: A randomized controlled trial on subacute stroke subjects. Brain Sciences, 11(1):104, 2021.

[131] Jeongin Moon, Prabhat Pathak, Sudeok Kim, Se-gon Roh, Changhyun Roh, Youngbo Shim, and Jooeun Ahn. Shoes with active insoles mitigate declines in balance after fatigue. Scientific Reports, 10:1–11, 2020.

[132] Luke M Mooney and Hugh M Herr. Biomechanical walking mechanisms underlying the metabolic reduction caused by an autonomous exoskeleton. Journal of neuroengineering and rehabilitation, 13(1):4, 2016.

[133] Pietro Morasso, Amel Cherif, and Jacopo Zenzeri. Quiet standing: The single inverted pendulum model is not so bad after all. PLoS ONE, 14(3), 2019.

[134] Pietro G Morasso, L Baratto, Roberto Capra, and Gino Spada. Internal models in the control of posture. Neural Networks, 12(7-8):1173–1180, 1999.

[135] Pietro G. Morasso and Marco Schieppati. Can muscle stiffness alone stabilize upright standing? Journal of Neurophysiology, 82(3):1622–1626, 1999.

[136] Dariush Mozaffarian, Emelia J Benjamin, Alan S Go, Donna K Arnett, Michael J Blaha, Mary Cushman, Sandeep R Das, Sarah De Ferranti, Jean-Pierre Després, Heather J Fullerton, et al. Heart disease and stroke statistics—2016 update: a report from the american heart association. circulation, 133(4):e38–e360, 2016.

[137] Debraj Mukherjee and Chirag G Patil. Epidemiology and the global burden of stroke. World neurosurgery, 76(6):S85–S90, 2011.

[138] Roy Müller, Christian Rode, Soran Aminiaghdam, Johanna Vielemeyer, and Reinhard Blickhan. Force direction patterns promote whole body stability even in hip-flexed walking, but not upper body stability in human upright walking. Proceedings of the Royal Society A: Mathematical, Physical and Engineering Sciences, 473(2207), 2017.

[139] Lewis M. Nashner and Gin McCollum. The organization of human postural movements: A formal basis and experimental synthesis. Behavioral and Brain Sciences, 8(1):135–150, 1985.

[140] Rezvan Nasiri, Arjang Ahmadi, and Majid Nili Ahmadabadi. Reducing the energy cost of human running using an unpowered exoskeleton. IEEE Transactions on Neural Systems and Rehabilitation Engineering, 26(10):2026–2032, 2018.

[141] Jeff A Nessler, Severne Heredia, Jacques Bélair, and John Milton. Walking on a vertically oscillating treadmill: phase synchronization and gait kinematics. PLoS one, 12(1):e0169924, 2017.

[142] Jeff A Nessler, Tavish Spargo, Andrew Craig-Jones, and John G Milton. Phase resetting behavior in human gait is influenced by treadmill walking speed. Gait & posture, 43:187–191, 2016.

[143] KM Newell, SM Slobounov, BS Slobounova, and PCM Molenaar. Short-term non-stationarity and the development of postural control. Gait & Posture, 6(1):56–62, 1997.

[144] Kailey Nishimura, Eva Martinez, Alexander Loeza, Jessica Parker, and Seung-Jae Kim. Effects of periodic sensory perturbations during electrical stimulation on gait cycle period. PloS one, 13(12):e0209781, 2018.

[145] Julieth Ochoa, Dagmar Sternad, and Neville Hogan. Treadmill vs. overground walking: different response to physical interaction. Journal of neurophysiology, 118(4):2089–2102, 2017.

[146] Shawn M. O'Connor and Art D. Kuo. Direction-dependent control of balance during walking and standing. Journal of Neurophysiology, 102(3):1411—-1419, 2009.

[147] Fredrik Olsson, Kjartan Halvorsen, and Anna Cristina Aberg. Neuromuscular controller models for quantifying standing balance in older people: A systematic review. IEEE Reviews in Biomedical Engineering, 2021.

[148] David E Orin, Ambarish Goswami, and Sung-Hee Lee. Centroidal dynamics of a humanoid robot. Autonomous robots, 35(2):161–176, 2013.

[149] Jerrom J Palazzolo. Robotic technology to aid and assess recovery and learning in stroke patients. PhD thesis, MIT, 2005.

[150] Chethan Pandarinath, Daniel J O'Shea, Jasmine Collins, Rafal Jozefowicz, Sergey D Stavisky, Jonathan C Kao, Eric M Trautmann, Matthew T Kaufman, Stephen I Ryu, Leigh R Hochberg, et al. Inferring single-trial neural population dynamics using sequential auto-encoders. Nature methods, 15(10):805–815, 2018.

[151] Fausto A Panizzolo, Gregory M Freisinger, Nikos Karavas, Asa M Eckert-Erdheim, Christopher Siviy, Andrew Long, Rebecca A Zifchock, Michael E LaFiandra, and Conor J Walsh. Metabolic cost adaptations during training with a soft exosuit assisting the hip joint. Scientific reports, 9(1):9779, 2019.

[152] Sukyung Park, Fay B Horak, and Arthur D Kuo. Postural feedback responses scale with biomechanical constraints in human standing. Experimental brain research, 154(4):417–427, 2004.

[153] Emanuel Parzen et al. An approach to time series analysis. The Annals of Mathematical Statistics, 32(4):951–989, 1961.

[154] Aftab E Patla. Understanding the roles of vision in the control of human locomotion. Gait & posture, 5(1):54–69, 1997.

[155] Kara K Patterson, William H Gage, Dina Brooks, Sandra E Black, and William E McIlroy. Evaluation of gait symmetry after stroke: a comparison of current methods and recommendations for standardization. Gait & posture, 31(2):241–246, 2010.

[156] James L. Patton and F. A. Mussa-Ivaldi. Robot-assisted adaptive training: custom force fields for teaching movement patterns. IEEE Transactions on Biomedical Engineering, 51(4):636–646, 2004.

[157] J Perry and JM Burnfield. Gait analysis: normal and pathological function. 2nd. Slack Incorporated, 2010.

[158] Robert J Peterka. Sensorimotor integration in human postural control. Journal of neurophysiology, 88(3):1097–1118, 2002.

[159] Ilona J Pinter, Roos Van Swigchem, AJ Knoek van Soest, and Leonard A Rozendaal. The dynamics of postural sway cannot be captured using a one-segment inverted pendulum model: a pca on segment rotations during unperturbed stance. Journal of neurophysiology, 100(6):3197–3208, 2008.

[160] BT Quinlivan, S Lee, P Malcolm, DM Rossi, M Grimmer, C Siviy, N Karavas, D Wagner, A Asbeck, I Galiana, et al. Assistance magnitude versus metabolic cost reductions for a tethered multiarticular soft exosuit. Sci Robot, 2(2):4416, 2017.

[161] David Quintero, Dario J Villarreal, Daniel J Lambert, Susan Kapp, and Robert D Gregg. Continuous-phase control of a powered knee–ankle prosthesis: Amputee experiments across speeds and inclines. IEEE Transactions on Robotics, 34(3):686–701, 2018.

[162] R Development Core Team. R Software, 2013.

[163] Denis Rancourt and Neville Hogan. Dynamics of pushing. Journal of motor behavior, 33(4):351–362, 2001.

[164] Denis Rancourt and Neville Hogan. Stability in force-production tasks. Journal of motor behavior, 33(2):193–204, 2001.

[165] Denis Rancourt and Neville Hogan. The biomechanics of force production. In Progress in Motor Control, pages 645–661. Springer, 2009.

[166] Emily A Ready, Lucy M McGarry, Cricia Rinchon, Jeffrey D Holmes, and Jessica A Grahn. Beat perception ability and instructions to synchronize influence gait when walking to music-based auditory cues. Gait & posture, 68:555–561, 2019.

[167] David J. Reinkensmeyer and James L. Patton. Can robots help the learning of skilled actions? Exercise and Sport Sciences Reviews, 37(1):43–51, 2009.

[168] Darcy S Reisman, Amy J Bastian, and Susanne M Morton. Neurophysiologic and rehabilitation insights from the split-belt and other locomotor adaptation paradigms. Physical therapy, 90(2):187–195, 2010.

[169] Darcy S Reisman, Hannah J Block, and Amy J Bastian. Interlimb coordination during locomotion: what can be adapted and stored? Journal of neurophysiology, 94(4):2403–2415, 2005.

[170] Darcy S Reisman, Robert Wityk, Kenneth Silver, and Amy J Bastian. Locomotor adaptation on a split-belt treadmill can improve walking symmetry post-stroke. Brain, 130(7):1861–1872, 2007.

[171] Darcy S Reisman, Robert Wityk, Kenneth Silver, and Amy J Bastian. Split-belt treadmill adaptation transfers to overground walking in persons poststroke. Neurorehabilitation and neural repair, 23(7):735–744, 2009.

[172] Shai Revzen, Samuel A Burden, Talia Y Moore, Jean-Michel Mongeau, and Robert J Full. Instantaneous kinematic phase reflects neuromechanical response to lateral perturbations of running cockroaches. Biological cybernetics, 107(2):179–200, 2013.

[173] Shai Revzen and John M Guckenheimer. Estimating the phase of synchronized oscillators. Physical Review E, 78(5):051907, 2008.

[174] Daniel Rigobon, Julieth Ochoa, and Neville Hogan. Entrainment of ankle-actuated walking model to periodic perturbations via leading leg angle control. In Dynamic Systems and Control Conference, volume 58271, page V001T36A002. American Society of Mechanical Engineers, 2017.

[175] Michael G Rosenblum, Arkady S Pikovsky, and Jürgen Kurths. Phase synchronization in driven and coupled chaotic oscillators. IEEE Transactions on Circuits and Systems I: Fundamental Theory and Applications, 44(10):874–881, 1997.

[176] L. A. Rozendaal and A. J. Van Soest. Stabilization of a multi-segment model of bipedal standing by local joint control overestimates the required ankle stiffness, 2008.

[177] Laurence Z Rubenstein and Karen R Josephson. Falls and their prevention in elderly people: what does the evidence show? Medical Clinics, 90(5):807–824, 2006.

[178] C. F. Runge, C. L. Shupert, F. B. Horak, and F. E. Zajac. Ankle and hip postural strategies defined by joint torques. Gait and Posture, 10(2):161–170, 1999.

[179] Marta Russo, Jongwoo Lee, Neville Hogan, and Dagmar Sternad Sternad. Mechanical effects of canes on postural control: Beyond perceptual information. (in preparation).

[180] Shun Sasagawa, Masahiro Shinya, and Kimitaka Nakazawa. Interjoint dynamic interaction during constrained human quiet standing examined by induced acceleration analysis. Journal of neurophysiology, 111(2):313–322, 2014.

[181] Andrew Sawers, Jessica L. Allen, and Lena H. Ting. Long-term training modifies the modular structure and organization of walking balance control. Journal of Neurophysiology, 114(6):3359–3373, 2015.

[182] Andrew Sawers and Lena H Ting. Beam walking can detect differences in walking balance proficiency across a range of sensorimotor abilities. Gait & posture, 41(2):619–623, 2015.

[183] Gregory S Sawicki, Owen N Beck, Inseung Kang, and Aaron J Young. The exoskeleton expansion: improving walking and running economy. Journal of NeuroEngineering and Rehabilitation, 17(1):1–9, 2020.

[184] Arlene Schmid, Pamela W Duncan, Stephanie Studenski, Sue Min Lai, Lorie Richards, Subashan Perera, and Samuel S Wu. Improvements in speed-based gait classifications are meaningful. Stroke, 38(7):2096–2100, 2007.

[185] Matthew A Schrager, Valerie E. Kelly, Robert Price, Luigi Ferrucci, and Anne Shumway-Cook. The effects of age on medio-lateral stability during normal and narrow base walking. Gait & Posture, 28(3):466—-471, 2008.

[186] Ryan Schroeder, James Croft, and John Bertram. The role of entrainment in human walking: Energy minimization in oscillating environments (under review). Scientific Reports, 2020.

[187] Timothy Schumann, Mark S Redfern, Joseph M Furman, Amro El-Jaroudi, and Luis F Chaparro. Time-frequency analysis of postural sway. Journal of biomechanics, 28(5):603–607, 1995.

[188] Nidhi Seethapathi. Transients, variability, stability and energy in human locomotion. PhD thesis, The Ohio State University, 2018.

[189] Keehong Seo, Jusuk Lee, Younbaek Lee, Taesin Ha, and Youngbo Shim. Fully autonomous hip exoskeleton saves metabolic cost of walking. In Robotics and Automation (ICRA), 2016 IEEE International Conference on, pages 4628–4635. IEEE, 2016.

[190] Reza Shadmehr. Learning to predict and control the physics of our movements. Journal of neuroscience, 37(7):1663–1671, 2017.

[191] Reza Shadmehr and Ferdinando A Mussa-Ivaldi. Adaptive representation of dynamics during learning of a motor task. Journal of neuroscience, 14(5):3208–3224, 1994.

[192] Kaymie Shiozawa, Jongwoo Lee, Marta Russo, Dagmar Sternad, and Neville Hogan. Frequency-dependent force direction elucidates neural control of balance. Journal of neuroengineering and rehabilitation, (accepted).

[193] Cole S Simpson, Cara G Welker, Scott D Uhlrich, Sean M Sketch, Rachel W Jackson, Scott L Delp, Steve H Collins, Jessica C Selinger, and Elliot W Hawkes. Connecting the legs with a spring improves human running economy. Journal of Experimental Biology, pages jeb–202895, 2019.

[194] Seungmoon Song and Hartmut Geyer. A neural circuitry that emphasizes spinal feedback generates diverse behaviours of human locomotion. The Journal of physiology, 593(16):3493–3511, 2015.

[195] Seungmoon Song and Hartmut Geyer. Predictive neuromechanical simulations indicate why walking performance declines with ageing. The Journal of physiology, 596(7):1199–1210, 2018.

[196] Seungmoon Song, Łukasz Kidziński, Xue Bin Peng, Carmichael Ong, Jennifer L Hicks, Serge Levine, Christopher Atkeson, and Scot Delp. Deep reinforcement learning for modeling human locomotion control in neuromechanical simulation. bioRxiv, 2020.

[197] Eduardo D. Sontag. Mathematical Control Theory, volume 6 of Texts in Applied Mathematics. Springer New York, New York, NY, 1998.

[198] Manoj Srinivasan. Fifteen observations on the structure of energy-minimizing gaits in many simple biped models. Journal of the Royal Society Interface, 8(54):74–98, 2011.

[199] Manoj Srinivasan and Andy Ruina. Computer optimization of a minimal biped model discovers walking and running. Nature, 439(7072):72–75, 2006.

[200] Dagmar Sternad. It's not (only) the mean that matters: variability, noise and exploration in skill learning. Current opinion in behavioral sciences, 20:183–195, 2018.

[201] Danielle M Stramel, Robert M Carrera, Sam A Rahok, Joel Stein, and Sunil K Agrawal. Effects of a person-following light-touch device during overground walking with visual perturbations in a virtual reality environment. IEEE Robotics and Automation Letters, 4(4):4139–4146, 2019.

[202] Steven H Strogatz. Nonlinear dynamics and chaos with student solutions manual: With applications to physics, biology, chemistry, and engineering. CRC press, 2018.

[203] Easton Tackett and Jeff Nessler. Sensorimotor synchronization during gait is altered by the addition of variability to an external cue. Human Movement Science, 71:102626, 2020.

[204] Gentaro Taga. Emergence of bipedal locomotion through entrainment among the neuro-musculo-skeletal system and the environment. Physica D: Nonlinear Phenomena, 75(1-3):190–208, 1994.

[205] Gentaro Taga, Yoko Yamaguchi, and Hiroshi Shimizu. Self-organized control of bipedal locomotion by neural oscillators in unpredictable environment. Biological cybernetics, 65(3):147–159, 1991.

[206] Carly M Thalman, Marielle Debeurre, and Hyunglae Lee. Entrainment during human locomotion using a soft wearable ankle robot. IEEE Robotics and Automation Letters, 6(3):4265–4272, 2021.

[207] Jenna E Thorp and Peter Gabriel Adamczyk. Mechanisms of gait phase entrainment in healthy subjects during rhythmic electrical stimulation of the medial gastrocnemius. Plos one, 15(10):e0241339, 2020.

[208] Austin Tielke, Jooeun Ahn, and Hyunglae Lee. Non-ideal behavior of a treadmill depends on gait phase, speed, and weight. Scientific reports, 9(1):1–12, 2019.

[209] Lena H Ting and Jane M Macpherson. A limited set of muscle synergies for force control during a postural task. Journal of neurophysiology, 93(1):609–613, 2005.

[210] Emanuel Todorov. Optimality principles in sensorimotor control. Nature neuroscience, 7(9):907–915, 2004.

[211] Emanuel Todorov and Michael I. Jordan. Optimal feedback control as a theory of motor coordination. Nature Neuroscience, 5:1226–1235, 2002.

[212] Edison Tse and H Weinert. Structure determination and parameter identification for multivariable stochastic linear systems. IEEE Transactions on Automatic Control, 20(5):603–613, 1975.

[213] Sarah F. Tyson, Marie Hanley, Jay Chillala, Andrea Selley, and Raymond C. Tallis. Balance disability after stroke. Physical Therapy, 86(1):30—38, 2006.

[214] United Nations, Department of Economic and Social Affairs, Population Division. World Population Prospects: The 2017 Revision, Key Findings and Advance Tables. ESA/P/WP/248. `https://population.un.org/wpp/Publications/Files/WPP2017_KeyFindings.pdf`, 2017.

[215] Herman van der Kooij, Ron Jacobs, Bart Koopman, and Frans van der Helm. An adaptive model of sensory integration in a dynamic environment applied to human stance control. Biological cybernetics, 84(2):103–115, 2001.

[216] Herman Van Der Kooij and Robert J Peterka. Non-linear stimulus-response behavior of the human stance control system is predicted by optimization of a system with sensory and motor noise. Journal of computational neuroscience, 30(3):759–778, 2011.

[217] Herman van der Kooij, Edwin van Asseldonk, and Frans CT van der Helm. Comparison of different methods to identify and quantify balance control. Journal of neuroscience methods, 145(1-2):175–203, 2005.

[218] Dario J Villarreal and Robert D Gregg. A survey of phase variable candidates of human locomotion. In 2014 36th Annual International Conference of the IEEE Engineering in Medicine and Biology Society, pages 4017–4021. IEEE, 2014.

[219] Dario J Villarreal and Robert D Gregg. Controlling a powered transfemoral prosthetic leg using a unified phase variable. In Wearable Robotics, pages 487–506. Elsevier, 2020.

[220] Dario J Villarreal, Hasan A Poonawala, and Robert D Gregg. A robust parameterization of human gait patterns across phase-shifting perturbations. IEEE Transactions on Neural Systems and Rehabilitation Engineering, 25(3):265–278, 2016.

[221] Saurabh Vyas, Matthew D Golub, David Sussillo, and Krishna V Shenoy. Computation through neural population dynamics. Annual Review of Neuroscience, 43:249–275, 2020.

[222] Wei Wang and Jean-Jacques E Slotine. On partial contraction analysis for coupled nonlinear oscillators. Biological cybernetics, 92(1):38–53, 2005.

[223] Edward P Washabaugh, Edward S Claflin, R Brent Gillespie, and Chandramouli Krishnan. A novel application of eddy current braking for functional strength training during gait. Annals of biomedical engineering, 44(9):2760–2773, 2016.

[224] Eric R Westervelt, Jessy W Grizzle, Christine Chevallereau, Jun Ho Choi, and Benjamin Morris. Feedback control of dynamic bipedal robot locomotion. CRC press, 2018.

[225] David A Winter. Biomechanics and motor control of human movement. John Wiley & Sons, 2009.

[226] David A. Winter, Aftab E. Patla, Shirley Rietdyk, and Milad G. Ishac. Ankle muscle stiffness in the control of balance during quiet standing. Journal of Neurophysiology, 85(6):2630–2633, 2001.

[227] Sophie Wist, Julie Clivaz, and Martin Sattelmayer. Muscle strengthening for hemiparesis after stroke: A meta-analysis. Annals of Physical and Rehabilitation Medicine, 59(2):114–124, 2016.

[228] Jonathan R Wolpaw and Ann M Tennissen. Activity-dependent spinal cord plasticity in health and disease. Annual review of neuroscience, 24(1):807–843, 2001.

[229] Ming Wu, Janis Kim, Deborah J Gaebler-Spira, Brian D Schmit, and Pooja Arora. Robotic resistance treadmill training improves locomotor function in children with cerebral palsy: a randomized controlled pilot study. Archives of physical medicine and rehabilitation, 98(11):2126–2133, 2017.

[230] Ming Wu, Jill M Landry, Brian D Schmit, T George Hornby, and Sheng-Che Yen. Robotic resistance treadmill training improves locomotor function in human spinal cord injury: a pilot study. Archives of physical medicine and rehabilitation, 93(5):782–789, 2012.

[231] XSENS. Mti 100-series specifications, xsens, 2006.

[232] Momoko Yamagata, Kreg Gruben, Ali Falaki, Wendy L. Ochs, and Mark L. Latash. Biomechanics of vertical posture and control with referent joint configurations. Journal of Motor Behavior, 2020.

[233] Akio Yamamoto, Shun Sasagawa, Naoko Oba, and Kimitaka Nakazawa. Behavioral effect of knee joint motion on body's center of mass during human quiet standing. Gait and Posture, 41(1):291–294, 2015.

[234] Heung-Suk Yang and Hyun-Do Nam. On the identification of the multivariable stochastic linear systems. The Korean Institute of Electrical Engineers, 31(5):51–57, 1982.

[235] Sheng-Che Yen, Brian D Schmit, Jill M Landry, Heidi Roth, and Ming Wu. Locomotor adaptation to resistance during treadmill training transfers to overground walking in human sci. Experimental brain research, 216(3):473–482, 2012.

[236] Aaron J. Young and Daniel P. Ferris. State of the art and future directions for lower limb robotic exoskeletons. IEEE Transactions on Neural Systems and Rehabilitation Engineering, 25(2):171–182, 2017.

[237] Aaron J Young, Jessica Foss, Hannah Gannon, and Daniel P Ferris. Influence of power delivery timing on the energetics and biomechanics of humans wearing a hip exoskeleton. Frontiers in bioengineering and biotechnology, 5:4, 2017.

[238] George Udny Yule. On a method of investigating periodicities disturbed series, with special reference to wolfer's sunspot numbers. Philosophical Transactions of the Royal Society of London, A226(636-646):267–298, 1927.

[239] Juanjuan Zhang, Pieter Fiers, Kirby A Witte, Rachel W Jackson, Katherine L Poggensee, Christopher G Atkeson, and Steven H Collins. Human-in-the-loop optimization of exoskeleton assistance during walking. Science, 356(6344):1280–1284, 2017.

[240] Zhaoran Zhang and Dagmar Sternad. The primacy of rhythm: how discrete actions merge into a stable rhythmic pattern. Journal of neurophysiology, 121(2):574–587, 2019.